Diss. ETH No. 14906

First Study of the Stopping Muon Sample with the ICARUS T600 Detector

A dissertation submitted to the

Swiss Federal Institute of Technology Zürich

for the degree of

Doctor of Natural Sciences

presented by

Francisco Javier RICO CASTRO

Dipl. Phys. University of Granada
born on December 2nd 1973, in Granada/Spain
citizen of Spain

accepted on the recommendation of
Prof. Dr. André Rubbia, examiner
and
Prof. Dr. Wulf Fetscher, co-examiner

November 2002

Abstract

A first study of the stopping muons measured with the very large liquid argon (LAr) time projection chamber, ICARUS T600, is presented. The ICARUS detector will be installed in the Gran Sasso underground laboratory in Italy, to study neutrino oscillations and to search for nucleon decays. The studied muons have been produced by interactions of cosmic rays in the atmosphere and stopped inside the detector's sensitive volume. The data have been acquired during the technical run, testing the detector at the surface of the earth in Pavia (Italy) during summer 2001. We have performed a first analysis of 259 stopping muon events from three days of data taking. The tools for the three-dimensional reconstruction of general events have been developed and optimized for the stopping muon event topology. The events reconstructed with these tools have been used to perform several analyses. First, we have determined the attachment rate of the drift electrons to electro-negative impurities in the LAr volume, parameterized by the free electron lifetime. The measured lifetimes for the considered data taking period are between 1.2 and 1.4 ms. For an electric drift field of 500 V/cm, this translates into a mean drift distance of electrons, before being captured by impurities, of 1.9 to 2.2 m, which has to be compared to the longest possible drift distance in the detector of 1.5 m. The charge collected at the wires of the drift chamber has been corrected for the effect of electron attachment in order to calculate the charge of drift electrons per crossed distance produced by the ionizing particle (muon) along its track. A comparison of the corrected measured charge with the theoretical expectation from the energy loss has been used to perform a determination of the electron recombination factor (R) as a function of the energy loss in LAr, at an electric field of 500 V/cm. A linear dependence of R^{-1} on dE/dx has been found, with a slope of 0.13 ± 0.01 cm/MeV and a value of $R_{mip} = 0.604 \pm 0.008$ for minimum ionizing particles. These results are used for a complete calorimetric reconstruction of the event sample. Next, we have studied the sample of muon decay electrons. We have measured the value of the Michel parameter ρ from the electron energy spectrum, obtaining $\rho = 0.77 \pm 0.22$ (stat.) ± 0.10 (syst.). A reduction of the error to an overall 10% is expected when the whole event sample available from the T600 technical run will be included. From a comparison of the measured and the a Monte Carlo generated electron energy spectra, the energy resolution in the range [0–53] MeV has been determined to be $\sigma/E = (9 \pm 1)\%/\sqrt{E[\mathrm{MeV}]} \oplus (3.9 \pm 0.2)\%$. Finally, we have studied the energy resolution which can be achieved when the electron energy is computed from the track length; the resolution found is about 15% for electron energies above 30 MeV, increasing to about 35% at 10 MeV.

These results demonstrate the capability of the novel liquid argon experimental technique to produce high quality data to perform physics analyses, in particular the study of neutrino oscillations with the data collected in the Gran Sasso Laboratory, starting in 2003.

A detailed description of the Slow Control system of the ICARUS T600 detector, and of the off-line analysis of the data acquired during the technical run, is also presented. This system was intended to monitor the behaviour of the detector during the different phases of the run. From the results some important conclusions could be drawn, which lead to a better understanding of the thermodynamical and mechanical behaviour of the detector as a large cryogenic device, using ultra-pure LAr.

Zusammenfassung

Eine erste Analyse der Spuren von gestoppten Myonen, die mit der grossen Flüssig-Argon (LAr) Driftkammer ICARUS T600 gemessen wurden, wird vorgestellt. Der ICARUS-Detektor soll im Gran Sasso Untergrundlabor in Italien aufgebaut werden, um Neutrino-Oszillationen zu studieren und nach Nukleonzerfällen zu suchen. Die Myonen wurden durch Wechselwirkungen von kosmischen Strahlen in der Atmosphäre produziert und stoppten im empfindlichen Volumen des Detektors. Die Daten wurden während des technischen Runs gesammelt, mit dem im Sommer 2001 der Detektor in Pavia, Italien, an der Erdoberfläche getestet wurde.
Wir haben eine erste Analyse von 259 gestoppten Myonen durchgeführt, was der Anzahl von Ereignissen von drei Tagen Datennahme entspricht. Die Programme zur dreidimensionalen Rekonstruktion von Ereignissen wurden entwickelt und für die Ereignis-Topologie von gestoppten Myonen optimiert. Mit den rekonstruierten Myon-Ereignissen wurden verschiedene Analysen durchgeführt. Zuerst haben wir die Einfangsrate der Driftelektronen durch elektronegative Verunreinigungen im flüssigen Argon bestimmt und durch die Lebensdauer von freien Elektronen im Argon parametrisiert. Die Lebensdauern, die während der betrachteten Periode gemessen wurden, liegen zwischen 1.2 und 1.4 ms. Für ein elektrisches Driftfeld von 500 V/cm entspricht dies einer mittleren Driftdistanz der Elektronen, bevor sie eingefangen werden, von 1.9 bis 2.2 m; zum Vergleich: die längste Driftdistanz im Detektor beträgt 1.5 m. Die auf den Drähten der Driftkammer gesammelte Elektronenladung wurde korrigiert für den Effekt des Elektroneneinfangs, um die Ladung der Driftelektronen, die durch das ionisierende Teilchen (Myon) entlang seiner Spur pro Längeneinheit erzeugt wurde, zu berechnen. Durch einen Vergleich der korrigierten gemessenen Ladung mit der vom Energieverlust theoretisch erwarteten Ionisationsladung wurde zum ersten Mal der Elektronen-Rekombinationsfaktor (R) als Funktion des Energieverlusts in flüssigem Argon bestimmt, bei einer elektrischen Feldstärke von 500 V/cm. Eine lineare Abhängigkeit von R^{-1} vom Energieverlust pro Längeneinheit wurde gefunden, mit einer Steigung von 0.13 ± 0.01 cm/MeV und einem Wert für minimumionisierende Teilchen von $R_{mip} = 0.604 \pm 0.008$. Diese Resultate wurden für eine komplette kalorimetrische Rekonstruktion der Ereignisse verwendet. Als Nächstes wurden die Elektronen vom Myonzerfall studiert. Der Michel-Parameter ρ wurde aus dem gemessenen Elektronen-Energiespektrum zu $\rho = 0.77 \pm 0.22 \pm 0.10$ bestimmt. Eine Reduktion des totalen Fehlers auf 11% wird erwartet, wenn alle Ereignisse vom technischen Run analysiert sind. Aus einem Vergleich der gemessenen Elektronenenergie mit den Resultaten einer Monte Carlo Studie von Zerfallselektronen wurde die Energieauflösung im Bereich [0–53] MeV zu $\sigma/E = (9 \pm 1)\%/\sqrt{E[\mathrm{MeV}]} \oplus (3.9 \pm 0.2)\%$ bestimmt. Schliesslich haben wir die Energieauflösung untersucht, die man von einer Energiemessung aus der Spurlänge erhält; die gefundene Auflösung ist ungefähr 15% für Elektronenergien über 30 MeV und ungefähr 35% bei 10 MeV.

Diese Resultate zeigen, dass die neuartige Experimentiertechnik mit flüssigem Argon Daten hoher Qualtät für die Physikanalysen liefert, insbesondere für das Studium von Neutrino-Oszillationen mit den Daten vom ICARUS-Detektor aus dem Gran Sasso Untergrundlabor, mit Beginn im Jahr 2003.

Eine detaillierte Beschreibung der "Slow Control" Sensoren des ICARUS-Detektors und der Analyse der Sensordaten vom technischen Runwird wird auch vorgestellt. Die "Slow Control" Sensoren dienen der Überwachung des Detektors während den verschiedenen Phasen des Runs. Aus den Resultaten konnten einige wichtige Schlüsse gezogen werden, die zu einem besseren Verständnis des thermodynamischen und mechanischen Verhaltens dieses grossen kryogenischen Detektors aus ultra-reinem flüssigem Argon geführt haben.

Contents

Abstract/Zusammenfassung i

List of figures xi

List of tables xiv

Introduction 1

1 Neutrino physics 3

1.1 Neutrino mass . . . 3

1.2 Neutrino oscillations . . . 6

2 The ICARUS project 11

2.1 Working principles of the LAr TPC . . . 11

2.1.1 Detection principle . . . 12

2.1.2 Technical considerations . . . 15

2.2 The ICARUS T600 detector . . . 19

2.2.1 ICARUS T600 as a milestone of the ICARUS project . . . 19

2.2.2 General description of the T600 detector . . . 20

2.2.3 The technical run in Pavia . . . 26

2.3 Physics program . . . 32

3 The ICARUS T600 Slow Control System 37

3.1 Description of the system . . . 37

3.1.1 LAr level meters . . . 38

3.1.2 Position meters . . . 42

3.1.3 Electronics . . . 49

3.1.4 Data acquisition and display software . . . 55

3.2 Results from the T600 technical run . . . 58
3.2.1 Calibration and sensitivity evaluation . . . 58
3.2.2 Wall movement . . . 65
3.2.3 Cooling down of the cryostat . . . 70
3.2.4 Thermal contraction of the frame and the cryostat . . . 70
3.2.5 LAr filling . . . 73
3.2.6 LAr level during the data taking . . . 74
3.2.7 LAr temperature during the data taking . . . 74
3.2.8 LAr thermal contraction . . . 76
3.2.9 Cryostat draining . . . 77
3.2.10 Heat current density . . . 79
3.2.11 Wire movement . . . 79
3.2.12 Recovery of the wall position . . . 81
3.3 Conclusions . . . 81

4 T600 data event reconstruction 85
4.1 Hit identification . . . 86
4.1.1 Hit identification algorithm . . . 86
4.1.2 Evaluation of the hit identification algorithm . . . 92
4.2 Fine hit reconstruction . . . 93
4.2.1 Fine hit reconstruction algorithm . . . 94
4.2.2 Evaluation and comparison of the reconstruction methods . . . 98
4.3 Cluster reconstruction . . . 100
4.3.1 Cluster reconstruction algorithm . . . 101
4.3.2 Evaluation of the cluster reconstruction . . . 105
4.4 Three-dimensional hit reconstruction . . . 107
4.4.1 Transforming wire/drift coordinates into 3D Cartesian coordinates . . . 107
4.4.2 3D reconstruction algorithm for a hit . . . 108
4.4.3 Evaluation of the 3D reconstruction of hits . . . 112
4.5 Conclusions . . . 112

5 The stopping muon sample 119
5.1 Event selection . . . 119
5.1.1 Visual scanning . . . 119

5.1.2 Event quality selection 120
5.2 Muon reconstruction 122
5.2.1 Spatial reconstruction 122
5.2.2 Kinematic variables 126
5.3 Electron reconstruction 133
5.3.1 Spatial reconstruction 133
5.3.2 Kinematic variables 135
5.4 Reconstruction of bremsstrahlung photons 139
5.4.1 Identification and spatial reconstruction of photons 140
5.4.2 Kinematic variables 142
5.4.3 Evaluation of the reconstruction algorithm 142

6 Data analysis **147**
6.1 Measurement of the drift electron lifetime 147
6.1.1 Measurement method 148
6.1.2 Results 153
6.2 Measurement of the electron recombination factor 158
6.2.1 Measurement of the recombination factor for minimum ionizing particles . 159
6.2.2 Determination of t_0 161
6.2.3 Measurement of the parameters in Birks' law 163
6.2.4 Lower bound of the δ-ray detection threshold 168
6.2.5 Conclusions on the determination of the recombination factor 172
6.3 Electron sample 173
6.3.1 Electron energy spectrum and determination of the Michel parameters . . 174
6.3.2 Electron energy resolution 182
6.3.3 Angular distribution 186
6.3.4 Range 188

Conclusions **195**

Acknowledgements **199**

Bibliography **201**

Curriculum Vitae **207**

List of Figures

2.1 Ionization chamber working principle 12
2.2 3D imaging principle 14
2.3 Particle identification in ICARUS 16
2.4 Artist's view of the ICARUS T600 cryostat 20
2.5 Cross-sectional view of the structure of the aluminum honeycomb panels 21
2.6 Cross-sectional view of the insulation panels 21
2.7 Internal view of the T600 first half-module 24
2.8 Electromagnetic shower 27
2.9 Muon decay 28
2.10 Hadron interaction 28
2.11 V_0 interaction 29
2.12 Long muon track 30
2.13 Multiple showers 31
2.14 Multiple muons 31
2.15 L/E resolution 34
2.16 L/E distribution for electron and muon samples 34

3.1 Schematic view of the cryostat seen from the top 38
3.2 Level meters mounted at the back left side of the dewar 41
3.3 Commercial level meter mounted inside the shielding 41
3.4 Precision level meter mounted inside the shielding 42
3.5 Wall position meter attached to the wire chamber frame 43
3.6 Wall position meter drawn in the OUT position 43
3.7 Picture of a wall position meter 44
3.8 Calibration measurements of the wall position meters 45
3.9 Position meter for horizontal wires attached to a spring 46

3.10 Drawing of a position meter for horizontal wires 46
3.11 Decomposed wire position meter 47
3.12 Calibration of the position meters for the horizontal wires 48
3.13 Drawing of the position meter for vertical wires 49
3.14 Calibration of the position meter for vertical wires 49
3.15 Position meter for vertical wires mounted behind the wire chamber 50
3.16 Outline of the charge capacity meter 51
3.17 Flange with connectors used as feed-through during installation 52
3.18 Linearity of the preamplifier and shaper 53
3.19 Connections to the EDAS ethernet interfaces 54
3.20 The Slow Control electronic setup in Pavia 55
3.21 Principle of operation of the calibration module 56
3.22 Schematic side view of the level meters arrangement at one of the detector's corner 59
3.23 Maximal LAr level difference measured by any two commercial level meters during the LAr filling 59
3.24 Room temperature effect on the capacity meters 60
3.25 Effect of the dynamic recalibration on the sensor measurement 61
3.26 Distributions of the sensor measurements for a time interval of one hour 63
3.27 Distributions of the sensor measurements for a time interval of three days 64
3.28 Pressure as a function of the effective pumping time 66
3.29 Wall displacement as a function of the cryostat pressure 66
3.30 Wall displacement during the vacuum phase 68
3.31 Schematic top view of the cryostat walls at the point of maximal deformation . . 68
3.32 Wall displacement at the end of the vacuum phase 69
3.33 Wall displacement around the re-pressurization point 69
3.34 Temperature in the cryostat during the cooling phase 71
3.35 Thermal contraction of stainless steel and aluminum 72
3.36 Wall displacement during the cooling phase 73
3.37 LAr level in the cryostat as a function of time 74
3.38 LAr level as a function of time during the data taking phase 75
3.39 Average LAr temperature during data taking phase 75
3.40 Average LAr temperature during the pump test 76
3.41 LAr level during the LN_2 pump test 77

3.42 LAr level during the cryostat draining 78
3.43 Temperature in the cryostat after the cooling system stop 78
3.44 Heat current density 80
3.45 Displacement of the springs attached to the wires 80
3.46 Deformation of the cryostat walls 82

4.1 Comparison of functions used in the low frequency noise filter 87
4.2 Effect of the low frequency filter on the wire signal 87
4.3 Example of the PMT induced signal 88
4.4 Hit produced by a mip track on a Collection wire 89
4.5 Effect of the selection of the free parameter values on the hit finding algorithm . 90
4.6 Example of close hits 91
4.7 Parameters characterizing a hit after the hit finding algorithm 92
4.8 Evaluation of the hit detection algorithm performance 93
4.9 Examples of computed local mean and hit window bounds 95
4.10 Function used in the hit fit 96
4.11 Fitted hit signals 97
4.12 Quality of the hit fit 98
4.13 Distribution of the measured hit areas 99
4.14 Comparison of the hit parameters from the two reconstruction methods 100
4.15 Illustration of the cluster pass I performance 102
4.16 Evaluation of the quality of the cluster reconstruction algorithm 104
4.17 Evaluation of the cluster reconstruction efficiency 105
4.18 Example of the performance of the cluster reconstruction algorithm 106
4.19 Sketch of the T600 first half-module and the Cartesian reference frame 108
4.20 Illustration of the wire coordinate restrictions in the hit three dimensional reconstruction 111
4.21 3D reconstruction of a muon decay event 113
4.22 2D projections of a passing through muon event 114
4.23 3D reconstruction of a passing through muon event 115
4.24 2D projections of a low multiplicity hadronic interaction 116
4.25 3D reconstruction of a low multiplicity hadronic interaction 117

5.1 Stopping muon events 120

5.2 Exemplification of δ-ray rejection on muon track reconstruction 123
5.3 Exemplification of crossing track rejection on muon track reconstruction 124
5.4 Measured hit charge distribution 127
5.5 Kinetic energy vs. range for muons 131
5.6 Optimal segment length as a function of the muon momentum 132
5.7 Comparison of measured ϕ values along hits and segments 133
5.8 Energy loss per crossed distance 134
5.9 Uncorrected hit charge distribution for electrons 136
5.10 Energy loss per crossed distance for electrons and positrons 137
5.11 Electron energy loss per crossed distance in LAr 138
5.12 Example of bremsstrahlung track identification 142
5.13 MC bremsstrahlung track features 144
5.14 MC bremsstrahlung energy spectrum 145

6.1 Evolution of the drift electron lifetime 148
6.2 Mean and most probable energy losses per crossed distance for muons 150
6.3 Mean normalized hit area as a function of the normalized drift time 152
6.4 Drift electron lifetime obtained from individual tracks 153
6.5 Distribution of the normalized hit area 154
6.6 Determination of the drift electron lifetime 155
6.7 Average electron lifetime as a function of z and x 157
6.8 Hints for the identification of well determined t_0 events 160
6.9 Measured energy deposition for muons with $t_0 = t_1$ 161
6.10 Distribution of the difference between t_1 and the measured t_0 for the well determined t_0 muon events 163
6.11 Measurement of the recombination factor as a function of dE/dx 165
6.12 Comparison of R as a function of dE/dx 169
6.13 R^{-1} dependence with dE/dx for various T_{cut} values 170
6.14 Fully calibrated and corrected mean energy loss per crossed distance for muons . 171
6.15 MC total and measured energy 174
6.16 Energy spectrum of muon decay electrons 175
6.17 Michel electron reconstructed track energy spectra 176
6.18 Comparison of data and MC bremsstrahlung track features 177
6.19 Michel electron reconstructed total energy spectra. 178

6.20 Comparison of the existing measurements of ρ in μ and τ decays 181
6.21 MC generated and measured electron energy 183
6.22 Electron track energy resolution 184
6.23 Electron total energy resolution 185
6.24 Electron ϕ angle 187
6.25 $\cos\theta$ and $\cos\alpha$ distributions for electrons 187
6.26 $\cos\theta$ distribution for electrons 188
6.27 Electron track range 190
6.28 Comparison of the three range measuring methods 191
6.29 Electron range resolution 192
6.30 Electron range vs. energy 194
6.31 Electron energy measured from the range 194

List of Tables

1.1 Experimental limits on neutrino masses 6
1.2 Features of the different usual neutrino sources 8

2.1 Parameters of some liquids with relatively high electron mobility. 14
2.2 Geometrical characteristics of the ICARUS T600 detector 22
2.3 Working parameters of the T600 cryogenics and purification systems 23
2.4 Main parameters of the internal detector mechanics of the T600 detector 25
2.5 Results from the ICARUS T600 technical run data inventory 27
2.6 Atmospheric neutrino rates 33

3.1 Summary of sensors labeling and positioning 39
3.2 Position of the Pt1000 40
3.3 Height covered by the LAr level meters 41
3.4 Fits to the calibration measurements of the wall position meters 42
3.5 Fits to the calibration measurements of the wire position meters 47
3.6 Measurement dispersion and uncertainty for the different sensor types 62
3.7 Wall displacements as a function of the pressure 65
3.8 Wall displacements at the end of the vacuum phase 67
3.9 Maximal temperature difference during the cooling phase 70
3.10 Maximal elongation of the springs attached to the wires 81

4.1 Values of the free parameters of the hit search algorithm 90
4.2 Values of the free parameters of the close hits resolution algorithm 91
4.3 Values of the parameters used in the hit expansion algorithm 91
4.4 Values of the parameters used in the hit local mean computation 94
4.5 Values of the free parameters of the cluster expansion hit finding algorithm . . . 103
4.6 Values of the free parameters of the cluster reconstruction algorithm 104

4.7 Values of the constant parameters entering the formulae for the three dimensional Cartesian coordinates 108

4.8 Correspondences of the wire coordinates with the different wire planes 109

4.9 Values of the constant parameters in the three dimensional hit reconstruction . . 110

5.1 Event selection efficiency 121

5.2 Values of the free parameters of the muon track spatial reconstruction algorithm 125

5.3 Partial and total energy losses for electron of various energies 138

5.4 Values of the constant parameters used for bremsstrahlung candidate identification 141

6.1 Summary of the runs used in the drift electron lifetime computation 154

6.2 Measured drift electron lifetimes 156

6.3 Average drift electron lifetime as a function of z 157

6.4 Average electron lifetime as a function of x 157

6.5 Existing measurements of the recombination factor in LAr at electric field $E =$ 500 V/cm 168

6.6 Existing measurement of the Birks' law parameters for different values of the electric field 169

6.7 Values of the maximum transferable energy in a single collision for various muon kinetic energies 170

6.8 Summary of the systematic error sources in the determination of ρ 179

6.9 Existing measurements of the ρ parameter 181

Introduction

Pauli proposed in 1930 the existence of of a new neutral, light fermion (neutrino) as a "desperate way out" to explain the continuous spectrum of the electrons emitted in nuclear β-decay [1]. At the time, this idea was considered as revolutionary as the alternative explanation: the violation of the principle of energy conservation. In this way, the neutrino became the first particle proposed as the solution to an elementary particle problem. However, neutrino detection seemed impossible since, according to Bethe and Peierls, the predicted strength of the weak interaction would allow a neutrino to pass through 80 billion kilometers of water without interacting. Neutrino detection requires, thus, both a large target and an enormous flux. The experimental confirmation of the neutrino was provided only 26 years after Pauli's proposal, by C. L. Cowan and F. Reines [2], who observed, for the first time, the absorption processes of free (anti-)neutrinos produced in a fission reactor in a large water target.

Today, the existence of neutrinos is well established. We know that they are electrically neutral and that they come in three different species (*flavours*). However, the question about their masses is still open. The Standard Model of electroweak interactions was constructed on the premise that the failure to observe right-handed neutrinos implies that neutrinos are massless. However, no basic physical principle requires neutrinos to be massless, contrary to the case of the masslessness of the photon, ensured by gauge invariance. Indeed, many of the extensions of the Standard Model predict the existence of massive neutrinos.

Back to 1957, B. Pontecorvo introduced the idea of neutrino oscillation [3]. If neutrinos are massive (and the masses are not all equal), there could occur mixing between neutrino flavours. One of the most striking manifestations of neutrino mixing would be neutrino oscillations, that appear because of the difference between weak interaction neutrino eigenstates and mass eigenstates. Neutrino oscillations are sensitive to the mixing matrix elements and neutrino mass differences, and thus provide a promising arena for a determination of intrinsic neutrino properties.

We have witnessed an explosion of theoretical and experimental work to study neutrino properties both in the laboratory and concerning astrophysical phenomena and cosmological theory. A first firm evidence of neutrino oscillation has been established by the SuperKamiokande detector. This experiment has studied the zenith angle distribution of neutrinos produced by the decay of mesons from cosmic ray interactions in the atmosphere [4]. SuperKamiokande has observed a clear deficit of upward going muon neutrinos, confirmed later by other experiments [5, 6]. The oscillation parameters are beginning to be pinned down from the detailed fits to the angular distributions. On the other hand, the long standing solar neutrino problem has got some major impacts during the last two years. By comparing neutrino-electron scattering rates from SuperKamiokande and first charged current results relying on inverse β-decay from SNO, it already became clear that other active neutrino flavours, besides the electron neutrino, are coming from the sun [7]. Recent results on neutral current data and day/night effects in

charged current events have led SNO to show that, indeed, the dominant part of the solar neutrino flux is composed of a non electron neutrino, but the total flux is in agreement with the Standard Solar model predictions [8, 9].

In spite of these important experimental results, the picture of neutrino physics is still not complete. Many experiments are running or planned for the near future, to obtain independent verification of the oscillation with more precise and/or new techniques, clarify the nature of the oscillation and precisely determine the parameters. Among these experiments, a novel technique, based on a liquid argon time projection chamber (ICARUS), was developed to help elucidate the neutrino oscillation phenomenon. This type of detector presents the advantage of being able to perform simultaneous measurements of neutrinos from different sources (including solar, supernova, atmospheric and long base-line accelerator neutrinos) with a single detector. The detector acts as a homogeneous tracker and a calorimeter of high granularity and accuracy, hence allowing the precise kinematic reconstruction of a large variety of events. The ICARUS project has reached maturity with the construction and full operation on earth's surface of a 735 ton, liquid argon device (ICARUS T600), which has allowed to demonstrate the feasibility of the technique and the detector's capability to collect high quality data for physics analyses. In this dissertation we present the results of the first physics study of cosmic ray data carried out with the ICARUS T600 detector.

The dissertation is organized as follows. The theoretical framework of neutrino masses and oscillations is reviewed in chapter 1. Chapter 2 is devoted to the description of the ICARUS liquid argon detector, as well as a brief summary of the ICARUS physics program. In chapter 3, the thermodynamical and mechanical responses of the T600 detector as a large cryogenic, ultrapure LAr device are studied analyzing the data acquired with the Slow Control system during a technical run, in summer 2001. The different components of the Slow Control system are also extensively described. The rest of the dissertation is devoted to the analysis of the cosmic ray data acquired with the detector during the technical run. Chapter 4 gives a detailed description of the tools developed for the spatial reconstruction of the ICARUS T600 events, and a preliminary evaluation of these tools performed with the acquired cosmic ray data. In chapter 5 we describe the reconstruction of the sample of stopping muon events, the optimization of the spatial reconstruction tools for this particular event topology, as well as the definition of the different kinematic variables describing the events. Finally, in chapter 6 we describe the analysis of the reconstructed data, which includes a measurement of the drift electron lifetime and the electron recombination factor in LAr, as well as the study of the sample of decay electrons.

Chapter 1

Neutrino physics

Neutrinos introduce a family hierarchy problem: why are neutrinos so much lighter than their charged partners in the lepton family? In the Standard Model of elementary particles (SM) the hierarchy is obtained by avoiding to generate neutrino masses through the vacuum expectation value of the scalar Higgs field, which gives origin to all other masses. Thus, neutrinos are exactly massless in the SM. However, this is a rather arbitrary choice and is not imposed by any basic principle. Recent experimental results strongly indicate the existence of oscillations for neutrinos produced in the atmosphere [4, 5, 6] and those coming from the sun [7, 8, 9], which can only happen in the case of finite, non-degenerate neutrino masses. The possibility to consider neutrinos as massive particles opens ways to new properties such as the already mentioned flavor mixing and oscillations, but also magnetic moments and decays, with very important consequences in astrophysics, cosmology and particle physics. Moreover, since most extensions of the SM predict the existence of massive neutrinos, this should be considered as a potentially rich field to look for physics beyond the SM.

In the present section we briefly review the theoretical framework and experimental status of neutrino masses and oscillations[10, 11].

1.1 Neutrino mass

Dirac mass

The standard Dirac particle provides the best known description of a neutral fermion without baryon number, such as a neutrino. The Lagrangian mass term, considering a single lepton generation, is given for a Dirac neutrino field ν by:

$$-\mathcal{L}_{\text{Dirac}} = m_D(\overline{\nu}\nu) \tag{1.1}$$

By defining the Weyl or *chiral* fields ν_L (left-handed neutrino) and ν_R (right-handed neutrino):

$$\nu_L \equiv \frac{1-\gamma_5}{2}\,\nu, \qquad \nu_R \equiv \frac{1+\gamma_5}{2}\,\nu \tag{1.2}$$

the Dirac neutrino mass term can be rewritten as:

$$-\mathcal{L}_{\text{Dirac}} = m_D[(\overline{\nu}_L\nu_R + \overline{\nu}_R\nu_L)] \tag{1.3}$$

which mixes the fields of opposite chirality. This is the type of mass generated in the SM. Thus, in the absence of right-handed neutrino (ν_R) and left-handed anti-neutrino components[1] (ν_L^c), neutrinos become massless. This mass term is invariant under a global gauge transformation $\nu \to e^{i\alpha}\,\nu$, which implies the conservation of a global quantum number, in this case the lepton number L.

All experiments to date are consistent with the neutrino being left-handed and the anti-neutrino being right-handed. Whether the two other states, ν_R and ν_L^c exist in Nature (in analogy to the electron states) is at present unknown. The simplest case of a SM extension resulting in massive neutrinos is the assumption of the existence of right-handed (left-handed) (anti-)neutrino fields, ν_R (ν_L^c) which, by definition, do not take part in the weak interactions (*sterile* neutrinos). The mass term can be generated by the Higgs mechanism, as for the charged leptons. The main theoretical problem associated with this mechanism is the smallness of the neutrino mass compared to the mass of the charged leptons. Since the particle masses are directly determined by the particle couplings to the Higgs field, this implies couplings differing by several orders of magnitude for particles of the same generation. The relation of lepton masses of different generations may be thought of as being "accidental", but a large mass difference of particles belonging to the same SU(2) doublet is more difficult to accept.

Majorana mass

Electrons and positrons are clearly different particles, since they have opposite electric charges. However, we have examples of neutral particles, such as the π^0, which coincide with their antiparticles. Majorana [12] first proposed that a neutral fermion could have this property. Although a Lagrangian mass term of the form given in equations 1.1 and 1.3 is the unique way to describe the mass of charged fermions, this is not the case for neutral fermions. Using neutrino and anti-neutrino fields, the mass terms we can build consistent with Lorentz invariance are $\overline{\nu}\nu$, $\overline{\nu^c}\nu^c$, $\overline{\nu^c}\nu$ and $\overline{\nu}\nu^c$. The first two are the Dirac mass terms (equation 1.1), the other two may be written in terms of:

$$\overline{\nu_R^c}\nu_L, \quad \overline{\nu_L}\nu_R^c, \quad \overline{\nu_L^c}\nu_R, \quad \overline{\nu_R}\nu_L^c \tag{1.4}$$

Let us construct a Majorana neutrino as

$$\nu_M = \nu_L + \nu_R^c \tag{1.5}$$

then, the mass term is given by

$$-\mathcal{L}_{\text{Majorana}} = m_L\,\overline{\nu_M}\nu_M = m_L(\overline{\nu_R^c}\nu_L + \overline{\nu_L}\nu_R^c) \tag{1.6}$$

Therefore, a mass term for purely left-handed particle states (and right-handed anti-particle states) can be constructed. In contrast to the Dirac case, a neutrino mass term is possible even without additional (unobserved) right-handed neutrinos. It requires just one helicity state of the particle and the opposite helicity state of the anti-particle. However, a right-handed Majorana neutrino can be equivalently defined as $\nu'_M = \nu_R + \nu_L^c$, whose associated mass term is given by:

$$-\mathcal{L}_{\text{Majorana}} = m_R\,\overline{\nu'_M}\nu'_M = m_R(\overline{\nu_L^c}\nu_R + \overline{\nu_R}\nu_L^c) \tag{1.7}$$

The right-handed Majorana neutrinos do not need to be the "partner" of the (ordinary) left-handed neutrino, but could be, instead, an independent heavier state.

[1] We assume the notation $\nu_L^c \equiv (\nu^c)_L$, which is a left-handed field, contrary to $(\nu_L)^c$, which is a right-handed field.

The Majorana mass term is not invariant under global gauge transformations. In fact, ν_M and ν'_M do not have a well-defined lepton number since they are linear combinations of two neutrinos with opposite lepton numbers. That is, a lepton number violation of $\Delta L = \pm 2$ is produced when considering a Majorana mass term.

Although Majorana and Dirac neutrinos have different properties, the differences vanish with the neutrino mass. However, the Majorana mass term for neutrinos is necessarily different from the (Dirac) mass term of the charged leptons, and a renormalizable theory can not be constructed using the Higgs sector of the SM. In general, indications for a Majorana mass of the neutrino would be interpreted as a hint of new physics beyond the SM, whereas a Dirac mass could be accommodated within the model by the minimal extension of adding the right-handed neutrino states.

Mixed Dirac-Majorana mass

A general neutrino mass term can involve both Dirac and Majorana mass terms. If we define the neutrino field as

$$\nu = \begin{pmatrix} \nu_L \\ \nu_L^c \end{pmatrix} \tag{1.8}$$

the Dirac-Majorana mass term can be written as

$$-\mathcal{L}_{\text{mixed}} = \frac{1}{2}\overline{\nu^c}\mathcal{M}\nu + \text{h.c.} = M\,\overline{\nu_L}\nu_R + \frac{1}{2}(m_L\,\overline{\nu_R^c}\nu_L + m_R\,\overline{\nu_L^c}\nu_R) + \text{h.c.} \tag{1.9}$$

with

$$\mathcal{M} = \begin{pmatrix} m_L & m_D \\ m_D & m_R \end{pmatrix} \tag{1.10}$$

where m_D is the Dirac mass (see equation 1.1), and m_L and m_R the Majorana masses (equations 1.6 and 1.7). As in the pure Majorana case, the mass matrix is symmetric. We can diagonalize $\mathcal{M}$ and obtain two Majorana mass eigenvalues:

$$m_{1,2} = \frac{1}{2}\sqrt{4m_D^2 + (m_R - m_L)^2} \pm \frac{m_R - m_L}{2} \tag{1.11}$$

corresponding to the eigenstates

$$\nu_1 = i\cos\theta\nu_L - i\sin\theta\nu_L^c \tag{1.12}$$

$$\nu_2 = \sin\theta\nu_L + \cos\theta\nu_L^c \tag{1.13}$$

The mixing angle θ is given by

$$\tan 2\theta = \frac{2m_D}{m_R - m_L} \tag{1.14}$$

There are two interesting limiting cases to be studied. In the first case, we consider $m_D \gg m_L, m_R$. Then, ν_1 and ν_2 become almost degenerate with mass $m_{1,2} \simeq m_D$ and mixing angle $\theta \simeq 45°$. Thus, the two Majorana eigenstates form a *pseudo-Dirac* neutrino state, since the associated mass term in the Lagrangian conserves leptonic number; ν_L and ν_R are the active and sterile components in the SM weak interactions, respectively, and are maximally mixed. However, as we have already mentioned, this solution would not explain the smallness of the neutrino mass.

An especially interesting case is the see-saw limit [13], given by $m_R \gg m_D \gg m_L$, in which case the masses of ν_1 and ν_2 are given by

$$m_1 \simeq m_R, \qquad m_2 \simeq \frac{m_D^2}{m_R} \tag{1.15}$$

which differ enormously from each other; m_2 increases with decreasing m_1 for a fixed value of m_D. Furthermore, the mixing angle θ approaches zero, so that ν_1 and ν_2 are completely decoupled. Usually, m_D is assumed to be of the order of the quark and charged lepton masses, and m_R is a large mass of the order of some unification scale beyond the SM. This forces the mass of the ordinary neutrino to be small, and postulates a very heavy right-handed neutrino, therefore decoupling it from interactions in the accessible energy range. This see-saw mechanism is by far the best explanation of the smallness of the ordinary neutrino masses.

Experimental situation

Direct searches for neutrino mass are based on kinematic arguments and do not distinguish between Dirac and Majorana mass types. So far, no indications in favour of non-zero mass have been found for any of the three neutrino families. Current experimental limits are summarized in table 1.1 and commented below [14].

ν type	limit		CL (%)
ν_e	3	eV	95
ν_μ	190	keV	90
ν_τ	18.2	MeV	95

Table 1.1: Experimental upper limits on neutrino masses.

Searches for ν_e mass are performed by studying the shape of the electron energy spectrum in nuclear β-decay. The total available energy in the decay is given by the Q-value of the reaction, $M_Z - M_{Z+1}$ (the difference between the initial and final nuclear masses). The energy is shared by the produced electron and neutrino. The minimum energy the neutrino can carry is its mass, and thus, the end point of the electron spectrum, given by $E_{max} = M_Z - M_{Z+1} - m_{\nu_e}$ is sensitive to the mass of the neutrino. The best constraints on m_{ν_e} come from the shape of the energy spectrum of electrons emitted in the Tritium decay (^{3}H $\rightarrow ^3$He $e^- \nu_e^c$) which, because of the low Q-value, allows to notice the effect in the spectrum even for relatively small m_{ν_e}.

The best upper bounds on m_{ν_μ} come from the measurement of the momentum of the μ produced in the decay of pions at rest ($\pi \rightarrow \mu\nu_\mu$). Finally, the best limit on m_{ν_τ} comes from the study of the τ 3-prong ($\tau^- \rightarrow 2\pi^-\pi^+\nu_\tau$) and 5-prong ($\tau^- \rightarrow 3\pi^- 2\pi^+(\pi^0)\nu_\tau$) decay modes of τ's produced in electron-positron collisions at LEP.

1.2 Neutrino oscillations

Neutrino mixing

The hypothesis of neutrino mixing has first been proposed by B. Pontecorvo for the $\nu_e \rightarrow \nu_e^c$ transitions [3], in analogy with the $K^0 \rightarrow \bar{K}^0$ process. After the discovery of the muon neutrino [15], the concept of neutrino mixing was adapted to oscillations between different

neutrino flavours [16]. This phenomenon appears because the neutrino current (or interaction or flavor) eigenstates ν_α ($\alpha = e, \mu, \tau$), which take part in weak interactions, are generally quantum-mechanical superpositions of different neutrino mass eigenstates ν_i ($i = 1, 2, 3$), which describe the propagation of neutrinos in space-time:

$$\nu_\alpha = \sum_i U_{\alpha i}\, \nu_i \tag{1.16}$$

where U is the unitary 3×3 matrix analogous to the Cabibbo-Kobayashi-Maskawa matrix for quarks. Due to the different propagation of the neutrino mass eigenstates, the flavour content of the propagating neutrino state changes with time. Since the neutrinos are detected by means of charged current processes, sensitive to the neutrino flavour, this oscillating behaviour may be observable.

Neutrino oscillations in vacuum

Let us assume a flavour eigenstate ν_α was produced at $x = 0$ and $t = 0$. The space-time dependence of the free mass eigenstate $\nu_i(t)$ of momentum $\vec{p}$ and energy $E_i = \sqrt{p^2 + m_i^2}$ is

$$\nu_i(t) = e^{i(\vec{p}\vec{x} - E_i t)}\, \nu_i \tag{1.17}$$

It follows from equation 1.16 that the space-time evolution of the state ν_α is given by

$$\nu(t) = e^{i\vec{p}\vec{x}} \sum_i U_{\alpha i}\, e^{-iE_i t} \nu_i \tag{1.18}$$

If the masses m_i are not equal (and non-zero), the three terms of the sum in equation 1.18 get out of phase and the state $\nu(t)$ acquires components ν_β with $\beta \neq \alpha$. The probability with which the neutrino produced as ν_α is converted into ν_β in a different point of space-time is given by:

$$\begin{aligned} P_{\nu_\alpha \to \nu_\beta} &= |\langle \nu_\beta \,|\, \nu(t) \rangle|^2 = \left| \sum_i U_{\beta i}\, e^{-i(E_i t - \vec{p}\vec{x})}\, U^*_{\alpha i} \right|^2 \\ &= \delta_{\alpha\beta} - 4 \sum_{j>i} U_{\alpha i} U^*_{\alpha j} U^*_{\beta i} U_{\beta j}\, \sin^2 \left(\Delta m^2_{ij} \frac{L}{4E} \right) \end{aligned} \tag{1.19}$$

where L is the distance between the production and detection points, and $\Delta m^2_{ij} \equiv m^2_i - m^2_j$. In the last line we have assumed that neutrinos are highly relativistic ($m_i \ll p$ and $L \equiv x = t$). We see that in order to have a non-vanishing oscillation probability it is necessary that at least two neutrino mass states are non-degenerate, and that there exist non-vanishing off-diagonal elements in the matrix U.

This probability satisfies some important relations. First of all, it becomes evident that neutrino oscillation experiments are not directly sensitive to neutrino masses, but to the difference of their squares. CPT invariance implies $P_{\nu_\alpha \to \nu_\beta} = P_{\nu^c_\beta \to \nu^c_\alpha}$. For two flavour mixing (or three or more flavours mixing if CP is conserved), we also have $P_{\nu_\alpha \to \nu_\beta} = P_{\nu_\beta \to \nu_\alpha}$ [17]. These relations are valid when neutrinos propagate in vacuum. When interactions with matter affect the neutrino propagation they may no longer hold because the medium itself is generally not symmetric under CP and CPT. Finally, the unitarity of U guaranties the normalization of the total probability to 1:

$$P_{\nu_\alpha \to \nu_\alpha} = 1 - \sum_{\beta \neq \alpha} P_{\nu_\alpha \to \nu_\beta} \tag{1.20}$$

The complete picture of the neutrino oscillation phenomenon is determined by five free parameters: of the three Δm^2_{ij} appearing in equation 1.19, only two are independent, since $\Delta m^2_{21} + \Delta m^2_{32} = \Delta m^2_{31}$. On the other hand, if we ignore possible CP violation, the matrix U is real and can be parameterized by three independent mixing angles, θ_{12}, θ_{13} and θ_{23}.

For simplicity, it is customary to consider the case of the mixing between two neutrino families only. In such a case, the mixing matrix U is described by only one real mixing angle θ, and the probability of oscillations simplifies to:

$$P_{\nu_\alpha \to \nu_\beta} = \left| \delta_{\alpha\beta} - \sin^2(2\theta) \cdot \sin^2 \left(\Delta m^2 \frac{L}{4E} \right) \right| \tag{1.21}$$

The amplitude of the oscillation is given by $\sin^2(2\theta)$ and the oscillation length (λ) by

$$\lambda = \frac{4\pi\, E}{\Delta m^2} = \frac{2.48\, E\ [\mathrm{GeV}]}{\Delta m^2\ [\mathrm{eV}^2]}\ [\mathrm{km}] \tag{1.22}$$

Thus, in order to observe neutrino oscillations, λ must be less or of the order of the source-detector distance. This can be rewritten as $\Delta m^2 \geq E/L$. Therefore, to search for small squared mass differences, the distance L should be large and/or the energy of the neutrinos should be small.

Back to the general three-flavour mixing framework, we may assume the following hierarchy $m_1 \ll m_2 \ll m_3$, which implies $\Delta m^2_{21} \ll \Delta m^2_{31} \simeq \Delta m^2_{32}$. In this case, the oscillation phenomena tend to decouple and the two-flavour mixing model is a good approximation in limited regions. Each oscillation probability can be written as the sum of a "short" and a "long" component:

$$P_{\nu_\alpha \to \nu_\beta} = P^{short}_{\nu_\alpha \to \nu_\beta} + P^{long}_{\nu_\alpha \to \nu_\beta} \tag{1.23}$$

with

$$\begin{aligned} P^{short}_{\nu_\alpha \to \nu_\beta} &\simeq 4U^2_{\alpha 3} U^2_{\beta 3} \sin^2(\Delta m^2_{31} \frac{L}{4E}) \\ P^{long}_{\nu_\alpha \to \nu_\beta} &= -4U^2_{\alpha 1} U^2_{\beta 1} U^2_{\alpha 2} U^2_{\beta 2} \sin^2(\Delta m^2_{21} \frac{L}{4E}) \end{aligned}$$

If we assume the mixing matrix to be almost diagonal ($\cos\theta_{ij} \gg \sin\theta_{ij}$), then $P_{\nu_e \to \nu_\tau}$ and $P_{\nu_\mu \to \nu_\tau}$ are dominated by the "short" component and are sensitive to m_3, whereas $P_{\nu_\mu \to \nu_e}$ is dominated by the long component and is sensitive to m_2. A neutrino oscillation experiment must be sensitive to either the "short" or both the "short" and "long" oscillations, by selecting the appropriate L/E range. Table 1.2 shows the typical energies, base-lines and minimum detectable Δm^2 for the usual neutrino sources, namely: nuclear reactor, accelerator, cosmic ray interaction with atmosphere and sun.

	reactor	accelerator		atmospheric	solar
		short base-line	long base-line		
E (MeV)	≤ 10	$30 - 10^5$	$30 - 10^5$	10^3	≤ 14
L (m)	10^1–10^2	10^2–10^3	10^4–10^7	10^4–10^7	10^{11}
Δm^2 (eV^2)	10^{-2}	10^{-1}	10^{-4}	10^{-4}	10^{-11}

Table 1.2: Neutrino energies, baseline distances and minimum testable mass square difference for reactor, accelerator, atmospheric and solar neutrinos.

Experimental situation

Three different sources of neutrinos have shown deviations from the SM expectations, consistent with neutrino oscillations:

- The first evidence comes from the LSND experiment [18], observing an effect in the $\nu_\mu^c \to \nu_e^c$ channel with most likely parameters $\Delta m^2 \simeq 1$ eV^2 and $\sin^2 2\theta \simeq 10^{-3}$. However, a large fraction of the allowed region in the parameter space is excluded by other experiments, especially KARMEN [19].
- The second evidence is coming mainly from the measurement performed by SuperKamiokande of the zenith angle distribution of the atmospheric neutrinos [4]. The distribution shows a clear deficit in the upward going ν_μ neutrinos. The observed effect is well described by oscillations with Δm^2 in the range $(1.6\text{–}4)\cdot 10^{-3}$ eV^2 and $\sin^2 2\theta > 0.89$ (at 90% CL) assuming $\nu_\mu \to \nu_\tau$ transitions.
- The third evidence comes from the solar neutrino deficit. The SNO experiment, by measuring independently both, charged and neutral current neutrino interactions, has determined that a substantial part of the total neutrino flux (which agrees with the Standard Solar model predictions) is composed of a flavour different to ν_e [8]. Furthermore, to describe the data, the so called "large mixing angle" (LMA) solution is strongly favoured, having a best fit value of $\Delta m^2 = 5 \cdot 10^{-5}$ eV^2 and a mixing of $\tan^2\theta = 0.34$ [9].

The overall experimental picture appears problematic. Indeed, we observe that we need three different Δm^2 regions in order to explain all experimental observations. With the three ordinary neutrinos, only two squared mass differences are independent. In order to satisfy all experimental constraints, one must therefore invent new schemes with more neutrinos, like for example in the case of new sterile neutrinos. On the other hand, one can argue that one ore more experimental results are incorrect (as we have already pointed out regarding the LSND experiment result). To prove the oscillation for atmospheric and solar neutrinos, new experiments are running at present or are planned for the near future. The oscillation parameters will be precisely determined with reactor and accelerator long baseline experiments. As a long term perspective, the measurement of all the mixing matrix elements together with a possible CP-violation and matter effects (which are at work in the sun), could be explored with what is generally called "neutrino factories" [20].

Chapter 2

The ICARUS project

During the 1960s and 1970s, bubble chamber detectors [21] led to the discovery of many new elementary particles. Filled with a superheated liquid, the bubble chamber creates a track of small bubbles when a charged particle crosses the chamber, locally bringing the liquid to boil. Bubble chambers produce high spatial resolution pictures of ionizing events, and allow a precise investigation of the nuclear processes occurring in the medium. However, in recent times, the use of bubble chambers has been superseded by electronic detectors, since bubble chambers are difficult to trigger, and experiments with high statistics are not really practicable because of the time consuming analysis of bubble chamber pictures. The attempt to merge the superb imaging capabilities of traditional bubble chambers and the advantages of electronic read-out in a single detector led C. Rubbia to propose the liquid argon (LAr) time projection chamber (TPC) in 1977 [22]. The detector is essentially a cryostat filled with a liquified noble gas and equipped with an electronic readout that measures the ionization charge produced by the passage of charged particles. This detector provides three-dimensional imaging and, since the ionization charge is proportional to the energy deposition, also acts as a calorimeter of very fine granularity and high accuracy. Thus, this device is ideal to study particle interactions and does not present the problems of traditional bubble chambers, since the electronic read-out allows the self-triggering and automatic processing and analysis of the events.

ICARUS is a project, proposed in 1985 [23, 24], for the installation of a large LAr TPC in the Gran Sasso Laboratory (LNGS), Italy, for the study of neutrino physics and matter stability. Several years of R&D with prototypes of increasing size have allowed to overcome the major technological problems in the establishment of this technique. In this chapter, we describe the LAr TPC detection technique and its actual realization in the form of the ICARUS T600 detector. Finally, we present a brief summary of its most important physics goals.

2.1 Working principles of the LAr TPC

The LAr TPC inherits the detection principle of the ionization chambers and the multi-wire proportional chambers to provide three-dimensional imaging of ionizing particles traversing a (large) reservoir filled with LAr. It presents higher ionization density compared to gases, but no charge multiplication happens at the wires. Since the measured charge is proportional to the energy lost by the ionizing particle, it also acts as a calorimeter. The technological challenges overcome in the establishment of this technique concern mainly the development of the cryogenics and purification system, and of low noise read-out electronics. The detection technique can be

considered now mature, after the construction and successful operation of prototypes of different scales.

2.1.1 Detection principle

Electronic detection of ionizing events

A *ionization chamber* [25] is a detector which measures the ionization produced by the passage of a charged particle through a given volume (the *sensitive* volume) filled normally with a gas[1]. The simplest case of an ionization chamber consists of a pair of parallel electrodes immersed in a dielectric liquid and connected to a high voltage power supply (see figure 2.1), producing a homogeneous electric field perpendicular to the electrodes and of strength $E = U_0/d$, where U_0 is the applied voltage and d the distance between the electrodes. As a consequence of the passage of an ionizing particle, electrons and positive ions are formed and drift toward the electrodes with opposite polarities. Electrons and ions induce a current on the capacitor plates, that flows across the working resistance R, producing a small voltage signal which can be further processed with a preamplifier.

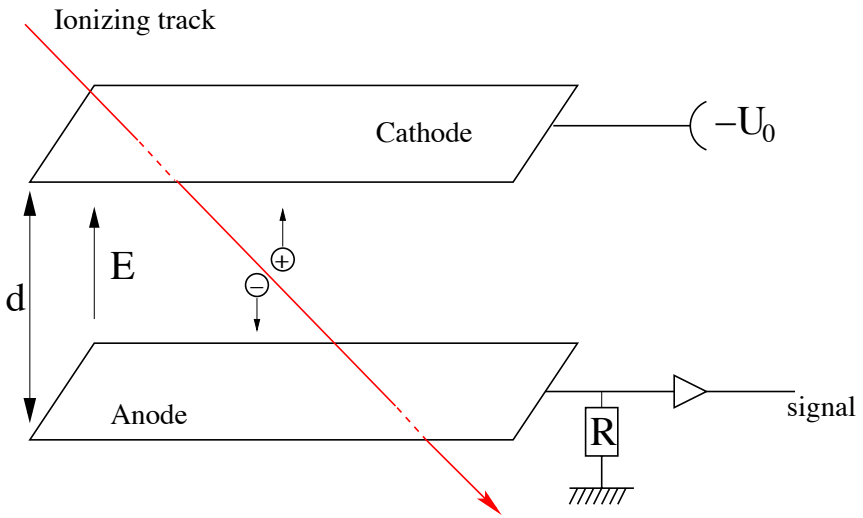

Figure 2.1: Schematic view of the ionization chamber working principle.

Suppose N electron-ion pairs (*charge carriers*) are produced at a given distance from the anode, the work the electric field exerts on the charge carriers is given by:

$$dW = N\, e\, E\, (v^+ + v^-)\, dt \tag{2.1}$$

where v^+ and v^- are the velocities of the positive ions and electrons, respectively. The parallel electrodes of the ionization chamber, acting as a capacitor initially charged with the voltage U_0,

[1] In principle, ionization chambers can also be filled with a liquid or even a solid, since the essential properties are not changed by the state of the counting medium.

will be discharged by an amount dQ due to the transport of the charge carriers in the dielectric medium. The work performed on the charge carriers during the discharging is given by:

$$dW = -U_0\, dQ \tag{2.2}$$

From equations 2.1 and 2.2 we obtain:

$$dQ = -\frac{N\, e\, E\, (v^+ + v^-)}{U_0}\, dt = -\frac{N\, e\, (v^+ + v^-)}{d}\, dt \tag{2.3}$$

The total discharge of the capacitor can be computed by integrating the previous equation:

$$\Delta Q = \Delta Q^+ + \Delta Q^- = -\frac{N\, e}{d}\left(\int_0^{t^+} v^+\, dt + \int_0^{t^-} v^-\, dt\right) = -\frac{N\, e}{d}\left((d - x_0) + x_0\right) = -N\, e \tag{2.4}$$

with ΔQ^+ (ΔQ^-) the total discharge due to the transport of the ions (electrons) in the dielectric, t^+ (t^-) the time the ions (electrons) take to arrive at the cathode (anode), and x_0 the distance between the point of ionization and the anode. In practice, the *mobility* ($\mu = v/E$) of the electrons is several orders of magnitude larger than the one of the ions [26] and the signal ΔQ^+ is spread out over a much larger time. Thus, in practice, the only useful information is given by ΔQ^-.

Selection of the dielectric medium

The choice of liquid argon as the dielectric medium is mainly motivated by two facts [22], namely:

- The liquid has a higher density (about 800 times) and lower charge diffusion (which worsens both the energy and spatial resolutions), than the gaseous media. The drawback is that cryogenic equipment is necessary to maintain the noble gas in the liquid phase.
- It is a noble gas, hence with zero electronegativity so that the electrons can drift over long paths.

Out of the five stable noble gases in nature (He, Ne, Ar, Kr and Xe) the two lightest ones (He and Ne) cannot be used as dielectric medium, due to the formation of micro-bubbles around the electron, which slows down the drift process ($\mu \approx 0.01$ cm^2/Vs) [27]. The electron mobility and other important properties of several liquids is shown in table 2.1. For all heavy liquefied noble gases electrons have a very high mobility. However, only argon has reached the industrial exploitation suitable for the application in a large volume detector. Argon is a by-product of the liquefaction of air and subsequent production of liquid Nitrogen and Oxygen. Argon is relatively abundant in air with a fraction of about 0.9%, and its cost in liquid form is relatively modest.

Imaging of events

As we have seen above, the read-out of the ionization electrons follows very closely the techniques used traditionally in the case of ionization chambers. However, the read-out cannot simply be a charge-collecting process. By replacing the planar anode by an array of sensing electrodes consisting of a plane of multiple parallel wires (hereafter called *wire planes*), we can obtain two-dimensional projections of the ionization point, constraining one spatial coordinate from the wire collecting the charge (or a current being induced) and the other from the drift time. In order to

Liquid	Density (g/cm^3)	dE/dx (MeV/cm)	Radiation length (cm)	Boiling point at 1 atm (°C)	Mobility (cm^2/Vs)
Argon	1.394	2.10	14.0	-185.7	500
Krypton	2.410	3.00	4.85	-153.1	1200
Xenon	3.057	3.79	2.77	-107.1	2200
Methane	0.425	1.02	109.4	-164.0	400
TMS	0.645	1.36	52.4	26.5	90
TMP	0.720	1.58	62.4	233.0	40

Table 2.1: Parameters of some liquids with relatively high electron mobility.

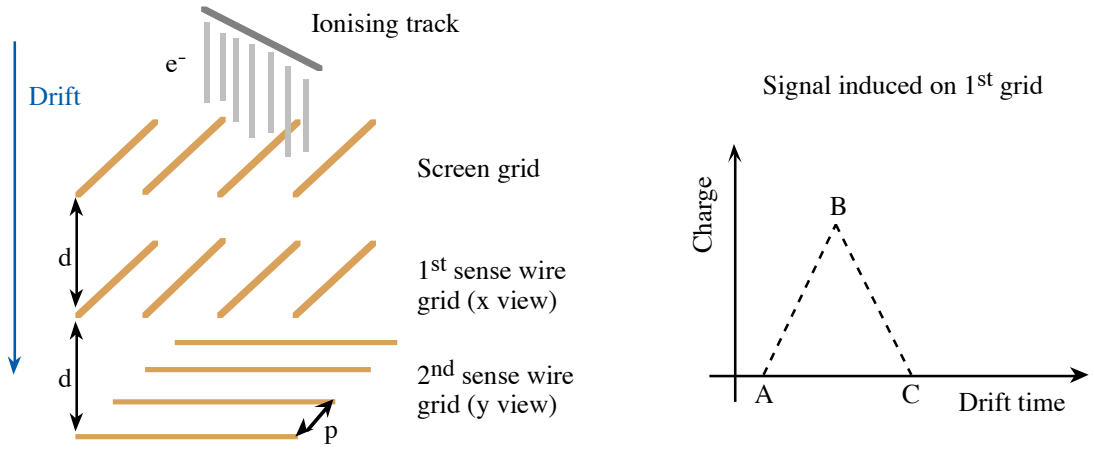

Figure 2.2: Geometry of the grids for multi-dimensional, inductive read-out. As an example, the signal induced by drifting electrons on a wire of the 1st grid is also shown: (A) electrons cross the screen grid, (B) electrons cross the 1st sense wire grid, (C) electrons cross the 2nd sense wire grid.

obtain three-dimensional coordinates, at least two wire planes with different wire orientations are necessary; therefore, the read-out system must be non-destructive. The transparency of a wire plane or grid for electrons drifting along the electric field lines has been calculated and published [28, 29]. It is a function of the ratio of the fields E_1 and E_2, in front and behind the grid respectively, and of the ratio $\rho = 2\pi r/p$ where r is the wire radius and p is the spacing between wires (*pitch*). Full transparency is reached when the following condition is satisfied:

$$\frac{E_2}{E_1} > \frac{1+\rho}{1-\rho} \tag{2.5}$$

The drifting electrons, following the electric field lines, can cross a succession of several planes of parallel tensed wires oriented in different directions (see figure 2.2), where the condition 2.5 is verified. The electrostatic separation between the sensing wires allows a very sharp localization of the drifting charge, hence a good spatial resolution. Each of the wire planes provides a two-dimensional projection of the event image with a common coordinate (the drift time), allowing the three-dimensional reconstruction of the event. The basic three-dimensional pixel (or "bubble") size is determined by the wire pitch and the resolution in the drift direction. A minimum of two wire planes is required to fully determine the three dimensional localization of the "bubbles", although additional planes can be used to resolve ambiguities during the event

reconstruction and improve the spatial resolution.

While approaching a plane, the electrons induce a current only on the wires nearby; when moving away, a current of opposite sign is induced. A detailed analysis of the induced signals for the geometrical configuration displayed in figure 2.2 has been performed by Gatti et al. [30]. Due to the shielding of the adjacent grids, the signals have a limited duration. Only the signals on the wires of the first grid are "prompt", i.e. start as soon as the ionizing particle crosses the chamber, and can be used to determine the reference time for the electron drift (t_0). The time t_0 can be also determined by the coincident detection of the scintillation light produced in the argon, using a suitable system of photomultiplier tubes.

Calorimetry and particle identification

Charged particles traversing the LAr sensitive volume produce ionization electrons in a number proportional to the energy transferred to the LAr. The ionization electrons drift along the electric field lines to the wire planes pushed by the electric field perpendicular to the wire planes, inducing a current on the wires near which they are drifting while approaching the different wire planes. Therefore, each wire of the read-out plane records the energy deposited in a segment of the ionization track. Thus, the combined spatial and calorimetric reconstructions, exploiting the fine granularity and imaging capabilities of the detector, allows the precise measurement of the energy loss per crossed distance (dE/dx) and hence the identification of the ionizing particle.

The complete calorimetric reconstruction of the events requires to take into account the effects of the electron-ion recombination and charge attenuation by electron attachment to electronegative impurities. Both effects reduce the amount of collected charge with respect to the one produced during the ionization. The recombination of ion-electron pairs occurs immediately after the ionization, due to their electrostatic attraction. The recombined electron-ion pairs form excited atomic states that release the energy in the form of (detectable) light. The magnitude of the recombination effect depends on both the electric field and the ionization density (dE/dx). Charge attenuation is due to the attachment of the drift electrons to the electronegative impurities, and depends also on the electric field and on the concentration of electronegative impurities present on the LAr volume. The precise knowledge of these two phenomena allows their off-line unfolding from the calorimetric data.

If the granularity of the read-out electrodes is high enough, a sampling of the energy loss per crossed distance (dE/dx) for several points along the ionization tracks is possible. If, on the other hand, the momentum of the particle is independently known, e.g. from its curvature in a magnetic field, or from its range (for particles stopping in the LAr sensitive volume only), or from multiple scattering, we can determine the mass of the ionizing particle by means of the Bethe-Bloch formula (see later section 5.2.2) of the energy loss per len (dE/dx), and hence identify the ionizing particle. The particle identification capability is illustrated in figure 2.3, where the dE/dx over the range (distance to the end point) of a stopping muon and a stopping kaon events (top), and a sample of stopping pions and kaons (bottom), are compared.

2.1.2 Technical considerations

The particularities of the detection technique described in the two previous sections, require special consideration of certain technical aspects, namely:

- A system to provide the time of the event occurrence (t_0) is needed in order to trigger the

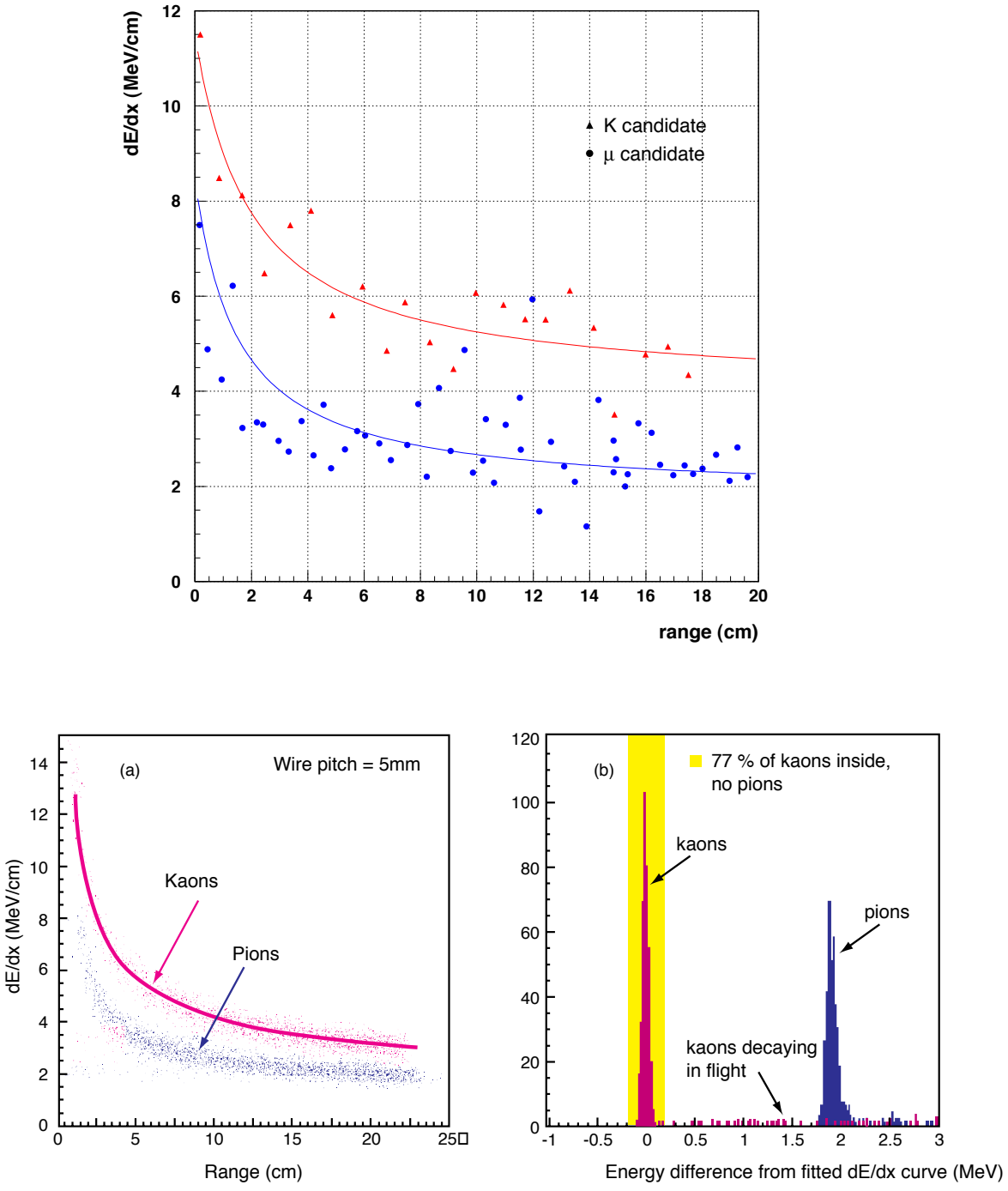

Figure 2.3: Top: Example of discrimination between single kaon and muon events (lines are drawn to guide the eye). Bottom: Discrimination between kaon and pion events.

data acquisition (DAQ) system and to determine the absolute position of the event along the drift direction.

- The electronic read-out system must be capable of detecting the signal produced by a few thousand electrons.
- The level of purity of the LAr must be high enough so that the signal is not strongly degraded along the drift path.

The present solutions provided by the ICARUS collaboration for each of these aspects are summarized below.

Trigger and t_0 determination

The trigger system must be suited for the rare events to be detected underground by ICARUS, and must provide the absolute time of the event occurrence. In principle, the drift time difference between any two points of the projected tracks allows to reconstruct the geometrical topology of the events. However, the absolute position along the drift direction must be known when correcting (off-line) the measured charge for the effects of the charge attenuation. A precise knowledge of t_0 is thus required to achieve a good energy resolution.

As we already mentioned in section 2.1.1, the signal on the wire plane facing the drift volume starts as soon as the ionizing particle crosses the detector, and the electron-ion pairs are formed. This feature can be used to trigger the DAQ system (hence referred as *self-triggering* capability) and to provide the time t_0. An alternative system can be provided by a set of photo-multiplier tubes (PMT's) immersed in the LAr, which detect the scintillation light produced in the LAr by the passage of an ionizing particle. Scintillation photons are produced basically by two different processes [31]:

- by the direct excitation of an argon atom followed by an excited molecule formation and de-excitation:
$$\mathrm{Ar}^* + \mathrm{Ar} \rightarrow \mathrm{Ar}_2^* \rightarrow 2\,\mathrm{Ar} + \gamma; \tag{2.6}$$
- by the formation of a molecular state through recombination processes between electrons and molecular ions:
$$\mathrm{Ar}^+ + \mathrm{Ar} + e^- \rightarrow \mathrm{Ar}_2^* + e^- \rightarrow 2\,\mathrm{Ar} + \gamma; \tag{2.7}$$

In both cases the average photon wavelength is $\lambda = 128$ nm, and the emission occurs within a time window which depends on the excited state. The de-excitation proceeds from two different states, with decay constants of about 5 ns (fast component) and about 1 μs (slow component), respectively. The detection of the scintillation light requires the use of PMT's equipped with suitable windows (like MgF_2, that transmits UV radiation down to 115 nm), or to provide the PMT cathode with a proper wavelength shifting system. This trigger system allows the detection of cosmic ray events with energies down to a few hundred keV.

Read-out system

One of the main problems which this detection technique must cope with is the relatively small amplitude of the signals. This is due to the absence of charge amplification during the electron drift process or near the anode. Typically, 1 mm of a minimum ionizing track delivers less than

10^4 electrons in LAr. The signal is even smaller at low electric fields due to the effects of the charge attenuation and the electron-ion recombination. The imaging of ionizing events requires, therefore, the use of low noise read-out electronics.

The present solution for the read-out system is the product of several years of tests and experience gained by the ICARUS collaboration on small scale prototypes [32, 33, 34, 35, 36]. The readout system is structured as a multichannel waveform recorder that stores the charge information collected by each sense wire during the drift of the electrons at a 2.5 MHz sampling rate. Each wire module (16 wires) is equipped with a current integrating amplifier feeding a 10 bit flash ADC that samples the (multiplexed) signal with a frequency of 40 MHz. The electronic read-out chain is composed of three basic units:

- The Decoupling Board (CAEN A793) distributes and decouples the wires from the bias voltage and distributes test signals and baselines.
- The Analogue Board (CAEN V791) provides amplification and shaping according to the two different configurations (charge and current reading) required for the different wire planes.
- The Digital Board (CAEN V789) stores and processes the waveforms, and performs the zero suppression.

Argon purification

In order to make long electron drift paths possible (of the order of one meter or more) LAr must be ultra-pure. An electron in the liquid undergoes about 10^{12} molecular collisions per second. Hence, impurities with large attachment probability must be kept at very low level, on the order or less than 0.1 ppb (ppb=10^{-9}), to achieve electron lifetimes in excess of a few milliseconds. The electro-negative impurities are mainly represented by oxygen, water, carbon dioxide and, in minor concentrations, some chlorine and fluorine compounds. Commercial LAr has a contamination level of the order of a few ppm (ppm=10^{-6}) of oxygen equivalent. LAr can also be contaminated inside the cryostat, by the degassing process of those parts (walls, electrodes, cables, etc.) covered by the (hotter) argon gas. Therefore, it is necessary not only to purify the LAr before the filling of the cryostat, but also to ensure a continuous purification inside the cryostat, forcing the LAr recirculation through a dedicated purifying unit.

Argon purification can be performed using molecular sieves and chemical attachment [37]. The first procedure provides a better efficiency against water and carbon dioxide, while chemical filters are more suitable against oxygen. The system developed for ICARUS consists of a cartridge containing a molecular sieve (Hydrosorb™) followed by a chemical compound based on a support of SiO_2, on which chromium oxide is deposited, which traps oxygen (Oxysorb™). A typical combination is one part of Hydrosorb and two parts of Oxysorb. The absorption capacity of the molecular sieve depends on the temperature and on the partial pressure of the water vapour. Two liters of molecular sieve can absorb more than 120 liters of water vapour, whereas the oxygen capacity in a cartridge of 4 liters (2/3 of Oxysorb) has been estimated to be greater than 30 liters. This system allows to purify argon in both, the gaseous (slower) and liquid (faster) phase, with similar efficiencies.

2.2 The ICARUS T600 detector

In the previous section, we have briefly reviewed the LAr TPC detection principle and the main technical problems to be overcome in the realization of an actual detector. This section is devoted to the description of the ICARUS T600 detector, the first large-scale LAr TPC built. It is fully operative and, although limited by its moderate mass, has a physics program of its own.

2.2.1 ICARUS T600 as a milestone of the ICARUS project

The ICARUS experiment was proposed for the first time in 1985 [23]. Since then, an extensive R&D program has led to the ultimate assessment of the technique. Several small scale prototypes have been constructed and operated, mainly at CERN, Pavia and the Gran Sasso Laboratory, in order to overcome the main technological problems in the establishment of the ICARUS technology, and demonstrate many of the physics capabilities of the detector. The name of these prototypes (for future reference), and their main features are:

- *3 tons* [32, 33, 34, 35, 36]: about 3 tons of LAr mass. The prototype was operated at CERN for more than four years, exposed to cosmic rays and gamma ray sources. This phase aimed at proving the ICARUS detection principle, to establish the LAr purification methods, the read-out technology and the performance of the electronics, as well as to show the capabilities to collect real events and to run stable for long terms.

- *50 liter* [38]: about 65 kg of LAr mass. The detector was exposed to the CERN WANF neutrino beam during the 1997 run, acquiring a substantial sample of quasi-elastic $\nu + n \rightarrow p + \mu^-$ events. The main goal was to demonstrate the capabilities of the detector with real neutrino events, in particular in the study of the nuclear fragments, measurement of missing transverse momentum, and a preliminary evaluation of the e/γ and e/π^0 separation capabilities.

- *10 m^3* [39]: about 14 tons of LAr mass. This prototype was a major step on the way to reach the necessary industrial construction of large scale detectors. It was conceived as a cryo-mechanical prototype to study the reliability of the cryogenics, the mechanics, and the LAr purification system designed for the T600 detector, to verify the feasibility of the technique with large mass devices. It may be considered as a "slice" of one T600 half-module.

As already described in the original proposal [24], the final phase of the ICARUS project requires a sensitive mass of LAr of 5000 tons or more. This is still true today, even after the advent of the SuperKamiokande detector, with its fiducial mass of 22.5 ktons [4]. In 1995 it was decided that the most conservative way to reach the LAr sensitive mass was to go through a first step: the T600 detector [40], progressively increasing the mass by the addition of several T600-like modules. This step-wise strategy allowed to develop progressively the necessary know-how to build a large LAr detector. The T600 is described in more detail in section 2.2.2. It contains a total (sensitive) LAr mass of 735 (476) tons, divided in two identical independent half-modules. This detector received approval and funding in 1996 and 1997. The construction of the first half-module was completed in 2001 and, immediately after, a full test of the detector was performed at surface conditions, briefly described in section 2.2.3.

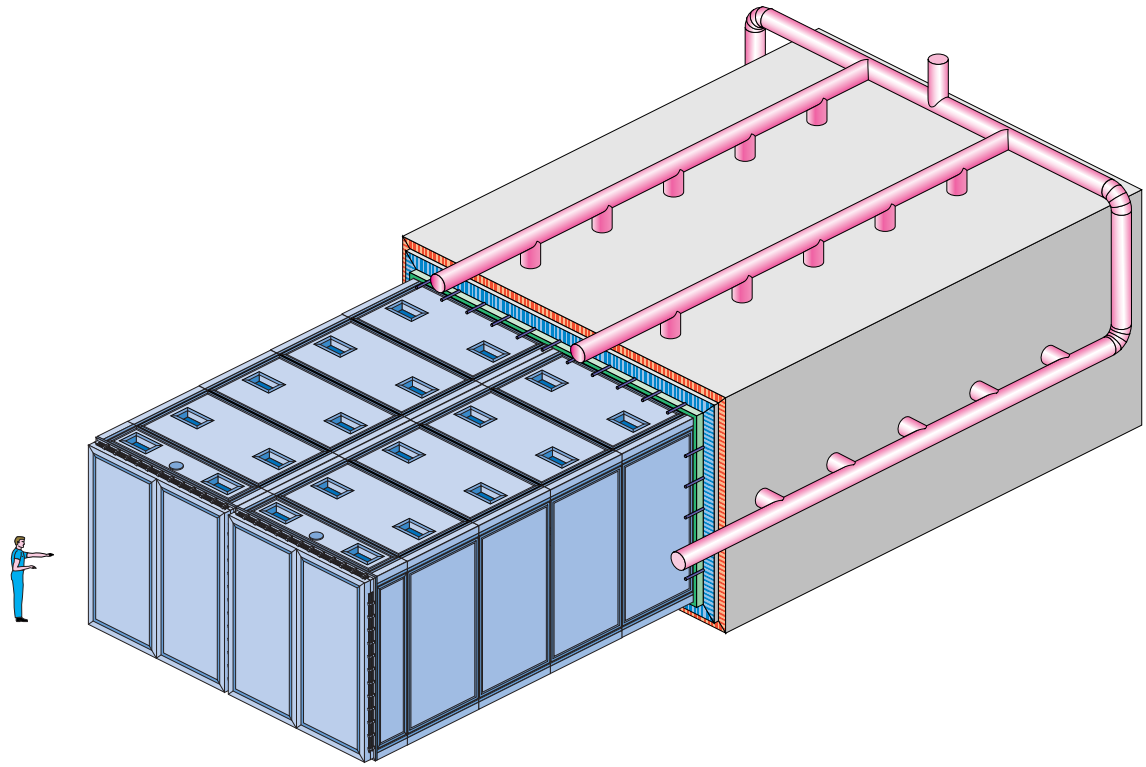

Figure 2.4: Artist's view of the ICARUS T600 cryostat.

The very good performance of the T600 first half module during the test run has led to the proposal and approval of the next step of the ICARUS program: the design and assembly of four additional modules (T600 equivalent) [41], reaching a total mass on the order of 3000 tons.

2.2.2 General description of the T600 detector

In this section, we briefly describe the different parts composing the ICARUS T600 detector. ICARUS T600 is a large cryostat divided in two identical, independent, adjacent reservoirs (*half-modules*), containing more than 300 tons LAr each (see figure 2.4). Both half-modules contain an internal detector (composed of two TPC's), the field shaping system, monitors, probes and PMT's; they are externally surrounded by a set of thermal insulation layers.

LAr container and insulation

A schematic external view of the detector is shown in figure 2.4 and its geometrical characteristics are summarized in table 2.2.

The two LAr containers are made of a structure of aluminum honeycomb panels reinforced by aluminum frames (see figure 2.5). They are surrounded by a common insulation layer made of Nomex (aramid fiber pre-impregnated paper) honeycomb panels (figure 2.6). There is an additional insulation layer (480 mm thickness) in between the two reservoirs to allow the independent filling and/or draining of each half-module. During normal run conditions (both half-modules filled with LAr) this extra layer has no effect, the heat exchange between the two intermediate walls being nominally zero.

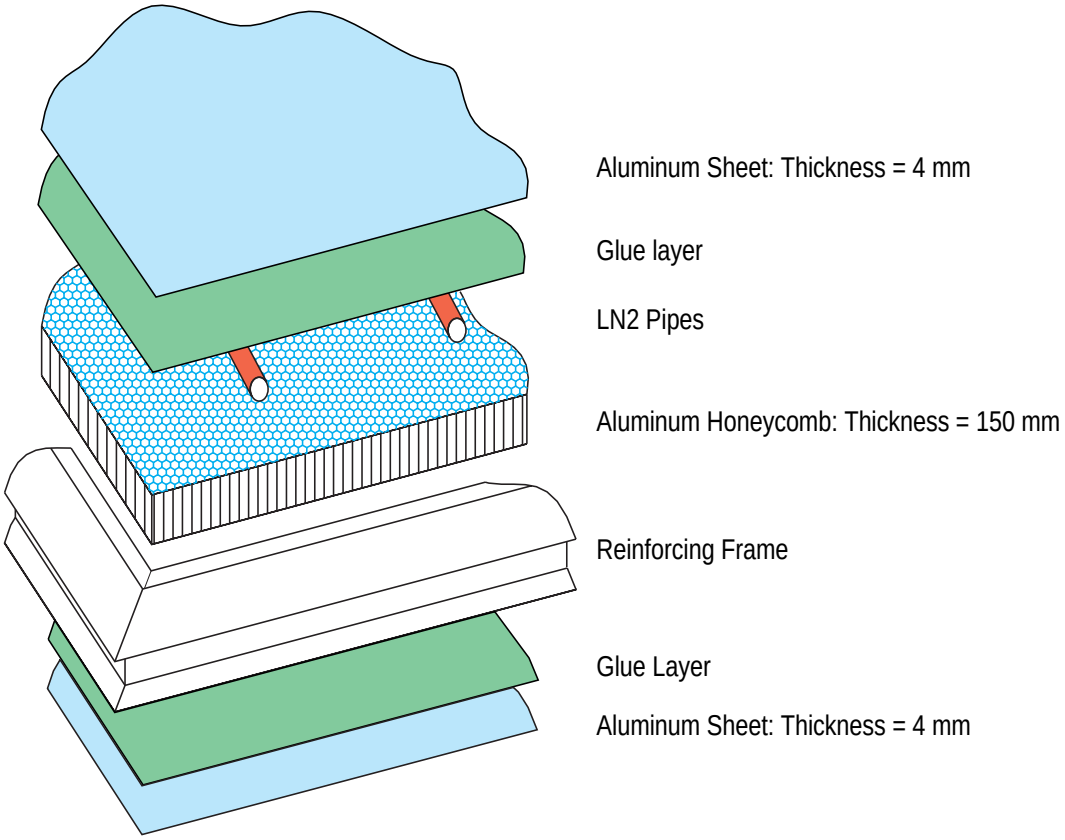

Figure 2.5: Cross-sectional view of the structure of the aluminum honeycomb panels.

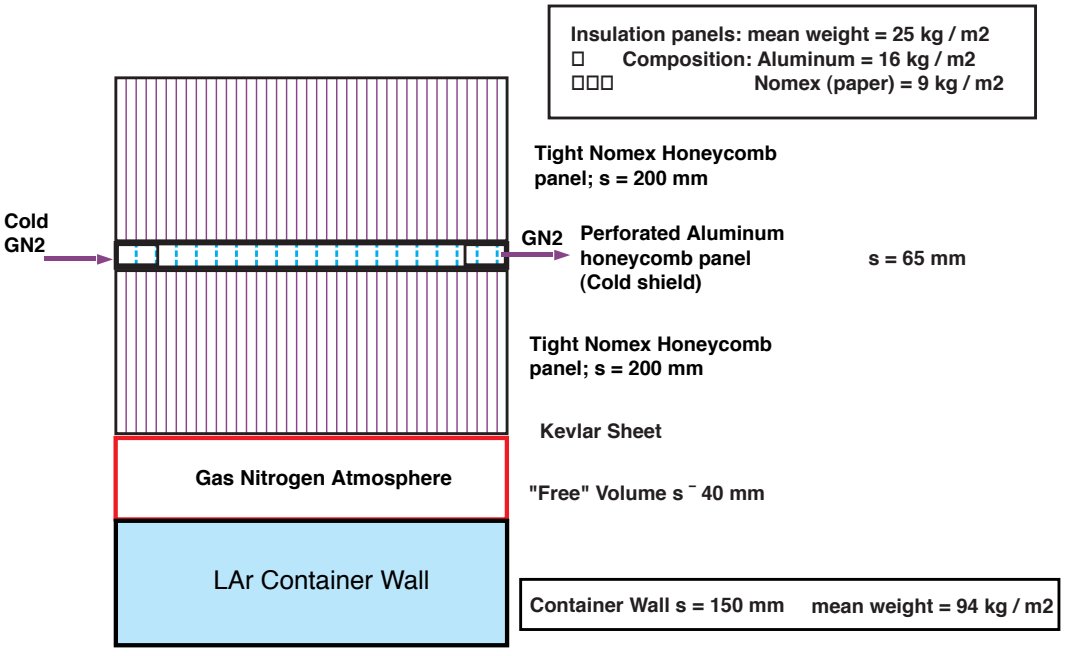

Figure 2.6: Cross-sectional view of the insulation panels.

Number of independent containers	2
Container material (honeycomb structure)	Al
Wall thickness (mm)	150
External insulation thickness (honeycomb+cold shield) (mm)	465
Single container weight (tons)	21.0
Single container internal dimensions (m):	
length	19.3
width	3.6
height	3.9
Single container internal volume (m^3)	271
Single container external dimensions (m):	
length	19.6
width	3.9
height	4.3
Total external dimensions (m):	
length	20.6
width	9.3
height (not including supports)	5.4
Internal (cold) volume (m^3)	
total	**534**
sensitive	**340**
LAr mass (tons)	
total	**735**
sensitive	**476**

Table 2.2: Geometrical characteristics of the ICARUS T600 detector.

The design of the T600 dewar was dictated by the following requirements:

- The shape and dimensions of the LAr containers are fixed by the requirement that each half-module, without insulation, has to be transported through the Italian highways into the Gran Sasso Laboratory.
- The choice of a structure made of aluminum honeycomb panels was also dictated by the transportability requirement. This solution, compared to the traditional reinforced structures made of stainless steel, requires much less material for the same mechanical stability and strength; the material is mostly concentrated along the edges where the reinforcing frames are located. The weight of each container is about 21 tons to be compared to about 70 tons for an equivalent container made of stainless steel. In addition, aluminum offers a better shielding against external electronics noise, and a better temperature uniformity inside the LAr volume.

Cryogenics and purification systems

The cooling of the LAr containers is provided by a forced circulation (with a transfer pump for cryogenic liquids) of LN_2 inside the aluminum pipes directly inserted into the aluminum honeycomb panels (see figure 2.5). The LN_2 pressure and circulation speed are fixed so that the LAr mass is maintained at about 89 K (LAr equilibrium pressure $\approx$ 1.25 bar) with a maximum temperature non-uniformity in the LAr smaller than 1 K. Additional cooling is obtained by

Design Ar pressure	Min.: 0 bar Max.: 1.5 bar
Working Ar pressure	1.25 bar
Cooling Liquid	LN_2 2.7 bar
LN_2 circulation speed	12.5 m^3/hr
Maximum temperature difference on the cryostat walls	1 K
LAr filling/purification speed	2 m^3/hr
LAr fast recirculation units per half-module	1
LAr forced recirculation speed	2 m^3/hr
GAr recirculation units per half-module	2
GAr maximum recirculation speed	100 m^3/hr
Required LAr purity (concentration of electronegative impurities)	0.1 ppb O_2 equiv. lifetime $\approx$ 3 ms

Table 2.3: Working parameters of the T600 cryogenics and purification systems. Filling and recirculation speeds are for one half-module.

circulating GN_2, coming from the evaporation of LN_2 from the main cooling circuit, into an aluminum shield inserted in the middle of the insulation panels (see figure 2.6).

The argon circuit is composed of four elements:

1. the two main LAr containers;
2. the main argon purifier;
3. the GAr recirculation units (2 per each half-module);
4. the LAr fast recirculation units (1 per each half-module).

LAr is purified by means of standard Oxysorb/Hydrosorb filters (see section 2.1.2). Table 2.3 summarizes the working parameters of the T600 cryogenic and purification systems.

Internal detector

Each half-module contains an internal detector composed of two TPC's, the field shaping system, monitors, probes and PMT's. Each TPC consists of three parallel planes positioned along the side walls of the half-module (see figure 2.7), the first (Induction I plane), facing the drift region, with horizontal wires, the other two (Induction II and Collection planes) with the wires at $\pm 60^\circ$. A high voltage system produces a uniform electric field, perpendicular to the wire planes, allowing the drift of the ionization electrons. The maximum drift path is 1.5 m.

The strategy for the mechanical design of the internal detector (wire chambers and HV system) is based on two basic concepts:

1. Independence of the internal detector and LAr container. The reason is to avoid imposing conditions on the cryostat structure from the mechanical rigidity required for the wire chamber (e.g. by the alignment precision of the chambers and also to avoid over-stress on the wires).

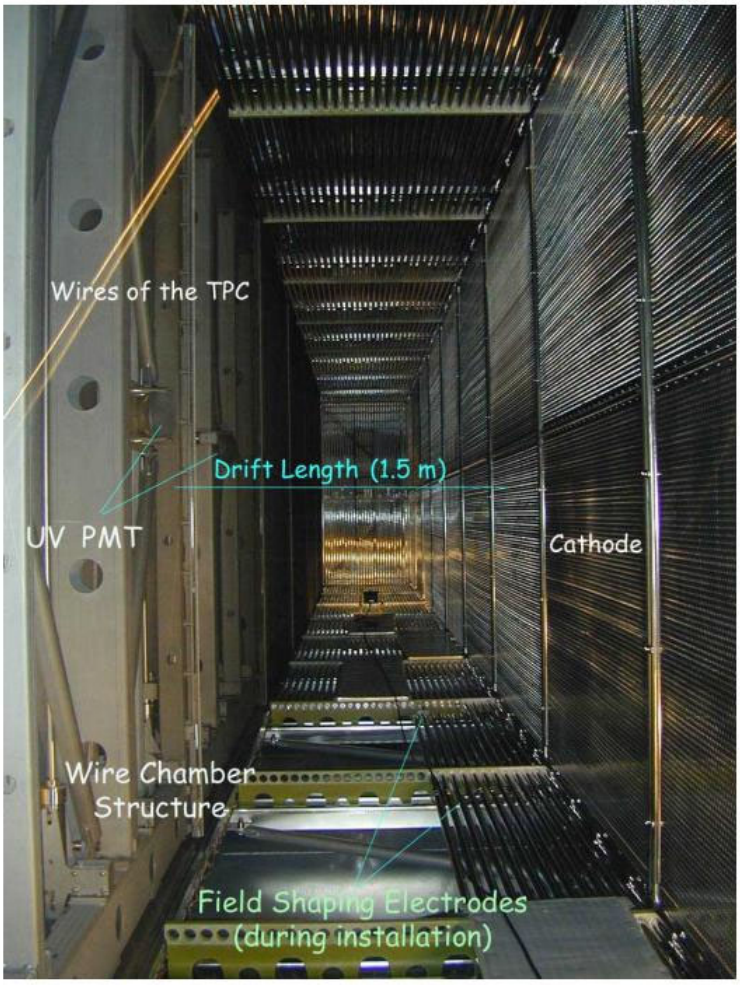

Figure 2.7: Internal view of the T600 first half-module (left half only).

2. Use of *variable geometry* frames for the wire chambers. This has been introduced to avoid the risk of wire breaking due to over-stress during the cooling phase, when the faster thermal contraction of the wires could produce a tension increase above the elastic limit. Variable geometry is realized by means of a set of calibrated springs attached to the backside of the rocking frames, which hold the wires. With this solution, a tension increase on the wires is partially compensated by the elongation of the springs. An additional feature of this solution is that it permits to release the tension on the wires allowing a transportation in much safer conditions.

For each wire chamber there are three planes of parallel wires. The first plane, facing the drift region, is composed of horizontal wires. The other two are composed of wires at $\pm 60^{\circ}$ from the horizontal direction. The pitch of the wires is 3 mm, and the distance between the different planes is also 3 mm. A field shaping system, consisting of the cathode and a series of so called "race-track" rings, produces a uniform electric field in the drift volume. The cathode is placed at the center of the half-module internal volume and serves the two wire chambers. The details about the internal detector are summarized in table 2.4.

The detector is also equipped with a system of large surface (8" diameter) PMT's (D727KFLB)

Number of readout chambers	4
Number of wire planes per chamber	3 (all readout)
Wire orientation with respect to horizontal	0°, $\pm 60^\circ$
Wire pitch	3 mm
Wire length:	
horizontal wires	9.40 m
wires @ $\pm\, 60^\circ$	3.77 m
wires at the borders ($\pm 60^\circ$)	0.24 m $\div$ 3.77 m
Wire diameter	150 μm
Wire nominal tensioning force	12 N
Number of wires / chamber:	
horizontal	2112
$\pm 60^\circ$	2×5728
Total	13568
Total number of wires	54272
Maximum drift length	1.5 m
Maximum drift time @500 V/cm	1.0 ms
Distance between race tracks	50 mm
Number of race tracks / sensitive volume	29
Sensitive volume / chamber:	85.1 m^3
length	17.95 m
width	1.5 m
height	3.16 m

Table 2.4: Main parameters of the internal detector mechanics of the T600 detector.

directly immersed in LAr to detect the scintillation light. The PMT's are equipped with bi-alkali photo-cathodes on a platinum layer, optimized to operate at low temperature. The overall quantum efficiency has been measured at LAr temperature to be about 10%. 21 PMT units have been installed in the first T600 half-module, and the installation of 60 units is foreseen for the second one.

Signals from the wires are transported outside the LAr containers through a set of flanges located on top of the cryostat. Custom made ultra-high vacuum feed-throughs (576 signals per flange) have been developed for this purpose. The readout electronics boards are located on top of the cryostat just in front of the signal flanges, to minimize the input capacitance of the cables.

Slow Control system

During the initial phase of leak testing with overpressure, evacuating, cooling and filling with LAr, the detector is exposed to extreme pressure and temperature conditions. A Slow Control system monitors and controls the behaviour of the detector under such conditions, and also during the data taking phase and detector draining at the end of the run. A detailed description of the different components of the Slow Control system is presented in section 3.1.

2.2.3 The technical run in Pavia

A full test of one of the two T600 half-modules was carried out at the surface of the earth in Pavia (Italy) between May and August 2001 (more than 100 days of operation). The test aimed at probing the performance of the T600 detector in real experimental conditions. Although the run was mainly intended as a technical run, a substantial amount of cosmic ray data was acquired, since the detector was not shielded against cosmic rays as will be the case in the Gran Sasso underground laboratory.

Technical tests

The technical run was divided into the following phases:

1. Clean up, lasting 10 days. During this period the cryostat was evacuated down to about 10^{-4} mbar pressure. Seven days were needed for the search for leaks and to fix them, and three days to pump the cryostat down to the pressure aimed at.

2. Cooling, lasting 14 days. During the first 11 days, the cryostat was pre-cooled down to 223 K. At this point, the circulation of liquid nitrogen was switched on, and the temperature of 95 K was reached in three days.

3. Filling with LAr, lasting 10 days.

4. Data acquisition, lasting 68 days. All technical aspects of the system were checked. In particular, some of the achievements are: the stability of the cryogenic plant during the whole run; the very high level of LAr purity reached (exceeding 1.5 ms drift electron lifetime); a good DAQ performance based on the capability of managing very large amounts of data from independent sections of the inner detector; a good performance of the internal PMT trigger system and an efficient performance of the high voltage system, providing the nominal electric field (500 V/cm) in the drift region.

5. Cryostat emptying, lasting seven days.

The response of the detector to the thermodynamical and mechanical processes happening during the different phases was monitored and controlled by means of the Slow Control system. The results of the off-line analysis of the collected data are presented in section 3.2.

Acquired data

The first long muon tracks were acquired immediately after the high voltage system was turned on, still far from the optimal LAr purity and read-out configuration, which was reached by the end of the run. The last three weeks of the run were dedicated to the systematic data acquisition. A large amount of data was acquired, which is at present being classified by visual scanning. Table 2.5 shows the present results of the data inventory. The scanned sample corresponds roughly to the two last weeks of data taking (20% of the total data sample). In the following, the different event categories used in the data inventory are roughly described and real event examples are presented (figures 2.8 to 2.14). The figures are a gray scale representation of the wire output signal for a selected region of the wire (horizontal) vs. drift time (vertical) plane, from the Collection wire plane. The real dimensions of the different events are provided in the figure caption. The considered categories are the following:

Event category	Number of events
Electromagnetic Shower	834
Muon decay/stopping	3030
Hadron interaction	951
V_0	57
Long track	750
Muon bremsstrahlung	1958
Multiple showers	844
Multiple muons	187
Total scanned events	4967

Table 2.5: Results from the ICARUS T600 technical run inventory. For every topology, the number of events containing at least one occurrence is quoted. Categories are not exclusive.

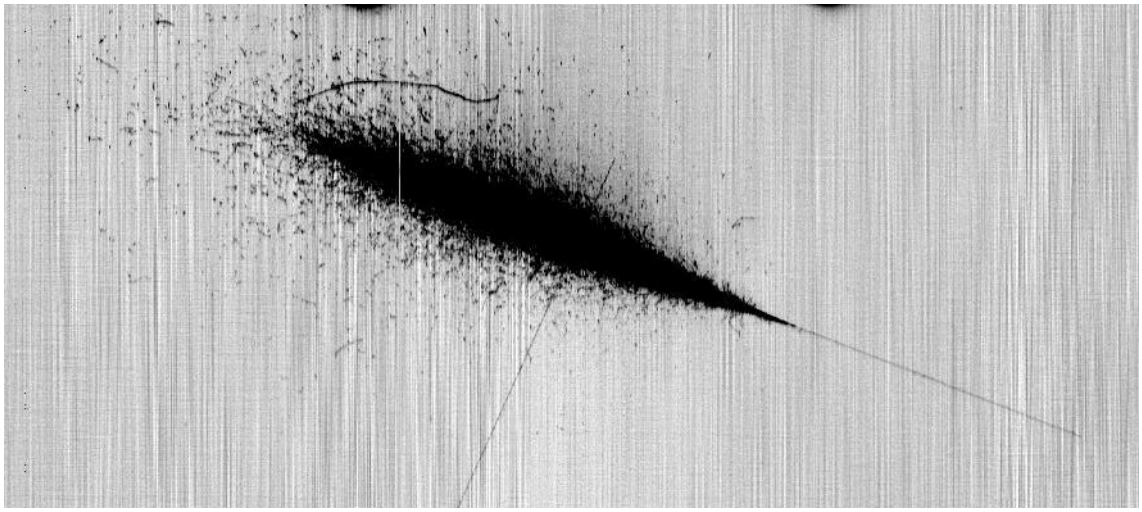

Figure 2.8: Example of an electromagnetic shower event from the T600 cosmic ray data. Real size of the event: 370×170 cm^2.

- Electromagnetic Shower (figure 2.8). These events provide a good demonstration of the imaging capabilities of the LAr TPC. The figure shows a high energy electron entering the detector at the bottom-right corner of the displayed area, and initiating an electromagnetic cascade propagating to the top-left corner. The small black dots surrounding the main cloud are low energy Compton electrons ($\sim$ 1 MeV).

- Muon decay/stop (figure 2.9). Some of the muons entering the detector deposit all their energy, stop and decay in the LAr active volume. This kind of events is easily recognized by the presence of a low energy muon track followed by an electron/positron emission. The muon track, due to the low momentum, undergoes large angle multiple scattering, and the ionization increases rapidly near the end point. In the example shown, the muon enters the detector at the bottom of the figure, propagates toward the top and decays into an electron/positron producing a smaller, lighter track.

- Hadron interaction (figure 2.10). High energy charged hadrons (π, K,...) entering the detector may undergo nuclear interactions, producing secondary hadrons subsequently undergoing different interactions. In the example shown, the primary hadron enters the detector from the right side of the figure (a δ-ray is visible at the beginning of the track),

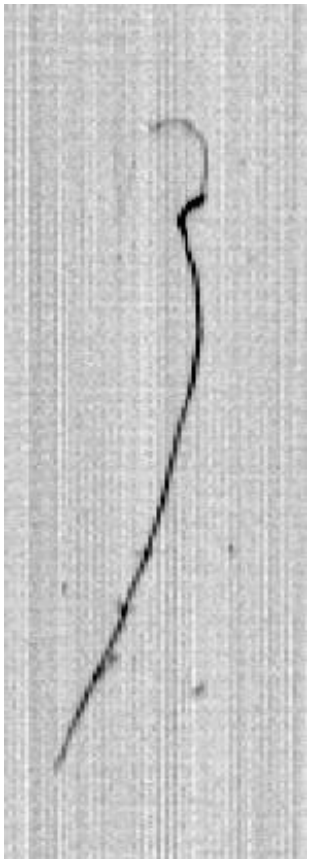

Figure 2.9: Example of a muon decay event from the T600 cosmic ray data. Real size of the event: 23×91 cm^2.

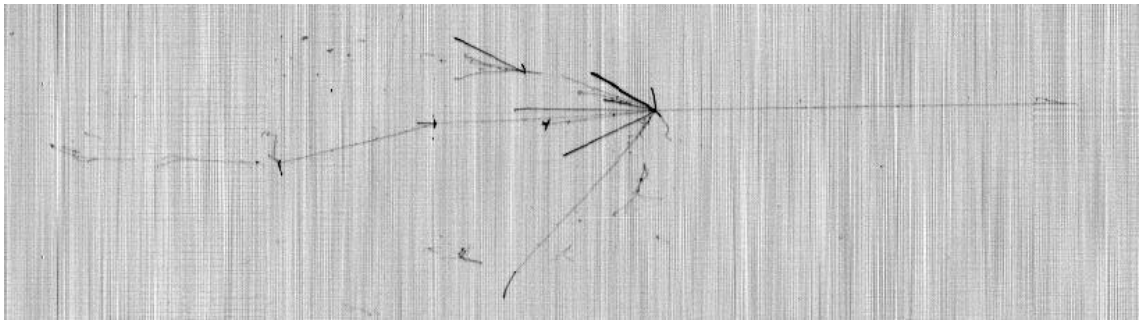

Figure 2.10: Example of a hadron interaction from the T600 cosmic ray data. Real size of the event: 270×80 cm^2.

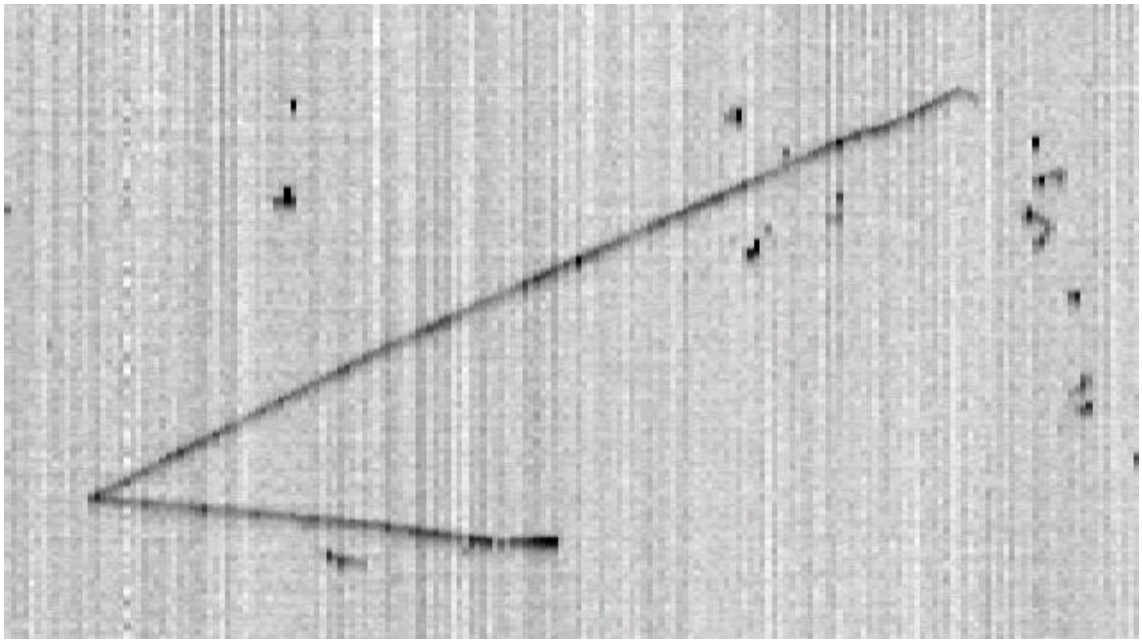

Figure 2.11: Example of a V_0 interaction from the T600 cosmic ray data. Real size of the event: 60×40 cm^2.

interacting after about 70 cm. Among the secondary particles, it is possible to distinguish, at the bottom of the figure, the shower produced by the conversion of a pair of photons, most likely coming from the decay of a π^0. A neutral particle (possibly a neutron) could also be produced, giving an additional hadronic interaction in the upper part of the figure. One of the charged hadrons coming from the main interaction vertex travels around 1.7 m undergoing secondary hadronic interactions along its path. Soft secondary, heavily ionizing nuclear debris is also visible.

- V_0 (figure 2.11). This type of event is the product of a neutral particle decaying into two charged particles, mainly $K^0 \rightarrow \pi^+\pi^-$ or $\Lambda \rightarrow p + \pi^-$. The example shows two tracks coming from the same interaction vertex and traveling toward the right side of the figure. The longest track deposits about 85 MeV and escapes the detector, whereas the other track deposits about 50 MeV and stops inside the detector.

- Long track and muon bremsstrahlung (see figure 2.12). This type of events is produced by high energy muons traversing the whole detector along the longitudinal axis. These events are particularly interesting since they show the capability of the DAQ system to record events spreading over many independent read-out channels. In the example (split in two parts), a muon enters the detector at the left side of the top figure, produces some bremsstrahlung emission (identifiable as electromagnetic showers along the muon track) and exits the detector at the right side of the bottom figure, after having traversed about 18 m of LAr.

- Multiple showers (figure 2.13) and multiple muons (figure 2.14) are produced by the passage of many parallel particles, coming from the interaction of a single, very energetic, cosmic ray in the atmosphere. The secondary particles traverse the detector producing electromagnetic showers or straight tracks, respectively.

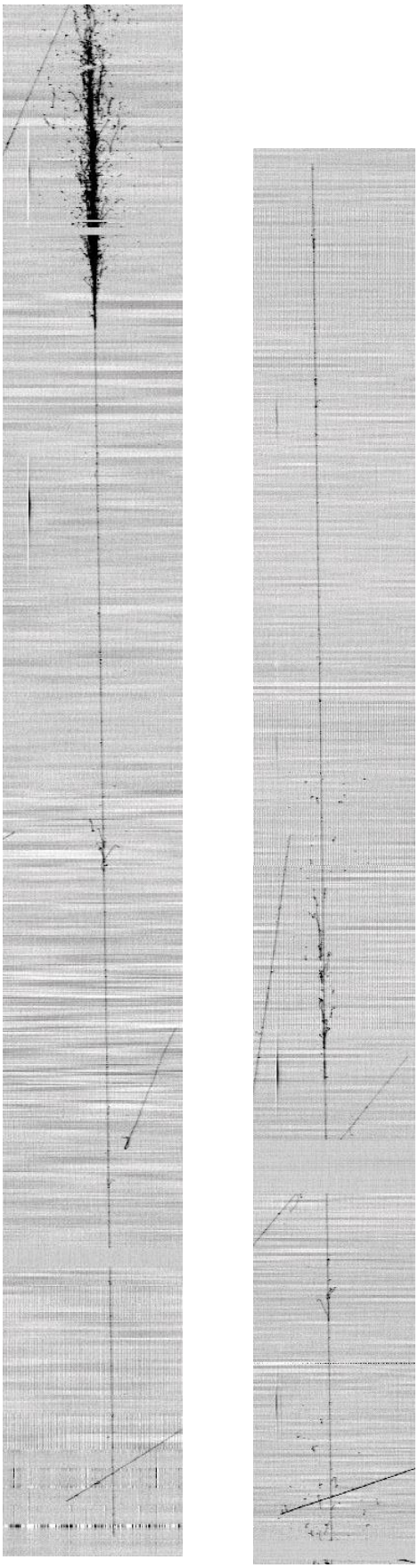

Figure 2.12: Example of a long muon track with bremsstrahlung emission from the T600 cosmic ray data. The event is split in two contiguous parts of real size 810×100 cm^2 and 750×100 cm^2, respectively.

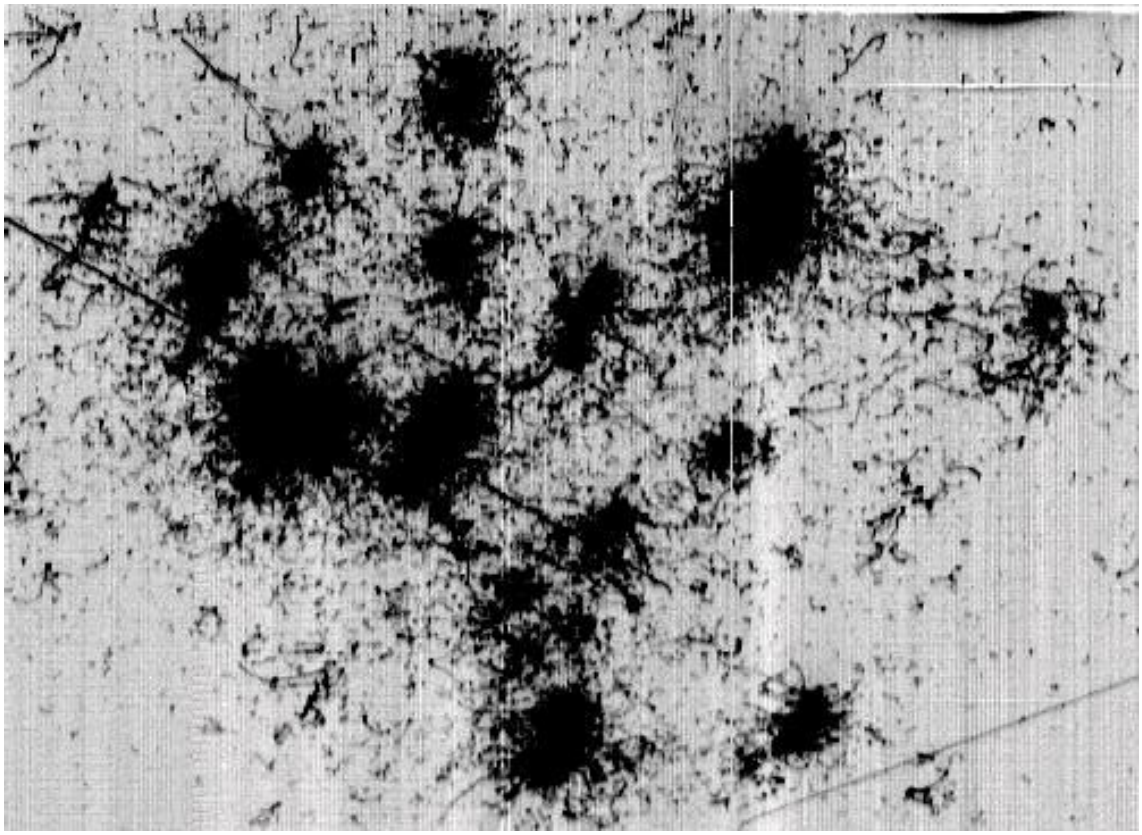

Figure 2.13: Example of a multiple shower event from the T600 cosmic ray data. Real size of the event: 140×150 cm^2.

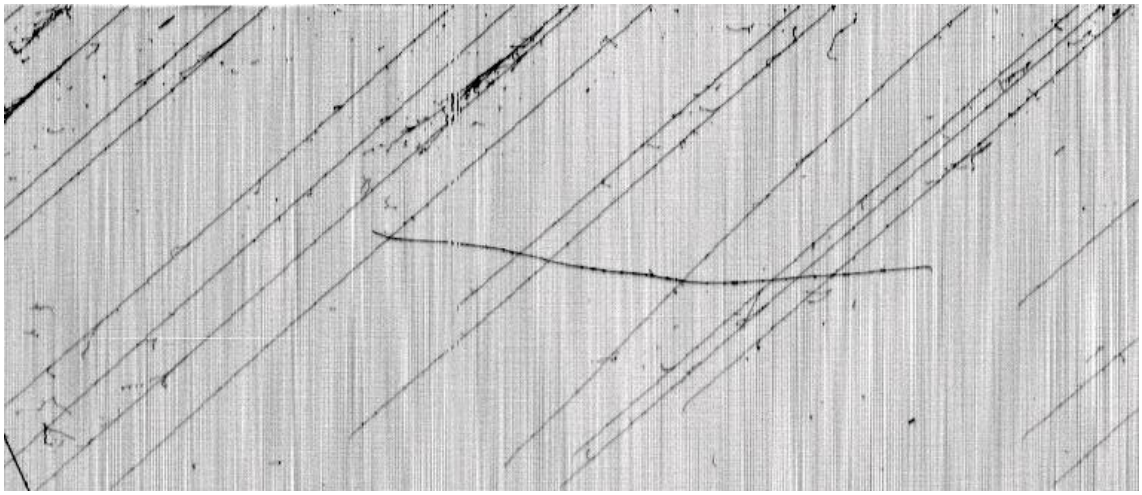

Figure 2.14: Example of a multiple muon event from the T600 cosmic ray data. Real size of the event 240×150 cm^2.

2.3 Physics program

The ICARUS physics program has been described in Volume I of the 1994 proposal [24] and was recently reviewed and updated for the initial phase of the T600 prototype at the Gran Sasso Laboratory [42].

The performance of a neutrino detector is proportional to its total mass but also to its geometrical granularity, which determines the quality with which signal events can be reconstructed and hence separated from background. The ICARUS LAr TPC, working as an "electronic bubble chamber" (continuously sensitive, self-triggering, with the ability to provide 3D imaging of any ionizing event, together with an excellent calorimetric response), offers the possibility to perform complementary and simultaneous measurements of neutrinos from different sources: neutrinos from the CERN beam to Gran Sasso (CNGS), atmospheric neutrinos, solar neutrinos and neutrinos from supernovae bursts. The same class of detector can also be envisaged for high precision measurements at a neutrino factory and can be used for background-free searches for nucleon decays. Hence, an extremely rich and broad physics program, encompassing both accelerator and non-accelerator physics, is addressed. This will answer fundamental questions about neutrino properties and about the possible physics of the nucleon decay. Some of the expected achievements of the ICARUS project in each of the listed fields are summarized in what follows. As an example, we further develop the case of atmospheric neutrinos.

Atmospheric neutrinos

The physics goal of new atmospheric neutrino measurements is to firmly establish the phenomenon of neutrino oscillations with a different experimental technique than that of the SuperKamiokande experiment [4], measure the oscillation parameters and clarify the nature of the oscillation mechanism. The capability to observe all processes, electron, muon and tau neutrino charged current events (CC) and all neutral currents (NC) without detector biases is also highly desirable. A detector based on the ICARUS technique will provide an observation of atmospheric neutrinos with very high quality, thanks to its unique performance in terms of resolution. Unlike measurements obtained so far in SuperKamiokande, which are in practice limited to the analysis of "single-ring" events, complicated final states with multi-pion products, occurring mostly at energies higher than a few GeV, will be completely analyzed and reconstructed in ICARUS. This will be a significant improvement with respect to previous observations. The perspective of ICARUS is to provide redundant, high precision measurements and minimize as much as possible the systematic uncertainties of experimental origin which affect the results of existing experiments. Improvements over existing methods are expected in the neutrino event selection, the identification of ν_μ, ν_e and ν_τ flavors and the identification of neutral currents.

The expected atmospheric neutrino rates obtained for an exposure of 5 kton $\times$ year (10 years of T600 running) are summarized in table 2.6, including and excluding the $\nu_\mu \to \nu_\tau$ oscillation hypothesis ($\sin^2 2\theta = 1$). Muon-like events contain an identified muon and correspond to $\nu_\mu/\bar{\nu}_\mu$ CC events. Electron-like events have an identified electron and are $\nu_e/\bar{\nu}_e$ CC events. Given the clean event reconstruction, the ratio R of "muon-like" to "electron-like" events can be determined free of large experimental systematic errors. In fact, the expected purity of the samples is above 99%. In particular, the contamination from π^0 decays in the "electron-like" sample is expected to be completely negligible. We split further the muon-like events into contained and partially-contained samples. For the contained events (62% of the total), the muon energy is precisely determined by integration of the dE/dx measurements along the track. For partially contained events (38% of the total, average neutrino energy 4.5 GeV), in which the muon escapes the

		Δm^2_{23} (eV^2)			
	No osci	5×10^{-4}	1×10^{-3}	3.5×10^{-3}	5×10^{-3}
Muon-like	675 ± 26	515 ± 23	495 ± 22	470 ± 22	455 ± 21
Contained	418 ± 20	319 ± 18	307 ± 18	291 ± 17	282 ± 17
Partially-Contained	257 ± 16	196 ± 14	188 ± 14	179 ± 13	173 ± 13
No proton	260 ± 16	190 ± 14	185 ± 14	170 ± 13	165 ± 13
One proton	205 ± 14	160 ± 13	150 ± 12	145 ± 12	140 ± 12
Multi-prong	210 ± 14	165 ± 13	160 ± 13	155 ± 12	150 ± 12
Electron-like	380 ± 19	380 ± 19	380 ± 19	380 ± 19	380 ± 19
No proton	160 ± 13	160 ± 13	160 ± 13	160 ± 13	160 ± 13
One proton	120 ± 11	120 ± 11	120 ± 11	120 ± 11	120 ± 11
Multi-prong	100 ± 10	100 ± 10	100 ± 10	100 ± 10	100 ± 10
NC	480 ± 22	480 ± 22	480 ± 22	480 ± 22	480 ± 22
TOTAL	1535 ± 39				

Table 2.6: Expected atmospheric neutrino rates for an exposure of 5 kton $\times$ year, in case no oscillations occur and assuming $\nu_\mu \to \nu_\tau$ oscillations with maximal mixing. Four different Δm^2 values have been considered. Only statistical errors are quoted.

active volume of the detector, the muon momentum is estimated with the multiple scattering method [43]. We illustrate also the expected kind of events, classified according to their final state multiplicity. Approximately 40% of the muon-like events contain no identified proton with kinetic energy above 50 MeV in the final state, corresponding to the "one-ring" sample of the SuperKamionande experiment. The rest of the events contain a proton or multi-prong final states, which provide a precise determination of the incoming neutrino energy and direction thanks to the precise reconstruction of all particles (for events with $E_{vis} > 1$ GeV). An improved observation of about 500 neutral current (NC) events per year is also expected, given the clean classification of charged current events based on the presence of an electron or a muon in the final state. In this case, the excellent e/π^0 separation plays a fundamental role to select an unbiased, neutral current sample free of background.

We highlight the L/E reconstruction performance (with L the distance to the neutrino production point), which is determined by the resolution of the measurement of the incoming neutrino energy E and direction $\cos\theta_Z$, where θ_Z is the zenith angle. The result of a full simulation of events in LAr yields an L/E resolution for events with visible energy $E_{vis} > 1$ GeV (approximately 40% of the events) of $\approx 30\%$ RMS (see figure 2.15). The L/E distribution of muon and electron like events assuming a three family mixing scenario with $\Delta m^2_{32} = 3.5 \times 10^{-3}$ eV^2, $\sin^2\theta_{23} = 1$ and $\sin^2 2\theta_{13} = 0.1$ is shown in figure 2.16. The electron sample is essentially unaffected by the $\nu_\mu \to \nu_e$ and $\nu_e \to (\nu_\mu/\nu_\tau)$ transitions and can be used as a reference sample. The plots are normalized to an exposure of 25 kton $\times$ years.

Solar and supernovae neutrinos

The ICARUS goal is not only to confront the Standard Solar Model (absolute event rate), but also to provide Solar Model independent measurements by observing various independent processes, differently affected by possible oscillations. ICARUS can detect solar neutrinos by

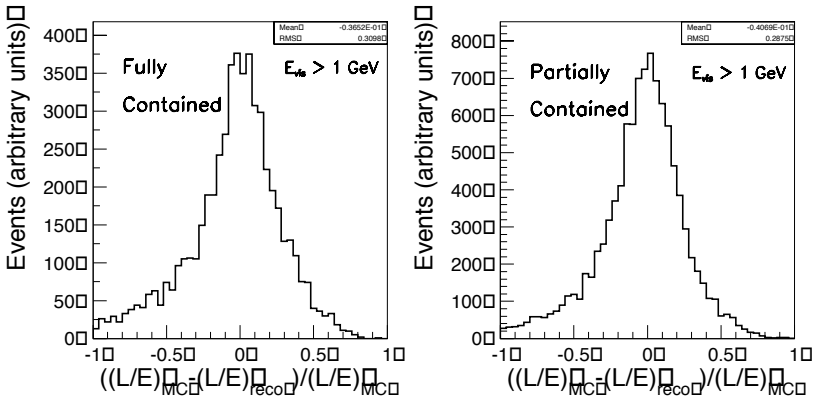

Figure 2.15: Full simulation of the L/E resolution in atmospheric events for contained and non-contained events ($(L/E)_{reco}$ is the fully reconstructed L/E value).

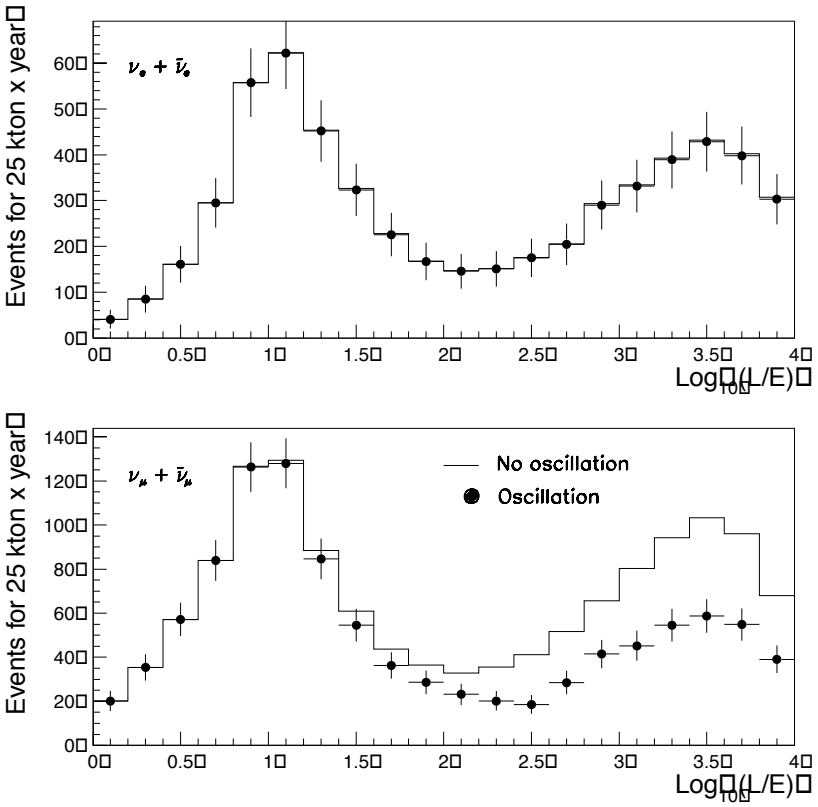

Figure 2.16: L/E distribution of muon and electron like events for three-family mixing. The electron sample can be used as a reference sample. The plots are normalized to an exposure of 25 kton $\times$ years. A three-family mixing scenario was assumed with $\Delta m^2_{32} = 3.5 \times 10^{-3}$ eV^2, $\sin^2\theta_{23} = 1$ and $\sin^2 2\theta_{13} = 0.1$.

observing the following two processes:

1. Elastic scattering on atomic electrons ($\nu_x + e^- \rightarrow \nu_x + e^-$), which occurs with all types of neutrino flavors and for both charged (only ν_e) and neutral currents;

2. Absorption on argon nuclei ($\nu_e + {}^{40}\mathrm{Ar} \rightarrow {}^{40}\mathrm{K}^* + e^-$), which only occurs for the electron neutrino.

These interactions usually result in the production of a primary electron track eventually surrounded by lower-energy secondary electron tracks. Small prototype detectors have demonstrated that, with the ICARUS technique, electrons with kinetic energy as low as 150 keV can be detected [38]. This performance allows a detailed reconstruction of the solar neutrino interactions. However, because of the increasing background at low energy, there is a minimum threshold (5 MeV) below which electrons produced by solar neutrinos can not be distinguished from other sources. Therefore, ICARUS is sensitive to the ^{8}B and *hep* part of the solar neutrino spectrum. About $3240 \times f_B$ solar neutrino electron scattering and absorption events are expected per kiloton and year, with an electron detection threshold of 5 MeV, where f_B is the Boron flux suppression factor.

ICARUS is sensitive to supernova neutrinos via elastic scattering on electrons and absorption on argon. The experimental signature of the elastic scattering consists of a single recoil electron. Since, the direction of this electron is highly correlated to the incoming ν direction, these events have the potentiality of precisely determining the location of the supernova source. A supernova at a distance of 10 kpc would produce about 72 events per kiloton.

Long base-line beam neutrinos

In order to achieve a better understanding of neutrino phenomenology, it is fundamental to have coherent results from different kind of measurements, showing that all of them can be interpreted within an unique model. Therefore, the possibility of measuring atmospheric neutrinos with the same detector operating in the long–baseline beam is considered a fundamental feature in order to establish a robust confidence on the results.

In the CERN-NGS beam [44], the expected ν_e and ν_τ contamination are of the order of 10^{-2} and 10^{-7} respectively compared to the dominant ν_μ composition. These properties allow to search for oscillations by looking at the appearance of ν_e or ν_τ charged current events. In this case, the detector must be able to tag efficiently the interaction of ν_e's and ν_τ's out of the bulk of ν_μ events. This requires a detailed event reconstruction that can be achieved only by means of a high granularity detector. This requirement is met by the LAr target.

A total of 2720 ν_μ CC events per kiloton and year (4.5×10^{19} protons on target –pots– from the SPS) are expected and accompanying smaller samples of $\bar{\nu}_\mu$, ν_e and $\bar{\nu}_e$ flavors. In addition, 91 ν_τ CC events for $\nu_\mu \rightarrow \nu_\tau$ oscillations are expected with $\Delta m^2 = 3 \times 10^{-3}$ eV^2 and $\sin^2 2\theta = 1$.

Nucleon decay

The SuperKamiokande collaboration has extensively probed classical decay channels (e.g. $p \rightarrow e^+\pi^0$) and the dominant decay mode according to SUSY Grand Unified Theories, $p \rightarrow \bar{\nu}K^+$. Plans exist to operate a megaton water Čerenkov detector [45] improving the current sensitivities for $p \rightarrow e^+\pi^0$ and $p \rightarrow \bar{\nu}K^+$ modes by at least one order of magnitude. However, to unmistakably

show the existence of a signal, these experiments have to rely on statistical background subtraction. A clear advantage and certainly the main strength of the ICARUS technique is, that a discovery will be possible with a single event, thanks to its superb imaging and energy resolution capabilities. In addition, a full understanding of the mechanism responsible for proton decay requires a precise measurement of all possible branching ratios. Since ICARUS provides a much more powerful background rejection, it can perform measurement of a large variety of exclusive decay modes. Inclusive searches are obviously also possible. Hence, a LAr detector is an ideal device, in particular for those channels that are not accessible to Čerenkov detectors due to the complicated event topology, or because the emitted particles are below the Čerenkov threshold (e.g. $K^{\pm}$).

In the case of LAr, 5 kton contain 3×10^{33} nucleons, which translates into background-free searches for lifetimes up to 2×10^{32} years for $p \to e^{+}\pi^{0}$ and 6×10^{32} years for $p \to K^{+}\bar{\nu}$ after 1 year of running (or 5 years of running with 1 kton).

Chapter 3

The ICARUS T600 Slow Control System

The main features of the ICARUS T600 detector and its first technical run have been described in chapter 2. As we pointed out, during the phases prior to the steady data acquisition conditions, the detector is exposed to extreme pressure and temperature conditions. During the search of leaks and cleaning of the internal container (cryostat), the detector is over-pressurized and pumped to vacuum consecutively. After vacuum is broken with purified gaseous argon, the cryostat is started to be cooled down to LAr temperature, and then filled with LAr. The temperature must be maintained roughly constant and uniform along the data taking period. Once the run is finished, the cryostat is drained and the internal temperature let to grow back gently to room temperature. In order to monitor and control the thermodynamical and mechanical behavior of the first T600 half-module during all these operations, a series of sensors with the corresponding readout electronics was built and/or tested at ETH-Zürich, calibrated, and installed in the detector. A detailed description of the system, and of the results of the off-line analysis of the data acquired during the technical run are presented in this chapter.

3.1 Description of the system

The Slow Control system of the ICARUS T600 first half-module consists of four different types of sensors [47, 48, 49]:

- 16 LAr level meters to monitor the LAr filling of the cryostat;
- 8 position meters to measure the inward movement of the cryostat walls when the cryostat is being pumped before filling it, and the outward movement of the walls during the filling with LAr;
- 7 position meters to measure the movement of the springs attached to the wires of the wire chamber; these springs are intended to compensate the thermal contraction of the wires during the cooling phase and hence, maintain them at a roughly constant tension;
- 30 platinum resistors (Pt1000) for temperature measurement.

The level meters and the two kinds of position meters are based on a capacity measurement, whereas the temperature is measured through the resistance of the Pt1000 resistors. Tables 3.1

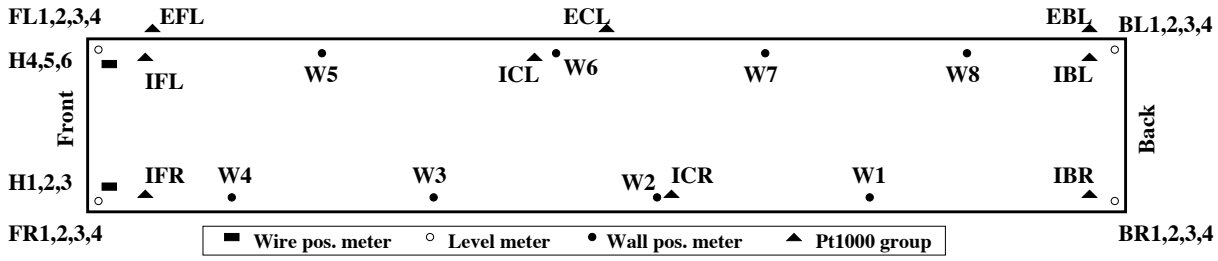

Figure 3.1: Schematic view of the cryostat seen from the top. Indicated are the approximate locations of the different Slow Control sensors. See tables 3.1 and 3.2 for the definition of the sensor's labeling.

and 3.2 summarize the sensors' labeling and positioning within the detector. Figure 3.1 shows a schematic view of the cryostat with the position of the different sensors.

3.1.1 LAr level meters

The level meters are cylindrical capacitors (see figures 3.2, 3.3 and 3.4). The relative dielectric constant of LAr is $\epsilon_{LAr} = 1.54$; hence, the capacity of the sensors changes linearly with the length of the sensor portion immersed in LAr. Four level meters are mounted at each corner of the cryostat to cover the full height of about 4 m (see figure 3.2). The sensors are all mounted inside a shielding, which is grounded to the chamber frame. The lower three sensors are commercial devices (from Cryo Anlagenbau GmbH, D-57234 Wilnsdorf, Germany) and have a length of 1.3 m to monitor the LAr level during the filling phase with a precision of about 1 cm. The four precision level meters at the top positions were built at ETH and serve as monitors of the LAr level during the detector operation when it is full, with a precision of about 1 mm. Table 3.3 shows the height, measured from the bottom of the cryostat (at room temperature),where the sensors are mounted. For the four precision level meters at the top, the distance from the ceiling of the cryostat is also given.

Commercial level meters

Eight of the twelve mounted commercial level meters were ordered together in a first series and have a length of 1300 mm. The remaining four level meters were ordered later and have a length of 1325 mm (sensors FL2/3 and FR2/3). Figure 3.3 shows the drawing of a commercial level meter inside its shielding. The sensors are hold inside the shielding by two polyethylene capsules (cross hatched). The capacity in air is about 250 pF and the sensitivity to LN_2 is about 0.8 pF/cm ($\epsilon_{LN_2} = 1.454$).

Precision level meters

The four level meters mounted at the top positions consist of two 500 mm long stainless steel tubes mounted in a 1050 mm long shielding, as shown in figure 3.4. Two polyethylene capsules (fiberglass enforced epoxy for the sensors at the front) are holding the tubes and are used to mount the sensor inside the shielding. The radial gap of the capacitors is 0.5 mm. In air the capacity is about 730 pF and the sensitivity to a change of LN_2 level is 0.7 pF/mm.

Sensor	Quantity	Label	Place
Level Meter	16	FLn, FRn, BLn, BRn ($n = 1...4$)	F/B = front/back, L/R = left/right n = level (1=bottom,... 4=top)
Wall Position Meter	8	Wn ($n = 1...8$)	half height of the walls W1-W4: right side, W5-W8: left side Distance to the front end-cap: W1: 14.8 m W2: 10.8 m W3: 6.8 m W4: 2.8 m W5: 4.6 m W6: 8.6 m W7: 12.6 m W8: 16.6 m
Wire Position Meter	7	Hn ($n = 1...6$) V1	Hn: front side, H1-H3: right side, H4-H6: left side. H1, H4: bottom, H2, H5: half height H3, H6: top. V1: 5th spring from the front, left side.
Pt1000	30 (internal) 15 (external)	IBR, ICR, IFR, IBL, ICL, IFL EBL, ECL, EFL	Arranged in groups of 5 Pt1000 in the same vertical line. I/E=internal/external. B/C/F=back/center/front L/R=left/right Single Pt1000 position in table 3.2

Table 3.1: Summary of sensors labeling and positioning. The front side is the one opened to the clean room. Left and right sides are defined looking to the detector from the front side.

Group	Label	x(cm)	y(cm)	z(cm)
IBR	PT01	-165	1815	40
	PT02	-175	1865	79
	PT03	-175	1865	232
	PT04	-175	1865	313
	PT05	-175	1815	352
ICR	PT06	-165	1215	40
	PT07	-175	1265	90
	PT08	-175	1265	196
	PT09	-175	1265	301
	PT10	-165	1215	352
IBL	PT11	165	1815	40
	PT12	175	1865	79
	PT13	175	1865	232
	PT14	175	1865	301
	PT15	165	1815	352
IFL	PT61	165	115	40
	PT62	175	65	90
	PT63	175	65	232
	PT64	175	65	301
	PT65	165	115	352
ICL	PT66	163	638	70
	PT67	175	665	106
	PT68	175	665	196
	PT69	175	665	286
	PT70	175	665	376
IFR	PT71	-165	115	40
	PT72	-175	65	90
	PT73	-175	65	232
	PT74	-175	65	301
	PT75	-165	115	352
ECL	PT21	195	965	-10
	PT22	195	965	30
	PT23	195	965	195
	PT24	195	965	360
	PT25	195	965	400
EBL	PT26	195	1365	-10
	PT27	195	1365	30
	PT28	195	1365	195
	PT29	195	1365	360
	PT30	195	1365	400
EFL	PT81	195	565	-10
	PT82	195	565	30
	PT83	195	565	195
	PT84	195	565	360
	PT85	195	565	400

Table 3.2: Position of the Pt1000. The reference system is centered at the bottom part of the internal front wall. The x axis goes along the drift direction from right to left, the y axis along the longitudinal axis of the cold vessel from front to back, the z axis along the vertical direction from bottom to top.

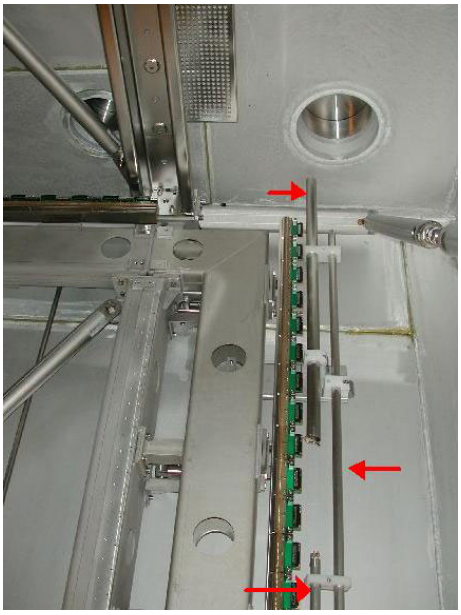

Figure 3.2: Level meters mounted at the back left side.

Level Meter	Height [mm]	Distance from top [mm]
FL1	0025 – 1325	
FL2	1126 – 2451	
FL3	2248 – 3573	
FL4	3348 – 3848	45.5 – 545.5
FR1	0025 – 1325	
FR2	1125 – 2450	
FR3	2244 – 3569	
FR4	3355 – 3855	45.0 – 545.0
BL1	0025 – 1325	
BL2	1127 – 2427	
BL3	2227 – 3527	
BL4	3345 – 3845	45.0 – 545.0
BR1	0025 – 1325	
BR2	1123 – 2423	
BR3	2231 – 3531	
BR4	3348 – 3848	44.0 – 544.0

Table 3.3: Height covered by the LAr level meters.

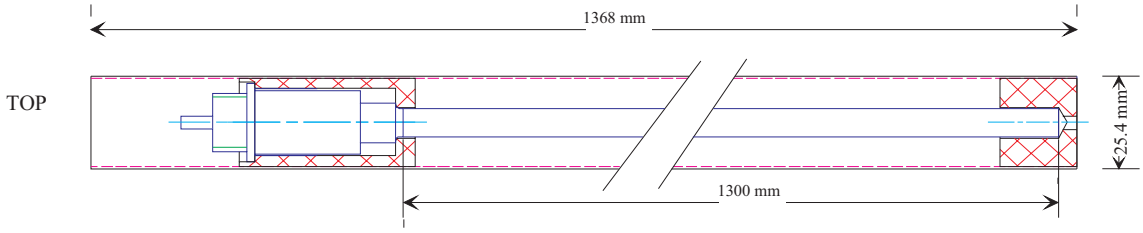

Figure 3.3: Commercial level meter mounted inside the shielding.

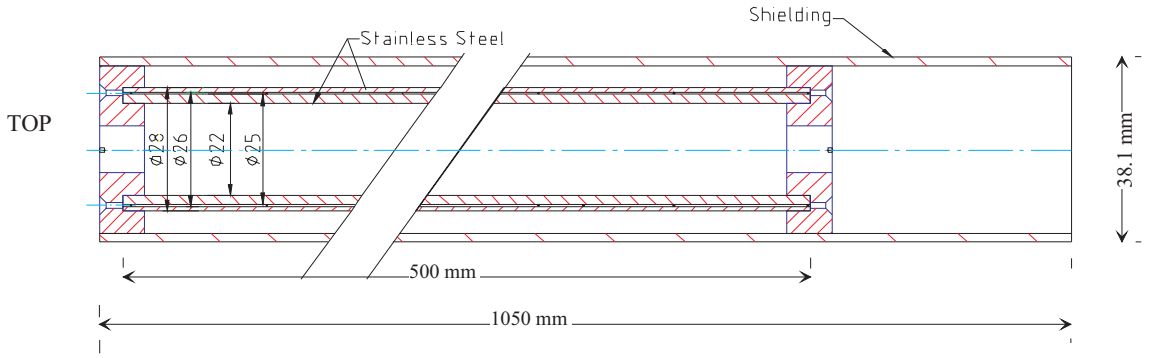

Figure 3.4: Precision level meter mounted inside the shielding.

Position Meter	Slope [pF/mm]	Fit error [pF/mm]
W1	-1.605	0.006
W2	-1.670	0.006
W3	-1.655	0.009
W4	-1.706	0.044
W5	-1.445	0.006
W6	-1.687	0.008
W7	-1.668	0.031
W8	-1.613	0.008

Table 3.4: Results of the fits to the calibration measurements of the wall position meters.

3.1.2 Position meters

The position meters are cylindrical capacitors with a capacitance depending on the relative position of the inner and outer parts. The outer cylinder and the inner shaft are stainless steel, and the end caps with the precise bearings for the inner shaft are made out of glass-fiber enforced epoxy. The radial gap between inner and outer cylinder is 0.5 mm for all the position meters.

Wall position meters

Four position meters are mounted along both sides of the cryostat at the locations shown in figure 3.1. They are mounted with polyethylene clamps at half height to the vertical poles of the wire chamber frame (see figure 3.5). The sensors measure the inward movement of the walls when the cryostat is evacuated to vacuum, and the outward movement, when it is filled with LAr; the precision is about 0.2 mm.

Figure 3.6 shows the drawing of a wall position meter in the OUT position. A spring is pushing the inner and outer cylinders apart. The outer cylinder is fixed to the wire chamber frame and the inner shaft is pushing against the wall. The extension of the outer cylinder holding the spring in the IN position is made out of polyethylene. Figure 3.7 shows a picture of an assembled wall position meter (at right) and of its parts (at left). The wall position meters have a linear measuring range of about 65 mm. Figure 3.8 shows the fits to the calibration measurements (in air) for the linear range of all the wall position meters, and in table 3.4 the fit results are summarized.

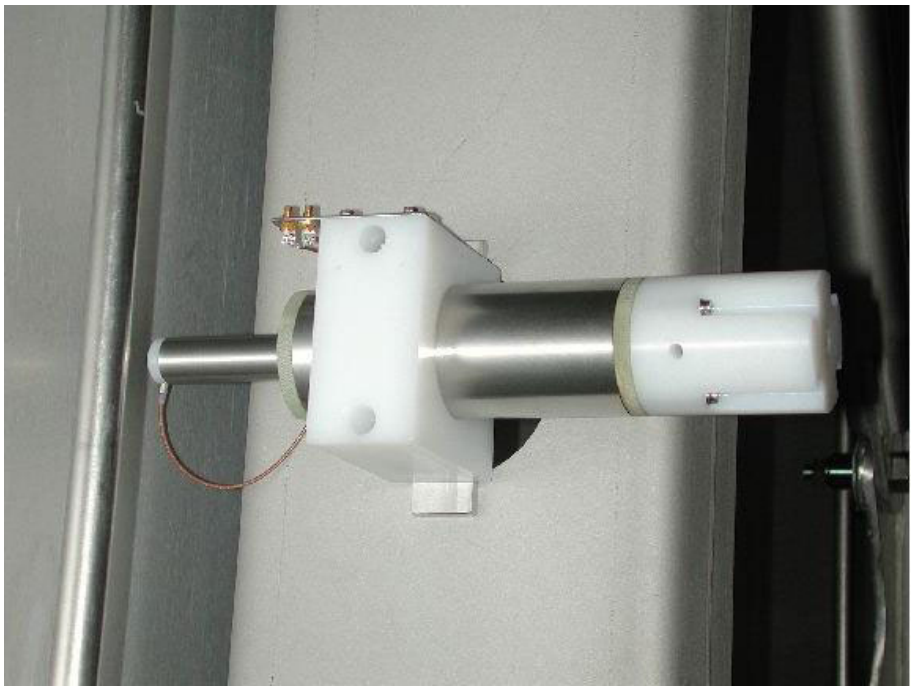

Figure 3.5: Wall position meter attached to the wire chamber frame. The inner shaft of the sensor is pushing against the cryostat wall.

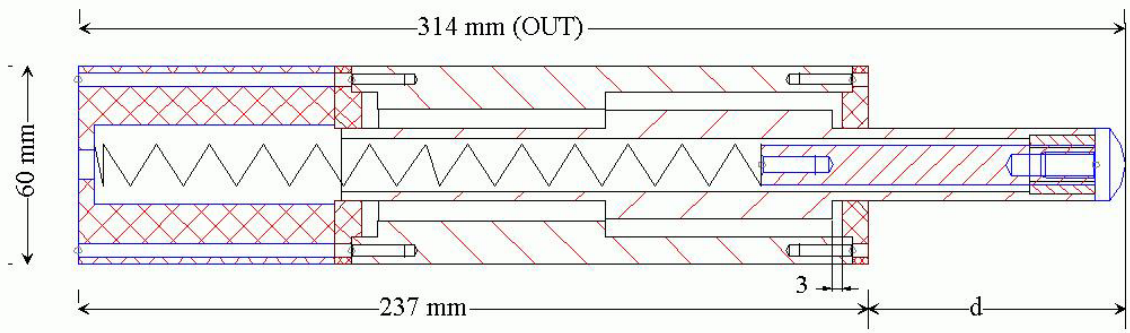

Figure 3.6: Wall position meter drawn in the OUT position.

Figure 3.7: Picture of a wall position meter dismounted (left) and assembled (right).

Position meters for horizontal wires

The horizontal wires of the wire chambers are split in two halves, the front-half and the back-half, 9 m long each. They are fixed at the center of the chamber and tensioned from the front and the back side. The wires on the left and on the right chamber are grouped in three groups, each of them attached to a spring, which is used for tensioning. The springs compensate the thermal contraction of the wires during the cooling phase, and hence maintain an approximately constant tension on the wires. Six position meters for the horizontal wires are attached to the springs at the front side (see figure 3.9) to measure their movement during the cooling phase (three on the left side and three on the right side); no wire position meters are installed at the back side. Figure 3.10 shows the drawing of a position meter for horizontal wires and figure 3.11 a picture of a decomposed sensor. The inner side of the outer cylinder also has the periodic structure seen on the inner shaft. Hence, the sensor consists of ten parallel cylindrical capacitors to increase the sensitivity to a change of the relative position of the inner and outer parts. The sensors have a linear measuring range of about 15 mm, and a total (mechanical) range of 20 mm. Figure 3.12 shows the fits to the linear part of the calibration measurements, and table 3.5 summarizes the fit results.

Position meter for vertical wires

The position meter for the vertical wires was built as a prototype for the wire position meters. It is similar to the type for the horizontal wires (see figure 3.13), but has about twice the total range. Figure 3.14 shows the measurements over the total range, which reflects the periodic (spatial) structure of the parallel capacitors, and the result of the fits to the two linear ranges with positive and negative slope respectively. The working point was set to $d_0 = 17.0$ mm, i.e.

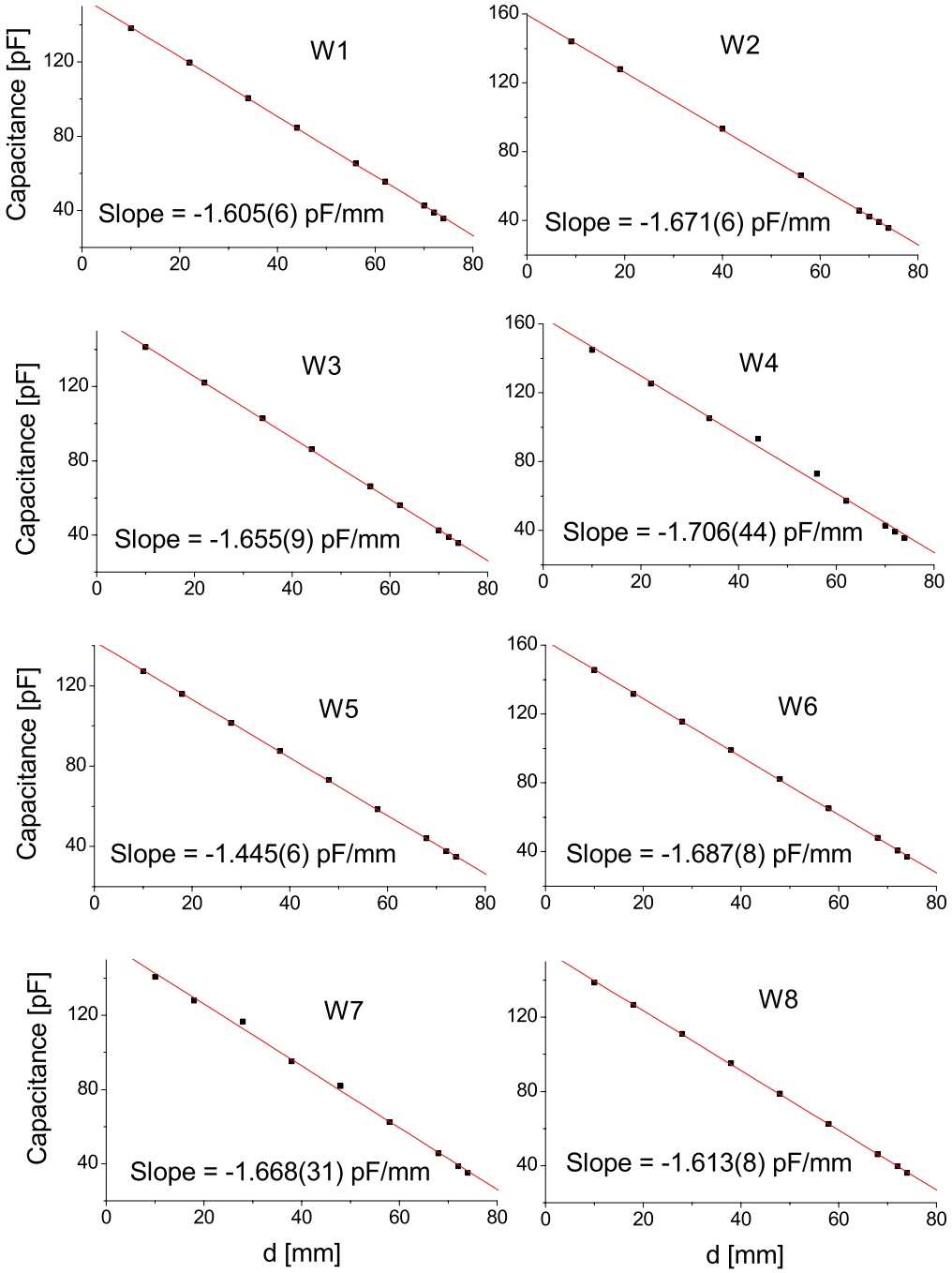

Figure 3.8: Linear fits to the calibration measurements of the wall position meters. d measures the relative position between the inner and outer cylinders (see figure 3.6).

Figure 3.9: Position meter for horizontal wires attached to a spring.

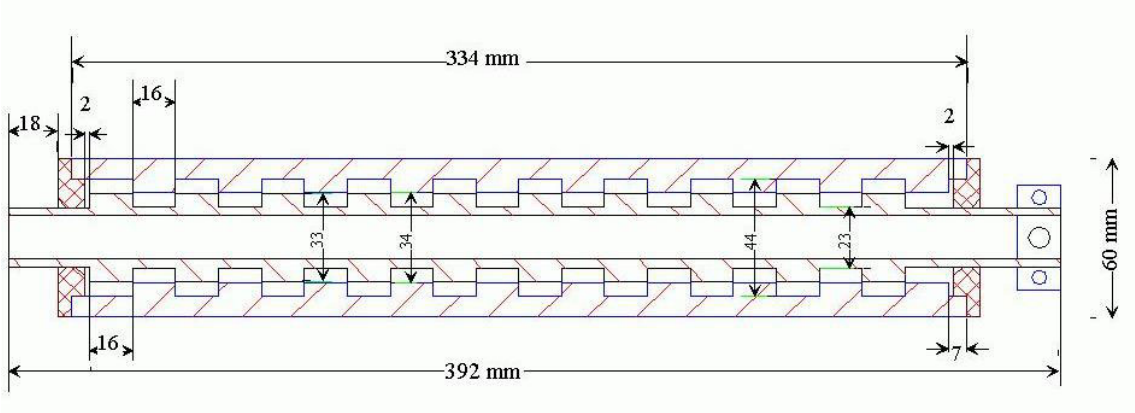

Figure 3.10: Drawing of a position meter for horizontal wires.

Position Meter	Slope [pF/mm]	Fit error [pF/mm]
H1	8.26	0.09
H2	8.61	0.12
H3	8.24	0.09
H4	8.21	0.10
H5	8.42	0.10
H6	8.64	0.14
V1 (positive slope)	14.79	0.10
V2 (negative slope)	-14.63	0.07

Table 3.5: Results of the (linear) fits to the calibration measurements of the wire position meters. H1 to H6 are the sensors for the horizontal wires, and V1 is the position meter for vertical wires (see paragraph 3.1.2).

Figure 3.11: Decomposed wire position meter.

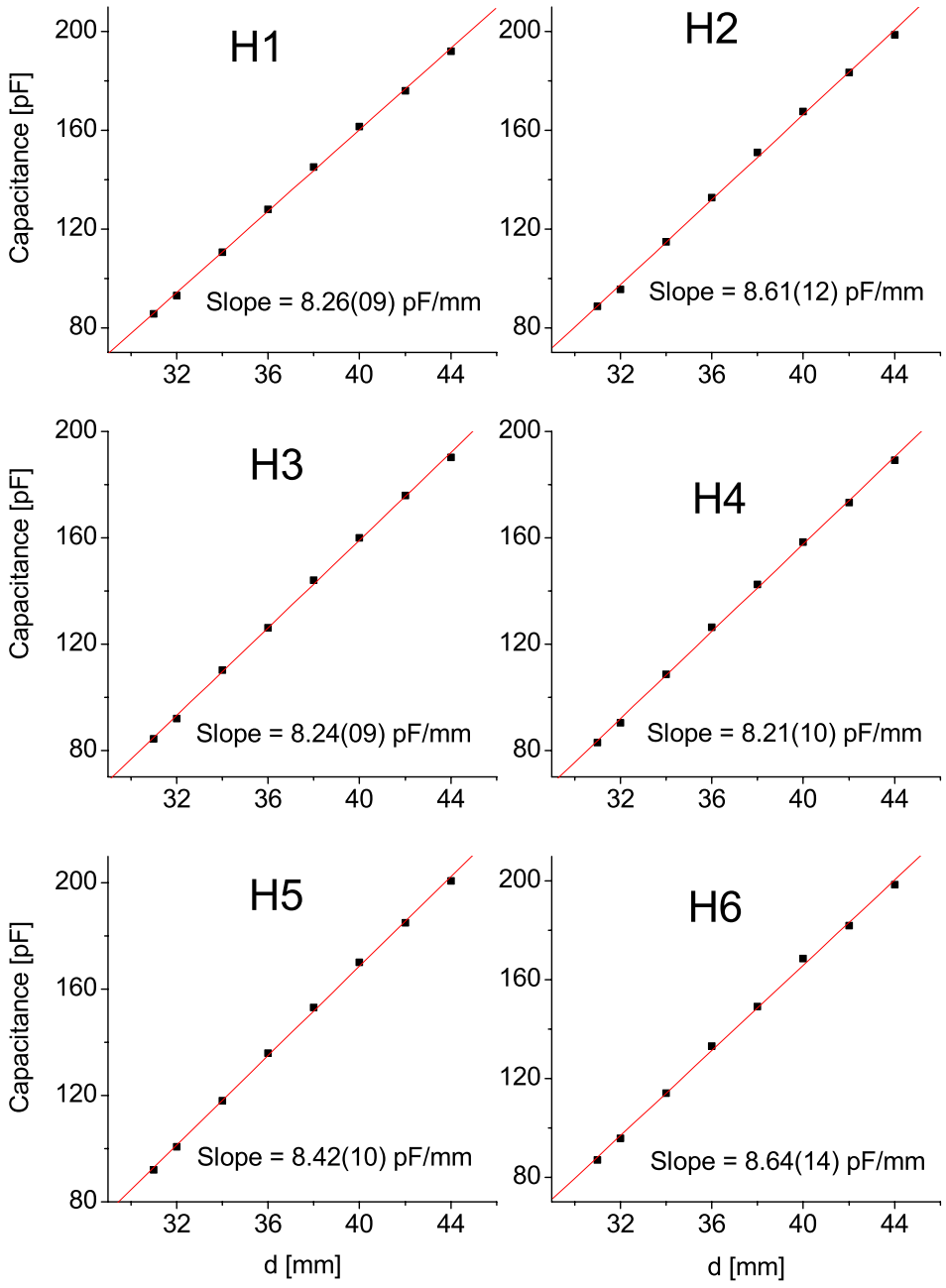

Figure 3.12: Fits to the calibration measurements of the position meters for the horizontal wires. d measures the relative position between the inner and outer cylinders (see figure 3.10).

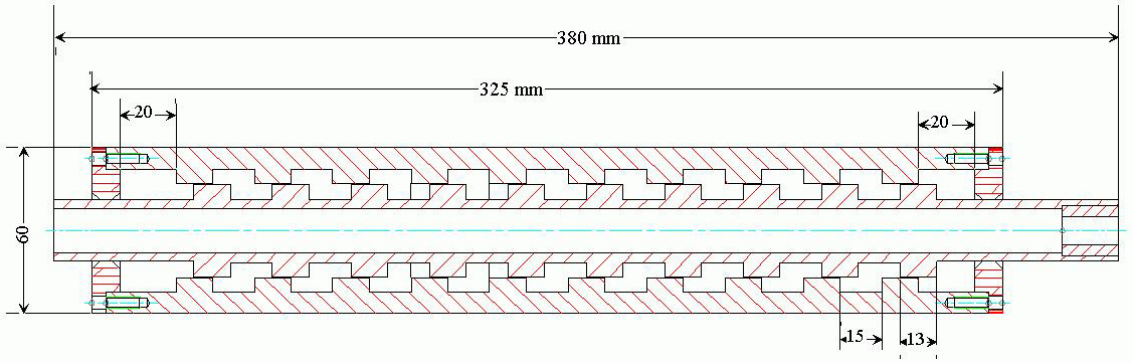

Figure 3.13: Drawing of the position meter for vertical wires.

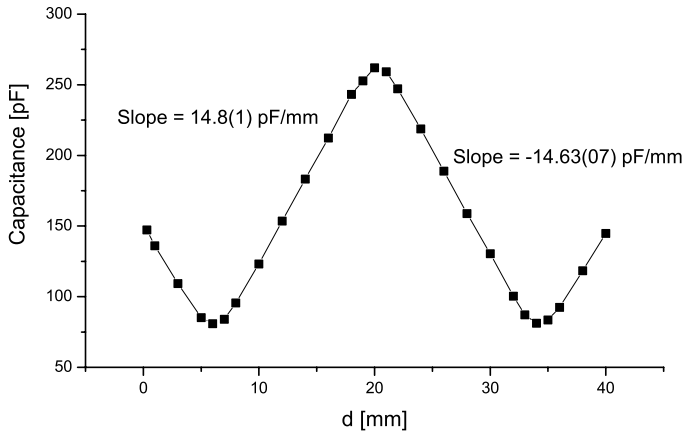

Figure 3.14: Calibration measurement of the position meter for vertical wires. d measures the relative position between the inner and outer cylinders (see figure 3.13). The slopes fitted for the two linear regimes are quoted.

the positive slope is used to measure the wire contraction. The sensor is attached to the fifth spring from the front on the left side (see figure 3.15).

3.1.3 Electronics

For all sensors, the dependence of capacitance vs. position (for position meters), or capacitance vs. LAr level (for level meters) is a well known function, defined by the sensor dimensions and confirmed by direct measurements (see figures 3.8, 3.12 and 3.14). To measure the sensor capacitance, a capacity meter was designed and implemented as a NIM module. The capacitance is measured using the principle of the charge measurement.

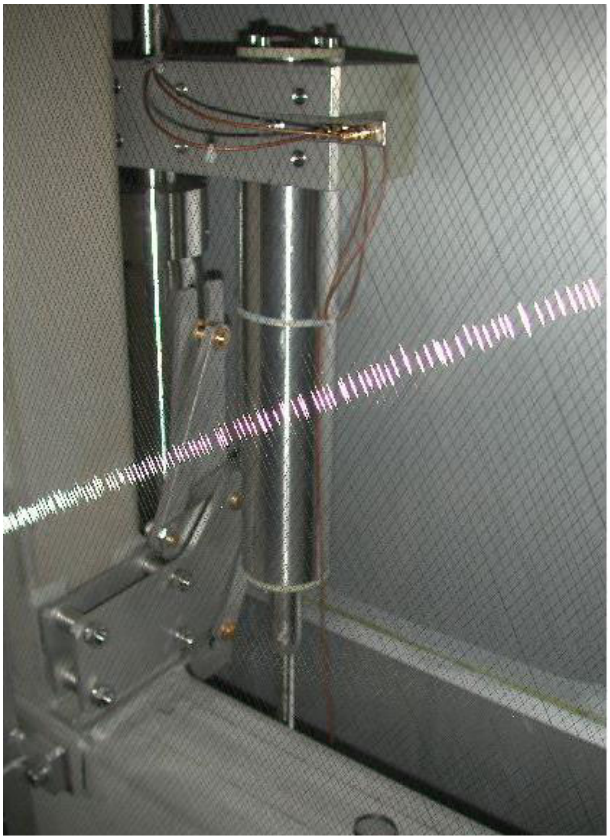

Figure 3.15: Position meter for vertical wires mounted behind the wire chamber.

Charge capacity meter

The outline of the capacity meter (one channel) is shown in figure 3.16. The charge preamplifier JJBP-450 [50] is used to integrate the charge coming from the sensor, when it is driven by an external pulse with a constant voltage. The measured charge (Q) is proportional to the amplitude of the driving pulse (U) and to the capacitance (C) of the sensor, $Q = U \times C$.

A driving pulse of 30 mV is generated in the capacity meter circuit with two mono-stable multi-vibrators (74 HCT 221), and is sent through a coaxial cable to the sensor (see figure 3.17). The charge passing through the sensor is fed to the preamplifier input by a returning coaxial cable. In this configuration, the capacitances of the coaxial cables, which load the preamplifier input, practically do not affect the measurement of the charge. They correspond to a capacitance with respect to ground and their effect is essentially to increase the noise at the output of the preamplifier. This effect is small because of the large transconductance of the J-Fet in the preamplifier (40 mA/V).

The output signal from the preamplifier passes through a shaper (τ = 600 ns) to reduce the noise. The semi-Gaussian (negative) signal on the shaper's output is still proportional to the measured capacitance. Its amplitude is stored with a sample-and-hold stage. For the sample, the falling edge of the driving pulse is used. The measurement is repeated every 100 μs.

A quasi DC signal is formed on the Hold circuit output. This signal is integrated with an RC circuit (τ = 2.2 s), and is measured through a separator with a LCD voltmeter. The sensitivities of the capacity meters are regulated for either 4 pF/dig or 20 pF/dig. The latter calibration

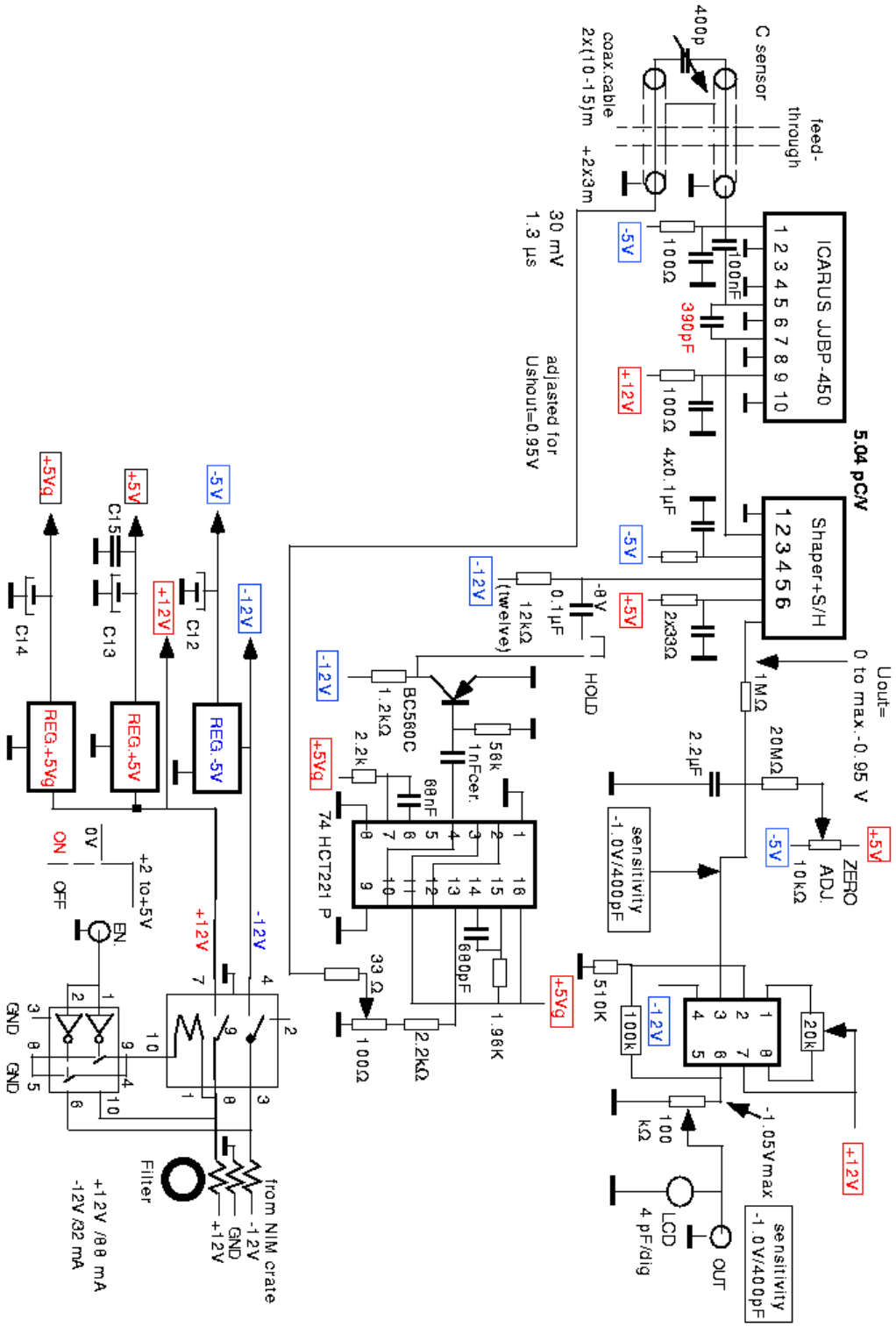

Figure 3.16: Outline of the charge capacity meter (one channel drawn).

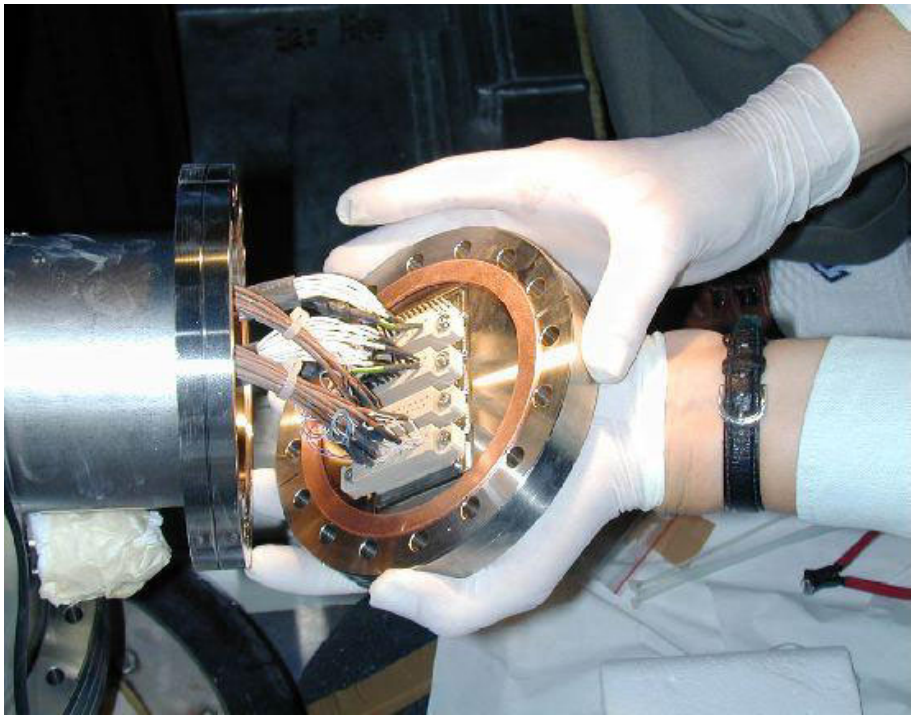

Figure 3.17: Flange with connectors used as feed-through during installation. The Teflon coated cables going to the sensors are visible.

is used for the precision level meters (the range of measured capacitance is from 730 pF to 1080 pF). The former one is convenient for all other sensors. The range can be adjusted by changing the feedback capacitor in the charge pre-amplifier (390 pF or 2060 pF).

The output characteristic of the ICARUS preamplifier with shaper is presented in figure 3.18. The linearity along a range of almost 2 V is shown (the range used by the capacity meter is 1 V). The pulse cable and the input cable of a given channel of a capacity meter go to the calibration module and then through 3 m coaxial cable to the feed-through (see figures 3.19 and 3.20).

Calibration module

This module has been designed to drive the capacity meters to different measurement modes (see figure 3.21), namely:

- The *Sensor* mode connects the capacity meter to the sensor. This is the default mode, happening whenever no input pulse is present.

- *Calibration* measurement mode is performed when relay R2 is ON (see figure 3.21B). For this mode, a +5 V TTL signal must be connected to the "CAL" input on the front panel. In this case, the sensor is disconnected and the capacity meter measures a reference capacitance C_{calib}. In addition, C_{cable} is connected to the capacity meter input (to GND) instead of the real cable capacitance. In principle C_{cable} is chosen to be approximately equal to the capacitance of the real cable. All reference capacitors were chosen as very stable and accurately measured before and after welding.

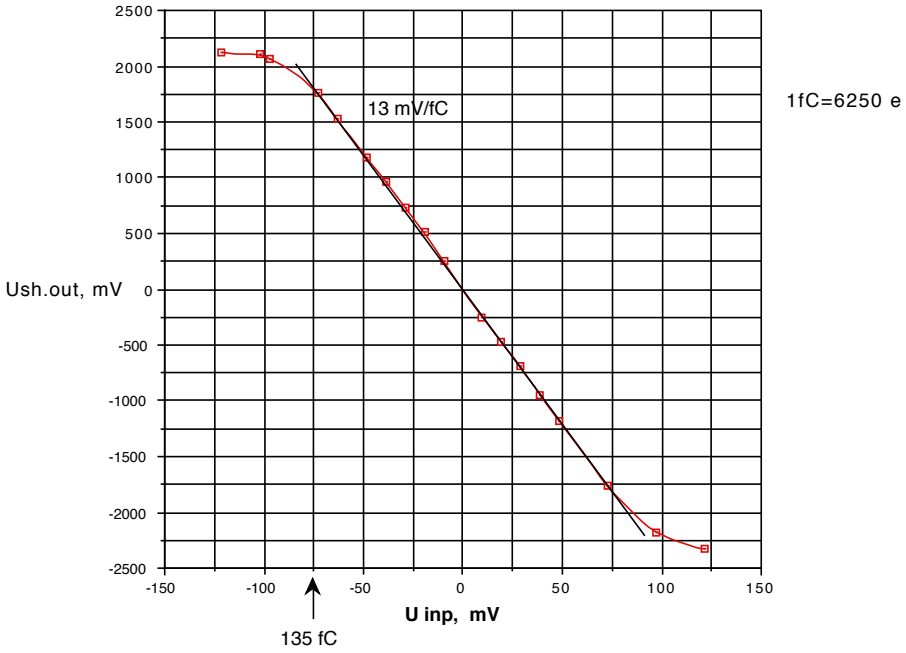

Figure 3.18: Linearity of the preamplifier and shaper.

- The *Zero* measurement mode is performed when both the pulses and the wires to the sensor are disconnected (R1 and R2 are ON), as shown in figure 3.21C. To perform this measurement mode, both input channels on the front panel ("ZERO" and "CAL") must be connected to a +5 V signal. In this situation the pulses are not going to the sensor, and C_{cable} is connected to the capacity meter input instead of the real cable capacitance. The capacity meter should indicate an output voltage equal to zero. Thus, any non-zero value can be subtracted from the output voltage for *Calibration* mode and related to C_{calib}, to obtain the capacity meter calibration constants.

Each calibration module drives 8 capacity meter channels in parallel. All R1 relays are driven from the same driving circuit (not shown in figure 3.21). A second circuit drives the R2 relays. There are some stray capacitances inside the calibration module. They are measured in the same way as the sensor capacitance. They are constant and lower than 0.4 pF.

Temperature measurements

The temperature at different regions of the cryostat are measured by means of the Pt1000 sensors. The resistance of the sensor changes from about 1000 Ω at 273 K, to about 200 Ω for LAr temperature. The calibration measurements of the Pt1000 resistors is described elsewhere [49]. There are 15 sensors installed at the chamber's back side, and 15 sensors at the front side. They are measured in sequence with two multiplexer modules, one at each side.

Connection to the EDAS ethernet interface

The Ethernet data acquisition system (EDAS) [51] type 1002E-2A independently measures the output voltages from the capacity meters through the analog input channels. The digital I/O

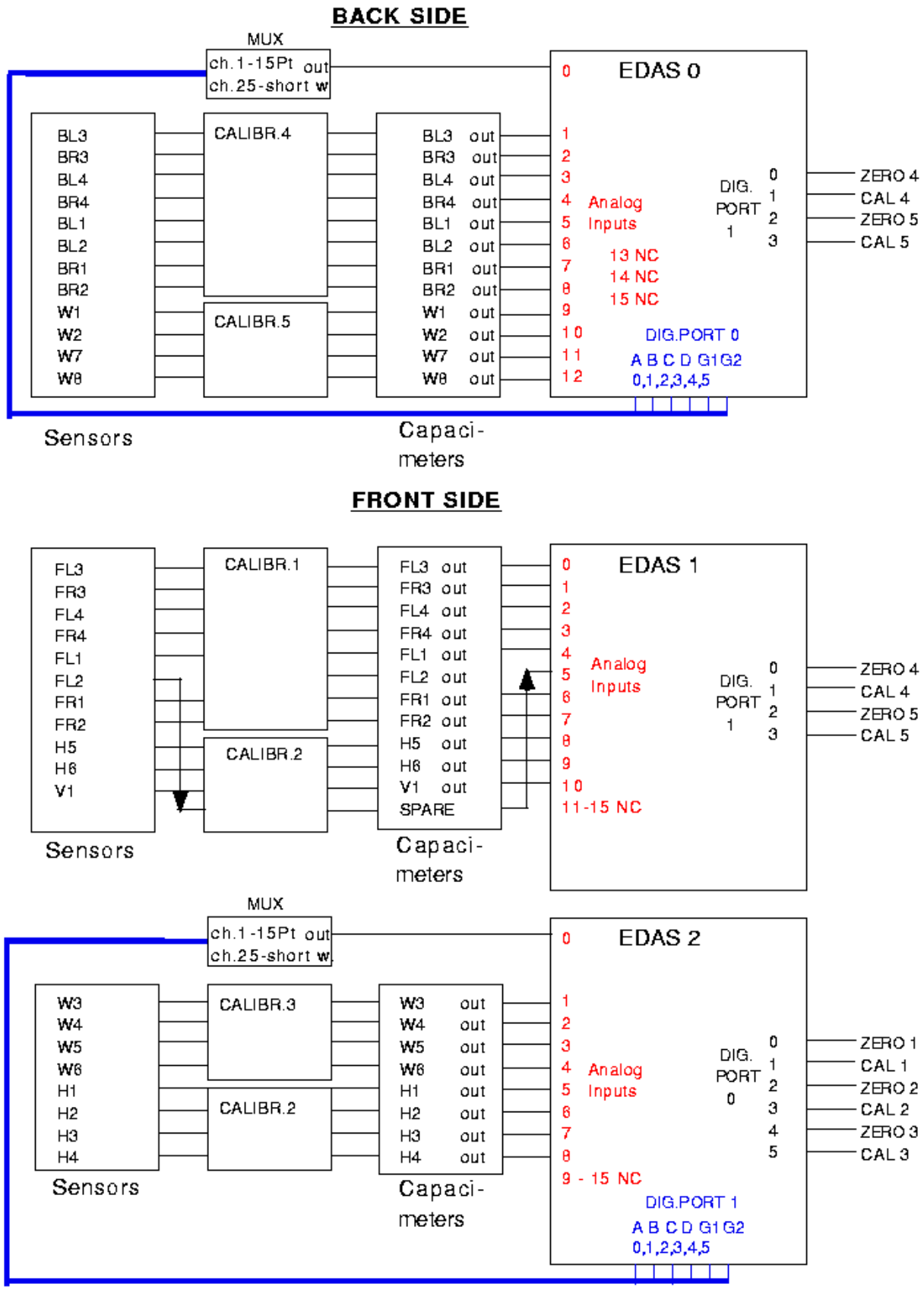

Figure 3.19: Connections to the EDAS ethernet interfaces.

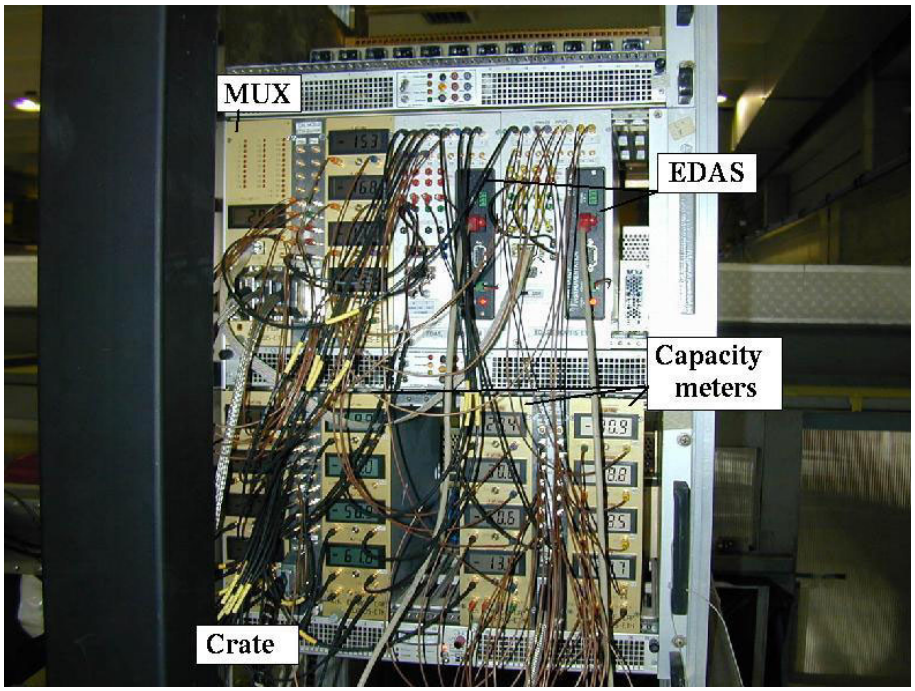

Figure 3.20: The electronic setup in Pavia. Two such setups (one at the front, one at the back) have been installed. See the text for a description of the different modules.

ports are used to address the calibration and multiplexer modules. A scheme of the capacity meters, calibration modules and MUX connections to the three EDAS modules is shown in figure 3.19. There are two modules at the front side of the chamber and one at the back side. All are connected to the Ethernet allowing for data taking and remote control. A picture showing one of the actual setups is shown in figure 3.20.

3.1.4 Data acquisition and display software

The software for the Slow Control data acquisition and display systems has been developed in a modular C++ object-oriented way, such that the different tasks of the whole process are carried out by different independent objects interacting among them.

The central part of the whole system is the Database, which stores the values coming from the measurements of the different sensors, as well as the information regarding the sensors sensitivity and calibration factors. The Database is physically stored in a local PC running Linux, and managed by the MySQL database administration package [52]. A periodic backup of the system ensures the accessibility to the data.

Data are organized in the Database in four different tables, namely: *sensor*, *cap*, *measurement* and *calib*. The first two store the information concerning the sensors (label, type, sensitivity, zero value, link to the capacity meter) and capacity meters (sensitivity, value of the calibration reference capacitance), respectively. These two tables are built according to the experimental setup (i.e. all the calibration parameters and connections are known) and remain unchanged during the data taking period. They contain the information needed to get the final calibrated values (in terms of distance or temperature) from the raw data (coming in volts). Actual data are stored in the two "growing" tables: *measurement* and *calib*. Table *measurement* stores the

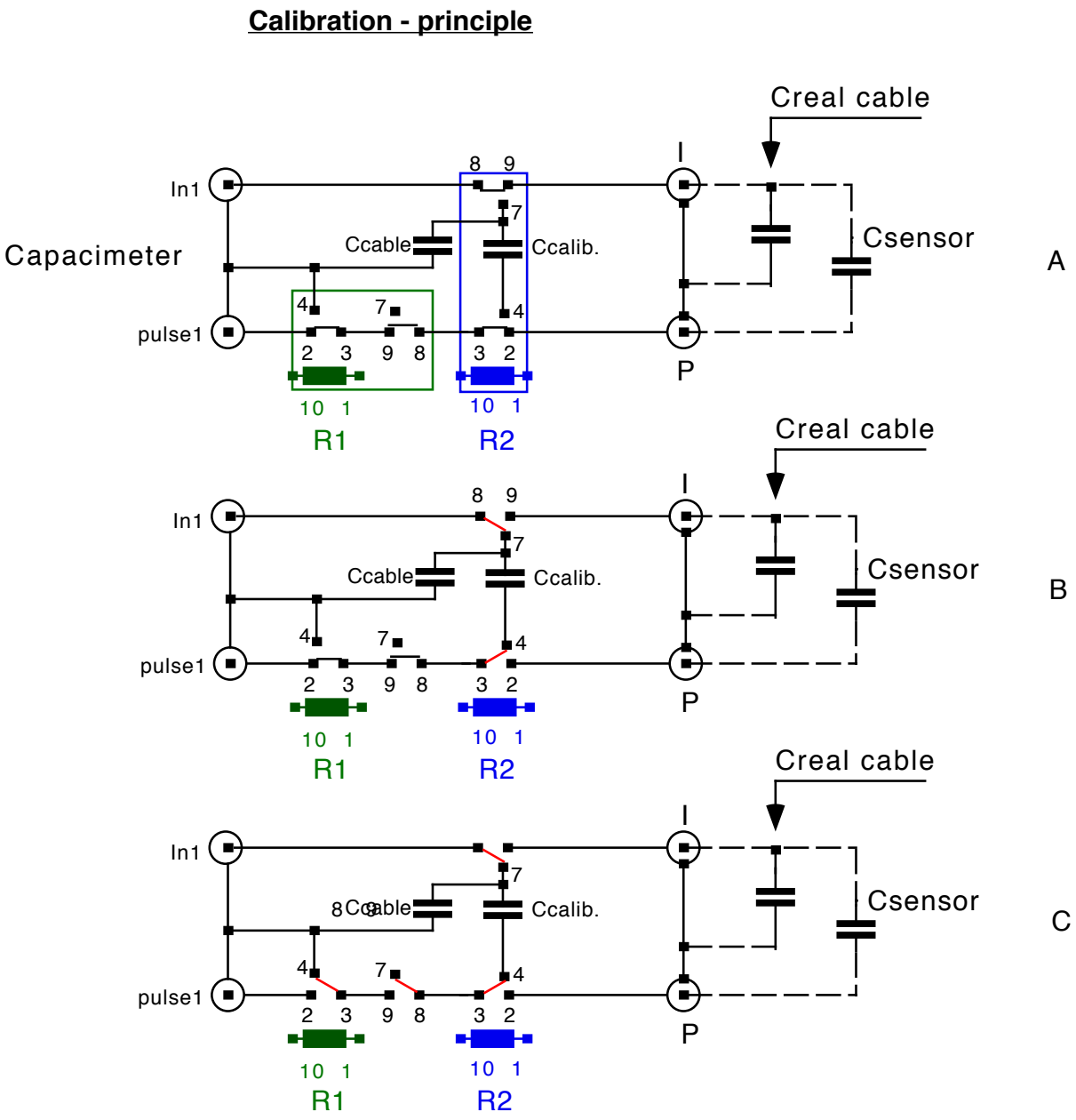

Figure 3.21: Principle of operation of the calibration module. The relays R1 and R2 are "OFF" on horizontal positions.

output signals from the periodical sensor reading, whereas *calib* is devoted to the values of the zero and reference capacitances used for calibration purposes.

Raw data are obtained from the EDAS for the different measurement methods described above are stored in the data base. An independent object combines several Database entries to build up objects containing meaningful information, namely: the value of a given measurement both in raw and calibrated values, the precise date and time when the measurement was performed, the sensor which performed it, and the status of the latest calibration parameters at the moment the measurement was performed. Finally, several basic tools based on the Trolltech's GUI, Qt [53] class library have been developed providing a full, easy and user-friendly access to the Database, to check both, the measurements from the different sensors in real time and their evolution in time.

3.2 Results from the T600 technical run

In this section we present the results of the analysis of the Slow Control data acquired during the T600 technical run (see section 2.2.3). The technical run lasted more than 100 days between May and August 2001. The stability checks of the Slow Control system started well before the beginning of the run and extended well after the cryostat draining, until the internal volume reached the thermal equilibrium with the surrounding medium, at room temperature. The first part of the section is devoted to report on the calibration of the LAr level meters and the determination of the sensors accuracy, using the data acquired during LAr filling and stability test, respectively. After this, an analysis of the mechanical and thermodynamical responses of the detector during the different phases of the technical run is presented.

3.2.1 Calibration and sensitivity evaluation

Calibration

The position meters and the Pt1000 resistors were calibrated at ETH before their installation in the detector and the results of the calibration have already been reported in the previous section. The calibration of the level meters was performed during the LAr filling of the cryostat.

For the calibration of the commercial level meters, two reference points were used (see figure 3.22): the bottom of the sensor (Bn in the figure), and the bottom of the overlapping sensor immediately above it (B$n+1$). The uncertainty of this calibration procedure can be estimated by a comparison of the four independent measurements of the LAr level performed at the four corners of the cryostat during the LAr filling. The cryostat is not exactly leveled and thus, there might be a real difference of the levels in the four corners relative to the floor of the cryostat. Figure 3.23 shows the maximal differences between the LAr level measured by any two commercial level meters during the LAr filling. Thus, the error is estimated from the figure to be between 10 and 20 mm.

The previous method can only be used for the calibration of the commercial level meters, since for the top level meters we lack the upper reference. For these sensors we use instead, the point B4 and the overlap with the level meter immediately below. A χ^2 function is built using about 150 points measured by both the top and the commercial level meters. The χ^2 was minimized to find the optimum calibration parameter for the top sensor. The error on this parameter is taken as the one for which $\chi^2 = \chi^2_{min} + 1$. This yields an uncertainty on the level meter calibration of 0.8% of the measurement, for a single sensor.

Room temperature dependence of the capacity meters

A dependence on the room temperature of the capacity meters, i.e. the electronics modules reading the position and level meters, was observed during the Slow Control stability test. This effect is illustrated in figures 3.24a and 3.24b. A calibration module was added to the electronics in order to correct for this temperature effect. This device connects the capacity meter alternatively to the sensor (normal measurement) and to a pre-calibrated capacitor, with a small temperature coefficient (calibration measurement). The calibration measurement records the temperature dependence of the capacity meter (figure 3.24c), and therefore can be used to calibrate it. Figure 3.25 shows an example of how this dynamic recalibration of the capacity meter corrects for the observed temperature dependence.

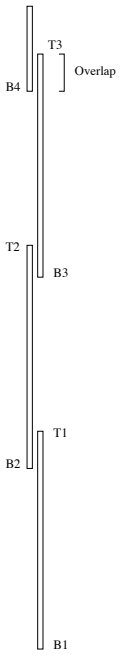

Figure 3.22: Schematic side view of the level meters arrangement at one of the detector's corner. Marked are the points used for the sensor calibration.

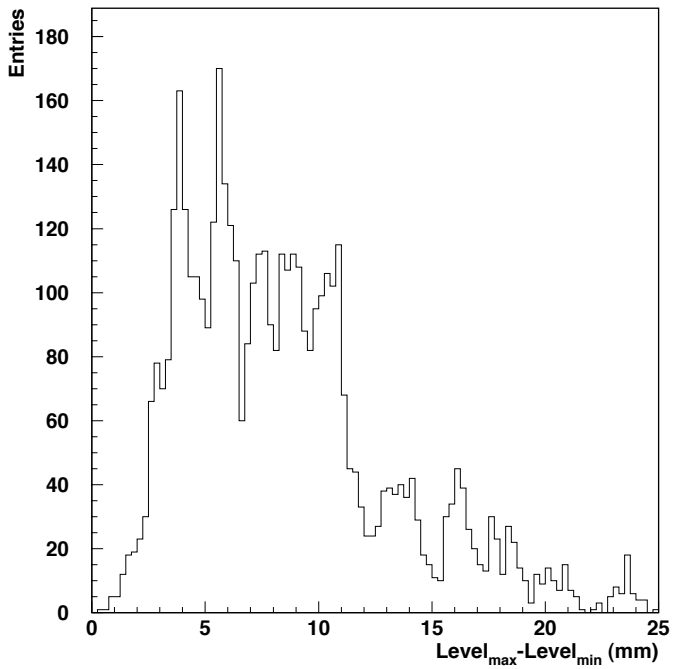

Figure 3.23: Maximal LAr level difference measured by any two commercial level meters during the LAr filling.

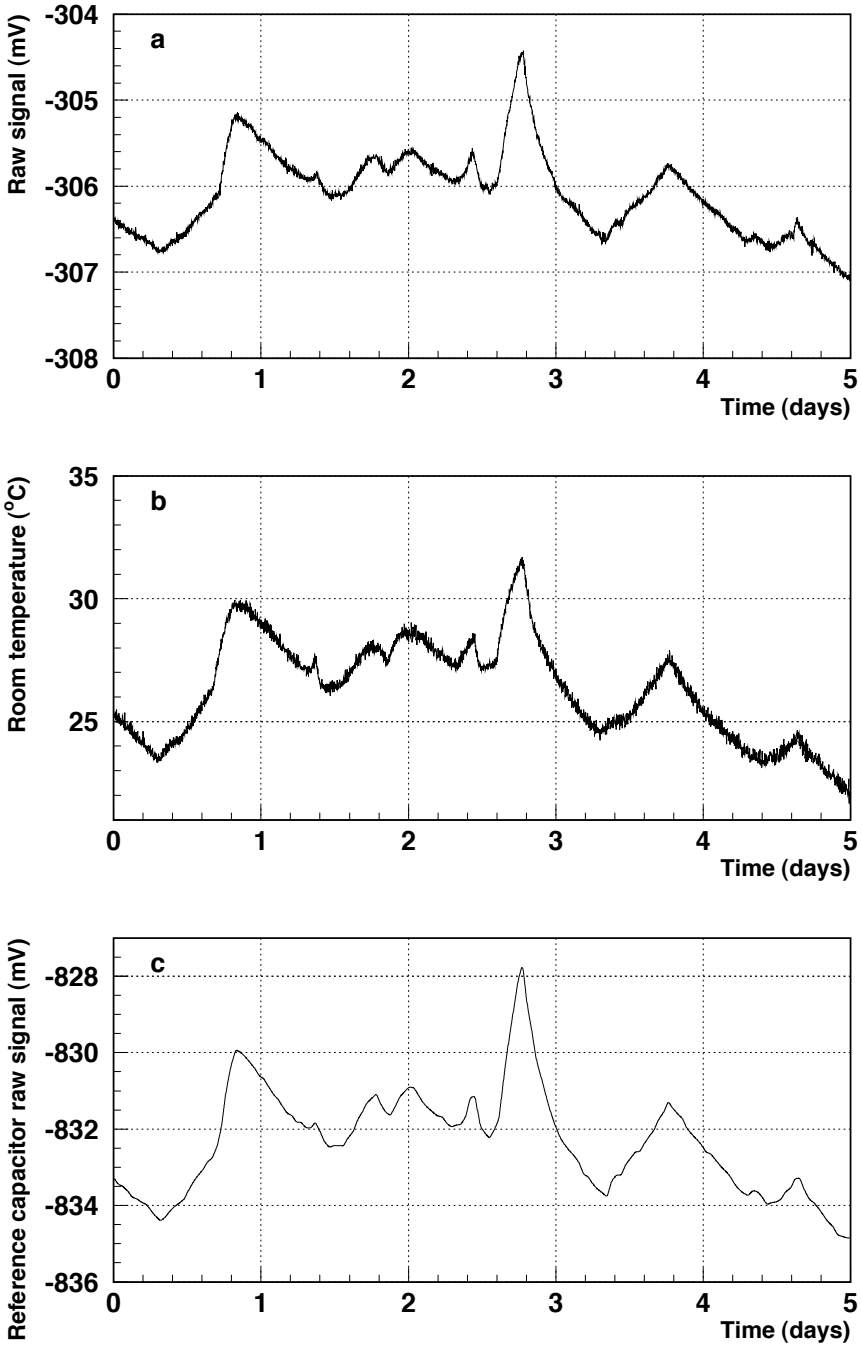

Figure 3.24: Room temperature effect on the capacity meters. The data were collected with the wire position meter H1 over a time period of 5 days during the Slow Control stability test, when the wire position is expected to be constant. a) Capacity meter raw output value when reading the sensor; b) Room temperature in the experimental hall; c) Capacity meter raw output value when reading the reference capacitor.

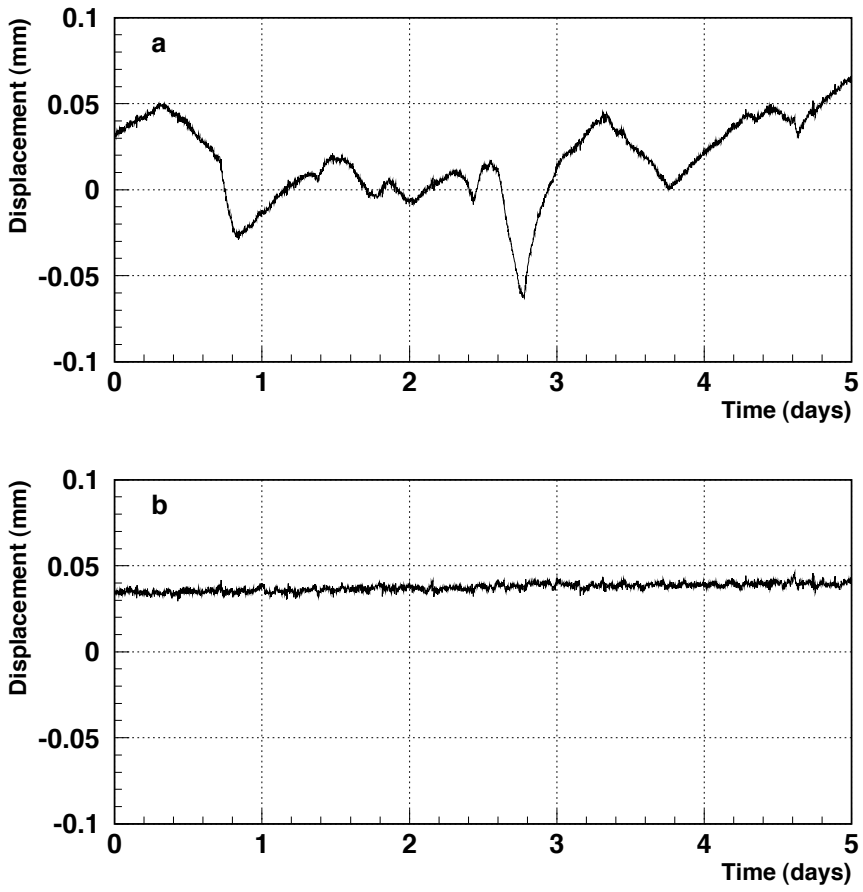

Figure 3.25: Effect of the dynamic recalibration on the sensor measurement. The data were collected with the wire position meter H1 over a time period of 5 days during the Slow Control stability test, when the wire position is expected to be constant. a) Measurement calibrated with the nominal capacity meter calibration; b) Measurement dynamically re-calibrated.

Measurement errors

The readout chain for the capacitor-like sensors (position and level meters) is composed of the sensor, the capacity meter and the Ethernet Data Acquisition System (EDAS). The capacity meter reads the sensor capacitance, and its output voltage is read by the EDAS, which stores the result in a database. For the Pt1000 sensors, the capacity meter is replaced by a multiplexer, which reads alternatively a group of Pt1000 sensors.

Each element in the readout chain introduces an uncertainty on the sensor measurement. The statistical dispersion (σ) on a measurement is determined by the electronics and the measurement procedure. The accuracy (Δ) reflects the uncertainty on the absolute calibration and depends on the EDAS resolution and the sensors' calibration systematic error. The different contributions to the measurement error have been estimated theoretically and checked experimentally during the Slow Control stability test. They are summarized hereby and in table 3.6.

- EDAS. This device reads a voltage from the capacity meter and the Pt1000 sensors, and digitizes the signals with 12 bit resolution (4096 channels). The input range was configured to the interval [-1,1] V, which covers the output range of all the sensors. This yields

Sensor	σ_{EDAS}	$\sigma_{EDAS} \oplus \sigma_{Cap}$	ΔDigitization	ΔCal	ΔGeom
Wall position (mm)	0.01	0.015	0.15	0.6%	—
Wire position (mm)	0.0013	0.0024	0.015	1.2%	—
Commercial level (mm)	0.25	0.6	2.4	10-20	2
Precision level (mm)	0.1	0.22	2	0.8%	2
Pt1000 (K)	0.05	0.05	0.1	0.5	—

Table 3.6: Estimated measurement dispersion and uncertainty induced by the different elements of the read-out chain for the different sensor types.

a resolution of 0.5 mV. Each measurement is taken as the average of a set of 200 measurements, performed at 10 kHz frequency. Thus, the expected dispersion on a measured data point is $\sigma_{EDAS} = 0.5/\sqrt{200} = 0.035$ mV. The dispersion, translated into the final units for every sensor, is shown in table 3.6 (σ_{EDAS}). This is the dispersion on the measurements expected for a short time interval of about 1 hour, when the room temperature (and, hence, the capacity meter response) can be considered as constant. Figure 3.26 (left column) shows, for the different sensors, how the measurements are distributed around their mean value (for a 1 hour time period, measured during the Slow Control stability test). The scattering of the measurements agrees in all cases with the expectation.

- Capacity Meter. This device reads the capacitor-like sensors (position and level meters), and is calibrated following the method discussed above. The precision of the calibration procedure lies on both the EDAS and the reference capacitor calibration precisions. The reference capacitances are stable within less than 0.01%. This yields, for the different sensors, an uncertainty of the measurement σ_{Cap}. The quadratic sum $\sigma_{EDAS} \oplus \sigma_{Cap}$ (second column in table 3.6) quantifies the dispersion of a sensor measurement when measured during time periods of several hours, when the temperature changes affect the capacity meter calibration. This dispersion was measured during the test and is shown in figure 3.26 (right column) for the different sensors, for a one day time interval.

  The EDAS intrinsic resolution, due to the digitization, is a source of inaccuracy of the measurement (ΔDigitization). This inaccuracy enters both in the normal and calibration measurement. For an EDAS step of 0.5 mV, the expected uncertainties on the measurement of the different sensors are shown in table 3.6. ΔDigitization corresponds to the minimal value for which the capacity meter calibration procedure is reliable. The effect of the EDAS digitization on the sensor final measurement is shown in figure 3.27, for the different sensors. For every sensor, two Gaussian distributions are found, which have widths approximately equal to $\sigma_{EDAS} \oplus \sigma_{Cap}$, and the peaks separated by ΔDigitization.

- Sensor Calibration. The sensors were calibrated either at the ETH or by direct measurement in the detector. The uncertainty in their calibration is tabulated in table 3.6 (ΔCal).

  For the level meters, we have to consider also the uncertainty of the sensor position within the detector (ΔGeom). There are two sources for ΔGeom, namely, the measurement of the sensor position with respect to the floor and/or ceiling of the cryostat, and the inclination of the detector floor with respect to the horizontal plane. ΔGeom is estimated to be about 2 mm, and has only an influence in the determination of the absolute value of the LAr level. For level differences, it cancels out.

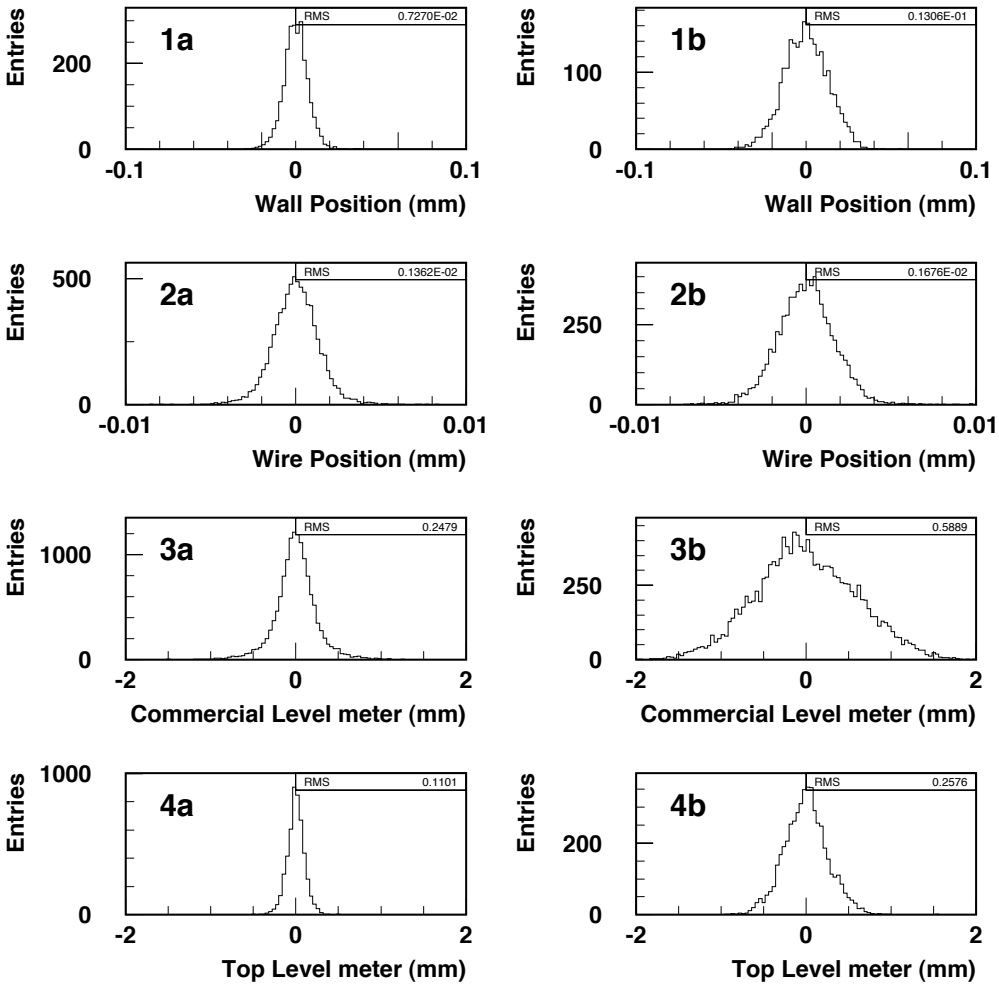

Figure 3.26: Distributions of the sensor measurements for a time interval of one hour (left column) and one day (right column) collected during the Slow Control stability test.

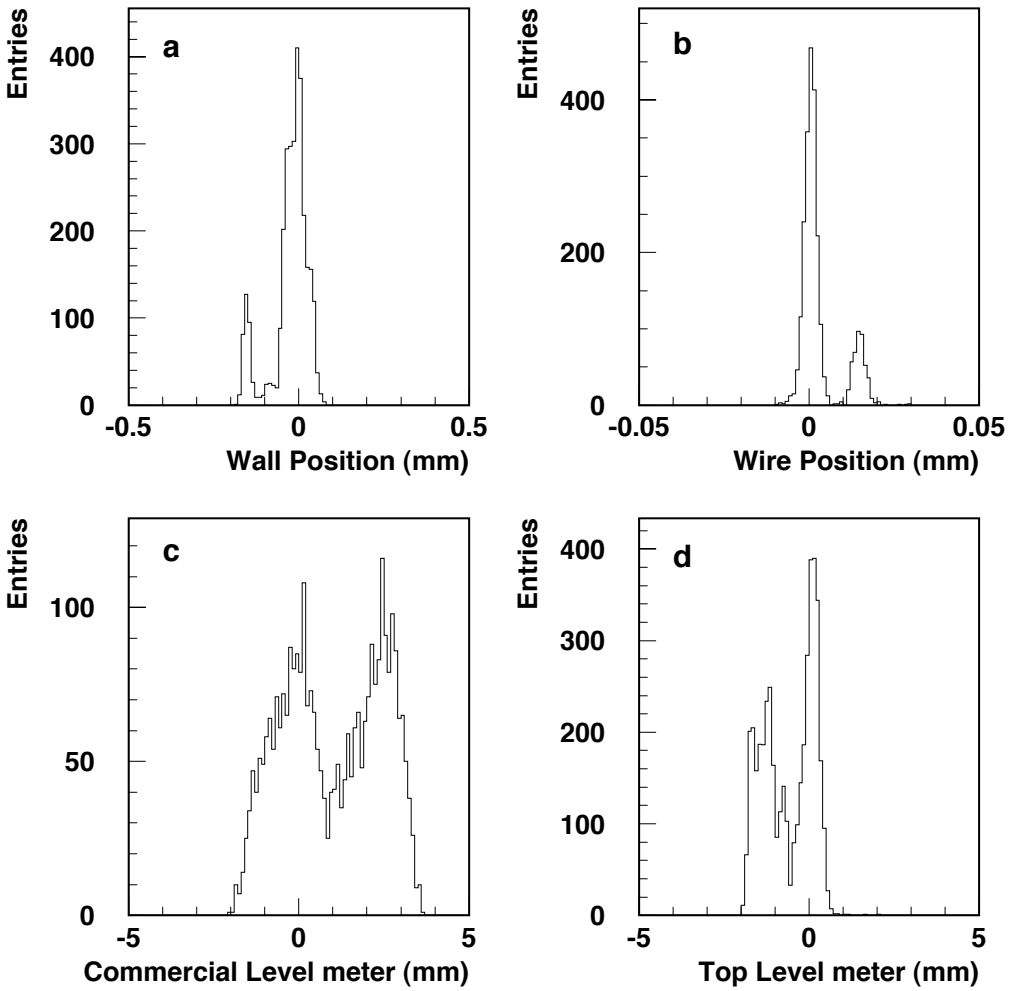

Figure 3.27: Distributions of the sensor measurements for a time interval of three days collected during the Slow Control stability test.

3.2.2 Wall movement

Changing the pressure in the cryostat causes a deformation of the cryostat walls. This deformation is inward (toward the internal detector frame) for a decreasing pressure (i.e. during vacuum phase), or outward for an increasing pressure (i.e. after LAr filling). The walls have to be kept within the elastic range and separated from the frame. To check this requirement, the distance between the cryostat walls and the frame was continuously monitored by means of the wall position meters. The displacement of the wall for a certain pressure P in the cryostat is defined as the difference of the distance wall/frame measured at atmospheric pressure and at the pressure P. It is defined as positive for an outward movement of the wall, and negative for a inward movement.

Wall movement during the vacuum phase

In order to clean it of any impurity, the cryostat was pumped to vacuum before being filled with purified argon. Figure 3.28 shows the pressure in the cryostat during the pumping phase. The curve is essentially compatible with the one obtained with the simulation in the design of the pumping system [54]. After having reached 1 mbar, the turbo-molecular pump was switched on. The required vacuum level (about 10^{-4} mbar) was reached after roughly 50 effective hours of pumping, that took place during a total period of 12 days. Deviations from linearity of the pressure as a function of time are a signal of the presence of leaks in the cryostat, which were repaired as they were detected.

Sensor	Slope (μm/mbar)
W1	22.40±0.04
W2	24.23±0.04
W3	27.75±0.04
W4	24.43±0.04
W5	26.48±0.04
W6	26.61±0.04
W7	22.43±0.04
W8	20.69±0.04

Table 3.7: Fitted slopes for the wall displacements as a function of the pressure in the cryostat.

The displacement of the walls, measured by the eight position meters, as a function of the internal pressure, is shown in figure 3.29. As expected, the walls are deformed linearly with the pressure. A χ^2 fit of a straight line to the data yields the slopes shown in table 3.7. The quoted errors correspond to the values for which a fit with $\chi^2 = \chi^2_{min} + 1$ is found. The slopes agree with the ones measured during the cryostat test in the Air Liquide workshop, prior to the detector installation in Pavia.

The final internal pressure of 3×10^{-4} mbar was reached in steps, between which the pumping was stopped for several days. Such a procedure allowed for the degassing of the surfaces of the internal detector components as well as for leak detection and reparation. The deformation as a function of time during the vacuum phase is shown in figure 3.30.

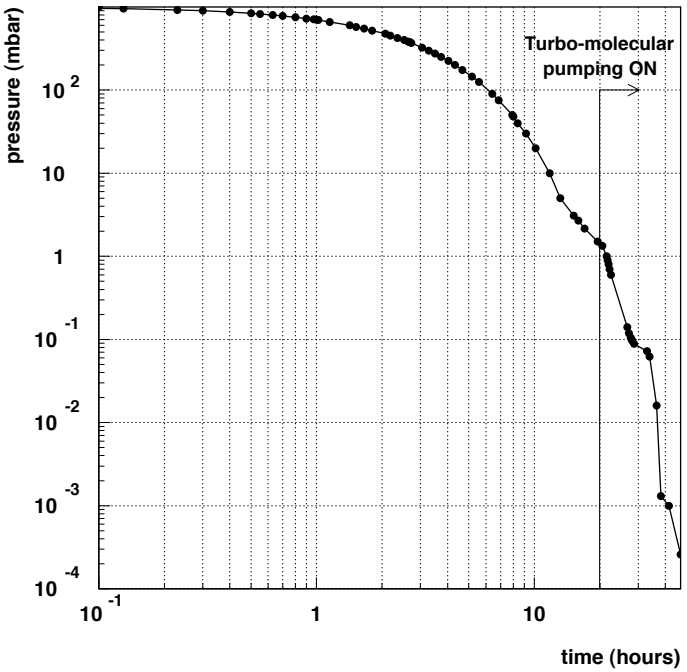

Figure 3.28: Pressure in the cryostat as a function of the effective pumping time.

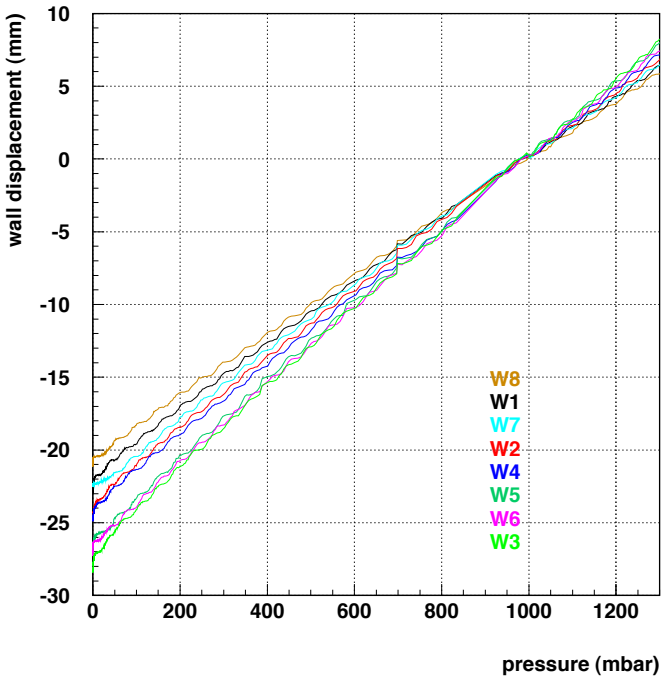

Figure 3.29: Wall displacement measured by the eight wall position meters, as a function of the cryostat pressure. Positive (negative) displacement values mean outward (inward) movement. The legend order corresponds to the curves order at zero pressure.

Sensor	Δd (mm)
W1	-1.3 ± 0.15
W2	-1.4 ± 0.15
W3	-1.5 ± 0.15
W4	-1.2 ± 0.15
W5	-0.7 ± 0.15
W6	-1.0 ± 0.15
W7	0.0 ± 0.15
W8	-0.6 ± 0.15

Table 3.8: Measured wall displacements between the start of the turbo-molecular pump (at about 1 mbar, April 22nd at 12:00h) and the breaking of the vacuum (April 30th).

Maximal wall deformation

The maximal deformation of the walls during the vacuum phase and a leak test with overpressure are shown in figure 3.31. Contrary to what could be a priori expected, the deformation of the cryostat walls is not front/back symmetric. Despite the small number of points where it is measured, the maximal deformation is found to be at about a quarter of the detector length from the front end, for both walls. The effect is most likely caused by the asymmetric distribution of the mechanical stresses within the wall, due to the fact that the end-cap at the front side is bolted to the cryostat, whereas at the back side it is welded.

Wall movement at vacuum ($P \lesssim 1$ mbar)

The walls moved off the linear regime at the end of the vacuum phase. From the moment when the turbo pump was switched on, until the vacuum breaking, the pressure change is 1 mbar, and the expected movement is less than 0.03 mm (see table 3.7). However, the walls continued moving for about 3 days, releasing the stresses in the cryostat. The right and left side walls moved on average 1.4 mm and 0.6 mm, respectively. The measured displacements for the individual sensors are shown in table 3.8. This left/right asymmetric behaviour could be due to a contact of the left side wall with the internal detector frame, as will be discussed below.

Contact between wall and frame

The cryostat wall most likely touched the internal frame at the left side of the detector, at the end of the vacuum phase. This can be deduced from the data of the wall movement during the time interval between the pumping stop and the vacuum breaking (figure 3.32). While the left side was almost at rest during this period, the right side wall still moved some tenths of millimeter. This could be interpreted assuming a contact between wall and frame at the left side, while at the right side the wall was still releasing the stress, toward its equilibrium position. The way the walls started to move back to their original position when the vacuum was broken (figure 3.33) also fits within this hypothesis. According to this, the left side wall started to move back some minutes after the vacuum was broken, when the pressure reached the value at which the wall had been stopped by the frame.

)

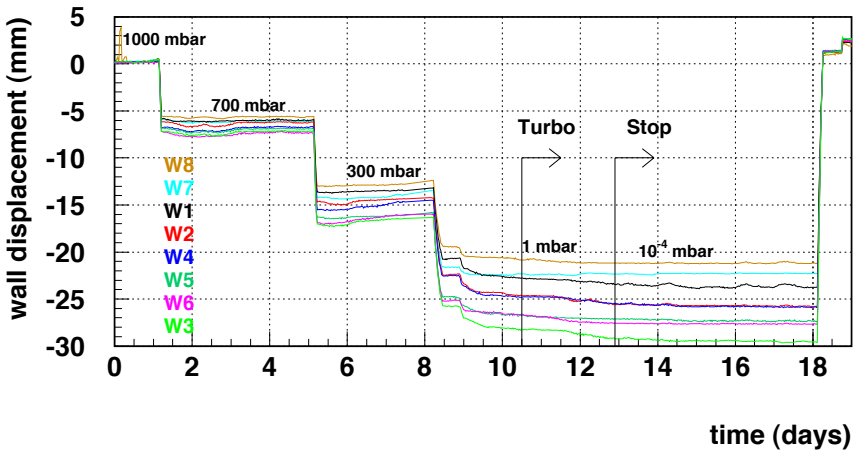

Figure 3.30: Wall displacement during the vacuum phase. The approximate values of the internal pressure are given for the different time periods. The arrows indicate the time when the turbo pump was switched on and when it was stopped. The legend order corresponds to the curves order at the maximal deformation point. The zero time corresponds to April 12th at 00:00h.

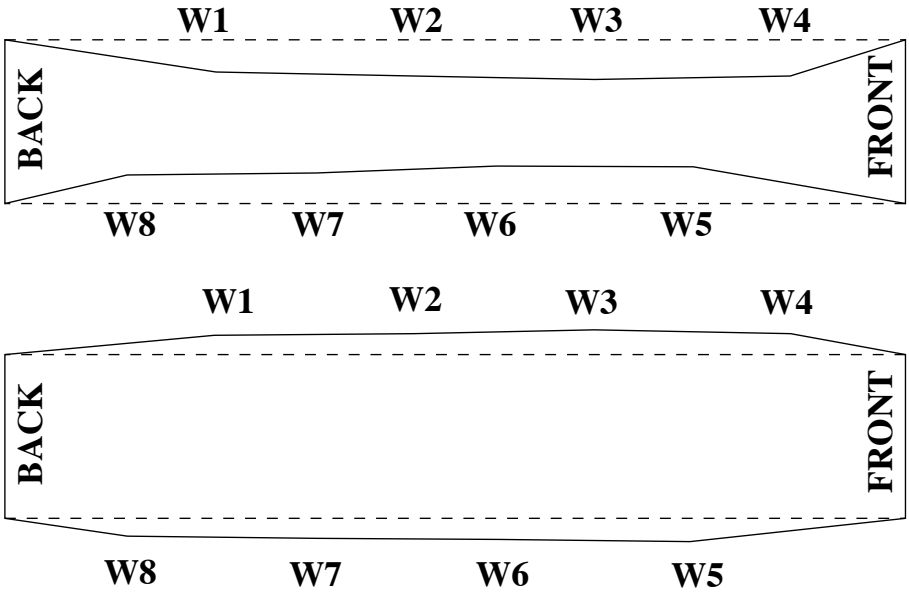

Figure 3.31: Schematic top view of the cryostat walls at the point of maximal deformation during the vacuum phase (top) and a leak search with overpressure (bottom). Indicated are the points where the deformation is measured by the wall position meters. The walls deformation is magnified.

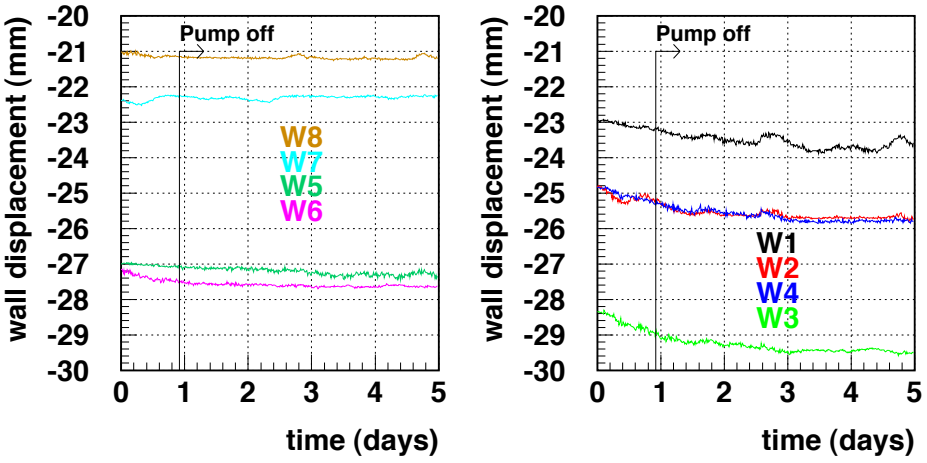

Figure 3.32: Wall displacement at the end of the vacuum phase. Left side: left wall. Right side: right wall. The arrows mark the time when the vacuum pump was stopped. The legend order corresponds to the curves order. The zero time corresponds to April 24th at 00:00h.

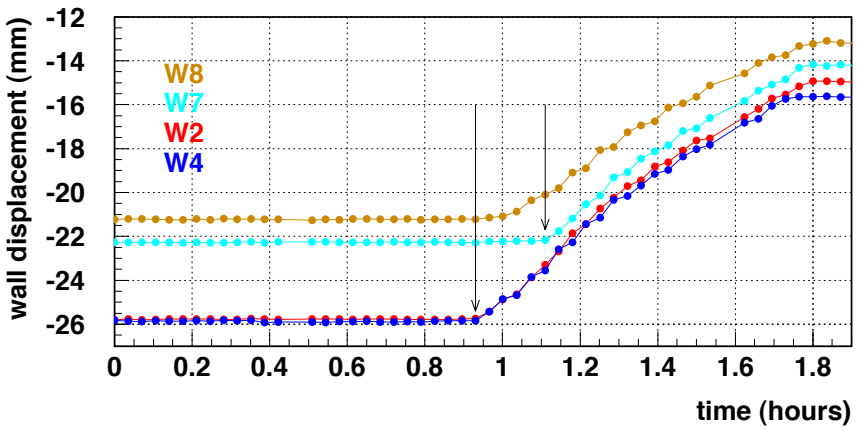

Figure 3.33: Wall displacement around the re-pressurization point. The arrows mark the times when the different sensors started to detect some outward movement. The legend order corresponds to the curves order. The zero time corresponds to April 30th at 14:00h.

3.2.3 Cooling down of the cryostat

After 17 days of vacuum phase, the vacuum was broken with purified gaseous argon (GAr) and the cooling of the cryostat started. The basic constraint of the cooling procedure was that the maximal difference between the temperatures of any two points of the chambers module never exceeds 40 K, to avoid large differences on the contractions of different parts of the chamber, which could cause a deformation on the frame.

To avoid large thermal stresses due to the abrupt injection of LN_2 into the cooling circuit, the first part of the cooling (see figure 3.34 top and center), down to about 233 K average internal temperature, was carried out by injecting a controlled temperature mixture of liquid and gaseous nitrogen. During this phase, lasting about 10 days, the average cooling speed was about -7 K/day. After this, the pre-cooling system was stopped and LN_2 was circulated. The average cooling speed increased to about -25 K/day. After four days, the average temperature reached 143 K. At this point, the filling of the cryostat with purified LAr was started, and a fast homogenizations of the internal temperature was observed. In this sense, the filling of the cryostat with LAr has to be considered as part of the cooling phase.

Figure 3.34 (bottom) shows the temperature difference in the cryostat measured by the different Pt1000 groups. The observed maximal temperature difference within the different groups are shown in table 3.9. Despite the specification, the maximal measured temperature difference between any two points inside the detector was about 77 K. In the case of Pt1000 sensors within the same vertical group, the maximal measured difference varies from about 70 K at the front and back ends, to about 75 K at the center. This maximal difference occurred during the LN_2 injection, due to the high cooling speed relative to the large volume of the cryostat. The difference became smaller when the cryostat was filled with LAr. This large temperature gradient can cause permanent deformations on the chamber frame. Indeed, an indication that such a deformation was produced is reported in section 3.2.12.

Pt Group	Max ΔT (K)
total	76.8±0.7
IBR	70.3±0.7
ICR	75.9±0.7
IFR	69.9±0.7
IBL	70.0±0.7
ICL	74.6±0.7
IFL	70.1±0.7

Table 3.9: Measured maximal temperature differences between any two Pt1000 sensors, and within the different Pt1000 groups, during the cooling down phase.

3.2.4 Thermal contraction of the frame and the cryostat

The different thermal contraction coefficients of the stainless steel (type 304) frame holding the wire chambers and the aluminum cryostat, results in a relative displacement between them during the cooling down phase. Since the frame is attached to the cryostat at the right side, and is allowed to slide in the direction of the drift at the left side, this relative displacement mostly reduces the distance between the cryostat wall and the frame at the left side. Figure 3.35 (top) shows the thermal contraction curves for stainless steel type 304 and aluminum, from 0 to 300 K. These curves allow us to compute Δd, defined as the expected relative movement between the frame and the cryostat left wall due to the thermal contraction, for a homogeneous

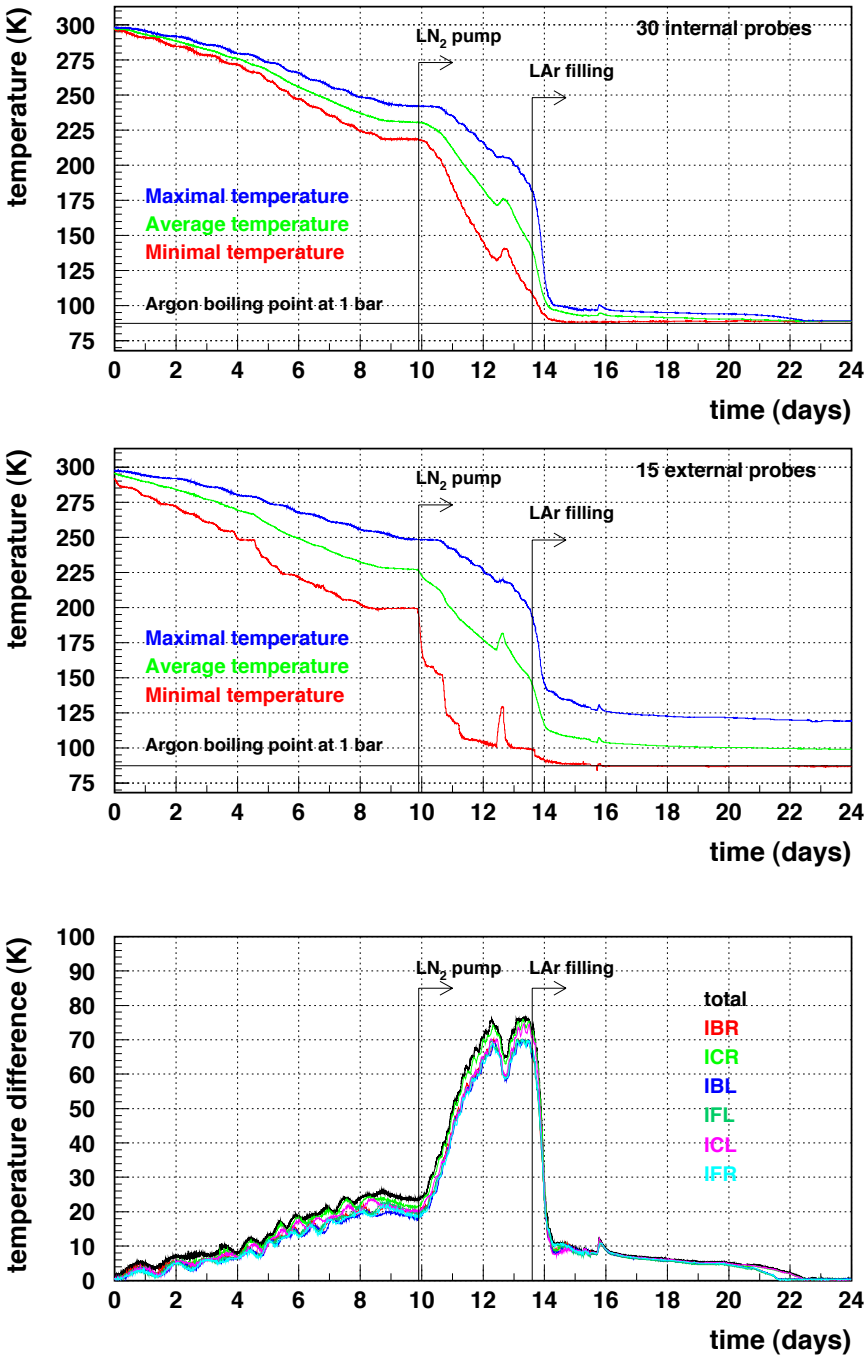

Figure 3.34: Top: Maximal, minimal and average temperatures in the cryostat during the cooling phase, measured by the 30 internal Pt1000 sensors. Center: Maximal, minimal and average temperatures measured by the 15 Pt1000 sensors placed on the external side of the cryostat walls. The argon boiling point is also shown. Bottom: Measured temperature differences between any two internal Pt1000 sensors, and within the different Pt1000 groups during the cooling phase (see table 3.1). The arrows mark the moment when the LN_2 circulation and LAr filling are started. The zero time corresponds to May 1st at 00:00h.

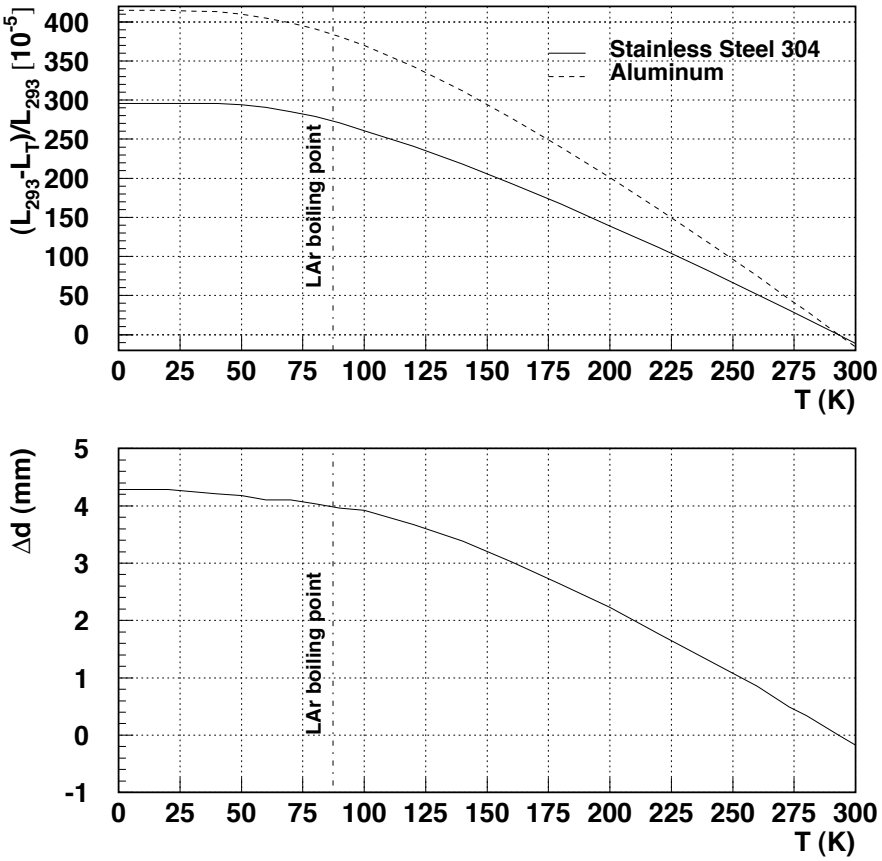

Figure 3.35: Top: Thermal contraction curves for stainless steel 304 and aluminum[55]. Bottom: expected difference of contraction along the drift direction for the cryostat and the frame being at a common temperature.

temperature. Δd is computed as the contraction difference between the frame and the cryostat in the direction of the drift (i.e. for a length of about 3.6 m). Figure 3.35 (bottom) shows the value of Δd in the temperature interval from 0 to 300 K.

The effect of the thermal contraction is illustrated in figure 3.36 (top), where the movement of the cryostat walls measured by the wall position meters during the cooling phase is shown. The measured average wall/frame distance at the right and left walls diverge during this period. The wall displacement is caused by two effects: the change of pressure in the cryostat and the thermal contraction of the frame and the cryostat. Since the thermal contraction only causes a displacement at the left side, whereas the change of pressure does it at both sides equally, we can extract the movement due to the thermal contraction by subtracting the average measured displacements of both walls. This difference is quantified by ΔD (bottom plot). The expected maximal relative displacement between the frame and the dewar in case of zero temperature gradient is Δd(T=88 K) = 4 mm. For the high temperature gradients happening during the cooling, the cryostat walls are colder than the frame, and thus, the displacement is expected to be larger. Hence, there exists a correlation between ΔD and the temperature gradient in the cryostat (see figure 3.34, bottom). For small temperature gradient values, ΔD is expected to be

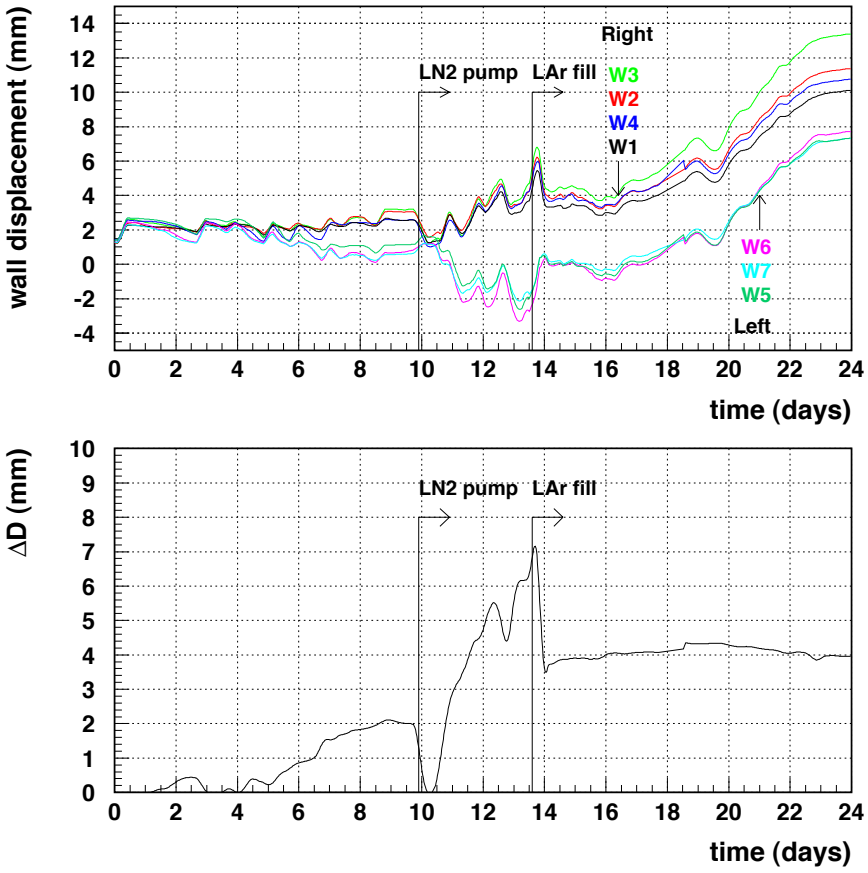

Figure 3.36: Top: measured wall displacement during the cooling phase. W1 to W4 correspond to the right side wall measuring points, W5 to W7 to the left side wall. The legends order corresponds to the sensors order at the point of maximal displacement. Bottom: difference of the average measured walls displacement at the left and right walls. The arrows mark the moment when the LN_2 circulation and the LAr filling started. The zero time corresponds to May 1st at 00:00h.

equal to Δd. In particular, ΔD is expected to be about 4 mm when the detector is thermalized at the LAr temperature. As shown in figure 3.36 (bottom) the observed value of ΔD during the cooling down phase is consistent with the expectation.

3.2.5 LAr filling

The cryostat filling with LAr started on May 14th and lasted about 10 days (see figure 3.37). The average filling speed was of about 1 m^3/hr, corresponding to a LAr level increase of about 1.5 cm/hr. Due to the static pressure exerted by the LAr, the cryostat walls are deformed outward (see figure 3.36) by about 11 mm on average (after correcting for thermal contraction effect).

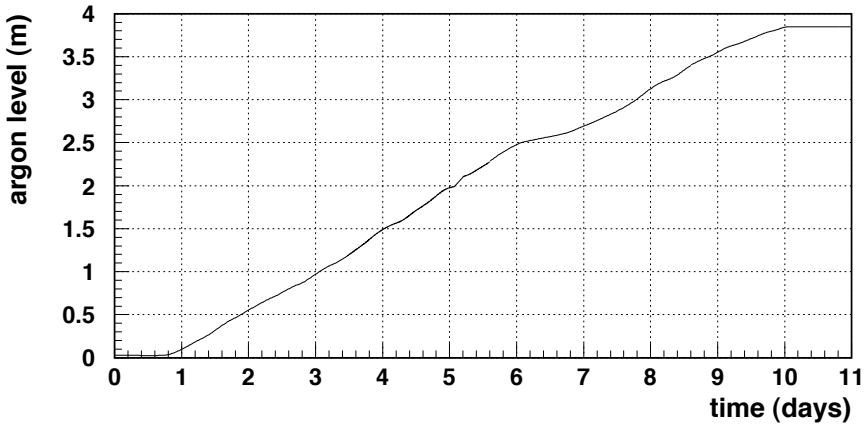

Figure 3.37: LAr level in the cryostat as a function of time. The zero time corresponds to May 14th at 00:00h.

3.2.6 LAr level during the data taking

The level of LAr in the cryostat has to lie between the safety limits. The upper limit is imposed by the Italian laws, according to which, 1.5% of the volume has to be reserved for the gas phase in any storage of cryogenic liquids, in order to allow for the liquid expansion. The lower limit aims to ensure the covering of the field shaping electrodes (race tracks) and the bottom end of the high voltage feed-through by the LAr [56]. If the LAr level goes below this limit, it could cause irreversible damages to the high voltage system. An alarm system ensured a quick reaction in case the LAr level would go out of the allowed bounds.

Figure 3.38 shows the measured change of the LAr level in the cryostat during the data taking period. Figure 3.39 shows the LAr temperature in the same period. During the first ten days, the LAr was still being cooled down, resulting in a contraction of the LAr volume and hence the decrease of the LAr level. After the equilibrium temperature was reached, the LAr level continued to decrease. A χ^2 fit of a straight line to the LAr level starting from day 10 of the data taking phase (June 3rd), to day 58 (July 21st), yields a decreasing rate of 0.570 ± 0.001 mm/day, corresponding to 39.6 ± 0.3 liter/day. This points toward the possible existence of a leak in the LAr container. The effect of such a leak mainly concerns the LAr purity, and is studied in detail in section 6.1.

3.2.7 LAr temperature during the data taking

The temperature measured at five different heights of the LAr volume during the data taking is shown in figure 3.39 (top). No significant temperature difference between different LAr levels is found.

The good performance of the detector depends on the temperature gradient of the LAr. Thus, the maximal temperature difference between any two points inside the cryostat is required to be less than 1 K. As shown in figure 3.39 (bottom), the maximal temperature difference oscillated between 0.5 and 0.7 degrees during the data taking phase.

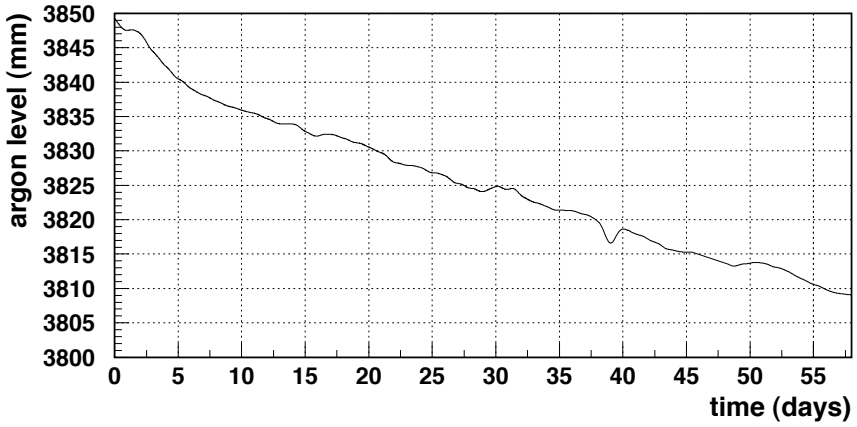

Figure 3.38: LAr level as a function of time during the data taking phase. The zero time corresponds to May 24th at 00:00h.

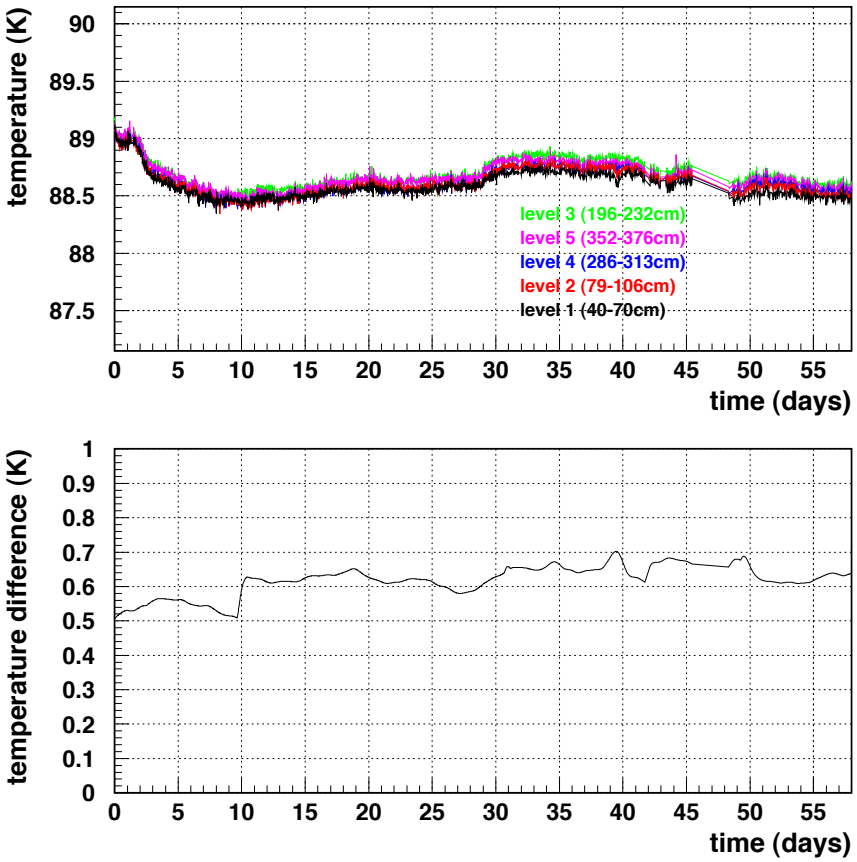

Figure 3.39: Top: Average LAr temperature measured at five levels during the data taking phase. Indicated are the height ranges of the different levels. The legend order corresponds to the curves order. Bottom: Maximal temperature difference in the cryostat during the data taking period. The zero time corresponds to May 24th at 00:00h.

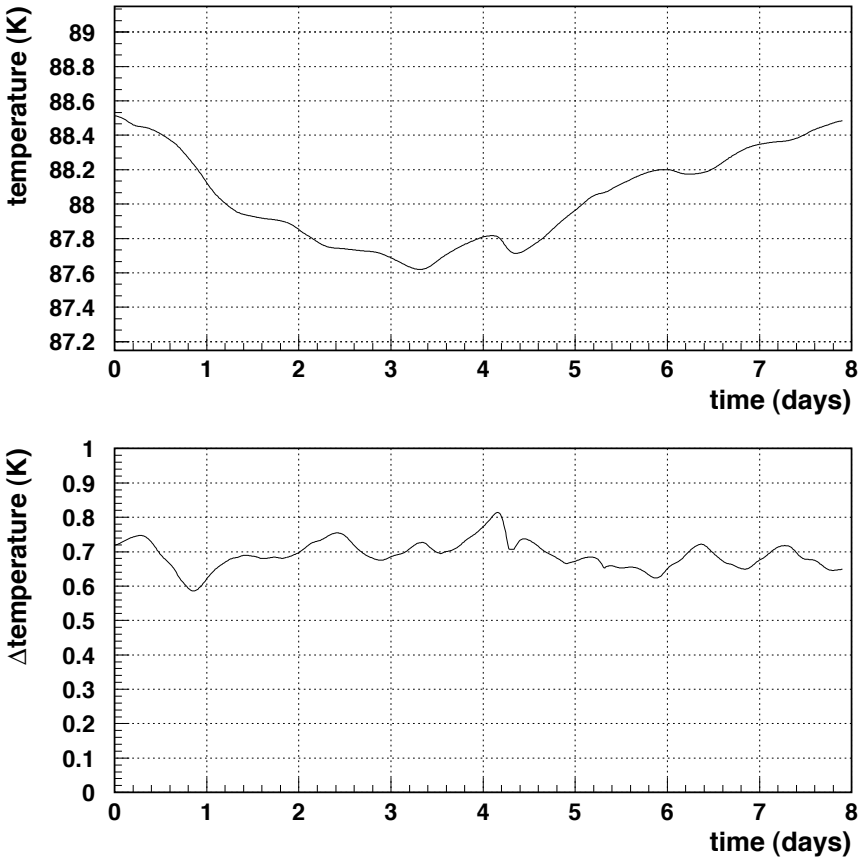

Figure 3.40: LAr temperature during the pump test. Top: Average LAr temperature. Bottom: Maximal temperature difference measured in the cryostat. The zero time corresponds to July 24th at 11:00h.

3.2.8 LAr thermal contraction

During the last week of the data taking phase, a test of the second LN_2 pump was performed on the second T600 half-module (see figure 3.40). As a result, an increased LAr cooling efficiency on the first half-module was observed. The average LAr temperature decreased about 1 K during this period. The maximal temperature difference stayed at about 0.7 K.

As a consequence of the cooling, the LAr volume underwent a compression (figure 3.41). This allows us to estimate the LAr thermal compression at about 88 K. A linear correlation between the LAr level and the temperature is found when the former is compensated by the constant decrease rate observed during the data taking (see section 3.2.6). Such a compensation yields the dashed curve shown in figure 3.41 (top). A χ^2 fit of a straight line to the corrected data (bottom) yields a level decreasing rate of 12.50 ± 0.01 mm/K. This can be translated into a value for the thermal contraction coefficient for the LAr at about 88 K and 1.2 bar, $\frac{1}{V}\frac{dV}{dT} = (3.3 \pm 0.3) \times 10^{-3}$ K^{-1}, comparable to the value quoted in the literature for a 2 bar pressure, $\frac{1}{V}\frac{dV}{dT} = 4.5 \times 10^{-3}$ K^{-1}.

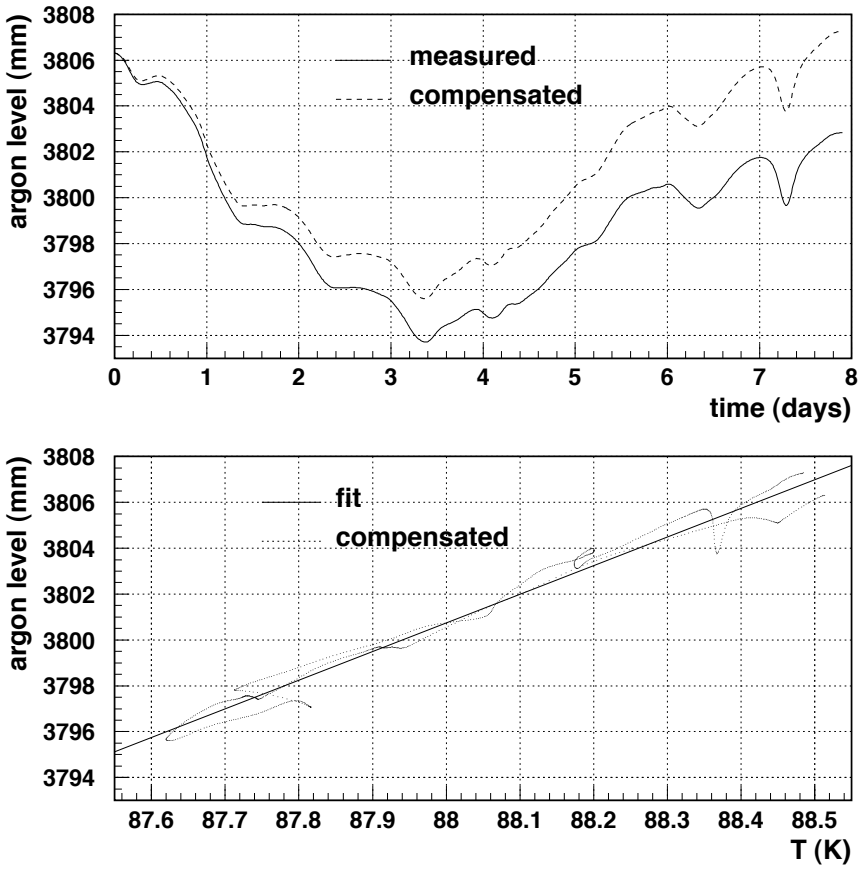

Figure 3.41: Top: LAr level measured during the LN_2 pump test (solid) and compensated for the constant level decrease observed during the data taking phase (dashed). The zero time corresponds to July 24th at 11:00h. Bottom: Linear fit of the corrected LAr level vs. LAr temperature.

3.2.9 Cryostat draining

After having completed several tests (cryogenics, HV, trigger, readout) and data taking, the detector was emptied of LAr (see figure 3.42). The LAr was filled from the cryostat into trucks. In a first phase, the cooling system was kept working, and the LAr was taken out from the bottom of the cryostat, profiting from the static pressure. After about 75% of the LAr was taken out, the cooling system was stopped and the remaining argon was pushed out by the gas pressure.

The cryostat started to heat up toward the external temperature when the cryostat started to be emptied (figure 3.43). At that moment, the cooling system was still working and both the absolute temperature and the temperature maximal difference were maintained low. When the LN_2 circulation pump was stopped, a big temperature difference, up to about 65 K, was observed between the regions covered with LAr and the regions in gas.

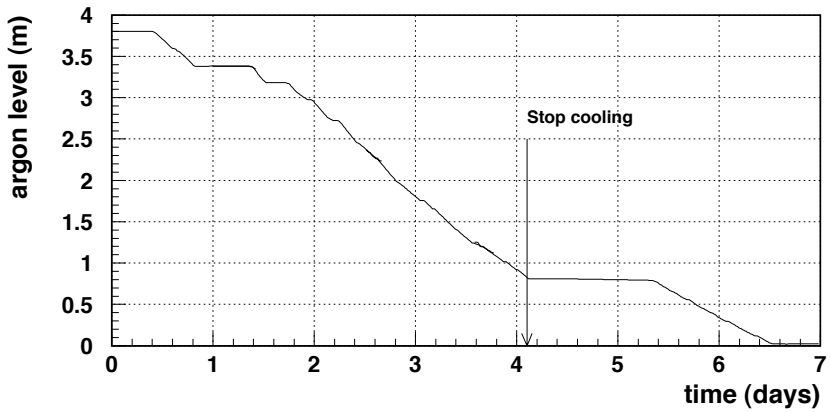

Figure 3.42: LAr level during the cryostat draining. The arrow marks the point when the cooling system was stopped. The zero time corresponds to August 1st at 00:00h.

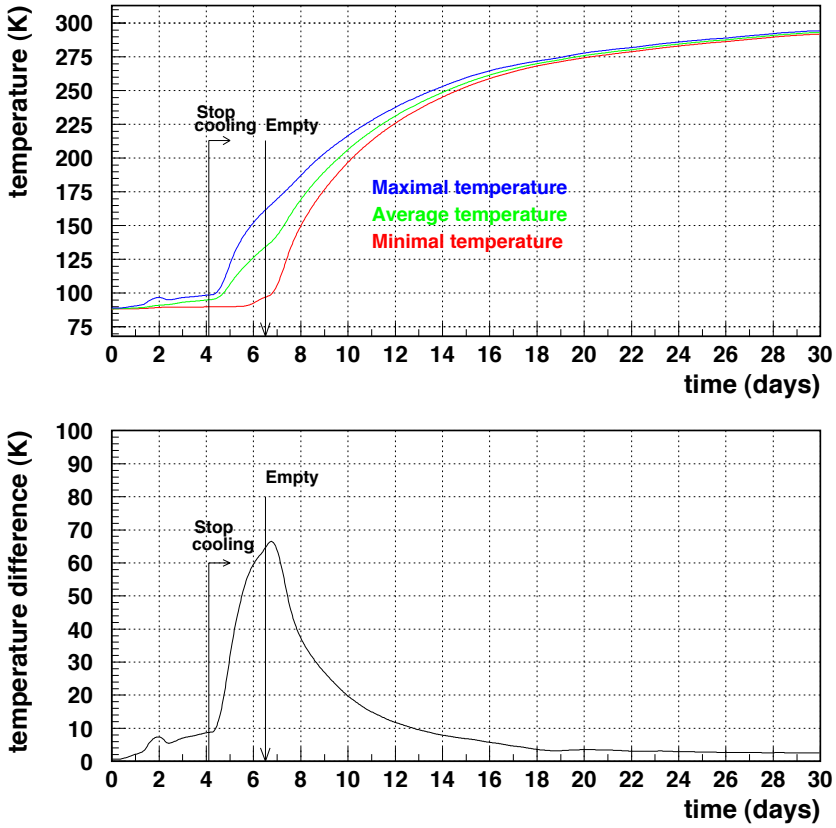

Figure 3.43: Top: maximal, minimal and average temperature in the cryostat after the cooling system stop. Bottom: maximal temperature difference between any two given points inside the cryostat. The arrows mark the moments when the cooling system is stopped and when the cryostat is completely empty of LAr. The zero time corresponds to August 1st at 00:00h.

3.2.10 Heat current density

The frame heating up curve (figure 3.43) allows us to obtain an estimate of the heat current density through the detector insulation. For the parts not covered with LAr, the temperature measured on the frame increases according to the law:

$$dT = \frac{1}{MC}\, dQ$$

where dT is the temperature increment, dQ the heat transferred through the insulation walls, M and C the mass and specific heat of the matter being heated. The heat current density through the insulation walls is then:

$$H \equiv \frac{1}{A}\,\frac{dQ}{dt} = \frac{MC}{A}\,\frac{dT}{dt}$$

where A is the total area of the considered wall.

We compute both the heat current density through the internal walls of the cryostat and through the external walls of the insulation. In the first case, $MC = M_{frame}C_{Steel}$, where $M_{frame} = 20\times10^3$ kg is the weight of the frame, C_{Steel} is the heat capacity of stainless steel type 304, and the total area is the internal cryostat walls' area for a single half-module, $A = 330$ m^2. In the second case, $MC = M_{frame}C_{Steel} + 2\cdot M_{cryostat}C_{Al}$, with $M_{cryostat} = 21\times10^3$ kg the weight of a single cryostat and C_{Al} is the heat capacity of aluminum; in this case the considered area is the external area of the whole insulation layer, which contains the two half modules, $A = 700$m^2. In both cases, $\frac{dT}{dt}$ is computed approximating T alternatively by the measured maximal and minimal temperatures on the frame. The values of C_{Steel} and C_{Al} for the considered temperature range are taken from reference [55].

Figure 3.44 shows the calculated heat current density through the internal cryostat walls (top) and through the external insulation walls (bottom) as a function of the measured maximal and minimal temperatures on the frame. For temperatures below the observed maximum of H, the heat transfer is partially compensated by the presence of LAr inside the detector, and the obtained value is not reliable in our computation. Thus, the heat loss can only be measured down to about 123 K. Using either the maximal or the minimal frame temperature for the calculation of H yields similar results. An extrapolation down to the LAr boiling point can be performed by fitting a polynomial of order 3 to the data in the range from 123 to 298 K (dashed line in the figure). Thus, the heat current density at LAr temperature is estimated to be between 20 and 25 W/m^2 through a single cryostat internal wall, and between 50 and 55 W/m^2 through the external insulation.

The thermal conductivity κ of the insulation is defined by

$$H = \kappa(T - T_0)$$

where T and T_0 are the cryostat internal temperature and the room temperature, respectively. Therefore, κ is the slope of the curve in figure 3.44. For high temperatures (above about 198 K) κ is observed to have a constant value of about 0.06 W/m^{2}K, whereas it grows rapidly for lower temperatures.

3.2.11 Wire movement

The movement of the springs attached to the wires was continuously monitored during the whole run. The springs were installed to avoid a rising of the tension of the wires beyond the elastic limit. This could happen if the wires, due to their small heat capacity, contract faster than

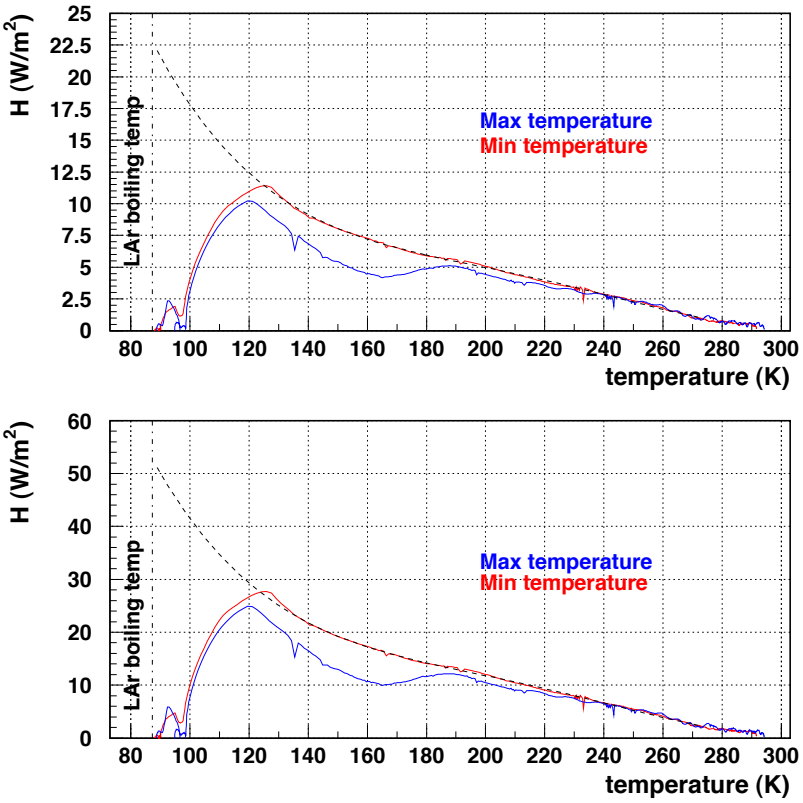

Figure 3.44: Heat current density through the cryostat internal walls (top) and through the external insulation walls (bottom) as a function of the cryostat internal temperature approximated alternatively by the maximal and minimal temperatures measured on the frame. Dashed line: extrapolation to low temperatures fitting a polynomial of order 3 to the data in the range from 123 to 298 K.

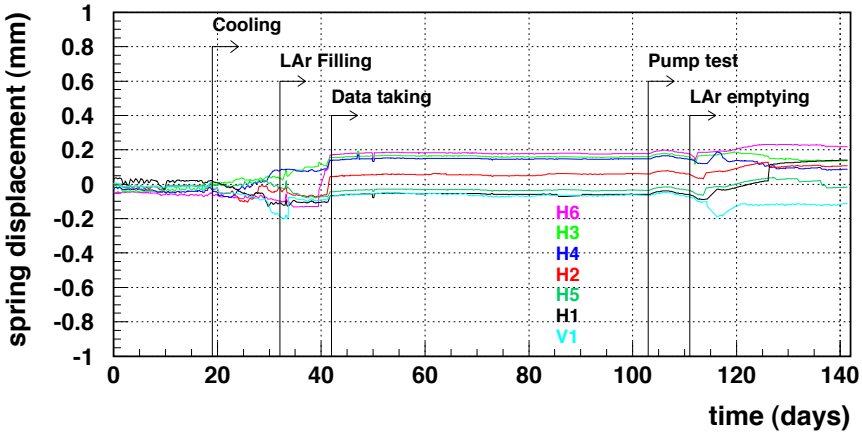

Figure 3.45: Displacement of the springs attached to the wires of the wire chamber during the whole run. The arrows mark the beginning of the different phases. The legend order corresponds the curves order at the central period. The zero time corresponds to April 12th at 00:00h.

Sensor	Max Δd (mm)
H1	0.14±0.02
H2	0.10±0.02
H3	0.27±0.02
H4	0.26±0.02
H5	0.04±0.02
H6	0.25±0.02
V1	-0.10±0.02

Table 3.10: Measured maximal elongation of the springs attached to the wires during the whole run.

the frame during the cooling phase; part of this tension increase would be compensated by the springs. Figure 3.45 shows the measured displacement of the springs during the whole run. The maximal displacement of the wires with respect to their original position occurs when the temperature difference inside the detector is maximal. The value measured by the different wire position meters are shown in table 3.10. We do not observe any significant elongation of the springs attached to the wires above 300 μm.

3.2.12 Recovery of the wall position

Once the detector is back to the initial room temperature and atmospheric pressure conditions, both the frame and the cryostat walls are expected to be found at their initial positions. In such a case, all wall position meters should measure 0, within the error bounds. However, as shown in figure 3.46, the difference of the average distance frame/wall between left and right walls when the final conditions were reached is ΔD=1.2±0.2 mm, which is a significant deviation from the expected value ΔD=0.

A hypothesis that explains this observation is suggested when we take into account how the frame is allowed to move with respect to the cryostat. The point at which the frame is fixed to the cryostat is located at the center of the wire chamber on the right side (looking from the assembly clean room) of the cryostat. The other four supports of the right chamber are free to slide in the direction parallel to the longitudinal cryostat axis (x axis) while the four supports of the left chamber are free to slide in the horizontal plane (x and y directions). The central point of the left chamber is free to slide in the y direction only. The maximal allowed displacement of the frame relative to the cryostat is about 13 mm along the x direction and 5 mm along the y direction.

The measured displacement between frame and the side walls of the cryostat, ΔD, is shown in figure 3.46 for the whole duration of the run. The maximal reached value, measured just before the LAr filling, when the maximal temperature gradient was reached, is about 7 mm, whereas the maximal mechanically allowed displacement is 5 mm. As a consequence of this, both the frame and the cryostat suffered a mechanical stress that could have led to a small deformation that explained the remnant ΔD value.

3.3 Conclusions

The Slow Control system of the first T600 half-module has been used to monitor the behaviour of the detector during the different phases of the technical run, performed from April to August

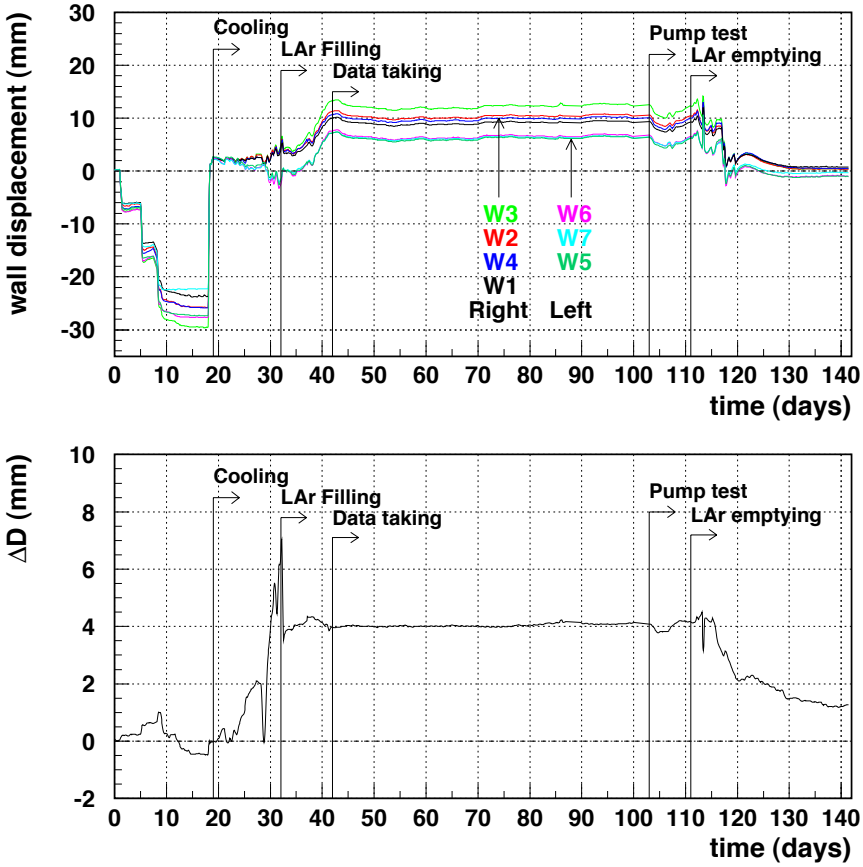

Figure 3.46: Top: Measured deformation of the cryostat walls during the whole run. W1 to W4 correspond to the right side wall measuring points, W5 to W7 to the left side wall. The legends order corresponds to the sensors order during the data taking period. Bottom: Difference on the average measured distance wall/frame at the left and right walls. The arrow mark the beginning of the different phases. The zero time point corresponds to April 12th at 00:00h.

2001 in Pavia. Several sensors were installed to measure the movement of the side walls and the springs attached to the wires, the LAr level and the temperature in the cryostat. The stability and accuracy of the different sensors have been understood thanks to the stability test performed before the run started. The acquired data have been used to better understand several aspects of the detector behaviour when exposed to extreme pressure and temperature conditions. In particular, the following important results have been obtained:

- The dewar walls deform linearly with the pressure, with slopes ranging between 20 and 28 μm/mbar, depending on the measuring point. The deformation is not front/back symmetric. Once the pressure has reached its minimal value, the walls continue deforming, releasing stresses for about 3 days.
- There are evidences to think that a contact between the cryostat walls and frame happened at the end of the vacuum phase.
- The maximal temperature difference in the cryostat during the cooling (draining) phase

reached 76 (65) K, well above the prescripted value (40 K). This fact has probably caused a permanent (small) deformation on the internal detector frame.

- The LAr temperature was maintained roughly constant along the run, at about 88 K. The maximal temperature difference between any two measuring points in the LAr volume was less than 0.7 K during the whole run (the maximal allowed value is 1 K).
- No significant elongation of the springs attached to the wires above 300 μm was observed.
- The LAr level was in continuous decrease along the run, with an average rate of 0.57 mm/day ($\sim$ 40 l/day) which could indicate the presence of one or more leaks in the cryostat.
- The heat current density through the detector external walls is estimated to be between 50 and 55 W/m^2.

This results constitute the base of a better understanding of the thermo-mechanical response of the T600 detector in view of future runs with this and other modules.

Chapter 4

T600 data event reconstruction

Charged particles traversing the LAr sensitive volume produce ionization electrons in a number proportional to the energy transferred from the particle to the LAr. The ionization electrons drift perpendicularly to the wire planes pushed by the electric field, inducing a current on the wires near which they are drifting while approaching the different wire planes. Therefore, each wire of the readout plane records the information of the energy deposited in a segment of the ionization track.

The goal of the reconstruction procedure is to extract the physical information contained in the wire output signals, i.e. the energy deposited by the different particles and the point where such a deposition has occurred, to build a complete three dimensional spatial and calorimetric picture of the event. The basic building block of a track is called hit, defined as the segment of track whose energy is read by a given wire of the readout wire planes. Therefore, the spatial and calorimetric information of the track segment is contained in the associated hit, and the sensitivity of the detector depends entirely on the hit spatial and calorimetric resolutions.

In the present chapter we describe a method developed to perform the hit spatial and calorimetric reconstruction. The reconstruction procedure consists of the following steps:

1. Hit identification: the hits are independently searched for in every wire as output signal regions of a certain width above the baseline output value.

2. Fine hit reconstruction: the parameters defining the hit (position, height, area), which contain the physical information, are precisely determined.

3. Cluster reconstruction: hits are grouped into common charge deposition distributions based on their position in the wire/drift coordinate plane.

4. Three-dimensional (3D) hit reconstruction: the hit spatial coordinates are reconstructed using the association of hits from different views to common track segments.

In the next sections, we describe in detail the different steps of the hit reconstruction procedure, and perform an evaluation of the different steps using the T600 data from the technical run.

4.1 Hit identification

4.1.1 Hit identification algorithm

The hit identification aims at distinguishing signals produced by ionization electrons from electronic noise. Hits are identified as signal regions of a certain width with output values above the local mean (defined as the average output value in a given signal region). The hit identification algorithm typically acts over the whole wire sample of a given readout plane. In the T600 configuration there are 6 wire planes per half-module (3 per wire chamber), referred to as Induction 1, Induction 2 and Collection wire planes. There are 5728 wires in the Induction 2 and Collection planes and 2112 wires in the Induction 1 plane. Each wire is sampled 4096 times for a given event. Therefore, computing speed is a critical parameter for the hit search, and the algorithm is based on basic geometrical principles of the wire signal. The hit identification procedure also establishes rough preliminary bounds to the hit range along the drift coordinate, which will be of utmost importance in ulterior steps of the reconstruction procedure. No information from adjacent wires is used at this stage.

The algorithm loops over the selected group of wires (i.e. a whole wire plane), skipping those with identified problems, such as large noise conditions or disconnections, where no signal identification is possible. Hits are searched for in the wire output signal after a low frequency filter has been applied. The different steps are described in the following paragraphs.

Low frequency noise filter

The contribution of low frequencies to the wire output signal is removed by performing a Fourier transform based filter. The Fourier transform of the wire signal in the 4096 output samples is computed using the Fast Fourier Transform (FFT) algorithm [57]. The amplitude of the low frequencies is reduced by convoluting the result with the following function of the frequency f ("soft" step function):

$$S(f) = 1 - \frac{1}{e^{\frac{f-R}{\alpha}}} \tag{4.1}$$

where R and α are the parameters determining, respectively, the mean frequency radius and the transition region thickness. Setting the parameters to $R = 4.5$ kHz and $\alpha = 0.9$ kHz effectively cuts low frequencies up to about 6.5 kHz while reducing the diffraction effect. This effect distorts the whole output range when a hit of high amplitude and sharp edges is present in the wire.

The shape of function S compared to the step function is shown in figure 4.1. Figure 4.2 illustrates the effect of the diffraction caused by the low frequency filter on the wire output signal. Figure 4.2a shows the raw data before the application of the filter. Figure 4.2b shows the result of the application of a sharp frequency filter, where all frequencies below 6.5 kHz are removed; the diffraction effect is clearly visible at both sides of the ionization signal peak as a strong depression at both sides of the peak and a wave extending through the whole drift coordinate range. Figure 4.2c shows the result of the application of the "smooth" step function; in this case the filter still produces a depression at both sides of the signal peak, but the corresponding diffraction wave is completely removed.

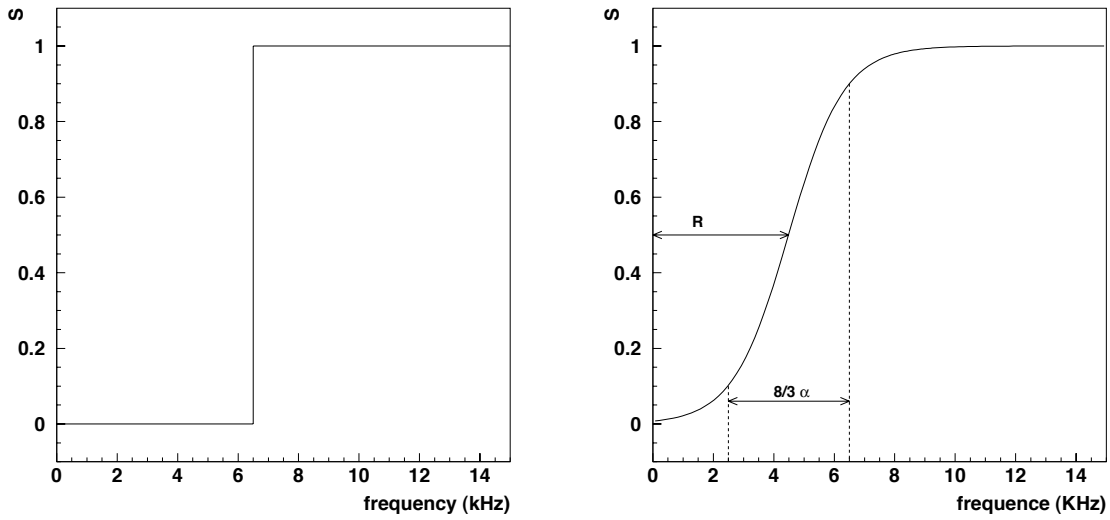

Figure 4.1: Comparison of functions used in the low frequency noise filter. Left: step function. Right: "soft" step function (see equation 4.1), with $R = 4.5$ kHz and $\alpha = 0.9$ kHz.

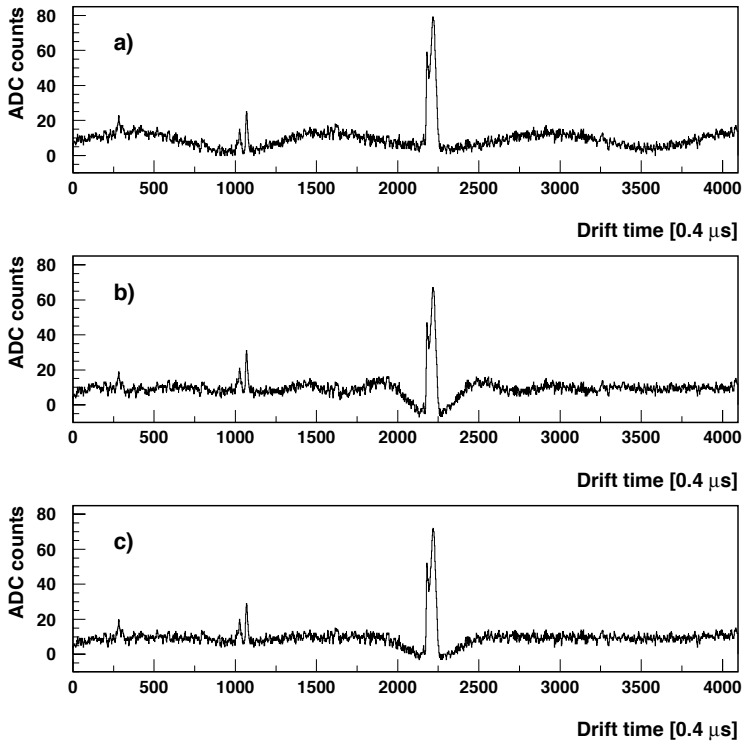

Figure 4.2: Effect of the low frequency filter on the wire signal. a) Raw data with no filter applied. b) Result of a step function based filter. c) Result of a "smooth" step function based filter.

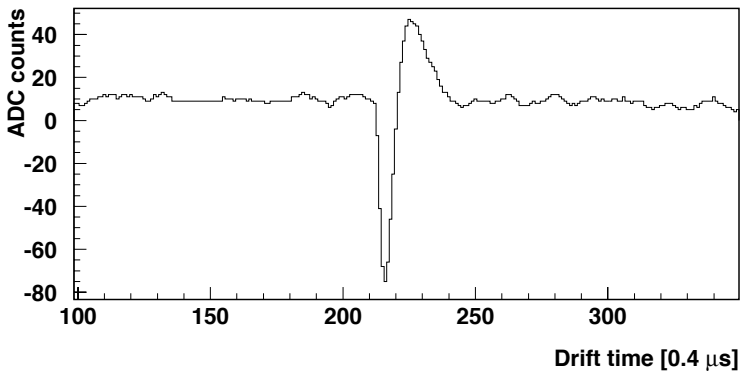

Figure 4.3: Example of the PMT induced signal.

Hit search

The hit search proceeds on the filtered wire output signal. The identification is based on the geometrical features of the wire output in a given region, i.e. the presence of a relatively broad region of output values above the baseline, eventually surrounded by a depression produced by the diffraction effect as discussed above. Correlations with the signal from neighbouring wires are not considered. The search algorithm follows the following steps for each wire:

- For every output sample, a local mean is computed as the average value in an interval of the output signal (window) built with the *nwindow* precedent output samples. For *nwindow*=0, the local mean is defined as 0. Output samples in excess of or less than 10 ADC counts with respect to the previous sample value are not taken into account for the local mean computation. This avoids the inclusion of sharp peaks such as those of the PMT induced signals (see figure 4.3) in the local mean computation.

- Every output sample is compared with its associated local mean. A value above the local mean by more than *threshold* samples triggers a hit candidate.

- The hit candidate is built with all the subsequent output samples above the threshold.

- The hit candidate is characterized by its width, i.e. the distance (in drift samples) between the hit initial and final points. Rejection of fake (noise) candidates is achieved by imposing a minimal width value of *width* samples.

- Further rejection can be carried out for Collection and Induction I wires, where the hits are expected to have an exponential falling slope. An extra requirement on the minimum distance from the peak position to the hit end (*fall*) is imposed.

Figure 4.4 illustrates the meaning of the hit search parameters. The values used for the different wire planes are shown in table 4.1. Figure 4.5 illustrates the effect of the correct selection of the free parameter values on the hit finding algorithm. The fake hit detections due to the loose values of the free parameters (see figure 4.5b) are almost completely removed when using the optimized values shown in table 4.1 (see figure 4.5c).

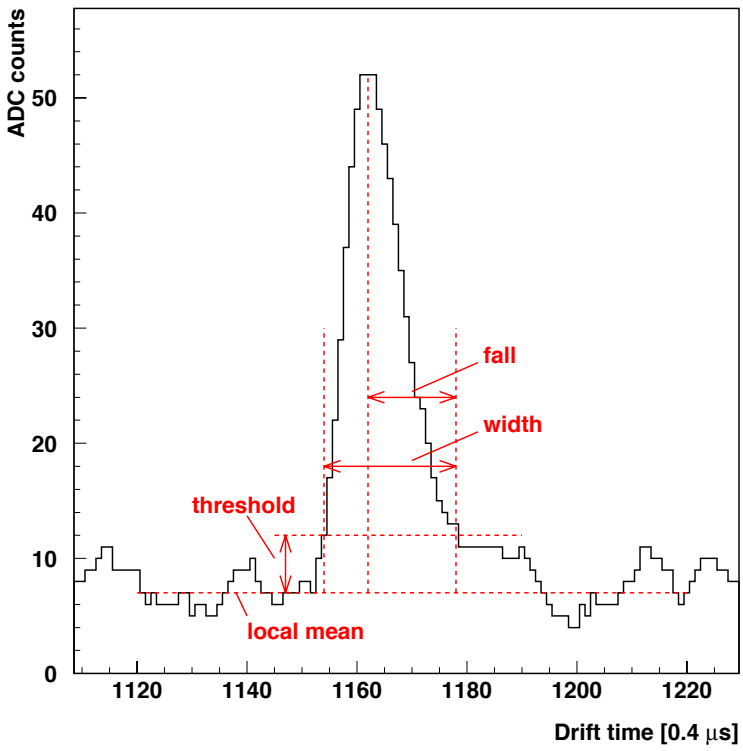

Figure 4.4: Example of a hit produced by a mip track on a Collection wire. Marked are the parameters used in the hit search. The output signal has been passed through the low frequency filter.

Resolving close hits

Close hits may appear when segments of tracks belonging to different ionizing particles produce a signal in the same region of the wire/drift plane (see figure 4.6a), or when a single ionizing particle travels with small angle with respect to the drift direction (see figure 4.6b). Identification of close hits results in a better hit calorimetric and spatial reconstruction.

The resolution of close hits is carried out within the hit finding procedure. When a hit candidate is found, an embedded algorithm looks for negative slopes followed by positive slopes on the output signal within the hit. A negative slope is flagged when at least *negnsamp* output values after the hit peak are below the peak output value by more than *negslopethreshold* ADC counts. For the identification of rising slopes, positive and negative differences between consecutive samples belonging to a window of *posnsamp* samples are counted; if the number of positive difference occurrences is greater than that of the negatives differences by more than *posslopethreshold*, the rising slope is found. The values of *negnsamp*, *negslopethreshold*, *posnsamp* and *posslopethreshold* used for resolution of close hits in Induction and Collection wires are summarized in table 4.2.

When a falling and a rising slope are found consecutively within a hit candidate, the algorithm splits the candidate into two hits separated by the starting point of the rising slope. Hit selection criteria are applied separately to both candidates.

	Induction I	Induction II	Collection
nwindow	25	0	25
threshold	4	3	4
width	8	7	8
fall	4	1	4

Table 4.1: Values of the free parameters on the hit search algorithm.

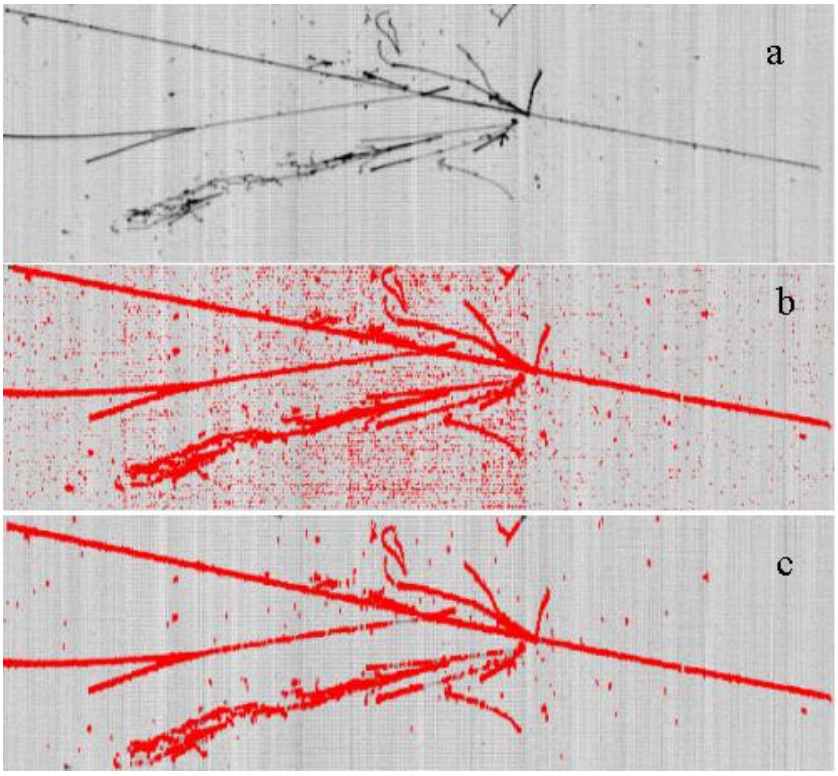

Figure 4.5: Illustration of the effect of the free parameter values on the hit finding algorithm. Top: gray scale mapping of the output signal in a selected region of the Collection view. Middle: in bold, hits found with a loose selection of the free parameters. Bottom: in bold, hits found with the parameters shown in table 4.1.

Hit expansion

The hit expansion aims at performing a fast preliminary determination of the hit range within the drift direction. This allows a better association of hits into clusters (see later on section 4.3).

The initial drift range limits come from the hit finding algorithm and are those samples bounding the region where the signal value is above the selected threshold. In the hit expansion, the lower (upper) bound is expanded toward lower (higher) drift values following the signal decreasing slope. The expansion finishes when the number of positive (negative) differences occurrences within a window of size *expnsamp* samples around a given sample is larger than the number of negative (positive) occurrences by more than *expdif*. The values of the free parameters used in the hit expansion are summarized in table 4.3.

The hit expansion is performed for the isolated hits just after applying the geometrical selec-

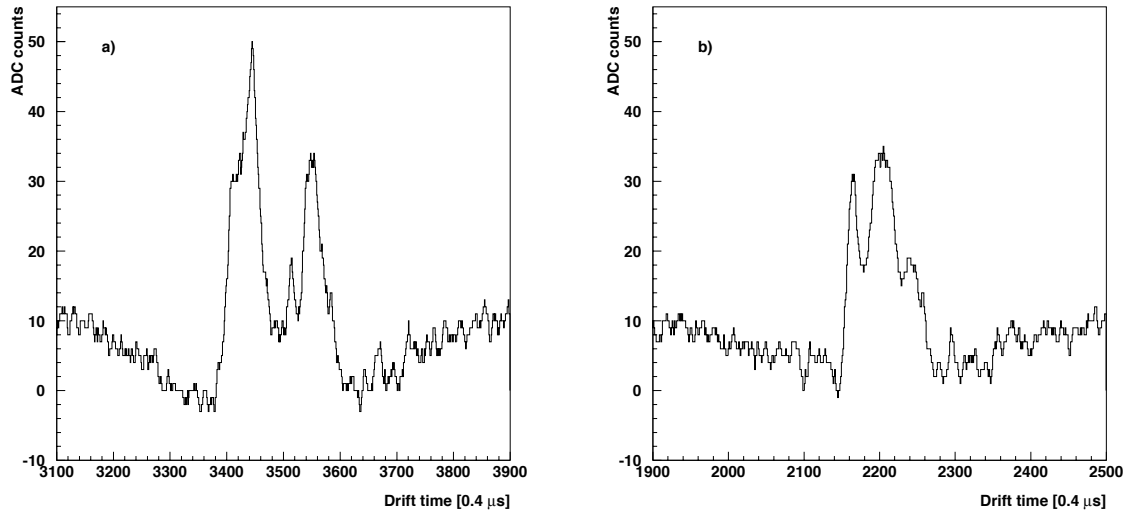

Figure 4.6: Example of close hits occurrences caused by close tracks in the same region (a), and a single track in the direction of the drift (b). Signal has been passed through the low frequency filter.

	Induction I	Induction II	Collection
negnsamp	3	3	3
negslopethreshold	4	3	4
posnsamp	5	5	5
posslopethreshold	3	3	3

Table 4.2: Values of the free parameters of the close hits resolution algorithm.

expnsamp	6
expdif	1

Table 4.3: Values of the parameters used in the hit expansion algorithm.

tion. For hit candidates coming from the resolution of close hits, the selection cuts are applied after the expansion, since the hit width is limited by the presence of neighbour hits.

Hit parameterization after the hit finding algorithm

The hit identification provides the following hit parameters (see figure 4.7):

- The view and wire indexes of the hit.
- The drift coordinate of the peak.
- The drift coordinate range of the hit, defined by the initial and final drift samples computed in the hit expansion.

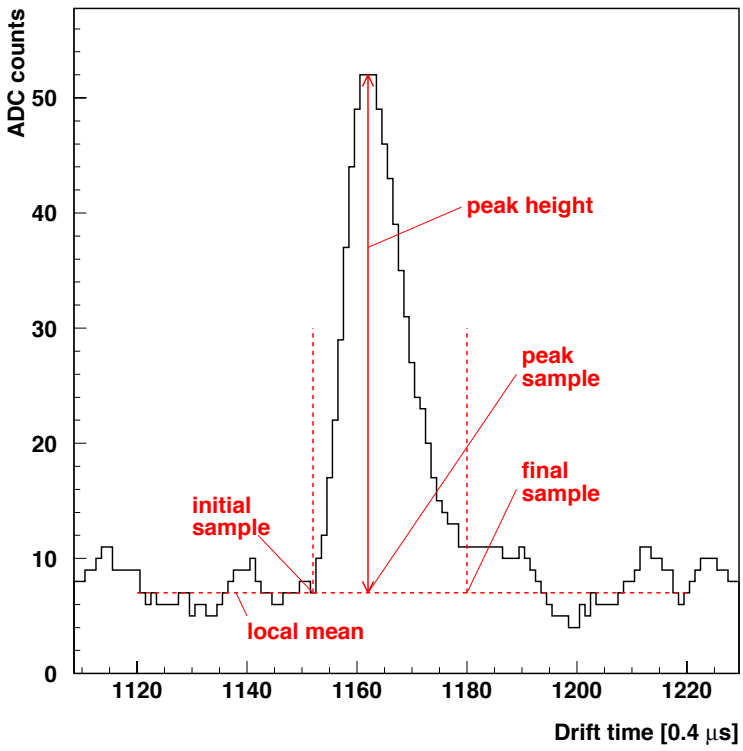

Figure 4.7: Parameters characterizing a hit after the hit finding algorithm. The output signal has been passed through the low frequency filter.

- The height of the peak taken as the difference (in ADC counts) between the peak and local mean output values.

4.1.2 Evaluation of the hit identification algorithm

For the evaluation of the quality of the hit detection algorithm, we compute two quantities, namely: the rate of fake hit detections and the detection efficiency within straight line tracks. Events 1, 2 and 5 from run 939, and event 163 from run 975 have been used for such an evaluation. Wires with identified problems, such as abnormally high noise conditions or disconnections, are discarded.

For the computation of fake hit detections, output signal regions where no ionization signal is present are visually selected. The hit finding algorithm is applied to the selected regions and the number of hit detections counted. The number of fake hit detections is evaluated to be about 4 hits per 100 wires in the Collection wires (figure 4.8a) and about 110 hits per 100 wires in the Induction II wires (figure 4.8c).

On the other hand, in order to evaluate the hit efficiency detection on real hits, all straight line tracks are visually selected. Hits are searched for exclusively within these tracks. The efficiency is computed as the number of detected hits over the number of wires where the selected track extends (disregarding wires with known problems). Figures 4.8b and 4.8d show, respectively, the distribution of the detection efficiency values for the selected tracks for Collection and

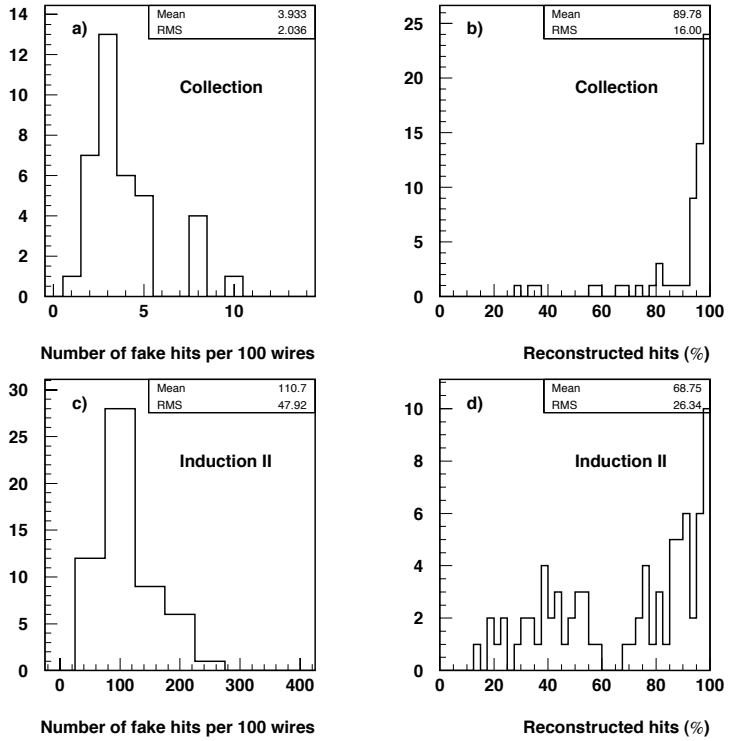

Figure 4.8: Left: number of fake hit detections per 100 wires for output regions free of ionization signal. Right: Rate of reconstructed hits within straight line tracks. Top plots correspond to Collection wires, bottom plots correspond to Induction II wires.

Induction II wires. The mean efficiency is about 90% in the case of Collection wires and about 70% for Induction II wires. The big difference existing in the performance of the hit finding algorithm between Collection and Induction II wires is mainly due to the difference of the signal shape from both wire planes. It is more difficult to distinguish a signal from electronic noise in Induction II than in Collection wires, since signal hits are narrower, and no exponential fall is present. Therefore, the hit finding algorithm parameters (see table 4.1) for the Induction II wires are looser, aiming at maintaining a wire detection efficiency reasonably high. The price to be paid is a large increase in the number of fake hit detections.

4.2 Fine hit reconstruction

Once the hit has been detected, a fine hit reconstruction is performed aiming at extracting in an optimal way the parameters defining the hit (position, height, area) which contain the physical information of the original associated track segment. The hit spatial reconstruction is entirely based on the determined hit peak position, whereas the hit area (height) in Induction I and Collection (Induction II) wires is proportional to the energy deposited by the ionizing particle, and therefore constitutes the base of the calorimetric reconstruction.

The fine hit reconstruction algorithm is meant to be performed on a set of hits after the application of some quality selection criteria (see section 4.1 and later on section 4.3). Hence,

computing speed becomes a non critical parameter for the reconstruction and a high level of refinement has been developed.

4.2.1 Fine hit reconstruction algorithm

In the present section we describe the fine hit reconstruction algorithm. Two independent methods have been developed to extract, in the most accurate possible way, the hit peak position, height and area. In a first approach (direct ADC counting method), these quantities are estimated directly from the output signal: the hit peak is associated to the highest output value sample, the height is the difference between the peak and the local average output value, and the hit area is the sum of the ADC counts of the output samples belonging to the hit. The second approach (hit fit method) consists of performing a fit of the output signal around the hit region with an analytical function that reproduces well the hit shape, and extracting the parameter values from the fitted function.

Both the direct ADC counting and fit methods are carried out using exclusively the output signal from a selected group of samples around the hit (defined as *hit window*). A determination of the average output value around the hit (*local mean*) is needed in the direct ADC counting method and for an optimal determination of the hit window bounds as well.

Local mean determination

The computation of the local mean around the hit proceeds as follows: The average output value at both sides of the hit are computed as the minimal average value obtained from any group of *meannsamp* consecutive samples taken from a group G. G contains the *totalnsamp* consecutive output samples (*totalnsamp*>*meannsamp*) starting from the hit initial (final) sample and extending to lower (higher) drift values samples. Samples lying within the limits of neighbouring hits are discarded when filling G. Following this procedure, the average output values at both sides of the hit are computed. If no neighbouring hit is found while constructing G at either hit side, the larger of the two computed average values is taken as the hit local mean. If a neighbouring hit is found at one side of the hit, the local mean is equal to the average output value at the opposite side. Table 4.4 shows the values of the parameters used in the local mean computation.

meannsamp	30
totalnsamp	100

Table 4.4: Values of the parameters used in the hit local mean computation.

Hit window determination

The hit window is defined as the region of the wire signal where the track segment contributes to the output value. The determination of the hit parameters in both reconstruction methods is based exclusively on the output samples from the hit window.

The determination of the optimal hit window proceeds in two steps: In a first step, the first sample with a value below the local mean is searched on both sides of the hit maximum. In the second step, these window bounds are expanded by 30 drift samples. For well isolated hits (see

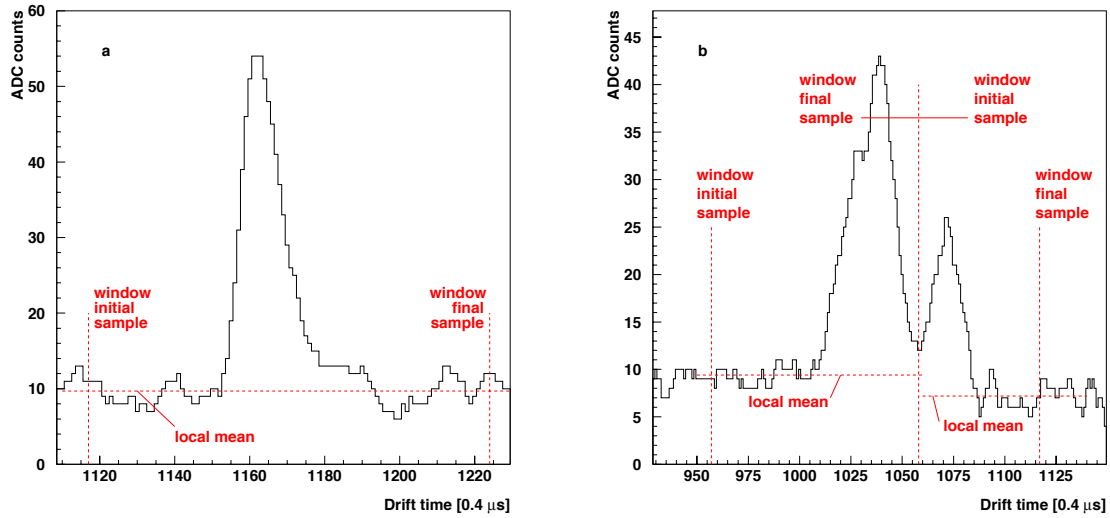

Figure 4.9: Examples of computed local mean and hit window bounds for an isolated hit (left) and two close hits (right). No frequency filter is applied to the signal.

figure 4.9a) this ensures the contribution to the window of the whole hit plus a sufficient number of baseline output values needed for the good behavior of the function fit. For overlapping hit windows, the common window limit is set in the sample where the local minimum between the two hits is found (see figure 4.9b).

Direct ADC counting reconstruction method

In this method, the position associated to the hit in the wire/drift plane is taken as the one of the hit peak as identified by the hit finding algorithm (see section 4.1). The peak height is the difference between the peak output value and the local mean. Finally, the hit area is taken as the largest area above the hit local mean value within the hit window.

Hit fit reconstruction method

In this method, the output signal within the hit window is fitted using the following analytical function of the drift time t:

$$f(t) = B + A \frac{e^{\frac{-(t-t_0)}{\tau_1}}}{1 + e^{\frac{-(t-t_0)}{\tau_2}}} \tag{4.2}$$

where B is the baseline, A the amplitude, t_0 the point for which the height of the function with respect to the baseline is equal to $A/2$, and τ_1 and τ_2 are related to the falling and rising characteristic times, respectively (see figure 4.10).

For a given hit, the values of the fit parameters are those obtained by minimizing the χ^2 of the fit of f to the output signal within the hit window. The minimization is performed using the MINUIT package [58].

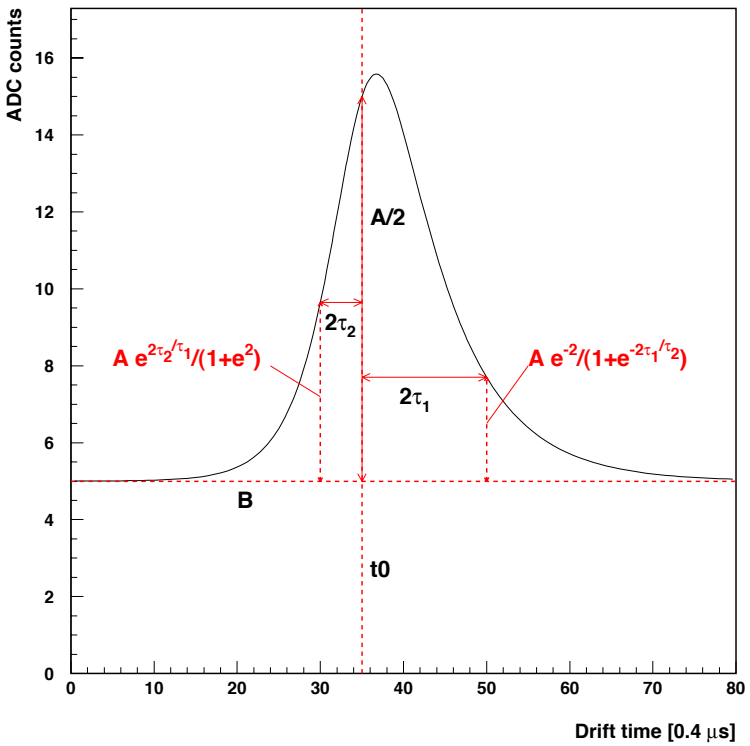

Figure 4.10: Function used in the hit fit (see equation 4.2) for the following parameter values: $B = 5$ ADC cnts, $A = 20$ ADC cnts, $t_0 = 14$ μs, $\tau_1 = 3$ μs, $\tau_2 = 1$ μs.

The hit area is obtained by numerical integration of the fit function in the hit window. The peak position (t_{max}) and height ($f(t_{max})$) are obtained analytically from the function f:

$$\begin{aligned} t_{max} &= t_0 + \Delta t \\ f(t_{max}) &= B + A \frac{e^{\frac{-\Delta t}{\tau_1}}}{1 + e^{\frac{-\Delta t}{\tau_2}}} \end{aligned} \tag{4.3}$$

with

$$\Delta t \equiv \tau_2 \ln \frac{\tau_1 - \tau_2}{\tau_2}$$

Figure 4.11 shows four examples of fitted hits corresponding to four hits along the track of a muon stopping inside the LAr active volume. Increasing peak areas (from left to right and top to bottom) exemplify the increase of the dE/dx toward the end point of the track.

Hit parameterization after the hit fine reconstruction algorithm

The hit fine reconstruction adds the following quantities to the hits' parameterization:

- The local mean value around the hit.

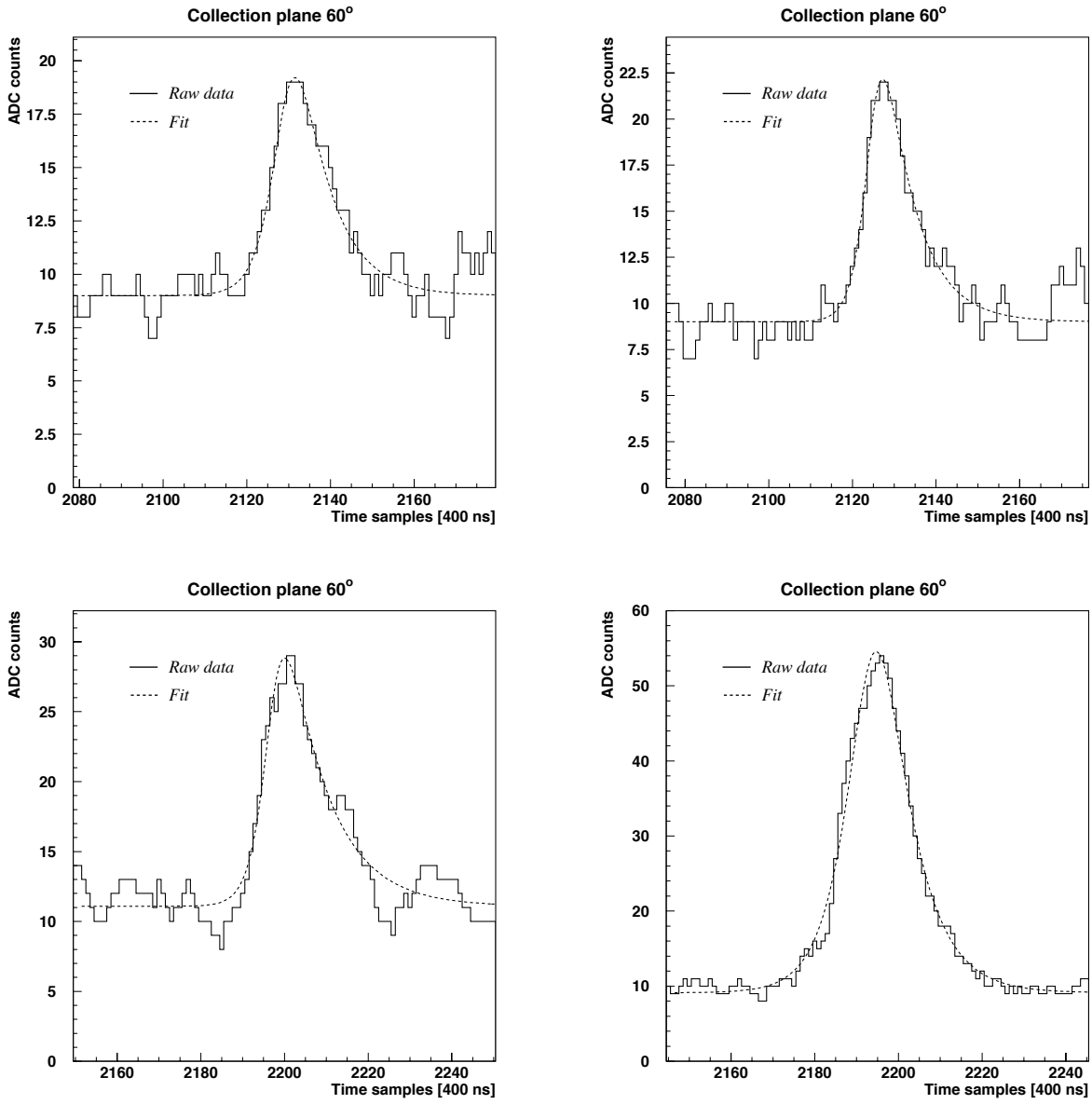

Figure 4.11: Fitted signals from four hits along the track of a muon stopping inside the detector (Collection view).

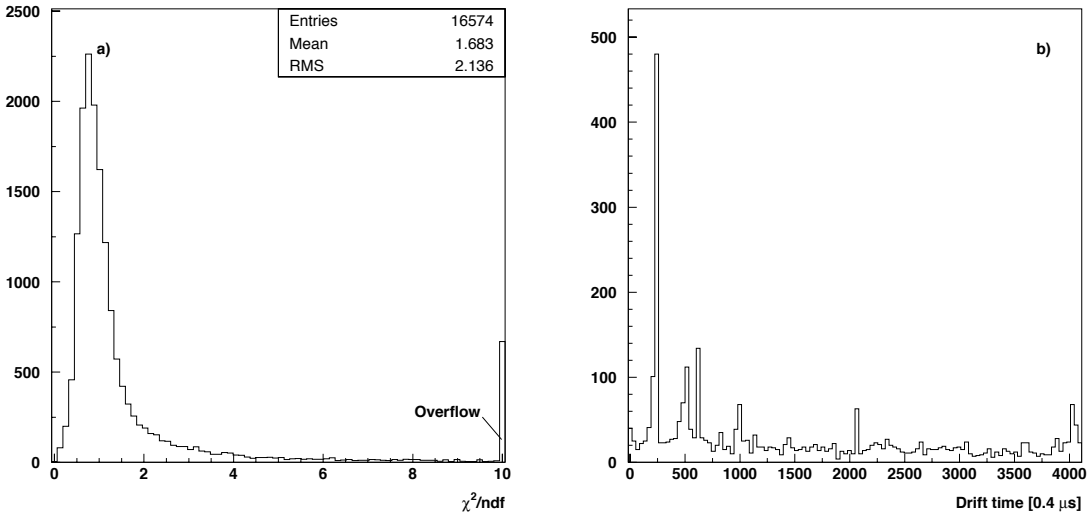

Figure 4.12: Run 939, Event 2. Left: Distribution of the χ^2/ndf values of the fit for the reconstructed hits in the Collection wire planes. Hits with non converging or non-physical fits have been discarded. Right: Drift time coordinate of hits with non converging fits, unphysical fitted parameters, or $\chi^2/ndf > 4$.

- The bounds of the hit window, where the different reconstruction procedures are carried out.
- The peak position, the peak height and the hit area as computed by the direct ADC counting method.
- The peak position, the peak height and the hit area as computed by the hit fit method.
- The values of the fit parameters values.
- The $\chi^2/n.d.f.$ of the fit.

4.2.2 Evaluation and comparison of the reconstruction methods

Evaluation of the fitting method

The quality of the fit has been evaluated by reconstructing all found hits from the Collection views in event 2 of run 939, where no large electromagnetic showers are present. Out of 18298 found hits, 1357 (7.4%) yield a non converging minimization procedure. From converging fits, 367 (2.0%) yield non-physical parameters, i.e. $A < 0$, $\tau_1 < \tau_2$ or $\tau_2 \leq \tau_1 \leq 0$. The χ^2/ndf distribution of the remaining 16574 hits (90.6%) is shown in figure 4.12a.

Most of the hits with fit convergence problems or high χ^2/ndf values are produced by the PMT induced signal (see figure 4.3) whose shape can not be reproduced by the function f (see equation 4.2). Figure 4.12b shows the drift coordinate of the reconstructed hits with fit problems (non convergence, convergence to unphysical parameters) and those with $\chi^2/ndf > 4$. PMT induced signals are present for this event at drift sample coordinate values 230, 500, 630, 990, 2050, 3550 3890 and 4030, in agreement with the visible peaks.

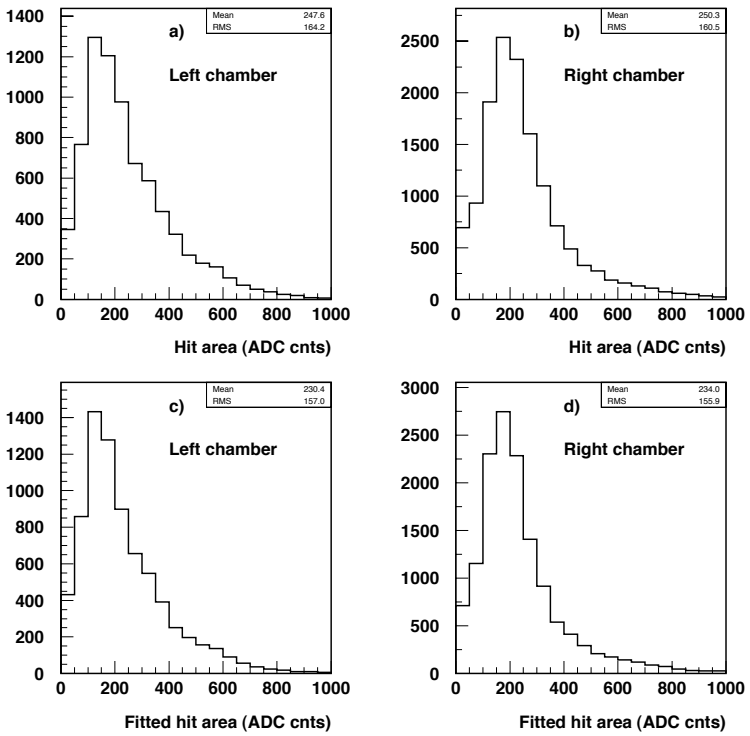

Figure 4.13: Measured hit area using the ADC direct counting (top) and fit (bottom) methods for the left (left side plots) and right (right side plots) chambers. Wires with high noise conditions or electronics problems are not used. Hits are further selected by imposing $\chi^2/ndf < 1.5$ and $N_{hits} > 100$ where N_{hits} is the number of adjacent hits group containing the hit (see section 4.3).

Comparison of the two reconstruction methods

The main goal of the reconstruction methods is to extract the hit area and height, as well as the position along the drift coordinate. Both, the methods based on direct ADC counting and fitting the hit, yield similar results measuring these two quantities. For the reconstruction methods comparison, all identified hits from events 1, 2, 5, 7 and 8 in run 939 have been reconstructed. The following criteria have been applied in the hit selection:

- For the right (left) chamber, the wires with coordinates $w > 3100$ ($1500 < w < 4000$) are selected. This selects signal regions with low noise conditions and no identified problems for both chambers.
- $\chi^2/ndf < 1.5$ and the hit belongs to a group of more than 100 adjacent hits. This ensures the rejection of fake (noise) hits.

Figure 4.13 shows a comparison of the measured hit area using the direct ADC counting (top) and the fit integration (bottom) methods. The comparison is shown independently for the left (left side plots) and right (right side plots) chambers. For both chambers, the distributions of the reconstructed hit areas agree within 2% accuracy, proving that no assymmetry on the LAr purity at both chambers is present. On the other hand, the area computed by direct ADC

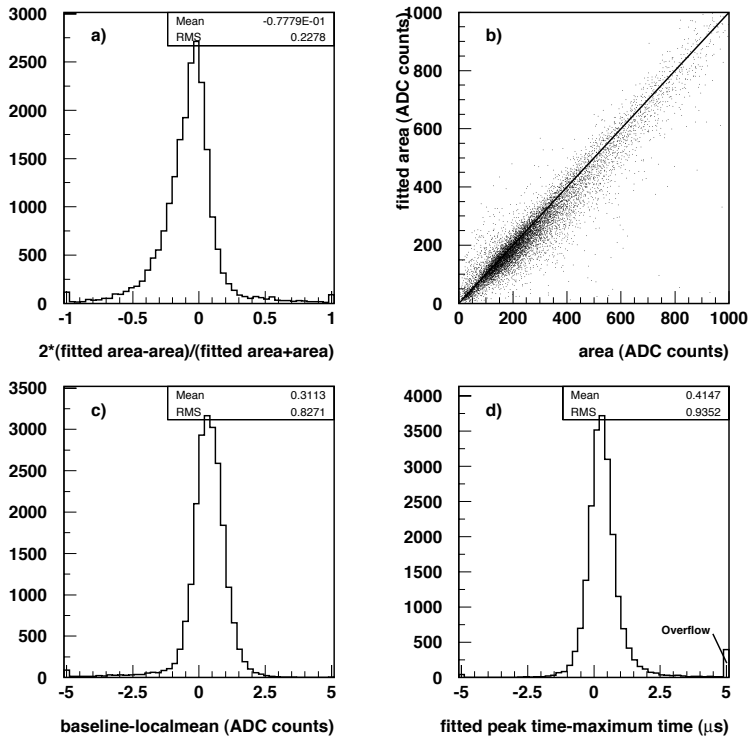

Figure 4.14: Comparison of the hit parameters from with two reconstruction methods. a) Difference between the hit area values. b) Correlation between the hit area values. c) Difference between the fitted baseline parameter and the computed local mean. d) Difference between the hit peak position computed values. Hit selection criteria as in figure 4.13.

counting is systematically higher than the fit function integration. The effect is again shown in figure 4.14a, where the area difference between the two methods is plotted. Areas computed by the fit integration are on the average about 8% lower than those computed as the ADC counts sum. Figure 4.14b shows the correlation between the area values obtained with the two methods. The systematic shift is due to the difference in the reference value used in both methods, namely, the computed local mean and fitted baseline (see figure 4.14c). The existence of this systematic shift implies that different calibration factors must be used for the two methods when translating the computed area into energy.

Figure 4.14d shows a comparison of the hit peak position values yielded by the two methods. In the ADC counting method, the peak is taken as the output sample with the maximal value whereas for the fit method, the peak position is obtained analytically from the fitted parameters. Both methods yield similar results within 0.4 μs (1 drift sample).

4.3 Cluster reconstruction

A cluster is defined as a group of adjacent hits within the wire/drift coordinate plane. The goal of the cluster reconstruction is to perform a first grouping of hits belonging to common charge deposition distributions, such as tracks or showers. Clusters provide identification criteria for

the different patterns, and thus determine which reconstruction procedure must be followed. Clusters also provide a criterion for discrimination between signal and noise hits, based on the cluster hit multiplicity.

A *link* is defined as a pair of hits coming from consecutive wires and having overlapping drift coordinate ranges, where the drift coordinate range of a hit is defined as the one computed by the hit finding algorithm (see section 4.1). Therefore, clusters can be defined as groups of hits with links between them. Links are also of utmost importance during the three dimensional hit reconstruction algorithm (section 4.4).

The description of the cluster reconstruction algorithm and an evaluation on the T600 test run data are presented in the following sections.

4.3.1 Cluster reconstruction algorithm

Clusters are built in a two step approach. In the first step (pass I), preliminary clusters are built as groups of hits being connected by links. The second step (pass II), attempts to expand and merge together the clusters found in pass I, in order to reduce the number of the resulting clusters. The reconstruction algorithm takes as input a list of hits from a given wire plane, and constructs all possible clusters out of them, using only the information obtained by the hit finding algorithm (see section 4.1).

Pass I

Pass I algorithm loops over the input hit list, aiming at associating each of them to a previously existing cluster, creating a new cluster otherwise. A hit is associated to a cluster when a link exists between the hit and at least one hit belonging to the cluster.

In pass I, a preliminary grouping of the hits to a cluster is performed. However, due to the hits ordering within the hit loop, pieces of a cluster joining at increasing hit loop index values are not associated to the same cluster during pass I. The effect is illustrated in figure 4.15. Figure 4.15a shows a gray scale representation of the raw output signal within an area of the wire/drift coordinate plane, where the hit finding and cluster reconstruction pass I processes are applied. Figure 4.15b shows in bold the drift coordinate range of the hits found by the hit finding algorithm. All visible hits have been identified. In the pass I hit loop, hits are ordered according to increasing wire index (from left to right in the plot), and increasing drift coordinate (from top to bottom in the plot) within the same wire. Therefore, since pass I associates each hit into a single cluster, without looking for possible multiple associations, it creates the clusters marked respectively in figures 4.15c and 4.15d.

Pass II

The goal of cluster reconstruction pass II is to expand and join cluster fragments produced by pass I. It proceeds as follows: the regions around the cluster borders are examined (where a cluster border is defined as a hit linked at most with one hit within the cluster). The cluster fragments found are merged hence eliminating the fragmentation produced in pass I. When no clusters are found, new hits are searched for in the region close to the cluster borders and are added to the cluster, hence reducing the cluster fragmentation caused by hit misidentification.

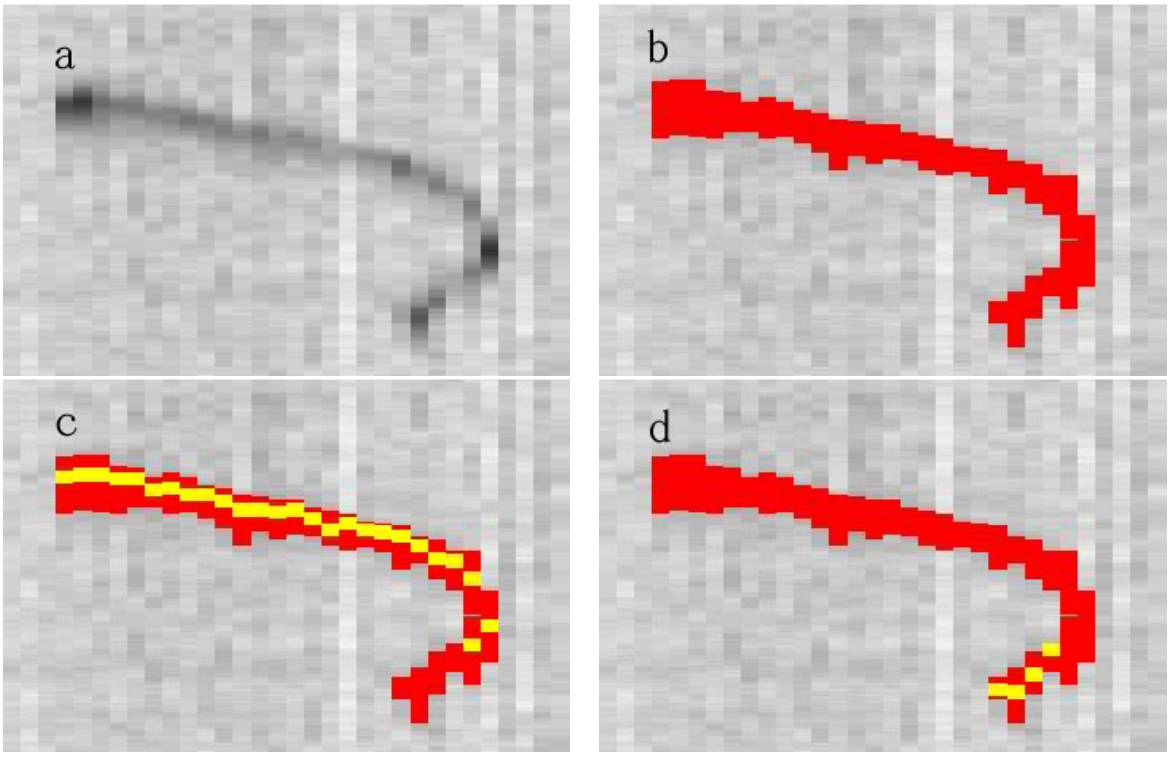

Figure 4.15: Illustration of the cluster pass I performance. The pictures show the signal in a 9×3 cm region of the drift coordinate (vertical) vs. wire (horizontal) plane. a) Gray scale mapping of the output signal. b) In bold, drift coordinate range of the identified hits. c) and d) In light, the two clusters reconstructed after pass I.

Attempts for clusters merging/expansion are performed both along the wire and the drift time coordinate directions.

The algorithm for the expansion along the wire coordinate direction proceeds in the following sequential steps for every cluster:

- Cluster borders are identified as those hits with at most one link to the cluster.
- The *direction* of the search is determined as wire coordinate increasing (decreasing) for borders linked with a hit from the previous (next) wire. For single hit clusters, both directions are consecutively inspected.
- A *slope* coefficient is determined as the difference between the drift time coordinates of the cluster border hit and its linked hit. For single hit clusters, $slope=0$.
- Hits are searched for in the *wiregap* consecutive wires along the determined direction. Hits whose drift coordinate range overlaps with that of the cluster border hit shifted by $shift*\Delta_{wire}$ drift samples (where *shift* value is subsequently selected as 0 and *slope*, and Δ_{wire} is the difference between the wire coordinates of the hit and its associated link hit) are selected.
- If one or more hits are selected, clusters containing them are merged with the initial cluster. If no existing hit is found in the inspected region, a search for new hits is performed on an output samples window of size equal to the drift coordinate range of the cluster border

	Induction I	Induction II	Collection
niter	2	2	2
minheight	4	4	4
minwidth	5	5	5

Table 4.5: Values of the free parameters of the cluster expansion hit finding algorithm.

hit, shifted by $slope*\Delta_{wire}$ samples. The new hit search algorithm is summarized below. Any new hit found is added to the expanding cluster.

- The borders of the new resulting cluster are identified and the whole process is repeated until no further expansion is possible.

The new hit search algorithm, performed during the cluster fragment expansion, proceeds as follows:

- The maximal output value within the selected signal window is searched. A hit candidate is built starting from the found maximum position and extending in both, increasing and decreasing drift coordinate values, until the output value crosses the local mean.
- The local mean value is computed in an iterative process of *niter* iterations. For each iteration, the local mean is computed as the average value in the selected window after removing those samples belonging to the hit candidate. The found local mean value is used to recompute the hit candidate bounds (see previous step), which will be eventually used in the local mean computation for next iteration.
- After the iterative process, the hit bounds are expanded by using the hit expansion procedure from the hit finding algorithm (see section 4.1).
- The hit candidate height is defined as the difference (in ADC counts) between the peak output value and the local mean. The hit candidate width is defined as the distance (in drift samples) between the hit bounds. Those hit candidates whose height and width are respectively greater than *minheight* ADC counts and *minwidth* drift samples, are selected and added to the cluster.

The value of the parameters *niter*, *minheight* and *minwidth* used for the different planes are summarized in table 4.5.

Once no further expansion along the wire coordinate is possible for any of the existing clusters, the merging of clusters along the drift coordinate direction is attempted. For that, the hits at the maximal and minimal drift coordinate values are compared among different clusters. Cluster merging is carried out for those pairs of clusters for which their respective minimal and maximal drift coordinate hits are in the same or consecutive wires, and whose drift coordinate ranges overlap.

After all possible cluster expansions have been carried out in both the wire and drift coordinate directions, those clusters having less than *nminhits* are removed unless any of the hits belonging to the cluster has a peak height greater than *minpeakheight* and a width greater than *minhitwidth*. This prevents removing single hit clusters produced by the ionization signal of low energy particles (for instance those produced by low energy photons). The values of the parameters *wiregap*, *nminhits*, *minpeakheight* and *minhitwidth* used for the cluster reconstruction in the different views are summarized in table 4.6.

	Induction I	Induction II	Collection
wiregap	1	2	1
nminhits	5	5	5
minpeakheight	10	10	10
minhitwidth	10	10	10

Table 4.6: Values of the free parameters of the cluster reconstruction algorithm.

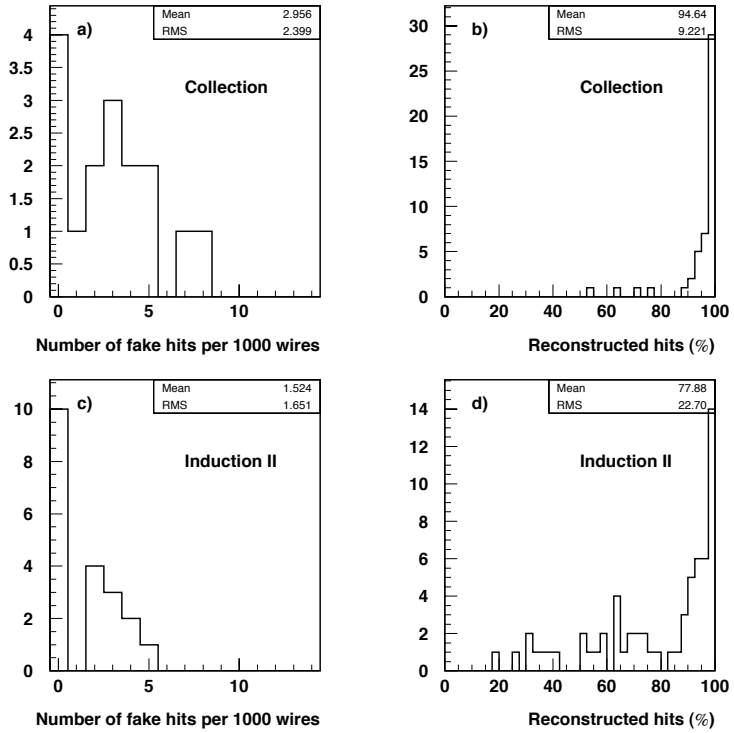

Figure 4.16: Evaluation of the quality of the cluster reconstruction algorithm. Left: number of fake hit detections per 1000 wires for output regions free of ionization signal, after cluster reconstruction. Right: Rate of reconstructed hits within straight line tracks after cluster reconstruction. Top plots correspond to Collection wires, bottom plots correspond to Induction II wires.

Hit parameterization after cluster reconstruction

Cluster reconstruction adds the following quantities to the hit parameters :

- The number of links associated to the hit.
- The list of hits to which the hit is linked.

These data are of utmost importance during the spatial reconstruction of the hit (see section 4.4).

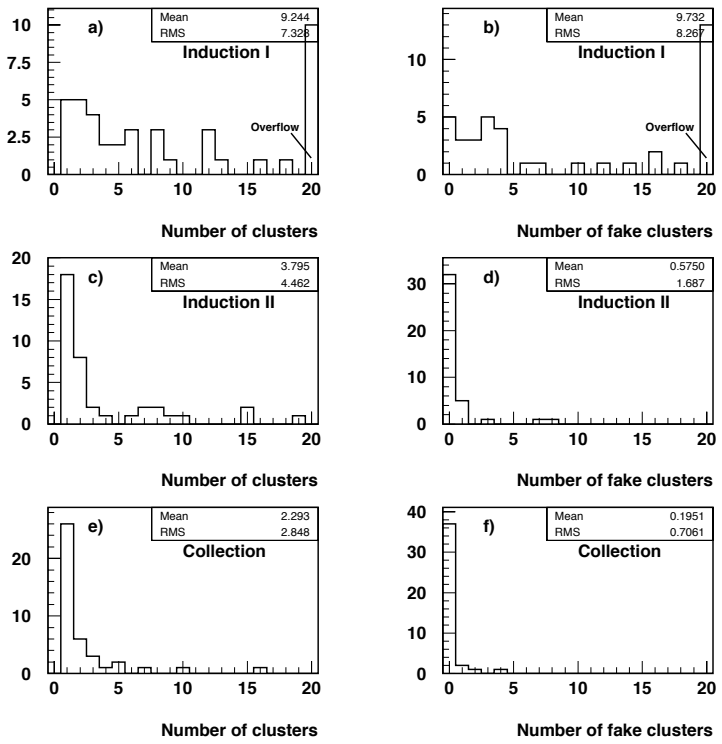

Figure 4.17: Distribution of the number of reconstructed clusters (left) and number of fake reconstructed clusters (right) in stopping muon events in the Induction I (top), Induction II (middle) and Collection (bottom) wire planes.

4.3.2 Evaluation of the cluster reconstruction

An evaluation of the cluster reconstruction has been carried out on the T600 test run data, similar to the hit reconstruction evaluation described in section 4.1.2. The hit detection efficiency and fake hit detection rate are recomputed after the application of the cluster expansion and selection based on the cluster hit multiplicity. Events 1, 2 and 5 from run 939, and event 163 from run 975 have been used for this evaluation.

Figures 4.16a and c show respectively the distributions of the measured fake hit detection rate on selected areas with no visible ionization signal present for Induction II and Collection planes. Fake detection rate is significantly reduced by cluster reconstruction (compare with figure 4.8) thanks to the cluster rejection based on the hit multiplicity. The reduction is of one order of magnitude for Collection wires (from about 50 to about 3 hits per 1000 wires), and of three orders of magnitude for Induction II wires (from about 1000 to about 2 fake hits per 1000 wires). This big reduction can be achieved thanks to the fact that fake hit detections are mainly caused by signal fluctuations due to incoherent noise sources, so that no expansion of fake hits clusters is carried out.

Figure 4.16b and d show respectively the distributions of the measured hit detection efficiency on straight line tracks for Induction II and Collection planes. Cluster expansion produces an increase of the detection efficiency from 90 to 95% for Collection wires and from 70 to 78% in the case of Induction II wires.

Induction I

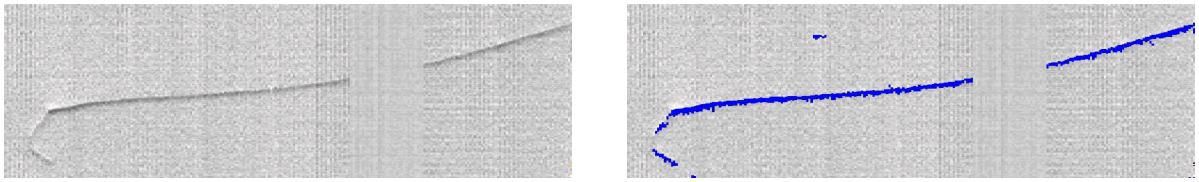

Induction II

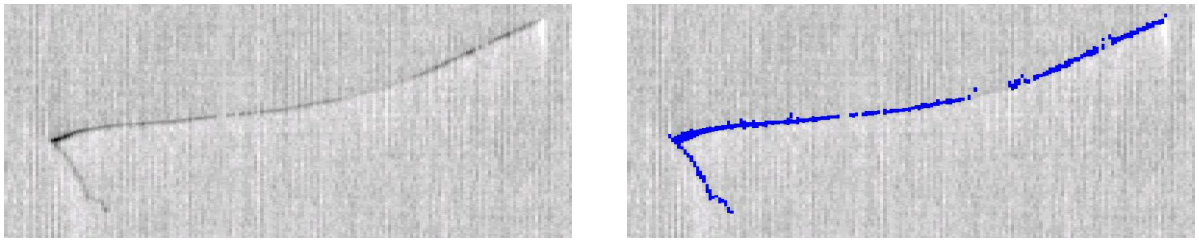

Collection

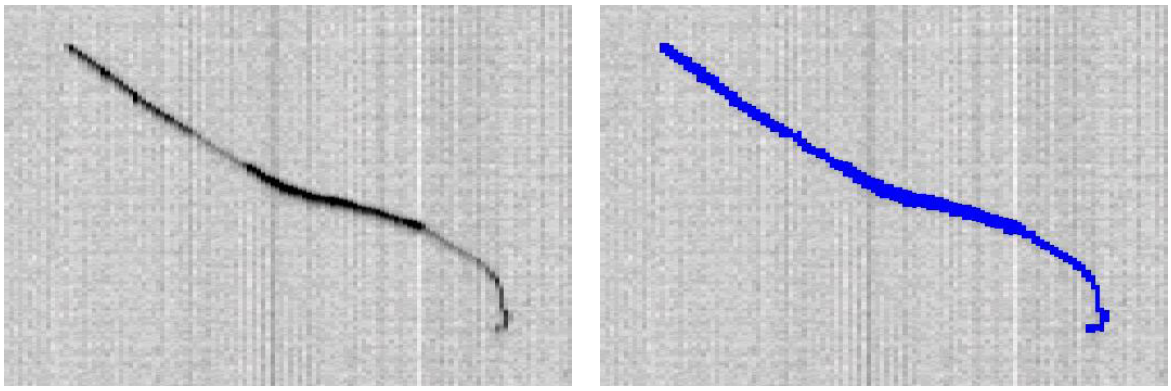

Figure 4.18: Run 939, Event 95. Example of the performance of the cluster reconstruction algorithm on a stopping/decaying muon event for the Induction I (top), Induction II (middle) and Collection (bottom) views. Left: gray scale representation of the wires output signal in the wire/drift time plane. Right: in bold, hits associated to any reconstructed cluster.

An independent evaluation of the cluster reconstruction can be carried out on stopping muon events. A sample of 41 stopping muon candidate events is visually selected from different events in run 939. The hit and cluster reconstruction processes are performed on the selected events, and the resulting number of clusters created from the muon and electron tracks (which in the ideal case should belong to the same cluster) is counted. The result for the three wire planes is shown in figure 4.17 (left side plots). The figure also shows the distribution of the number of fake reconstructed clusters (defined as clusters created from fake identified hits) in the same event sample, for the three wire planes (right side plots).

Figure 4.18 shows the reconstructed clusters in the different views for a decaying muon event.

To summarize, the cluster reconstruction aims at grouping the hits produced by a common ionizing particle. The clusterization of the hits is useful mainly in two different aspects of the event reconstruction. First, it provides a way to increase the final hit detection efficiency and reduce the fake hit detection. Second, it establishes relations between the hits based on their relative positions in the wire/drift plane, which are of utmost importance during the three-dimensional reconstruction (see next section).

4.4 Three-dimensional hit reconstruction

The goal of the three dimensional (3D) reconstruction of a hit is the determination of the space coordinates of the different energy deposition segments produced by the ionizing tracks traversing the LAr sensitive volume. Each wire plane constrains two spatial degrees of freedom of the hits, one common to all the wire planes (the drift coordinate) and one specific for each plane (the wire coordinate). The redundancy on the drift coordinate allows the association of hits from different planes to a common energy deposition, and together with the wire coordinates from at least two planes, allows the hit spatial reconstruction of the hit

In the following sections we describe the hit 3D reconstruction of a hit and an evaluation of its performance. We start summarizing the expressions for the transformation from the wire/drift coordinates system into the Cartesian system.

4.4.1 Transforming wire/drift coordinates into 3D Cartesian coordinates

We define the Cartesian reference frame (see figure 4.19) centered at the bottom left corner of the front end of the LAr sensitive volume (by looking at the detector from the clean room end). Coordinates x, y and z go from bottom to top, from left to right and from front to back sides of the detector, respectively. Coordinate x can be determined either by the wire coordinate of the horizontal wire plane (x_3) or by combining the wire coordinates from the $\pm 60^\circ$ planes ($x_{1,2}$). Coordinate y is uniquely determined by the drift coordinate sample. Coordinate z can be determined in three different ways ($z_{1,2}$, $z_{1,3}$ and $z_{2,3}$) by combining the three available wire coordinates. The different possible coordinate determinations are related to the wire and drift coordinates by means of the following expressions:

$$\begin{aligned} x_{1,2} &= \frac{p}{2\cos\theta_w}(w_1 - w_2 + w_0) \\ x_3 &= p\, w_3 \\ y &= \frac{s\, v}{f} \\ z_{1,2} &= \frac{p}{2\sin\theta_w}(w_1 + w_2 - w_0) \\ z_{2,3} &= \frac{p}{\tan\theta_w}\left(w_3 + \frac{w_2 - w_0}{\cos\theta_w}\right) \\ z_{1,3} &= \frac{p}{\tan\theta_w}\left(\frac{w_1}{\cos\theta_w} - w_3\right) \end{aligned} \tag{4.4}$$

where the constants entering the formulae are the following: p, the wire pitch at LAr temperature; θ_w, the angle of the Induction II/Collection wires with respect to the horizontal (in the range $[0, 90^\circ]$); w_0, half the number of wires from the Induction II (Collection) planes intersecting with a wire from the Collection (Induction II) plane; and f, the readout sampling frequency. The values of the constants are summarized in table 4.7. v is the electron drift velocity, which depends on the drifting field and the LAr temperature [59]. Finally, w_1, w_2, w_3 and s are related to the indexes of the wires sensing the hit in the different wire planes and the drift time coordinate (in number of samples), respectively. w_1 corresponds to the wire index in the 60° wire plane whose wire number 0 is placed at coordinates $(x, z) = (0, 0)$; w_2 is the index of the wire

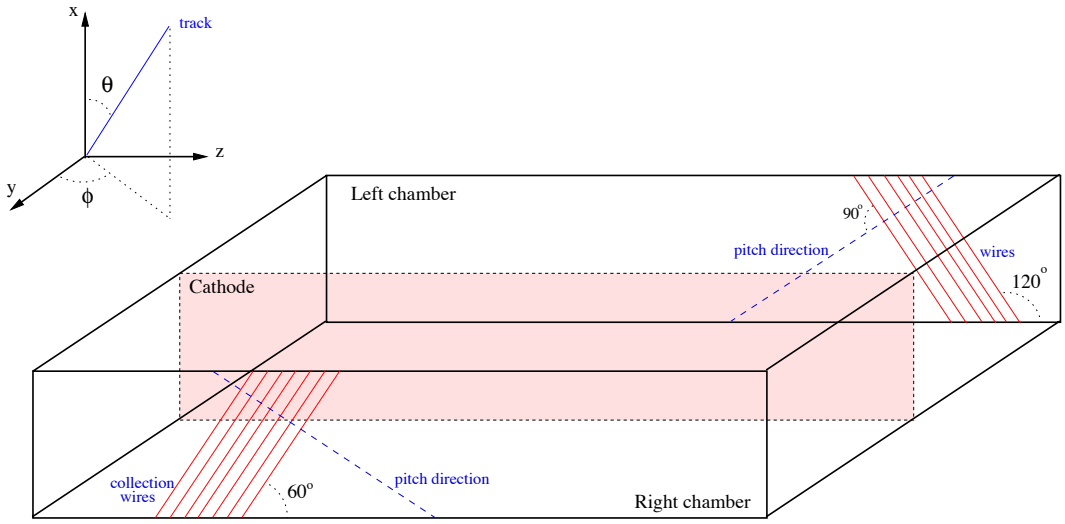

Figure 4.19: Sketch of the T600 first half-module and the Cartesian reference frame.

Parameter	Value
p	2.991 mm
θ_w	60°
w_0	528
f	2.5 MHz

Table 4.7: Values of the constant parameters entering the formulae for the three dimensional Cartesian coordinates.

sensing the hit in the complementary 60° wire plane (with wire number 0 at $(x, z) = (x_{max}, 0)$). The correspondence of coordinates w_1 and w_2 with the different wire planes for both right and left chambers is summarized in table 4.8. Given the numbering of the horizontal wires, w_3 is related to the wire coordinate in the horizontal wire plane (w_3^0) by

$$\begin{aligned} w_3 &= w_3^0 && \text{for } w_3^0 < 1056 \\ w_3 &= 2111 - w_3^0 && \text{for } w_3^0 \geq 1056 \end{aligned} \tag{4.5}$$

Finally, $s = s^0$ (where s^0 is the drift coordinate) for the left chamber, and $s = 2S_{max} - s^0$ (with $S_{max} = 4096$ the total number of samples in an event) for the right chamber.

The possibility of multiple determinations of x and z coordinates is due to the presence of three wire planes, providing each of them a two dimensional projection of the event. The combination of the different values results in an improvement on the precision of x and z coordinates determination. On the other hand, any combination of wire coordinates from two wire planes, together with the drift sample coordinate allows the determination of the spatial position of a hit within the LAr active volume, by means of the appropriate formulae from equation 4.4.

4.4.2 3D reconstruction algorithm for a hit

The hit 3D reconstruction algorithm takes as input the sample of hits belonging to any reconstructed cluster from an arbitrarily selected view (called *main view*), and searches for hits from

	Left	Right
w_1	Collection	Induction II
w_2	Induction II	Collection

Table 4.8: Correspondences of the wire coordinates w_1 and w_2 with the different wire planes at left and right chambers.

complementary secondary views corresponding to the same ionizing track segment. Such a hit is called *associated* hit. The combined information from a hit and its associated hit from one or more complementary views allows the determination of the hit spatial coordinates.

The algorithm proceeds in three steps (passes). In pass I, all possible associations between hits from the main and the complementary views are carried out. The associations are established based on the redundancy of the drift coordinate and the relations between hits within the clusters (links). Pass II searches for deficiently associated hits, redefining their position based on the neighbouring hits. Finally, in pass III, we compute the optimal spatial coordinates for unassociated hits.

Pass I

The goal of pass I is to identify the maximum possible number of associations for hits from the main view, combining intra-view (links) and inter-view (associations) relations between hits.

The first and most important step is the search of associations of the cluster bound hits (i.e. hits with at most one link to the cluster). This provides a starting reference point for the association of the remaining hits of the cluster. Cluster bound hits are required to be associated to cluster bound hits from the complementary views. The remaining hits are looped over following the cluster links. In first approximation, a given hit h_1 linked to a hit h_2 is associated to a hit h_1^c from the complementary view only if h_1^c is linked to a hit h_2^c associated to h_2. If the previous condition cannot be fulfilled, h_1 is associated to the hit association candidate h_1^c closest to h_c^2 if the difference between h_1^c and h_c^2 wire coordinates is smaller than *wireshift*. The spatial reconstruction of those hits having a single hit association candidate in any complementary view fulfilling the previous requirement is performed by using the appropriate expressions from equation 4.4.

The hit association candidates are those hits from a complementary view with equal drift coordinates (within a given tolerance of *driftshift* drift samples, and after correcting for the expected shift due to the distance between the compared wire planes) and compatible wire coordinates. The shift on the drift coordinates of the associated hits is due to the time the drift electrons take to travel from a wire plane to the next (about 2 μs) and the difference on the shapes of the induced signals in the different planes (about 1 μs). The total shift between two consecutive views is estimated to be between 4 and 5 drift samples.

The association of a given hit is restricted to those hits appearing on wires with a common spanned LAr region. This is illustrated in figure 4.20, where a Collection wire (in dashed green) is shown together with the allowed associated wires (in dotted red) in the Induction II (top) and I (bottom) views. Only those wires whose projection in the wire plane intersect can contain associated hits. In general, every wire of coordinate $w_{1,2}$ from a 60° view (Collection or Induction II), intersects with wires with coordinates from $w_{2,1} = w_{1,2} - w_0$ to $w_{2,1} = w_{1,2} + w_0$ of the complementary -60° view. Wires with coordinates from $w_{1,2} = 0$ to $w_{1,2} = 3129$ from any

Parameter	Value
driftshift	5
wireshift	4
maxdistance	20 mm

Table 4.9: Values of the constant parameters in the three dimensional hit reconstruction.

of the $\pm 60^{\circ}$ views intersect with wires from $w_3 = 0$ to $w_3 = 1055$ of Induction I plane, whereas those from $w_{1,2} = 2600$ to $w_{1,2} = 5727$ intersect with wires $w_3 = 1056$ to $w_3 = 2111$.

The values of the free parameters in pass I three dimensional hit reconstruction are summarized in table 4.9.

Pass II

The inefficiencies of the hit finding and cluster reconstruction algorithms (see sections 4.1 and 4.3) together with the presence of ambiguities in the determination of the hit association result in a non negligible level of bad hit associations and unassociations after pass I.

In order to increase the hit association rate and quality, pass II searches and repairs failures on the hit associations. For this, we loop over the hits starting from cluster bounds and following the links within the cluster. The following algorithm is applied:

- For every two consecutive (linked) hits, h_a and h_b, having both an associated hit in a complementary view, the position in space of the next hits are compared to the extrapolation defined by the straight line joining h_a and h_b.
- All the hits $(h_1, ..., h_n)$ found until the first hit h_{n+1} whose distance to the extrapolated line is smaller than $maxdistance^{*}\Delta_{wire}$ (where Δ_{wire} is the difference between h_{n+1} and h_b wire coordinates) are flagged for an ulterior 3D coordinates (re)assignment. Flagged hits are freed when no h_{n+1} hit fulfilling the previous condition is found before a cluster bound is reached.
- Spatial coordinates of the flagged hits are (re)computed in the following way: coordinate y is computed by using the corresponding expression from equation 4.4; coordinates x and z are interpolated by the straight line defined by the projection of h_b and h_{n+1} in the (x, z) plane.

This algorithm repairs in an efficient way the position of those hits coming from straight line or small angle tracks, yielding no effect on hits coming from large angle scattering tracks. A third pass is needed in order to reduce to zero the hit unassociation rate.

Pass III

Hits remaining unassociated after pass II are reconstructed during pass III, in order to reach the required 100% efficiency on the hit 3D reconstruction. Pass III algorithm proceeds as follows:

- Starting from every unassociated hit h_0, the hits in the cluster are looped over, following the link path in both increasing and decreasing wire coordinate directions. For each direction, the loop continues until the first associated hit (reference hit) is found.

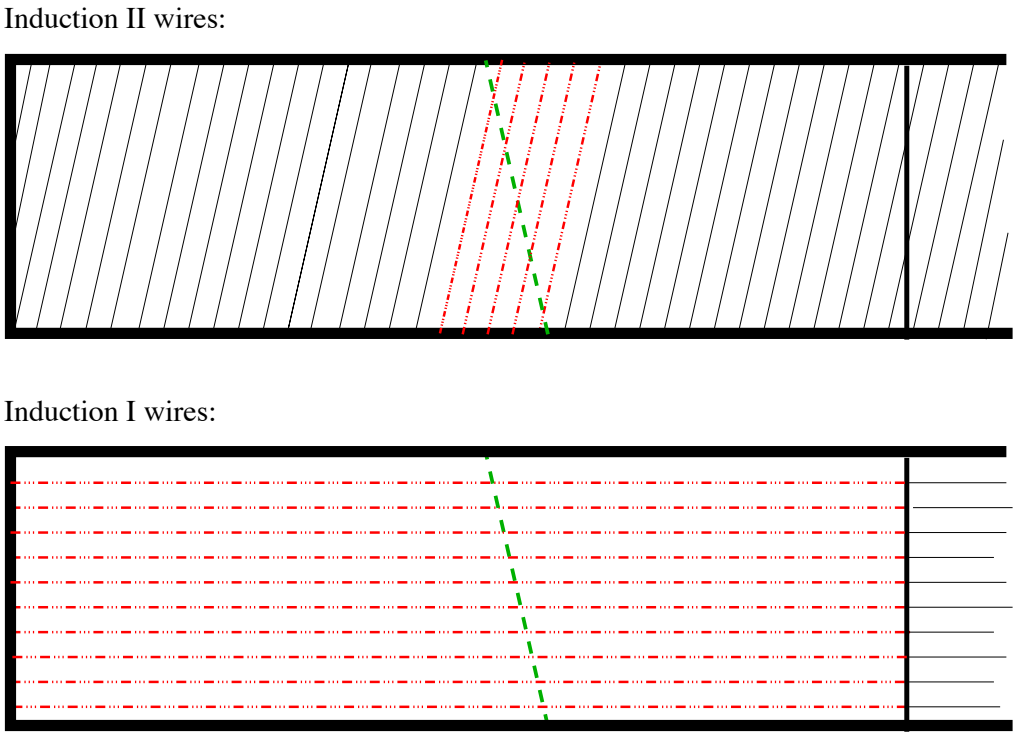

Figure 4.20: Illustration of the wire coordinate restrictions in the hit three dimensional reconstruction. A hit from a Collection wire (in dashed green) is searched for in the intersecting wires (shown in dotted red) for Induction II (top) and Induction I (bottom) wire planes. Not all wires are drawn.

- If reference hits at both sides of h_0 (h_a and h_b) are found before the cluster bounds are reached, the spatial coordinates of all unassociated hits between them are computed as in pass II.
- If one of the reference hits is not found, the spatial coordinates of the unassociated hits are computed by the straight line extrapolation defined by the found reference (h_a or h_b) and the closest associated hit following the links in the direction of the found reference.

Hit parameterization after 3D reconstruction

The picture of the hit is completed by adding the following information to the hit parameterization:

- The associated hit(s) from the complementary view(s).
- The space coordinates, x, y and z in the Cartesian reference frame.

4.4.3 Evaluation of the 3D reconstruction of hits

The 3D reconstruction of hits performs efficiently on events of low track multiplicity composed of tracks (not necessarily straight). Since it is purely based on geometrical criteria, the reconstruction method is not meant to be carried out on events with more complex energy deposition patterns, such as electromagnetic or hadronic showers. For these kind of events, a method combining spatial and calorimetric relations among hits needs to be developed.

In this section we present some examples of the performance of the spatial reconstruction algorithm on events of different nature. The presented figures show different views of the reconstructed hits in their spatial positions, joined by lines representing the links between the hits. Figure 4.21 shows two views of a muon decay event (see figure 4.18 for the initial wire/drift plane views). Figures 4.22 and 4.23 illustrate the hit spatial reconstruction performance on straight line muon tracks, where it is important to stress the reconstruction of the δ-ray sub-track. Finally, figures 4.24 and 4.25 illustrate the reconstruction of simple low multiplicity hadronic interaction events, where all the tracks and interaction vertexes have been properly reconstructed.

4.5 Conclusions

In the present chapter, we have described a method for the spatial reconstruction of simple events such as stopping/decaying muons, passing through muons and low multiplicity hadron interactions. The different steps have been tested directly on the T600 first half module data from the test run, showing a satisfactory performance. The described method represents a key tool toward the complete event reconstruction (tracking, momentum determination, particle identification), and allows the analysis of simple topology events within a common reconstruction framework.

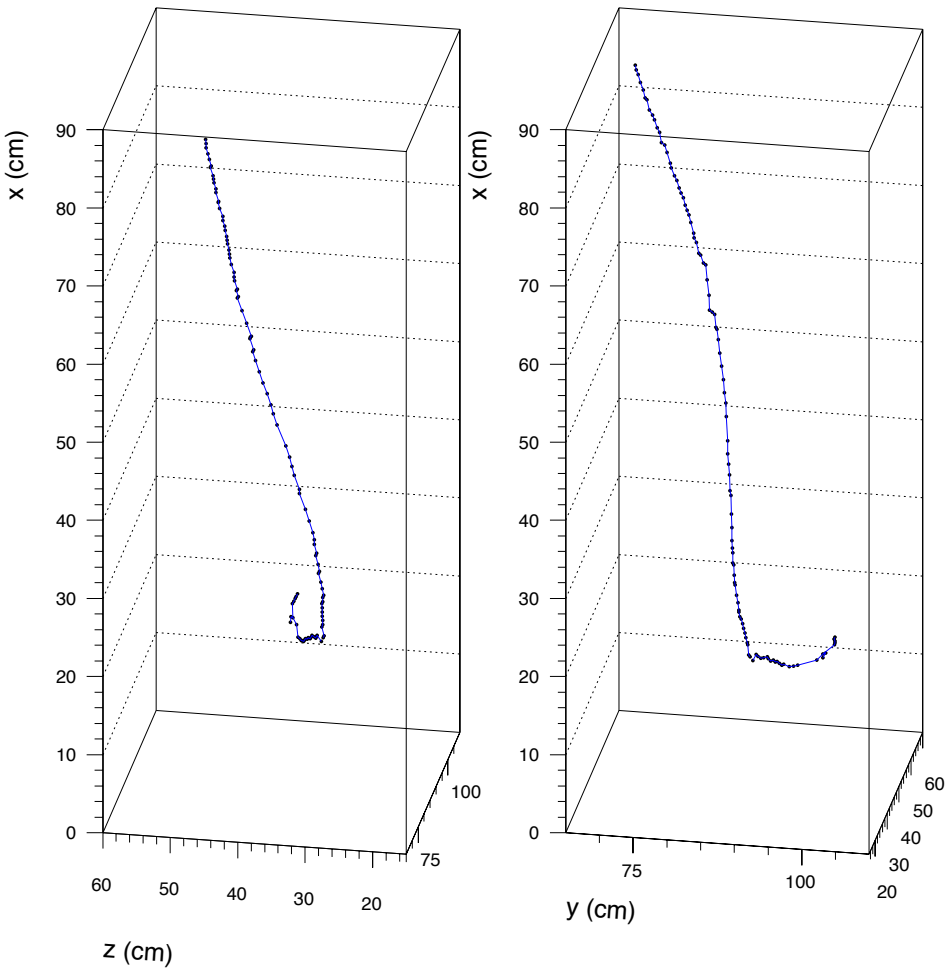

Figure 4.21: Muon decay event. The pictures show two different views of the 3D reconstructed hits (dots) together with the links established among them (lines). The corresponding 2D projections provided by the wire planes are shown in figure 4.18.

Induction I

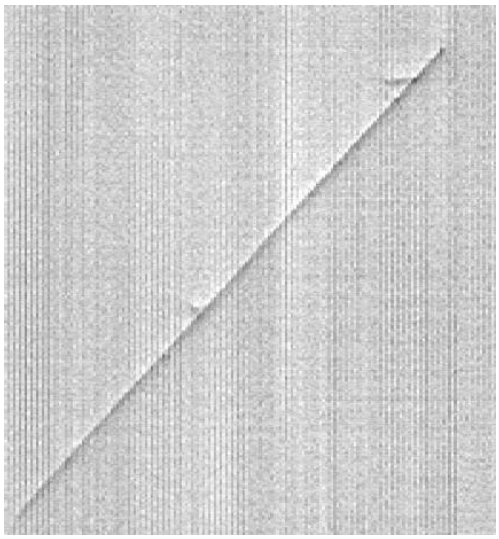

Induction II

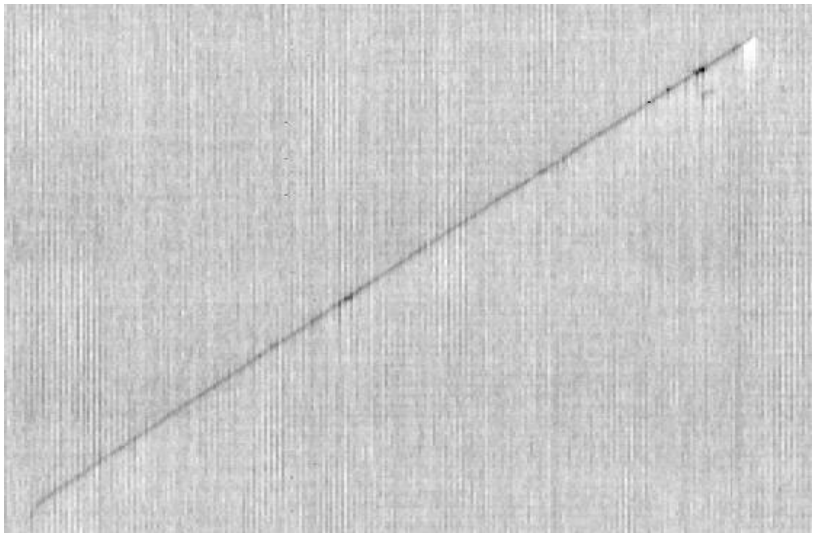

Collection

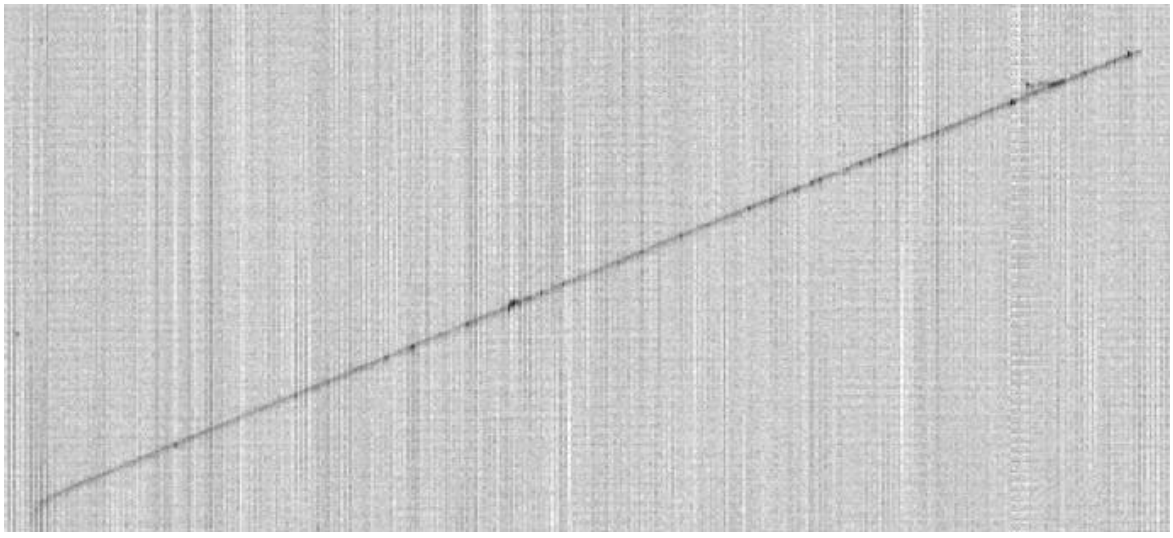

Figure 4.22: Passing through muon event with a δ-ray emission. From top to bottom, Induction I, Induction II and Collection view projections. The pictures are a gray scale representation of the output signal in the drift coordinate (vertical) vs. wire (horizontal) plane.

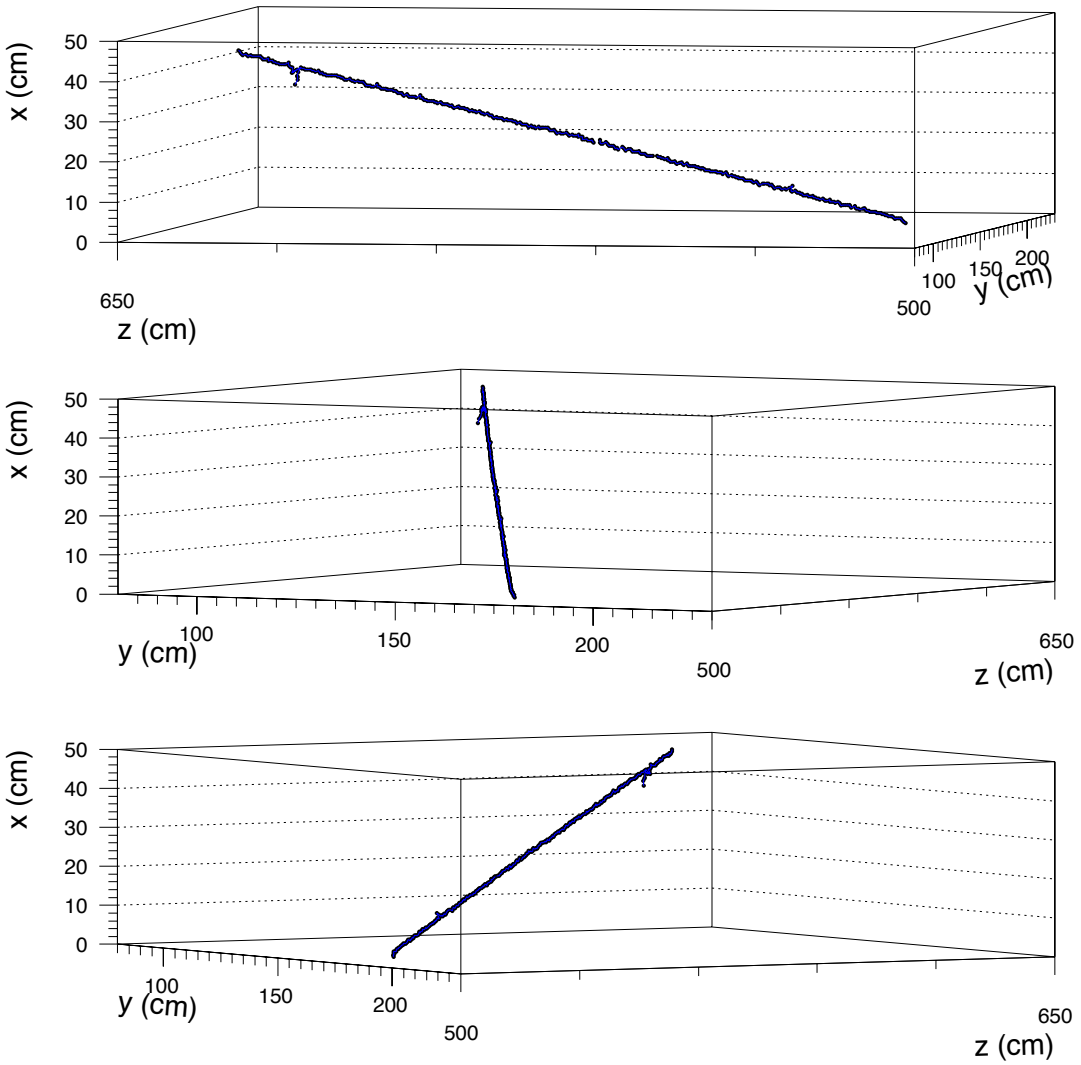

Figure 4.23: Passing through muon event with a δ-ray emission. The pictures show three different views of the 3D reconstructed hits (dots) together with the links established among them (lines). The corresponding 2D projections provided by the different wire planes are shown in figure 4.22.

Induction I

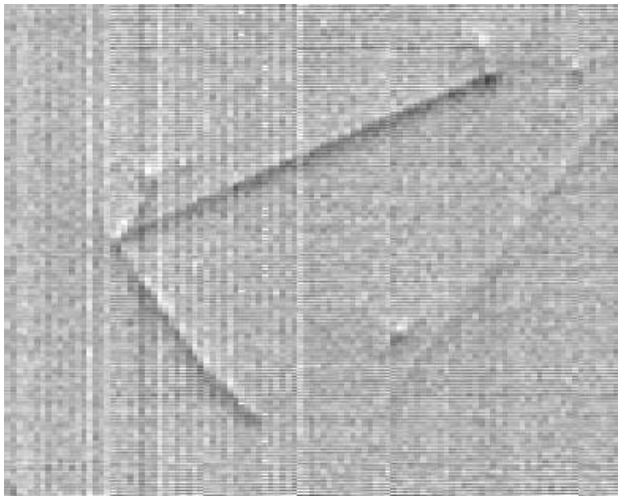

Induction II

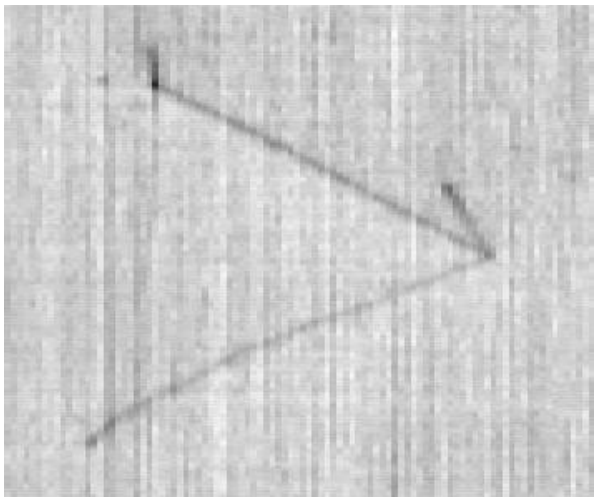

Collection

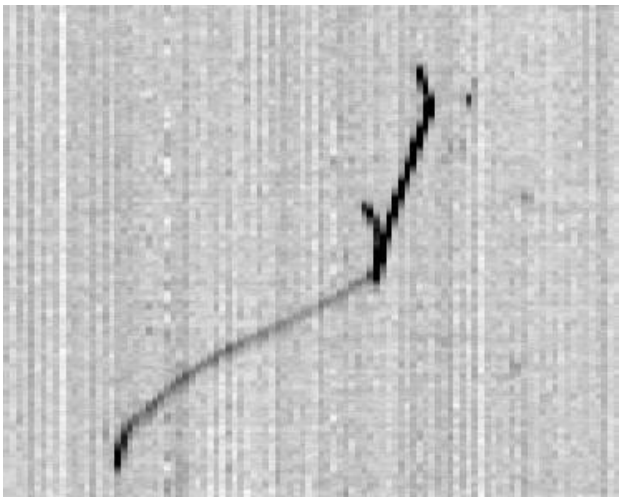

Figure 4.24: Low multiplicity hadronic interaction. From top to bottom, Induction I, Induction II and Collection view projections. The pictures are a gray scale representation of the output signal in the drift coordinate (vertical) vs. wire (horizontal) plane.

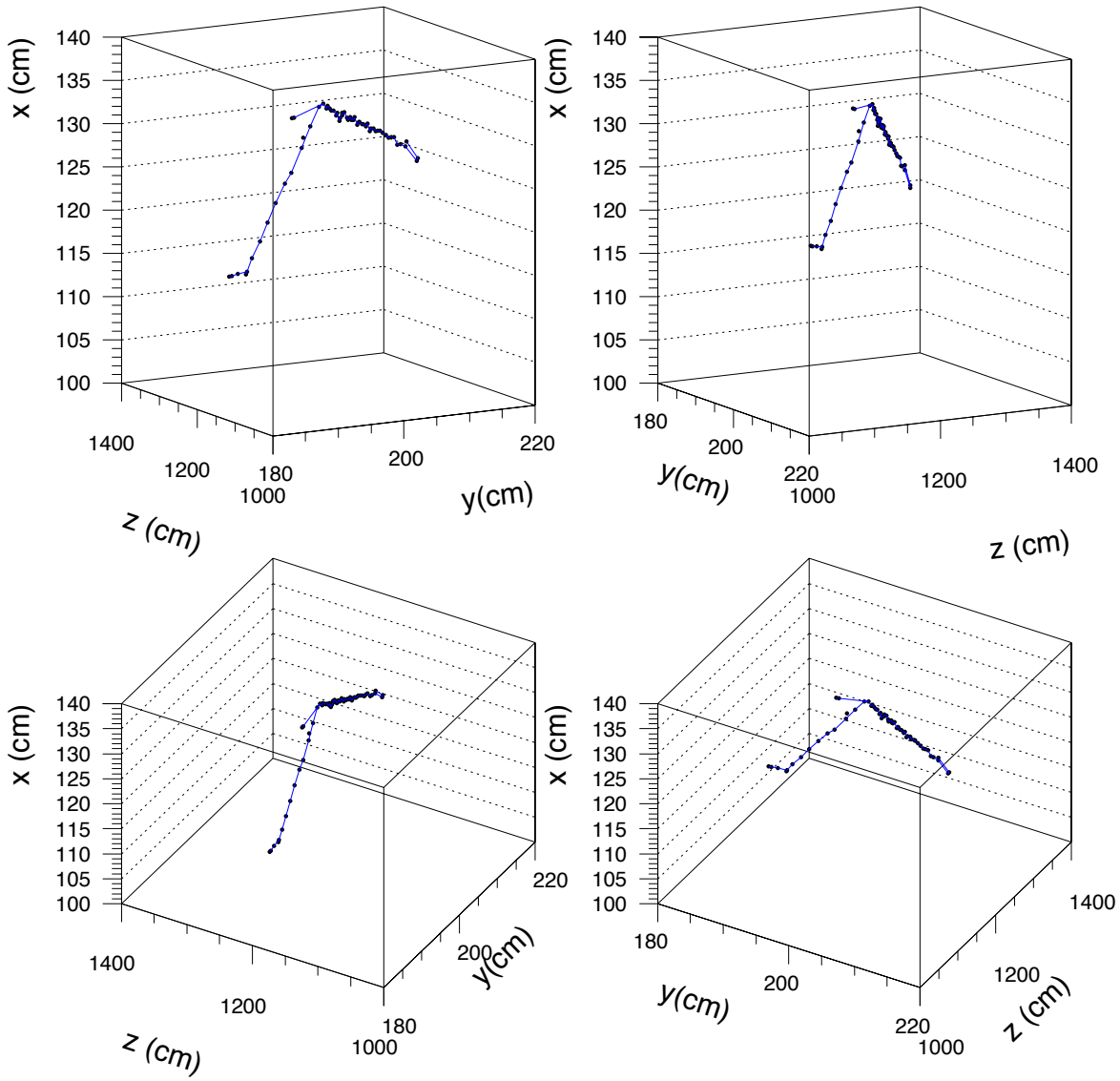

Figure 4.25: Low multiplicity hadronic interaction. The pictures show four different views of the 3D reconstructed hits (dots) together with the links established among them (lines). The corresponding 2D projections provided by the different wire planes are shown in figure 4.24.

Chapter 5

The stopping muon sample

The sample of events where a muon enters the detector, stops and eventually decays in the LAr sensitive volume –hereafter called *stopping muon* sample– constitutes an important bench mark to evaluate the physics performance of the ICARUS detector. Because of their simple geometry, the stopping muon events are relatively easy to reconstruct. With them we can measure the cosmic ray muon spectrum at low energy (below 1 GeV) and obtain the decay electron/positron spectrum. At the same time, the stopping muon sample contains the information needed to carry out the measurement of the drift electron lifetime, recombination factor and the detector energy calibration and resolution.

The stopping muons lead to two different kind of processes with different topologies, namely: *decay* and *absorption* by a neighbouring nucleus. The two kind of events are easily distinguishable by the presence or absence of an electron/positron track. The probability of each of these processes to happen depends on the muon charge sign [60, 61, 62]. Positive muons decay into a positron in 100% of the cases, whereas negative muons are absorbed in about 73% of the cases. In the present chapter, we describe the method developed to reconstruct the stopping muon events of both topologies. We start by briefly summarizing the event selection procedure and efficiency, followed by a detailed description of the reconstruction of the variables describing the event.

5.1 Event selection

5.1.1 Visual scanning

The stopping muon event selection is carried out by visual scanning, using a dedicated event display program (Qscan) based on Trolltech's GUI, Qt [53]. Qscan performs, for each wire plane, a two dimensional gray scale representation of the output signal in the wire/drift coordinate plane, i.e. perpendicular to the direction of the wires. This allows the visual inspection of the tracks produced by the different charged particles traversing the active LAr volume, in the three two-dimensional projections corresponding to the three wire planes.

In a first phase, a systematic scan of the whole T600 technical run data set has been performed in order to establish an inventory of the different acquired event types. The events are scanned in order inverse with respect to the acquisition time, since the optimal technical conditions (higher LAr purity, lower noise) were reached by the end of the technical run. The results of the inventory for the last 225 runs has been shown in table 2.5. In this phase, a preliminary

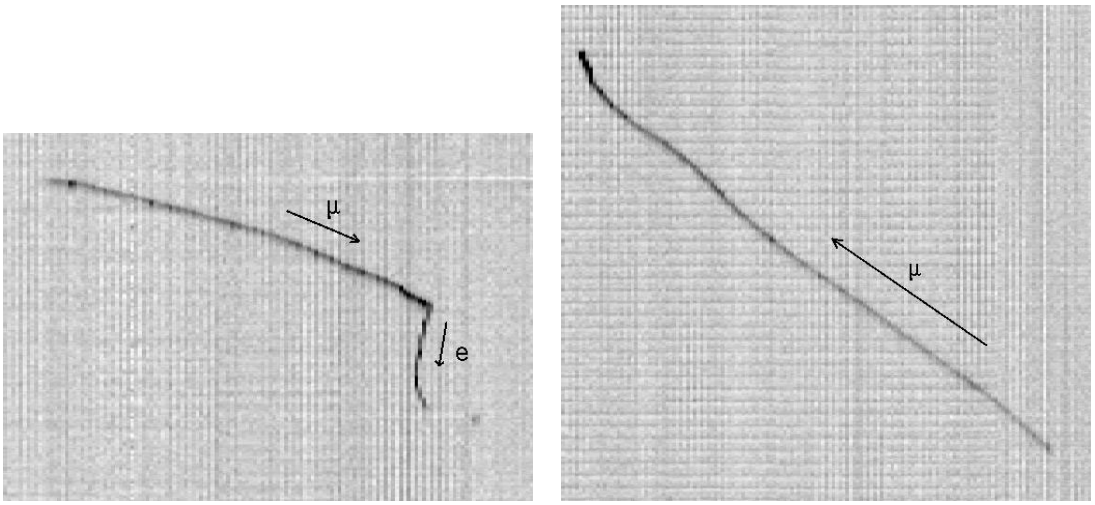

Figure 5.1: Two examples of real stopping muon events as represented in the event display program Qscan. The pictures are a gray representation of the output signal in the drift coordinate (vertical) vs. wire (horizontal) plane for the Collection wire plane. Left: decaying muon event. Right: absorption muon event.

classification based on the event topology is performed. As shown in table 2.5, about two triggers out of three contain at least one stopping muon event. Stopping muon events are identified by the presence of a low momentum muon track eventually followed by an electron. The muon, due to the low momentum, typically undergoes large angle multiple scattering, and ionization increases rapidly near the end point. Figure 5.1 shows an example of a stopping muon decaying into an electron/positron (left), and an example of a muon absorption event (right).

In a second phase of the visual scanning, those data files containing one or more stopping muon events are rescanned and the regions of the wire/drift plane containing the stopping muon event are saved in a separate file. This aims at the reduction of the data file size as well as at the definition of the region of interest for our analysis. A reduction of data file size is desirable since full-sized data files contain the signal output value (stored in a 2-byte field) for the 4096 sampling times of all the wires (~ 27000), yielding a total size of about 200 Mbyte per event. On the other hand, since data were acquired at earth's surface, there is typically a high number of (independent) different events within a common data file. Thus, the saved region must include at least the muon and decay electron tracks, as well as all candidate tracks from Compton electrons or electron/positron pairs produced by bremsstrahlung photons emitted by the decay electron (see later section 5.4). These files, of much smaller size (typically about 5-8 Mbyte) and hence much easier to handle, contain the whole drift range output signal of the wires around the region of the stopping muon event, for the three complementary views. The event reconstruction and analysis are performed exclusively on these files. For the present work, the whole sample of data files belonging to 12 of the latest data runs have been scanned (runs 939, 960, 961, 963, 965-969, 973-975). Out of them, 360 single muon event candidates have been extracted.

5.1.2 Event quality selection

During the second phase (described in the previous section), an event quality selection is also performed (see table 5.1). 101 events are rejected due to one of the following problems (indicated between brackets the percentage of the rejected events with respect to the total number of muon

Scanning stage	Event/file number
Total scanned files	561
Files containing stopping muon	315
Stopping muon event candidates	360
Event quality selection	259

Table 5.1: Event selection efficiency of the different steps of the visual scanning event selection.

event candidates):

- 37 events (10%) occur in the so called "bad" sector of the right side chamber [63]. In this sector the Induction wire planes are not completely transparent for the drifting charge, most likely due to an incorrect polarization of the wires, resulting in a loss of charge at the Collection wire plane. Only those events for which the muon candidate end point and/or part of the electron is found in the bad sector are rejected. Those for which only a fraction of the muon travels in the bad sector are reconstructed, starting from the point where the muon leaves the bad sector.

- 24 events (6.7%) occur in regions with a substantial component of high amplitude noise correlated between neighbouring wires. This kind of noise is particularly pernicious, since the wire correlation may fake the presence of an ionizing track, difficult to be recognized with the event reconstruction tools. For these events, many fake clusters are built and merged with the muon and/or electron cluster during the cluster reconstruction algorithm Pass II (see section 4.3.1), which completely distorts the stopping muon event.

- 20 events (5.5%) cannot be reconstructed due to geometrical reasons: electron and muon tracks overlap in the main or secondary views.

- 13 events (3.6%) overlap with complicated geometry events, causing the failure of the reconstruction algorithm.

- 5 events (1.4%) lack the corresponding projection from the secondary views due to failures on the DAQ system.

- 2 events (0.6%) do not contain the whole electron track in the recorded drift range.

In summary, we keep 259 events (72% of the total scanned sample) from 315 data files.

A note on the selection of absorption events

The lack of an electron track makes visual identification of absorption events more difficult than the decay events. Since most of the stopping muon events occur independently of the data acquisition trigger, they are generally *out of time* events, i.e. the absolute position along the drift direction is not determined. This introduces an additional problem for the identification of absorption events, since for many track orientations, the visual end point could correspond to the point where the muon leaves the LAr sensitive volume. However, 11 absorption muon event candidates with a clearly identified end point are included in the sample.

5.2 Muon reconstruction

5.2.1 Spatial reconstruction

The spatial reconstruction of the muon track is performed based on the general spatial reconstruction algorithms described in detail in section 4.4. Nevertheless, in view of the specific features of this kind of events, several modifications are introduced in order to increase the efficiency and quality of the reconstruction, namely:

- The Collection view, where the hit detection efficiency is maximal (see section 4.3.2) is always chosen as the main view. A single complementary view is used, which is chosen for each event (as part of the visual scanning) as the one providing the best reconstruction quality.
- The reconstruction algorithm is seeded with the coordinates of the muon initial hit in the two views, and with the muon end point coordinates in the main view. This has two main effects: on the one hand, the muon track is uniquely determined by the initial and final hits and, hence, the reconstruction inefficiencies due to the presence of other tracks crossing the same area of the wire/drift plane are eliminated. On the other hand, the efficiency and quality of the association between hits from the complementary views is increased thanks to the provided initial association.

The reconstruction process consists of three steps (passes), following the scheme described in section 4.4.2. In the following paragraphs we discuss the particularities taken into account in the muon track reconstruction.

Pass I

The search for an association of the cluster end is skipped since the muon initial hit is determined by the initial hit coordinates, provided as an input to the Pass I routine.

Starting from the initial hit, the hits belonging to the cluster are looped over, following the links. Whenever a hit with more than two associated links is found, the loop continues with the link leading to the final muon hit (provided as an input) in the shortest number of links. Hits reached following the remaining links are discarded in the construction of the muon track. The loop stops at the indicated muon final hit. As a consequence, δ-rays (see figure 5.2) and crossing tracks (see figure 5.3) are not included in the muon track. The former are effectively removed down to an energy threshold (cut-off) depending on the relative orientation of the δ-ray with respect to the muon track. The effect of the removal of δ-ray tracks is studied in section 5.2.2.

In order to profit from the geometrical features of the stopping muon tracks, the restrictions imposed in Pass I hit association described in section 4.4.2 are slightly modified. For every hit h_i from the main view with an associated candidate hit h_i^c from the complementary view, the following quantity is computed:

$$\Delta_i \equiv \frac{1}{2}\left(\frac{W(h_i^c) - W(h_{i-1}^c)}{W(h_i) - W(h_{i-1})} + \Delta_{i-1}\right) \tag{5.1}$$

where $W(h)$ represents the wire coordinate of hit h; h_{i-1} and h_{i-1}^c are, respectively, the previously matched hit from the main view and its associated hit from the secondary view; and Δ_{i-1}

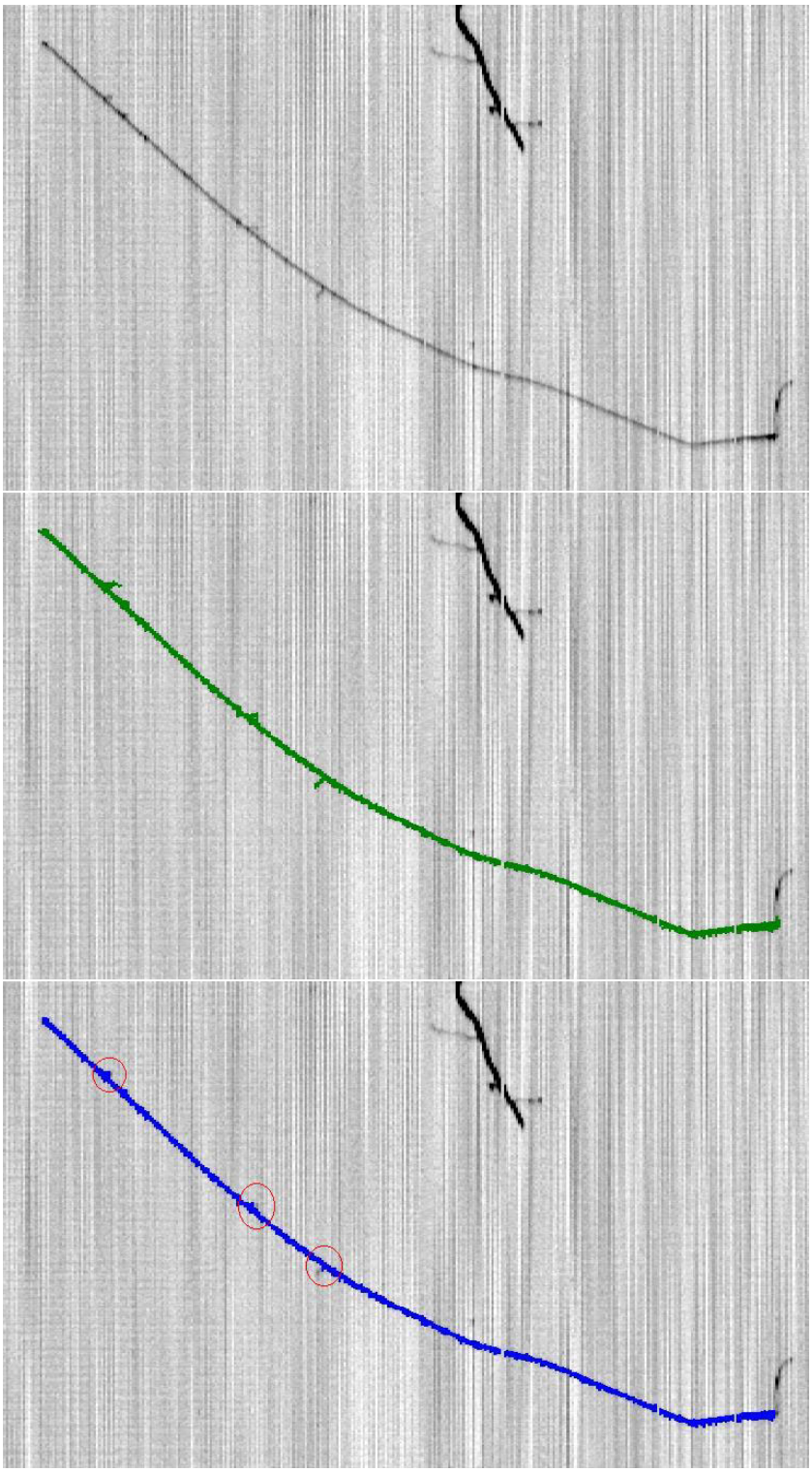

Figure 5.2: Run 961, Event 50, Right chamber, Collection view. Exemplification of δ-ray rejection on muon track reconstruction. The pictures show the signal in a selected region of the drift coordinate (vertical) vs. wire (horizontal) plane containing the muon track. Top: mapping of the output signal. Middle: superimposed, the position of all reconstructed hits in cluster containing the muon track. Bottom: superimposed, the position of reconstructed hits in the muon track; marked are the rejected hits corresponding to δ-rays.

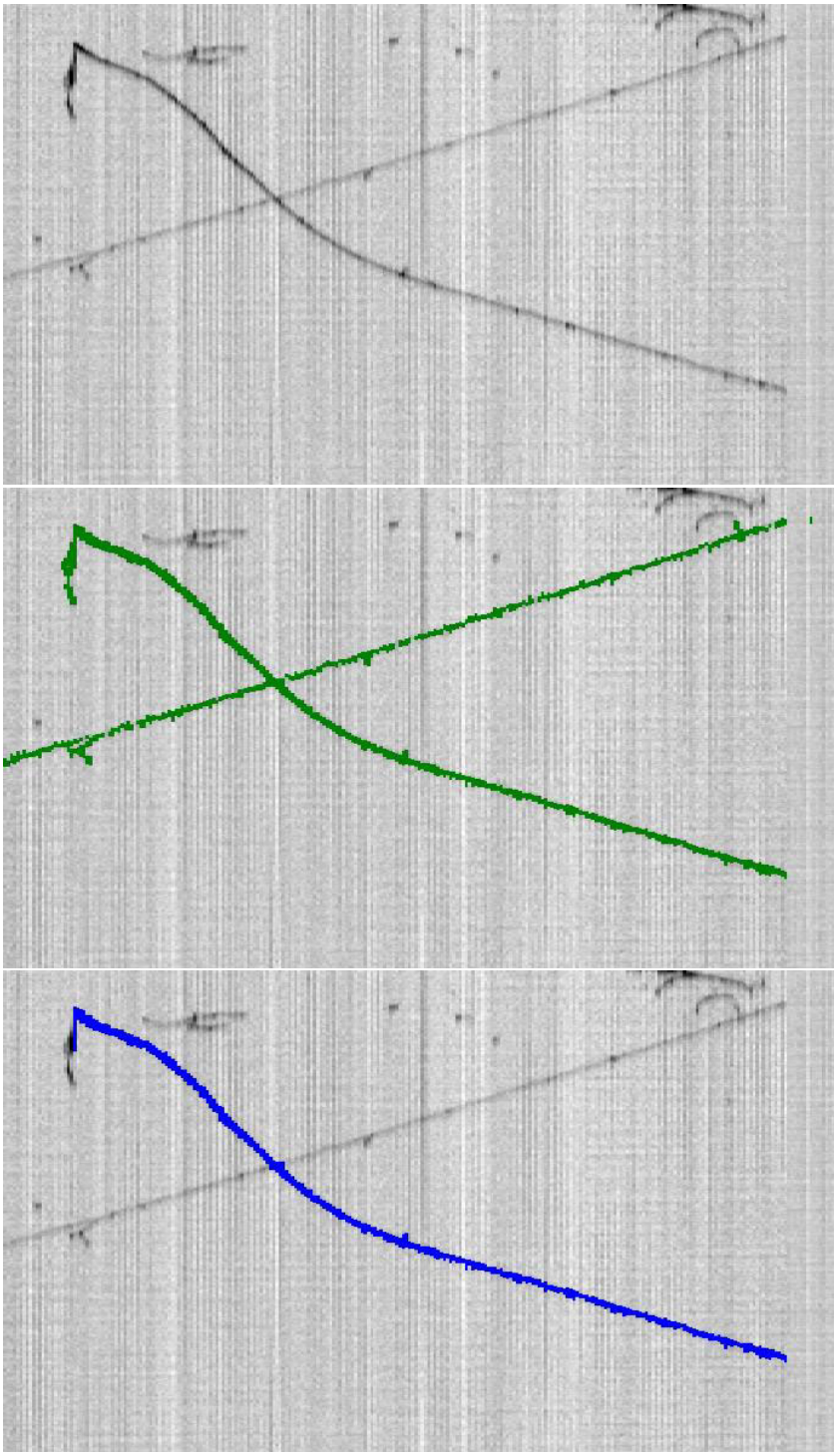

Figure 5.3: Run 966, Event 28, Left chamber, Collection view. Exemplification of crossing track rejection on muon track reconstruction. The pictures show the signal in a selected region of the drift coordinate (vertical) vs. wire (horizontal) plane containing the muon track. Top: mapping of the output signal. Middle: superimposed, the position of all reconstructed hits in cluster containing the muon and electron tracks. Bottom: superimposed, the position of reconstructed hits in the muon track.

Parameter	Value
maxdist	10
wfcut	2
nhitsline	3
maxlinedist	7 mm

Table 5.2: Values of the free parameters of the muon track spatial reconstruction algorithm.

the value of Δ associated to the hit h_{i-1}. If $W(h_i) = W(h_{i-1})$, then $\Delta_i = \Delta_{i-1}$ by definition. Δ quantifies the increment in the wire coordinate of the complementary view per increment in the wire coordinate of the main view, during the association of the hits belonging to a track. For approximately straight line tracks, this quantity is expected to remain approximately constant. Since muon tracks may be locally approximated by straight lines, the use of Δ decreases the number of muon hit missassociations. Let h_i be a hit linked to a hit h_{i-1}, associated to h^c_{i-1}. The following selection criteria are imposed to the associated hit candidates (h^c_i):

- The difference in the wire coordinates of hits h^c_i and h^c_{i-1} must be smaller than *maxdist* (see table 5.2) and the following condition must be fulfilled:

$$\frac{\Delta_i}{|\Delta_i|} = \frac{\Delta_{i-1}}{|\Delta_{i-1}|} \tag{5.2}$$

  (for $\Delta = 0$ the condition is true by definition)

- Among all found candidates fulfilling previous condition, h_i is associated to the one whose *drift* coordinate is the closest to the one of h_i (considering the expected shift –see section 4.4.2).

- If no hit candidate remains, the selection procedure is repeated suppressing condition 5.2.

If no associated hit candidate remains after the previous selection process, or if hit h_i is not linked to any associated hit, we apply the following criteria:

- The associated hit candidate, h^c_i, must fulfill the following condition:

$$\begin{aligned} (1 - wfcut) \cdot \Delta_{i-1} \leq \quad \Delta_i \quad \leq (1 + wfcut) \cdot \Delta_{i-1} \qquad \text{for } \Delta_i \geq 0 \\ (1 + wfcut) \cdot \Delta_{i-1} \leq \quad \Delta_i \quad \leq (1 - wfcut) \cdot \Delta_{i-1} \qquad \text{for } \Delta_i < 0 \end{aligned} \tag{5.3}$$

  where the value of the parameter *wfcut* is shown in table 5.2. That is, Δ must not change by a big factor from one link to a neighbouring one.

- Among all found candidates fulfilling previous condition, h_i is associated to the one whose drift coordinate is the closest to the one of h_i (considering the expected shift –see section 4.4.2).

- If no associated hit candidate remains, the selection process is repeated replacing condition 5.3 by the following one:

$$|W(h^c_i) - W(h^c_{i-1})| < maxdist \tag{5.4}$$

Pass II

Spatial reconstruction Pass II algorithm is also slightly changed with respect to the general algorithm described in section 4.4.2, in order to profit from the geometrical features of the muon track. The modified algorithm loops over all hits associated in Pass I, proceeding as follows:

- For every hit h, the *nhitsline* matched hits in both directions (toward the muon initial and end points) are used to build, by linear regression, a straight line in the $x-z$ plane. The distance from the hit projection in the $x-z$ plane to the fitted line is computed. If the distance is greater than *maxlinedist*, the hit is flagged for an ulterior reassignment of the spatial coordinates, and is not used in the linear regression of other hits' associated lines. The values of the free parameters are shown in table 5.2.
- In a second loop over the track hits, the spatial coordinates of the flagged hits are corrected minimizing, as a function of the wire coordinate of the associated hit, the distance to the reference straight line.

Pass III

Pass III remains unchanged with respect to the general scheme described in section 4.4.2, except for the fact that a single hit loop is performed, from the muon starting point to the muon end point (both provided as an input to the spatial reconstruction algorithm). The hit coordinate assignments are performed as described in the previous paragraph (pass II).

Estimation of the muon track reconstruction efficiency

The efficiency of the muon track spatial reconstruction is estimated by visual scanning. Qscan provides OpenGL [53] based three dimensional representations of the reconstructed tracks, making possible the examination of the results of the event spatial reconstruction. Out of the 259 available muon tracks, 49 are not properly reconstructed, mainly because the hits are associated to hits from a wrong track in the secondary view, or because a lack of reconstructed hits corresponding to the muon track in the secondary view. The remaining 210 muon tracks sample is referred to as *good calorimetry* muon sample, since the spatial reconstruction quality allows us to perform the fully calorimetric reconstruction, including the electron lifetime and t_0 corrections (which depend on the spatial distribution of the hits), as presented later in chapter 6. Out of the good calorimetry muon sample, 45 events are reconstructed using a low number of direct associations (pass I), and most of the hits are reconstructed during passes II and III. The remaining 165 tracks are referred to as the *good spatial reconstruction* muon sample. This sample is used to determine the electron lifetime in the different data taking periods and, the subsample with identified t_0, to perform the energy calibration of the detector, presented later in chapter 6. The goodness of the spatial reconstruction is confirmed by measurements of dE/dx vs. range.

5.2.2 Kinematic variables

Once the muon track is spatially and calorimetrically reconstructed, the kinematic variables are reconstructed based on the hits' position and associated energy. In the next sections we describe how the different variables are reconstructed. The following notation will be used:

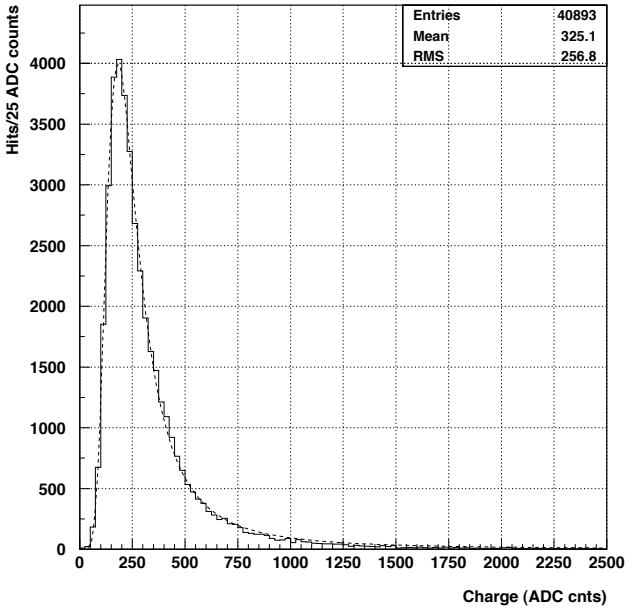

Figure 5.4: Histogram: uncorrected hit charge distribution for the whole sample of muon track hits. Superimposed in dashed: fitted convoluted Landau-Gaussian distribution.

- N: total number of hits in the muon track.
- h_i: i-th hit taken from a list where the hits are ordered from the initial ($i = 1$) to the end point ($i = N$).
- $\mathbf{r}_i$: position vector of hit h_i in the Cartesian reference system defined in section 4.4.1.

Energy deposition

The ionization charge is precisely measured in the Collection wire planes. The charge associated to a given hit is proportional to the energy deposited in the LAr by the associated muon track portion. In order to obtain the track segment energy, the charge must be corrected for the effects of the finite drift electron lifetime and the electron-ion recombination. The complete expression of the energy associated to the i-th hit (fully corrected and calibrated) is given by:

$$\boxed{E_i = \frac{CW}{R}\, e^{(t_i - t_0)/\tau_e}\, A_i} \tag{5.5}$$

where C is the calibration factor, W the average energy expended on the creation of an electron-ion pair, R the electron recombination factor, $(t_i - t_0)$ the time the electrons have drifted from the ionization point to the Collection wire planes, τ_e the drift electron lifetime and A_i the measured charge associated to the hit h_i. The uncorrected hit charge distribution for the whole sample of muon tracks is shown in figure 5.4, together with a fitted convoluted Landau-Gaussian fit.

The following comments about the different quantities entering equation 5.5 may be done:

- The calibration factor C converts the detector measuring units (ADC counts) into charge units (fC), and is obtained from a set of dedicated test pulses, simulating signals ranging

from single to several tens of minimum ionizing particles (*mip*'s) [63, 64]. Its value is:

$$C = (0.0142 \pm 3\%) \text{ fC/ADC counts} \tag{5.6}$$

The 3% uncertainty reflects the variation of the value for different wires, and is mainly due to the test capacitances nominal accuracy. CW converts charge into energy, and may be expressed in units of MeV/ADC counts as:

$$\begin{aligned} CW &= (0.0142 \pm 3\%) \text{ fC/ADC counts} \cdot \frac{(23.6^{+0.5}_{-0.3}) \cdot 10^{-6} \text{ MeV/free e}}{1.60218 \cdot 10^{-4} \text{ fC/e}} \\ &= (2.092 \cdot 10^{-3} \pm 3\%) \text{ MeV/ADC counts} \end{aligned} \tag{5.7}$$

where we have used the value of W in LAr measured by Miyajima *et al.* [65]. The calibration factor is obtained by comparing the area of the test pulse signals in the Collection wire plane with the known injected charge. The area is computed using the integral of the hit fit function (see section 4.2). In our case, in order to be consistent with the calibration procedure, we must compute the charge associated to a given hit from the area obtained with the fit method. However, for those hits with a non converging fit, convergence to unphysical parameters, or those with $\chi^2/ndf > 2$, the hit area is computed using the alternative direct ADC counting method, and scaled by a factor 0.92 as obtained in section 4.2.2.

- The recombination factor R accounts for the fraction of charge reabsorbed by the ionized atoms immediately after the passage of the ionizing particle. This factor depends on the absorber, the density of ionization electrons and the applied electric field. In practice, the recombination factor is computed by comparing the measured and the theoretically expected ionization charges for the given particle traversing the given medium. A measurement of the recombination factor as a function of the energy loss per crossed distance is performed in section 6.2.

- The exponential term in equation 5.5 accounts for the charge attenuation due to the attachment to electro-negative impurities in the LAr sensitive volume. Assuming a constant electron attachment rate proportional to the concentration of impurities, the number of electrons surviving a given time of drift is well described by a negative exponential function, characterized by a *drift electron lifetime* (τ_e) inversely proportional to the concentration of impurities. The electron lifetime can be measured by fitting a negative exponential function to the rate of collected vs. produced charge as a function of the drift time. A measurement of the electron lifetime for the different data taking periods, for the data used in the present analysis, is performed with the data themselves. The measurement method and results are reported in section 6.1.

- In order to correct for the effect of the finite electron lifetime, the drift time of the electrons from the ionization point to the wire plane ($t - t_0$) must be known. The time t_0 is normally provided by the trigger system, except for those events occurring independently within the DAQ time window (1.64 ms), called *out of time* events, which in general have an unknown associated t_0. Except for a small fraction, most of our data consists of out of time events, and a method to estimate the time t_0 has been developed. The method and its performance are described in section 6.2.2.

Crossed distance

The length of the track portion associated to a hit (hereafter called *crossed distance*) depends on the wire pitch and the orientation of the track with respect to the wire plane. It can range

from the pitch length ~ 3 mm (for track pieces parallel to the wire pitch direction) to the total drift range length ~ 1.5 m (for tracks perpendicular to the pitch direction). We approximate the hit associated crossed distance by:

$$\begin{aligned} \Delta x_i &= \frac{1}{2}(|\mathbf{r}_i - \mathbf{r}_{i+1}| + |\mathbf{r}_i - \mathbf{r}_{i-1}|) \qquad \text{for } i = 2, \ldots, N-1 \\ \Delta x_1 &= \frac{1}{2}|\mathbf{r}_1 - \mathbf{r}_2| \\ \Delta x_N &= \frac{1}{2}|\mathbf{r}_N - \mathbf{r}_{N-1}| \end{aligned} \tag{5.8}$$

Energy loss per crossed distance (*dE/dx*)

Moderately relativistic muons lose energy in matter primarily by ionization. The theoretical mean energy loss per crossed distance or *stopping power* is given by the Bethe-Bloch equation [14, 25, 66]:

$$-\frac{dE}{dx} = 2\,\pi\,N_a\,r_e^2\,m_e c^2\,\rho\,\frac{Z}{A}\,\frac{1}{\beta^2}\left[\ln\frac{2\,m_e c^2\,\gamma^2\,\beta^2\,W_{max}}{I^2} - 2\,\beta^2 - \delta\right] \tag{5.9}$$

with N_a Avogadro's number; r_e and m_e the electron classical radius and mass; the density of LAr is $\rho = 1.4$ g/cm^3, the mean excitation potential $I = 188$ eV, the atomic weight $A = 39.95$ and the atomic number $Z = 18$; β is the muon velocity (in units of c), and $\gamma = 1/\sqrt{1-\beta^2}$; W_{max} is the maximum energy transfer in a single muon-electron collision, given by:

$$W_{max} = \frac{2\,m_e c^2\,\eta^2}{1 + 2s\sqrt{1+\eta^2} + s^2} \tag{5.10}$$

where $s = m_e/m_\mu$ and $\eta = \beta\gamma$. δ is the density effect parameter, which can be approximated by [14, 66]:

$$\delta = \begin{cases} 0 & X < X_0 \\ 2\ln(10)X + C + a(X_1 - X)^m & X_0 < X < X_1 \\ 2\ln(10)X + C & X > X_1 \end{cases}$$

where $X = \log_{10}(\beta\gamma)$ and the remaining constants have, for LAr, the following values [67]: $X_0 = 0.201$, $X_1 = 3$, $m = 3$, $a = 0.196$ and $C = -5.217$.

It is also of interest to consider the mean energy loss excluding energy transfers greater than some cutoff T_{cut} (*truncated* mean energy loss) [14]:

$$-\left.\frac{dE}{dx}\right|_{T<T_{cut}} = 2\,\pi\,N_a\,r_e^2\,m_e c^2\,\rho\,\frac{Z}{A}\,\frac{1}{\beta^2}\left[\ln\frac{2\,m_e c^2\,\gamma^2\,\beta^2\,T_{upper}}{I^2} - \beta^2\left(1 + \frac{T_{upper}}{W_{max}}\right) - \delta\right] \tag{5.11}$$

where T_{upper} is the minimum between T_{cut} and W_{max}, so that the equation reproduces the Bethe-Bloch equation for $T_{cut} > W_{max}$. In practice, the cut-off T_{cut} is given by the energy threshold for δ-ray detection.

In our case, the energy loss per crossed distance measured at every hit is approximated by:

$$\left(-\frac{dE}{dx}\right)_i = \frac{E_i}{\Delta x_i} \tag{5.12}$$

with E_i and Δx_i the energy (equation 5.5) and crossed distance (equation 5.8) associated to hit h_i. As we mentioned in section 5.2.1, detected δ-rays are removed from the muon track during the

spatial reconstruction, and therefore expression 5.11 must be used to compare the mean energy loss measured by expression 5.12 with theory. The value of T_{cut} depends on the δ-ray detection threshold, which in our case depends strongly on both the energy and the spatial orientation of the δ-ray with respect to the muon track. Essentially, δ-rays with enough energy and sufficiently separated from the muon track so that the spatial reconstruction algorithm separates them, are discarded, whereas the remaining are accounted as part of the muon track. In principle one could reassign the energy of the identified δ-ray tracks to the hit where the emission is produced, hence eliminating the effect of the cut-off except for the geometrical effects[1]. Such a procedure is not carried out in the present work. A determination of the average δ-ray detection threshold is computed in section 6.2.4.

Range and kinetic energy

The range of the muon at a given point is defined as the length of the path crossed by the muon from the considered point until it completely stops. We can approximate the range measured at a given hit h_a by:

$$R_a = \sum_{i=a}^{N} \Delta x_i \tag{5.13}$$

The track length is therefore given by

$$L \equiv R_1 \tag{5.14}$$

On the other hand, the muon kinetic energy measured at a given hit h_a is obtained by adding the energy depositions measured from the given hit to the muon stopping point:

$$T_a = \sum_{i=a}^{N} E_i \tag{5.15}$$

The mean muon kinetic energy can be obtained from the range value, by integration of equation 5.9 along the muon path. The result of such an integration for range values up to 5 m is shown in figure 5.5 (left). The right side figure (solid line, left axis) shows the expected mean energy loss per crossed distance (dE/dx) vs. the kinetic energy obtained from equation 5.9 (no δ-ray detection threshold is considered); dots (right axis) show the measured charge per crossed distance dQ/dx (no lifetime nor recombination corrections applied) vs. the kinetic energy computed from the range, measured at the hits from three muon tracks. Even before corrections the shape is similar to the expected one.

Direction. Track segmentation

The direction of the muon, measured at a hit h_i, is defined in first approximation by the unit vector in the direction joining the positions of h_i and h_{i+1}:

$$\mathbf{d}_i = \frac{\mathbf{r}_{i+1} - \mathbf{r}_i}{|\mathbf{r}_{i+1} - \mathbf{r}_i|} \tag{5.16}$$

The error of the muon direction determination yielded by this method can be approximated by:

$$\Delta\theta_{meas} = \frac{\Delta d}{p} \simeq \frac{0.4\text{mm}}{3\text{mm}} \simeq 0.13 \text{ rad} \tag{5.17}$$

[1] If the δ-ray is overlapped to the muon track it is not possible to distinguish it from the muon track, and it contributes to the dE/dx of the muon with an additional mip along its range.

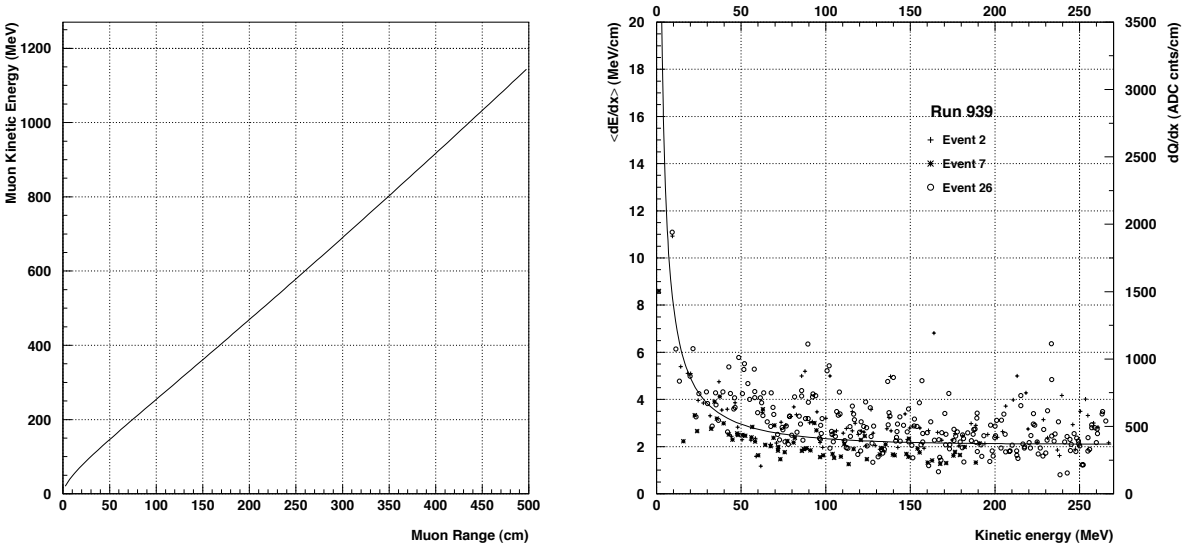

Figure 5.5: Left: Theoretical mean muon kinetic energy vs. range from numerical integration of equation 5.9. Right: in solid (left axis), theoretical mean energy loss (dE/dx) vs. kinetic energy for muons; dots (right axis), uncorrected ionization charge per crossed distance measured at the hits of three different muon tracks, the kinetic energy is estimated using the range.

where Δd is the resolution in the drift coordinate [41], and p the wire pitch. In order to reduce this error, hits can be grouped into *segments* of several consecutive hits. The direction of the muon at a given segment is given by the vector joining the positions of the first hit from the considered and next segments. The error in the determination of the muon direction can then be approximated by:

$$\Delta\theta_{meas} = \frac{\Delta d}{x} \tag{5.18}$$

where x is the length of the segment, selected by imposing $\Delta\theta_{meas}$ to be equal to the expected variation of the muon direction due to the multiple Coulomb scattering. The Coulomb scattering angle distribution is described by Molière's theory [68]. The distribution is approximately Gaussian at the peak, with a width given by:

$$\Delta\theta_{scat} = \sqrt{2}\,\frac{13.6\ \text{MeV}}{\beta c\, p}\sqrt{x/X_0}\,[1 + 0.038\ln(x/X_0)] \tag{5.19}$$

where βc and p are the muon velocity and momentum, respectively; x is the LAr length crossed by the muon; and $X_0 = 14$ cm the LAr radiation length. Therefore, the segment length is computed so that the following condition is fulfilled:

$$\Delta\theta_{meas} \simeq \Delta\theta_{scat} \tag{5.20}$$

Keeping only the term proportional to $\sqrt{x/X_0}$ in expression 5.19, we obtain:

$$x = \left(\frac{\Delta d\,\sqrt{X_0}\,\beta c\, p}{19.2\ \text{MeV}}\right)^{2/3} \tag{5.21}$$

The momentum entering the previous formula is approximated by:

$$p_i = \sqrt{T_i^2 + 2T_i\, m_\mu c^2} \tag{5.22}$$

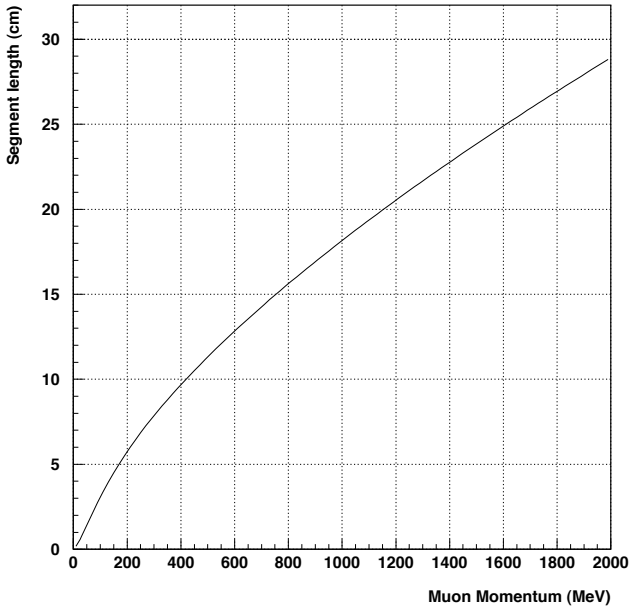

Figure 5.6: Optimal segment length (see the text) as a function of the muon momentum.

where T_i is the kinetic energy at the given hit estimated from the range. Figure 5.6 shows the segment length as a function of the muon momentum obtained from equation 5.21.

In order to build the segments of a muon track, hits are looped over, starting from the muon end point to the initial hit. The length of a given segment is computed by means of equation 5.21 using the momentum measured at the segment's initial hit. All subsequent hits h_i fulfilling the condition

$$0 \leq R_i - R_1 < x \tag{5.23}$$

(with R_i and R_1 the range at h_i and the segment initial hit, respectively), are used to build the segment. The first hit not used in a particular segment construction is the initial hit for the next segment.

Angles θ and ϕ (see figure 4.19) defining the track direction at a given point can be computed using the direction vectors:

$$\begin{aligned} \theta_i &= \arccos\left(d_i^x\right) \\ \phi_i &= \arccos\left(\frac{d_i^y}{\sqrt{(d_i^y)^2 + (d_i^z)^2}}\right) \end{aligned} \tag{5.24}$$

where the index i may refer to a hit or a segment, and $\mathbf{d}_i = \{d_i^x, d_i^y, d_i^z\}$ is the corresponding associated direction vector. Figure 5.7 shows the comparison of the measured values of ϕ along the muon track hits (left) and segments (right), for three different tracks. The scattering is very much reduced due to the better muon direction determination obtained from the segments.

All kinematic variables can be recomputed at the muon segments. The energy deposition associated to a given segment is the sum of the corresponding values for the hits belonging to the segment, whereas the crossed distance is approximated by the segment length. The remaining variables are computed based on the segments in a way equivalent to the one used

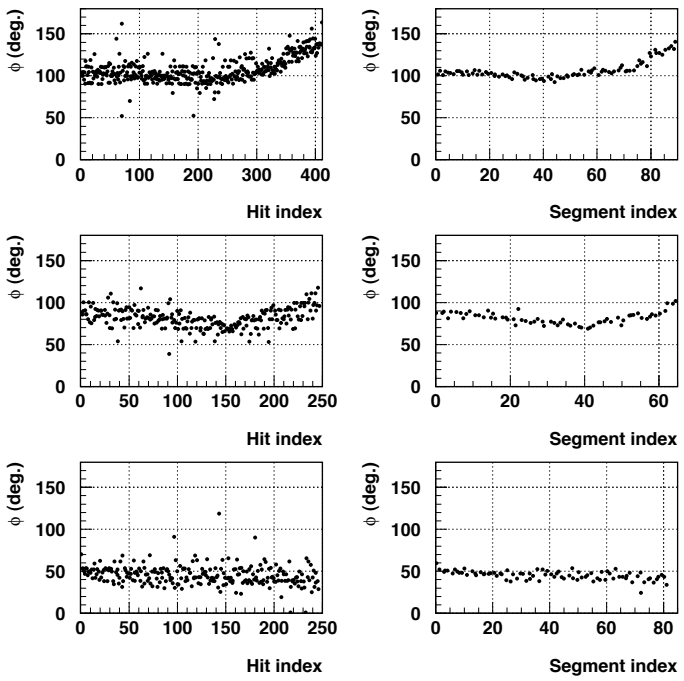

Figure 5.7: Comparison of measured ϕ values along the hits (left) and segments (right) of three muon tracks.

for the hits. Figure 5.8 shows, as an example, the comparison of the expected mean energy loss (dE/dx) and the measured charge per crossed distance (dQ/dx) as a function the kinetic energy (from the range), for the segments from three different muon tracks.

5.3 Electron reconstruction

5.3.1 Spatial reconstruction

For the electron spatial reconstruction, we use the same algorithm as in the case of the muon (section 5.2.1). The few exceptions are summarized in the present section.

As in the muon track reconstruction, the algorithm is seeded by the coordinates of the electron initial and end point hits in the main view. The electron end point is determined by visual scanning and provided as an input to the spatial reconstruction algorithm. On the other hand, the initial hit is automatically determined as the first hit not belonging to the muon track found when going from any of the muon track hits to the electron final hit following the links. This definition imposes the condition that no more than one electron hit can be linked to the muon track, in which case, the electron is not reconstructed and the muon is treated as an absorption event.

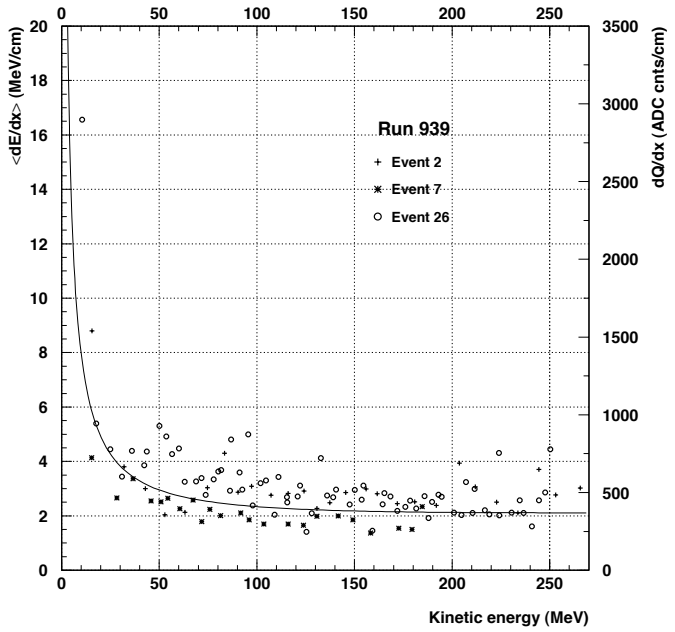

Figure 5.8: In solid (left axis), theoretical mean energy loss (dE/dx) vs. kinetic energy for muons. Dots (right axis), ionization charge per crossed distance measured from the segments of three different muon tracks, the kinetic energy is estimated using the range.

Pass I

During Pass I, a first loop over all hits belonging to the muon/electron cluster is performed. All hits between the electron initial and final hits (where a hit h_i is *between* two other hits h_a and h_b when the paths followed to go from h_i to h_a and h_b, are different) are considered as part of the electron track. Therefore, events with one or more tracks crossing the electron in the main view cannot be spatially reconstructed by this method, since all the hits belonging to the crossing track would be considered as part of the electron track. These types of event are identified during the visual scanning, and only the muon track is used, treated as an absorption event.

During the association, selected hits are looped over, starting from the initial hit and following the links leading to the specified final hit. Hits from the complementary view already used in the association of muon track hits are discarded.

Pass II

Pass II is skipped for electron tracks, since the algorithm is based on the assumption that tracks can be locally approximated by straight lines (which is true for most of the muon tracks, but not for electrons).

Pass III

Pass III algorithm for electron tracks is identical to that for muon tracks.

Estimation of the electron track reconstruction efficiency

As in the muon sample, the efficiency of the electron track spatial reconstruction is visually estimated using Qscan and a posteriori confirmed by the comparison of different quantities relying on the reconstruction quality with the theoretical expectations. Out of the 259 initial events, 25 are either absorption events or have an electron track overlapped to another track (in some cases, the muon). The electron track is discarded for the latter kind of events. Out of the remaining 234 electron tracks, 59 yield a deficient spatial reconstruction, mainly due to the lack of electron hits reconstructed in the secondary view, or the association with hits from the wrong track in the secondary view. The remaining 175 electron tracks are referred to as *good calorimetry* electron sample, since they can properly be corrected for the drift electron lifetime and t_0 effects, as presented later in chapter 6. Out of the good calorimetry electron sample, 38 events yield a poor spatial reconstruction quality due to the low fraction of hit associations between the main and secondary views. The 137 remaining events are referred to as *good spatial reconstruction* electron sample, used in the study of the electron angular distribution and range in chapter 6.

5.3.2 Kinematic variables

Electron initial and end points

It is useful to define the following notation:

- N: total number of hits in the electron track.
- h_i: i-th hit taken from a list where the hits are ordered from the initial ($i = 1$) to the end point ($i = N$).
- $\mathbf{r}_i$: position vector of hit h_i in the Cartesian reference system defined in section 4.4.1.

Energy deposition, crossed distance and range

The electron energy deposition is measured at every hit using a procedure identical to that used for the muon tracks (see section 5.2.2). Figure 5.9 shows the uncorrected hit charge distribution of the whole sample of electron track hits (234 events).

Expression 5.8 must be generalized in order to compute the effective crossed distance associated to a hit h_i in the case of hits with more than two associated links. The following expression is used:

$$\Delta x_i = \frac{1}{2} \sum_{j=1}^{n_i} (|\mathbf{r}_i - \mathbf{r}_j|) \tag{5.25}$$

where n_i is the number of hits linked to h_i and $\mathbf{r}_j$ the position vector of the j-th linked hit.

Range and track length are computed by means of equations 5.13 and 5.14.

Energy loss per crossed distance (dE/dx)

The difference of the electron/positron dE/dx with respect to that of the muons is basically due to the smaller mass of the former and, in the case of electrons, to the identity between the

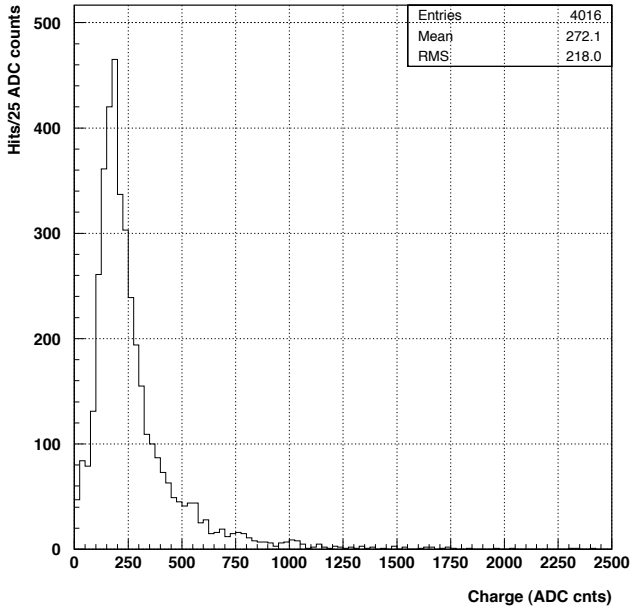

Figure 5.9: Uncorrected hit charge distribution for the whole electron track sample.

incoming and the atomic electrons. The total energy loss per crossed distance of electrons and positrons is composed of two parts:

$$-\left(\frac{dE}{dx}\right)_{tot} = -\left(\frac{dE}{dx}\right)_{ion} - \left(\frac{dE}{dx}\right)_{rad} \tag{5.26}$$

where the first term is the contribution from the ionization losses, and the second term is due to radiation losses.

Electrons and positrons of low energies (below ~ 50 MeV) mainly lose energy by ionization, with a rate given by the Bethe-Bloch formula for electrons/positrons [66, 69, 70]:

$$-\left(\frac{dE}{dx}\right)_{ion} = 2\,\pi\,N_a\,r_e^2\,m_e c^2\,\rho\,\frac{Z}{A}\,\frac{1}{\beta^2}\left[\ln\frac{\tau^2(\tau+1)}{2(I/m_e c^2)^2} + F(\tau) - \delta\right] \tag{5.27}$$

where τ is the kinetic energy in units of $m_e c^2$, and $F(\tau)$ is given by

$$\begin{aligned} F(\tau) &= 1 - \beta^2 + \frac{\tau/8 - (2\tau+1)\ln 2}{(\tau+1)^2} && \text{for } e^- \\ F(\tau) &= 2\,\ln 2 - \frac{\beta^2}{12}\left(23 + \frac{14}{\tau+2} + \frac{10}{(\tau+2)^2} + \frac{4}{(\tau+2)^3}\right) && \text{for } e^+ \end{aligned} \tag{5.28}$$

The remaining quantities are described in equation 5.9. Figure 5.10 shows the rate of energy loss by ionization for electrons and positrons (top) and the difference between them (bottom). In the energy range between 1-50 MeV, the difference between electron and positron dE/dx values is about or less than 3%. Since no distinction between positrons and electrons is made in the present work, and the number of positrons to electrons is expected to be about 5:1, we consider hereafter the expression for positrons[2]. This introduces a systematic error in the theoretical

[2]The ratio μ^+/μ^- at sea level is between 1.2-1.3 depending on the geomagnetic latitude [71, 72], and only about 27% of the μ^- produce decays [60, 61, 62].

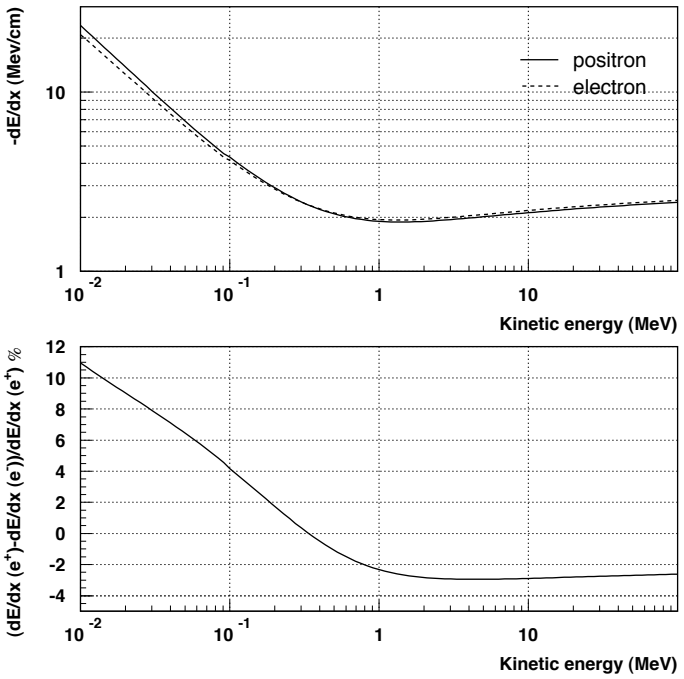

Figure 5.10: Top: Energy loss per crossed distance by ionization in LAr for electrons and positrons. Bottom: difference between the energy loss per crossed distance by ionization in LAr for electrons and positrons.

energy loss per crossed distance of about 0.6% which must be taken into account, mainly when computing the electron kinetic energy from the range. As will be shown later (see section 6.3.4) this effect is completely negligible.

The energy loss by ionization grows logarithmically with the electron energy. On the other hand, bremsstrahlung radiation losses increase linearly with the electron energy. The critical energy, i.e. the energy at which the collision and radiation losses are equal is about 50 MeV for LAr. Given the muon decay electrons energy range (0–53 MeV), radiation losses constitute a non negligible fraction of the total energy loss of electrons in LAr (see table 5.3), and must be taken into account. The expected rate of energy loss by radiation is given by:

$$-\left(\frac{dE}{dx}\right)_{rad} = N \int_0^{\nu_0} h\nu \, \frac{d\sigma}{d\nu}(E_0, \nu)\, d\nu \tag{5.29}$$

with N the density of atoms, $\frac{d\sigma}{d\nu}(E_0, \nu)$ the cross section for an electron with energy E_0 radiating a photon of energy $h\nu$, and $\nu_0 = E_0/h$. In the present work we use the values of the energy loss by radiation tabulated by the National Institute of Standards and Technology [73].

Table 5.3 shows the partial and total energy losses for several electron kinetic energies in the Michel spectrum range. Figure 5.11 (left) shows the total rate of energy loss in LAr and the different partial contributions for positrons (and electrons with a precision better than 3%) in the Michel spectrum energy range. Both, positrons and electrons, will hereafter be referred to as electrons.

In our case, the ionization energy loss is measured using equation 5.12. Radiation energy losses

Energy (MeV)	$(dE/dx)_{ion}$ (MeV/cm)	$(dE/dx)_{rad}$ (MeV/cm)	$(dE/dx)_{tot}$ (MeV/cm)
5	2.0	0.16	2.2
10	2.1	0.36	2.5
20	2.2	0.79	3.0
30	2.3	1.2	3.5
40	2.3	1.7	4.0
50	2.3	2.2	4.5

Table 5.3: Partial and total energy loss for electron of various energies.

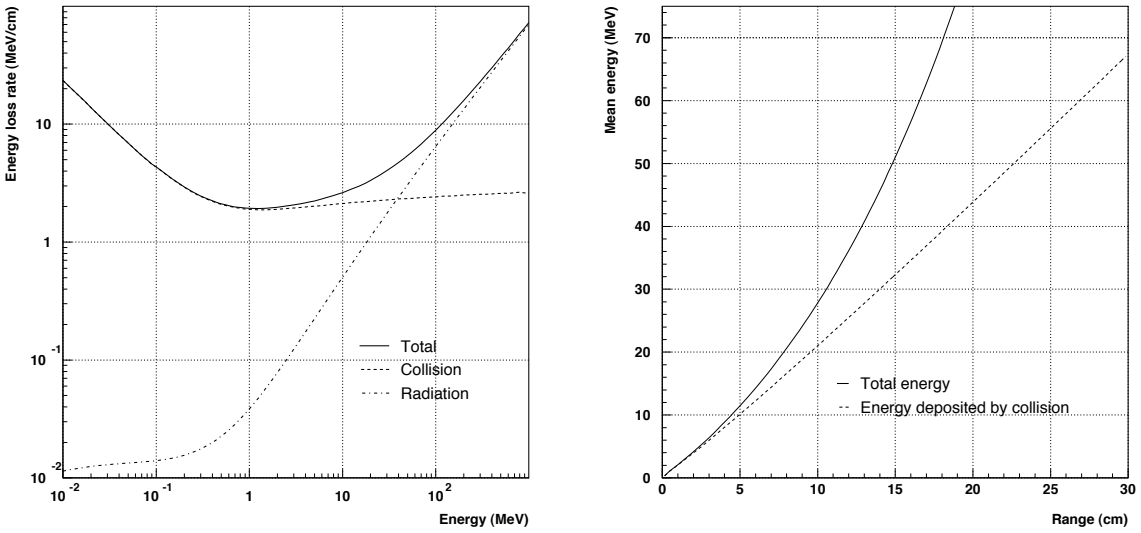

Figure 5.11: Left: Total (solid), collision (dashed) and radiation (dashed/dotted) electron energy loss per crossed distance in LAr. Right: Mean electron total energy loss (solid) and energy deposited by collision (dashed) as a function of the electron track range (from numerical integration of equations 5.26 and 5.27, respectively).

cannot be measured at every hit since, although the energy of the bremsstrahlung photons can be measured (see later section 5.4), the emission point is not determined.

Total kinetic energy

The electron/positron total kinetic energy is approximated by the following expression:

$$T = \sum_{i=1}^{N} E_i + \sum_{j=1}^{N_B} T_j^B \tag{5.30}$$

where the first sum loops over the electron track hits, and the second over the tracks associated to bremsstrahlung photons; E_i is the energy associated to the i-th hit of the electron track (see equation 5.5), and T_j^B the energy associated to the j-th bremsstrahlung photon. Reconstruction of bremsstrahlung photon tracks is described in detail in the next section.

The mean electron kinetic energy can be computed from the electron range, through integration of equation 5.26 along the electron path with both, the collision and radiation losses, included. Similarly, the mean energy deposition through collision can be obtained from integration of equation 5.27 only. The result of such integrations for electron ranges up to 30 cm are shown in figure 5.11 (right). An extensive analysis of the performance of the energy determination through the electron range is carried out in section 6.3.4.

5.4 Reconstruction of bremsstrahlung photons

Identification and reconstruction of bremsstrahlung photons is of utmost importance since, as we pointed out in the previous section, a substantial fraction of the electron kinetic energy is lost by radiation.

The behaviour of photons in matter is different from that of charged particles. Photons lose energy mainly due to absorption by atomic electrons (photoelectric effect), scattering with atomic electrons (Compton scattering) or electron/positron pair production. The photoelectric effect can be neglected in the present analysis since the energy range at which this process has any significance is well below the detector energy detection threshold. Compton scattering produces an electron in the final state with kinetic energy ranging from 0 to T_{max} (the most probable value), given by [14]:

$$T_{max} = h\nu \left(\frac{2\gamma}{1+2\gamma} \right) \tag{5.31}$$

where $h\nu$ is the energy of the incoming photon, and $\gamma = h\nu/m_e c^2$. T_{max} is larger than 90% of the photon energy for a photon of more than 2.3 MeV energy. This means that in our case most of the photon energy is transferred to the atomic electron, which deposits it in the LAr by ionization and secondary bremsstrahlung emissions. In the case of pair production, the total kinetic energy of the electron and positron pair is equal to the energy of the initial photon minus 1.022 MeV to account for the electron and positron masses. An additional process must be taken into account in the case of positrons. If the positron comes to rest, it will annihilate with an atomic electron, yielding two back-to-back emitted photons of 0.511 MeV each, which will remain undetected given their low energy. The cross section for annihilation in flight is given by [70]:

$$\sigma(E) = \frac{Z\pi r_e^2}{\gamma+1} \left(\frac{\gamma^2+4\gamma+1}{\gamma^2-1} \ln(\gamma + \sqrt{\gamma^2-1}) - \frac{\gamma+3}{\sqrt{\gamma^2-1}} \right) \tag{5.32}$$

which, considering positrons from muon decay in LAr, yields about 20% of positrons annihilating in flight. This process will produce a photon pair with energy equal to the positron kinetic energy plus 1.022 MeV from the electron and positron masses. The annihilation photons are produced in the same energy range as the bremsstrahlung photons, and since no distinction of these two processes is carried out, they are detected, reconstructed and processed as bremsstrahlung photons, as described in the following sections.

The identification and reconstruction of the electrons and positrons coming from the bremsstrahlung or annihilation photons is therefore of great importance, since it allows a much more accurate reconstruction of the energy of the electrons produced in the muon decay.

5.4.1 Identification and spatial reconstruction of photons

Bremsstrahlung (or annihilation) photons produced by the electron from the muon decay (hereafter called *main* electron), and those subsequently produced by secondary electrons, are identified with the electrons produced by Compton scattering or the created electron-positron pairs. The signal left by these electrons in the LAr are short tracks (called hereafter *bremsstrahlung tracks*) in the region around the main electron. Since our data were acquired on the surface of the earth, the events are not in general well isolated, and tracks produced by other charged particles may traverse the same LAr zone, producing a contamination of bremsstrahlung or bremsstrahlung-like tracks. In order to reject the highest number of these tracks, while keeping a high detection efficiency of bremsstrahlung tracks from the main electron, the selection procedure is carried out based on the geometrical features and position of the tracks.

Identification of candidate tracks

The first step in the identification of bremsstrahlung candidates is performed as part of the visual scanning phase (section 5.1.1), when all short tracks around the main electron must be included in the saved region. The second step is based on the selection of the candidates according to their position with respect to the electron track.

In order to determine the spatial coordinates of the candidate, the search of associations with the secondary view is carried out at the level of the clusters, rather than hits. To this purpose, we do a loop over the whole sample of clusters from the main view, skipping the one containing the muon and electron as well as those composed of more than *maxnhits* hits. Out of the remaining clusters, those not having an associated partner in the secondary view (defined below) are discarded. The constraint on the number of hits rejects tracks produced by other particles, different from bremsstrahlung photons, whereas the requirement of association with the secondary view rejects fake tracks produced by electronic noise, and allows further selection based on the tracks position in space, relative to the main electron track.

For a given cluster (c) the search for an associated partner proceeds as follows:

- The associated hit candidates (see section 4.4.2) corresponding to each hit in c are identified. Secondary view clusters with multiplicity greater than that of c by more than *maxnhitsdiff* hits are discarded. Secondary view clusters containing hits associated to the muon or main electron tracks are discarded.
- The associated cluster is the one providing the maximum number of hit associated candidates in the previous step. If no possible association is found for any of the hits, c is discarded as bremsstrahlung track candidate. Otherwise, a bremsstrahlung track candidate is built out of the hits in c.
- The hits from the created bremsstrahlung track are associated to the hits of the cluster associated partner, or any other secondary cluster at a distance of less than *clusnmax* wires.
- The remaining unassociated hits are spatially reconstructed using the hit 3D reconstruction pass III algorithm described in section 4.4.2.

The values of the free parameters used in the identification and reconstruction of bremsstrahlung track candidates are quoted in table 5.4.

Parameter	Value
maxnhits	25
maxnhitsdiff	8
clusnmax	5

Table 5.4: Values of the constant parameters used for bremsstrahlung candidate identification.

Spatial selection

Once the bremsstrahlung track candidates have been identified, further selection criteria are applied, based on their position relative to the main electron track, in order to increase the rejection of tracks produced by other particles, different from the main electron bremsstrahlung photons.

Due to momentum conservation, bremsstrahlung photons are expected to be emitted within a cone with the direction of the electron as axis and an opening angle depending on the inverse electron energy, at the emission point. In practice, the emission point is not known, and the bremsstrahlung selection is carried out based on a generic electron direction, defined as:

$$\mathbf{d}^e = \frac{\mathbf{r}_N^e - \mathbf{r}_1^e}{|\mathbf{r}_N^e - \mathbf{r}_1^e|} \tag{5.33}$$

where $\mathbf{r}_1^e$ and $\mathbf{r}_N^e$ are, respectively, the position vectors of the initial and end point electron hits. On the other hand, the direction of the bremsstrahlung emission is defined as:

$$\mathbf{d}^\gamma = \frac{\mathbf{r}_1^\gamma - \mathbf{r}_1^e}{|\mathbf{r}_1^\gamma - \mathbf{r}_1^e|} \tag{5.34}$$

where $\mathbf{r}_1^\gamma$ is the position vector of the hit from the bremsstrahlung track candidate closest to the electron initial point. The angle of the bremsstrahlung emission is approximated by:

$$\theta^\gamma = \arccos(\mathbf{d}^e \cdot \mathbf{d}^\gamma) \tag{5.35}$$

The distance of the bremsstrahlung candidate to the electron is defined as:

$$l^\gamma = |\mathbf{r}_1^\gamma - \mathbf{r}_1^e| \tag{5.36}$$

Based on these two quantities, we perform the spatial selection of bremsstrahlung candidates by imposing the following two conditions:

$$\begin{aligned} \theta^\gamma &< 40^\circ \\ l^\gamma &< 60 \text{ cm} \end{aligned} \tag{5.37}$$

The total number of selected bremsstrahlung events amounts to 66, out of the sample of the 137 events with a well reconstructed electron track.

Figure 5.12 exemplifies the identification and reconstruction of bremsstrahlung tracks. The Collection (Induction II) view is shown at the left (right) side. Top figures show a gray scale representation of the output signal in a region containing a stopping muon decay event. Muon and electron tracks are clearly identified. Various bremsstrahlung track candidates are found around the electron (see middle figures). The association between the two views allow to reconstruct the candidates in space and select them according to their position relative to the electron track. In the example (see bottom plots), one of the candidates is selected and one rejected, even if it appears closer to the electron track in one of the views.

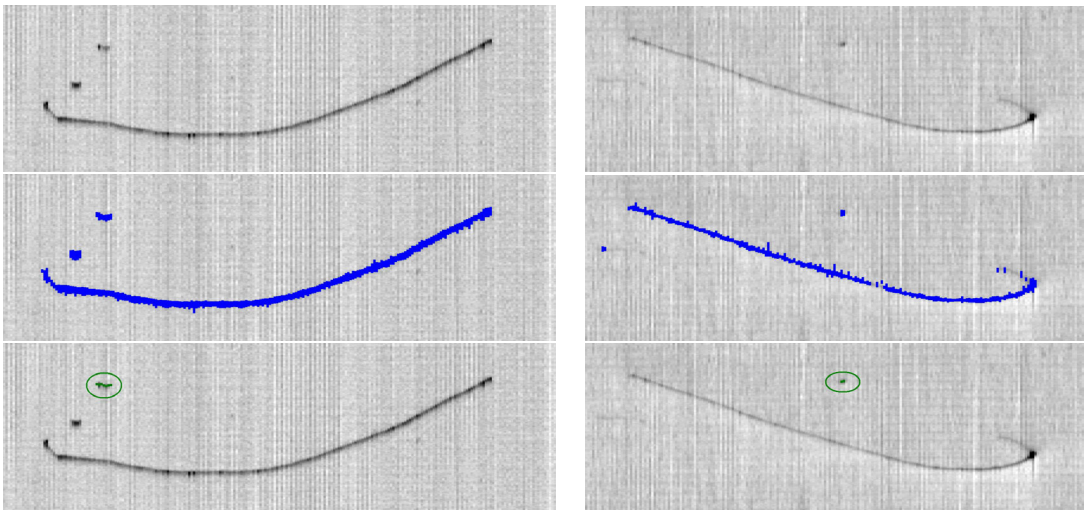

Figure 5.12: Run 961, Event 37, Left chamber. Example of bremsstrahlung track identification. Top: gray scale representation of the output signal in the wire/drift plane for Collection (left) and Induction II (right) views, for a stopping muon event. Middle: reconstructed clusters. Bottom: encircled, the reconstructed bremsstrahlung track.

5.4.2 Kinematic variables

In principle, all kinematic variables reconstructed for the main electron can be reconstructed for bremsstrahlung tracks as well. However, we are mainly interested in the total kinetic energy, (T^B) needed in the reconstruction of the main electron total energy (see equation 5.30). T_B is approximated by:

$$T^B = \sum_{i=1}^{N} E_i \tag{5.38}$$

where the sum runs over all hits in the bremsstrahlung track.

5.4.3 Evaluation of the reconstruction algorithm

The efficiency of the bremsstrahlung reconstruction algorithm is evaluated with a Monte Carlo (MC) sample containing 5000 electrons coming from muon decay.

Monte Carlo generation of decay electrons

The electrons are generated in the center of one of the chambers of the T600 half-module, and propagated in the LAr sensitive volume using FLUKA [74]. The energy deposition at every LAr cell ($3 \times 3 \times 3$ mm^3) is projected onto the different wire planes, and used to simulate the wire output signal. The signal produced by the drift electrons is simulated using the expected signal shape (see section 4.2.1) properly digitized. The wire noise is simulated with a frequency spectrum that matches the real noise spectrum present during the T600 technical run [75]. Therefore, similarly to real data, generated MC events consist of a mapping of the output signal of the wires from the different wire planes. The generated electron events are hence processed using the same reconstruction algorithm as for the real data, for electron and bremsstrahlung reconstructions, in order to check the quality of the bremsstrahlung reconstruction algorithm.

However, several important differences of the MC generation with respect to real events must be taken into account:

- The effect of the finite drift electron lifetime is not simulated.
- No out-of-time events happening in the same LAr region are simulated.
- The simulated noise corresponds to the pattern obtained from the wires with no problems such as large noise, disconnections, etc.
- All wire planes are simulated with the Collection wire plane patterns for signal and noise.

In spite of these differences, we can evaluate the real performance of the reconstruction procedure, since most biases introduced by the detector effects have been removed. A direct comparison of a more realistic MC sample with data is performed in section 6.3.1.

Reconstruction of Monte Carlo events

Generated electron tracks are reconstructed using the algorithm described in section 5.3.2, except for the method used to provide the electron initial and final points. On the one hand, since all electrons are generated at a fixed point in the detector, the initial electron hit is taken as the hit with a single link, closest to such a generation point. Differences between the generation point and the position of the electron initial hit are due to the fact that the actual generated particle is a muon at rest (and hence the finite muon lifetime may cause a shift in the drift direction), and the orientation of the electron track. On the other hand, the electron end point is selected as a hit with a single link to the cluster which contains the initial hit. If several candidates are present, the one at the largest distance with respect to the initial hit is chosen. If no hit satisfies the previous condition, the end point is taken as the hit at the greatest distance with respect to the initial hit. From this point onward, the reconstruction of MC events follows the electron and bremsstrahlung reconstruction algorithms described in sections 5.3.1 and 5.4. In 184 cases (3.6%), this procedure is not able to find any electron candidate and the event is rejected.

Results

Figure 5.13 shows some of the features of the MC bremsstrahlung tracks, namely: the distance and angle with respect to the main electron track (as defined in equations 5.36 and 5.35), hit multiplicity and energy. No selection cuts have been applied to bremsstrahlung candidates at this level. The cuts used in the bremsstrahlung selection for real events are marked in the plot. As can be seen, the selection by hit multiplicity produces no loss of efficiency, whereas in the case of the selection based on the position relative to the electron track, the long tails in the distance and angle distributions (mainly due to emission of secondary photons from the electrons produced in the primary emission), prevents the selection of all bremsstrahlung photons.

The generated electron energy spectrum (Michel spectrum) is shown in figure 5.14a. Figure 5.14b shows the distribution of the total visible energy. This is the cumulated energy of all reconstructed tracks (including the main electron), with no selection cut imposed to the bremsstrahlung tracks, and corresponds to the energy that would be reconstructed under the ideal conditions assumed in the MC generation and described above (essentially, good noise conditions and no other event tracks around the stopping muon event). The total visible energy

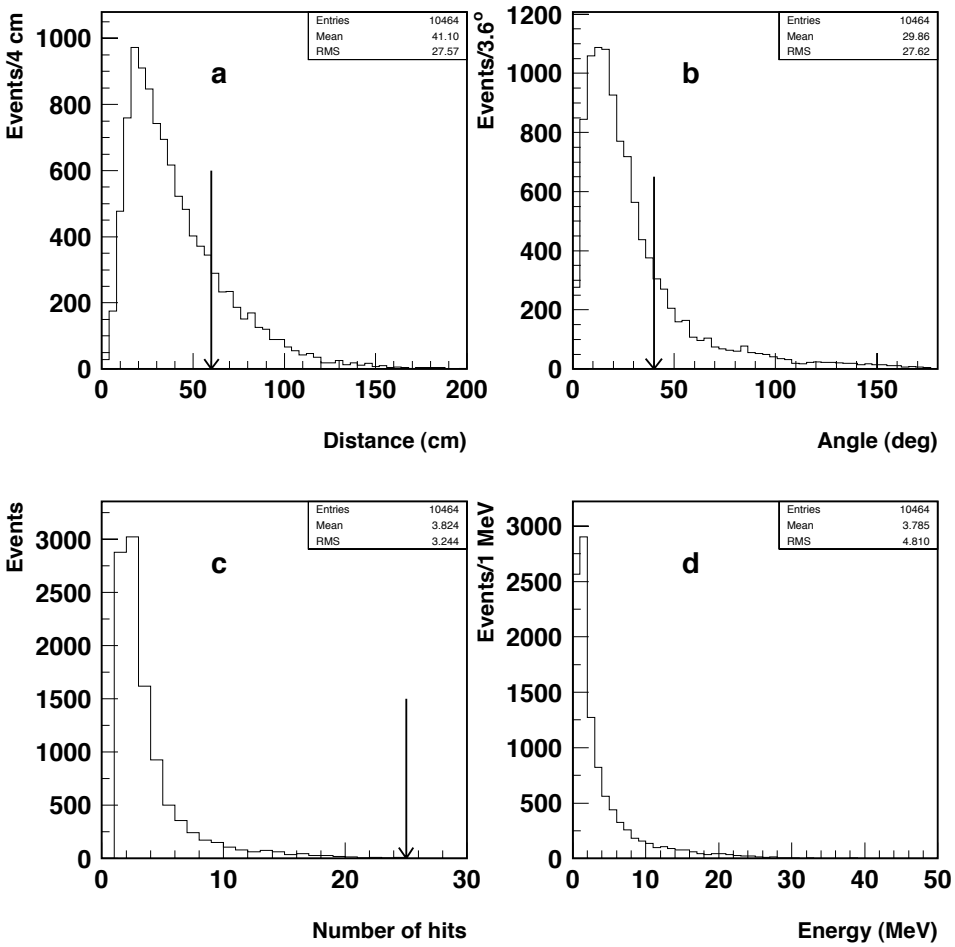

Figure 5.13: MC bremsstrahlung track features. The arrows mark the selection cuts applied for the data. a) distance bremsstrahlung-electron tracks as defined in equation 5.36; b) angle bremsstrahlung-electron tracks as defined in equation 5.35; c) number of hits in bremsstrahlung clusters; d) kinetic energy of bremsstrahlung tracks.

is on average about 6% lower than the generated energy. This shift is caused by several mechanisms: energy deposited in the detector below the detector energy threshold, photons escaping from the LAr volume and the non-accounting for the masses of the created electron/positron pairs. Figure 5.14c shows a comparison between the electron track associated energy and the total visible energies. The energy loss in this case is about 25% on average with respect to the total visible energy, as can also be seen in figure 5.14e. Figure 5.14d shows a comparison between the electron plus bremsstrahlung selected tracks (applying the data selection criteria) and total visible energies. The energy loss in this case is reduced by about a factor 2 with respect to the case where only the electron is considered, as can also be seen in figure 5.14f.

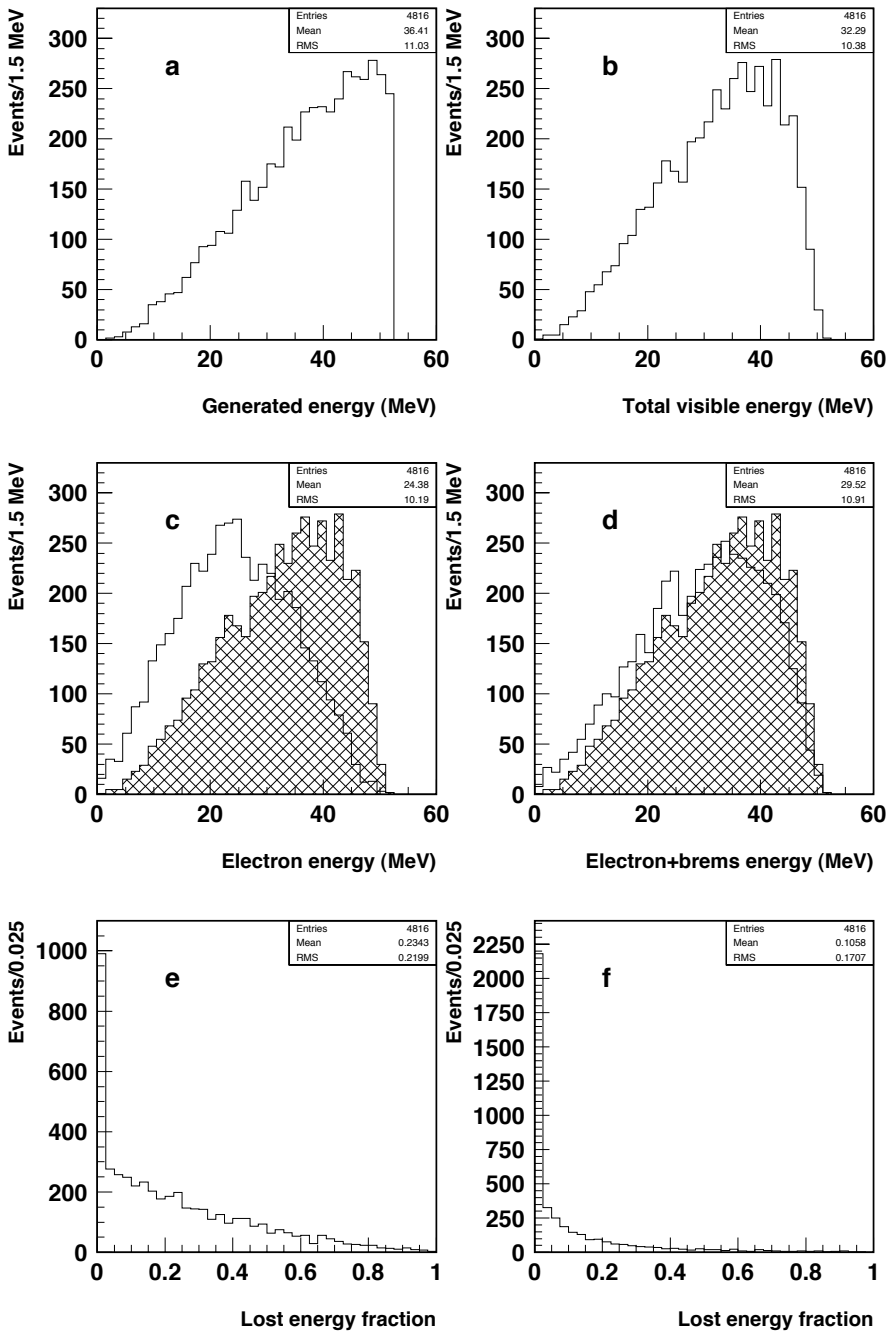

Figure 5.14: a) Distribution of the MC generated electron energy (Michel spectrum); b) Distribution of the total visible energy; defined as the cumulated energy of all reconstructed tracks; c) empty: distribution of the electron track energy; cross hatched: for comparison, distribution of the total visible energy; d) empty: distribution of the electron plus recovered bremsstrahlung tracks energy; cross hatched: for comparison, distribution of the total visible energy; e) lost fraction of the visible energy when approximating the electron energy by the electron track energy; f) lost fraction of the visible energy when approximating the electron energy by the electron plus recovered bremsstrahlung tracks energy.

Chapter 6

Data analysis

In the previous two chapters, we have extensively described the spatial and calorimetric reconstruction of tracks in ICARUS T600, and defined the different kinematic variables characterizing the stopping muon events. However (as expressed by equation 5.5), in order to complete the calorimetric reconstruction of the events, the corrections accounting for the effects of the drift electron lifetime and the electron recombination must be taken into account. In the particular case of our data sample, we must also provide a method for the estimation of t_0. Therefore, the first part of the data analysis presented in this chapter is devoted to extract the values of the drift electron lifetime, recombination factor and t_0 from the stopping muon sample, hence completing the event reconstruction. After this, we use the fully reconstructed event sample to study the electrons/positrons coming from the decay of the muon (Michel electrons). The energy spectrum is used to measure the Michel parameter ρ, which determines the type of interaction governing the decay process. We also study the angular distribution of the measured electrons. Finally, we compute the energy resolution obtained by both, the calorimetric (direct) and range based (indirect) methods, in the range [0–50] MeV, using a MC sample of muon decay electrons.

6.1 Measurement of the drift electron lifetime

The presence of electronegative impurities in the LAr active volume causes a fraction of the ionization electrons to be captured in their drift from the ionization point to the collection plane. The probability for an electron to be captured during the drift is proportional to the concentration of impurities in the LAr. Assuming a homogeneous distribution of the impurities (i.e. constant capture rate) the process of electron capture may be described by an exponential function with a characteristic time, the drift electron lifetime, depending on the LAr purity level. Within this framework, the number of surviving electrons at the time t is given by:

$$N(t) = N_0 \, e^{-(t-t_0)/\tau_e} \tag{6.1}$$

with N_0 the number of electrons released at the time $t = t_0$ (after having survived the recombination process), and τ_e the drift electron lifetime.

The drift electron lifetime was measured during the technical run by a set of dedicated purity monitor devices, and by the off-line analysis of long muon tracks [76]. The two sets of measurements are in very good agreement (see figure 6.1). In the present section, we describe a measurement of the drift electron lifetime based on the stopping muon data, which provides a precise measurement for the short data taking intervals composing the studied sample. Only muon tracks from the good spatial reconstruction muon sample (see section 5.2.1) are used.

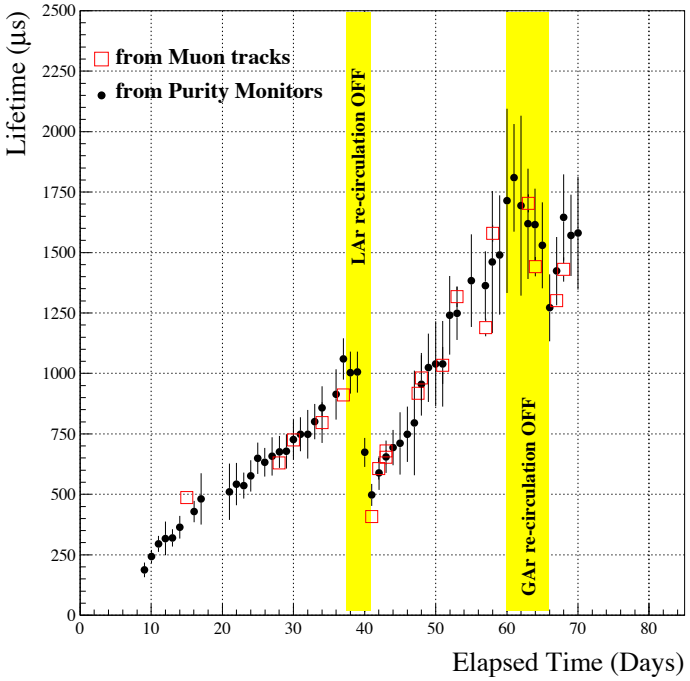

Figure 6.1: Evolution of the drift electron lifetime during the T600 technical run as measured by the dedicated purity monitors (dots) and from the off-line analysis of crossing muon tracks (squares). Shaded are two periods when the liquid and gas purification systems, respectively, were stopped.

6.1.1 Measurement method

The basic principle for the drift electron lifetime measurement is the parameterization of the attenuation of the measured hit charge as a function of the drift time by means of equation 6.1, with N_0 and τ_e being free parameters. However, several aspects must be taken into account in order to properly carry out such a parameterization.

First of all, we must choose the optimal way to quantify the measured energy loss. The energy loss fluctuations are described by the Landau distribution [77], an asymmetric distribution parameterized by the mean and most probable values. The mean value is given by:

$$\bar{\Delta} = \int_0^{\Delta x} -\frac{dE}{dx}\, dx \tag{6.2}$$

where dE/dx comes from the Bethe-Bloch formula (equation 5.11). The most probable value is given by:

$$\Delta_{mp} = \xi(\ln(\xi/\varepsilon) + 0.198 - \delta) \tag{6.3}$$

where

$$\xi = 2\pi\, N_a r_e^2\, m_e c^2\, \rho \frac{Z}{A} \left(\frac{z}{\beta}\right)^2 \Delta x \tag{6.4}$$

and

$$\ln \varepsilon = \ln \frac{(1-\beta^2) I^2}{2mc^2\beta^2} + \beta^2 \tag{6.5}$$

The remaining quantities are defined as in equation 5.9. In practice, Δ_{mp} is extracted by fitting the energy loss distribution with a Landau-Gaussian convoluted function, where the Gaussian accounts for the resolution in the charge measurement, mainly due to the electronic noise. The Landau-Gaussian convolution is defined by the following expression:

$$f(\epsilon) = \frac{K}{\sqrt{2\pi}\sigma} \int_{-\infty}^{+\infty} f_L(\epsilon')\, e^{-\frac{(\epsilon-\epsilon')^2}{2\sigma^2}}\, d\epsilon' \tag{6.6}$$

where K is an overall normalization factor depending on the statistics, σ is the width of the convoluted Gaussian distribution, ϵ the energy and f_L is the Landau distribution, given by:

$$f_L(\Delta) = \frac{1}{\xi}\,\phi(\lambda) \tag{6.7}$$

where

$$\phi(\lambda) = \frac{1}{\pi} \int_0^{\infty} e^{-u\ln u - \lambda u} \sin \pi u\, du \tag{6.8}$$

and λ is the normalized deviation from the most probable energy loss (see equation 6.3):

$$\lambda = \frac{\Delta - \Delta_{mp}}{\xi} \tag{6.9}$$

We could, in principle, parameterize the measured charge by means of either $\bar{\Delta}$ or Δ_{mp}. However, the use of the mean value presents two technical problems, one intrinsic to the definition of this quantity, the other related to the limited available statistics. On the one hand, the fluctuations of the energy loss are determined by a few high-energy δ-rays, and thus $\bar{\Delta}$ depends on the δ-ray detection threshold (T_{cut}) entering expression 5.11. This quantity is not a priori known since it has a strong dependence on the performance of the spatial reconstruction algorithm. On the other hand, since $\bar{\Delta}$ strongly depends on the Landau tail, large statistics are needed in order to significantly populate the tail and hence obtain a reliable estimation of $\bar{\Delta}$. None of the previous considerations affects the determination of Δ_{mp}, and hence, we may exploit the better reliability of this quantity to parameterize the measured charge for the different values of the drift time coordinate.

The use of Δ_{mp} as energy loss estimator presents an additional problem: while $\bar{\Delta}$ is linear with the crossed distance (Δx), as shown in equations 5.9 and 6.2, Δ_{mp} behaves as $\Delta x \ln \Delta x$, as seen from equations 6.3 and 6.4. This means that the energy loss per crossed distance measured at hits from muon segments of equal kinetic energy but different associated crossed distances yields Landau distributions with equal $\bar{\Delta}$ but different Δ_{mp} values. The effect is shown in figure 6.2, where the mean and most probable energy losses per crossed distance are plotted as a function of the muon kinetic energy for various Δx values. In order to cope with this effect, hits are selected from a narrow Δx interval containing sufficiently high statistics, and for which the $\Delta x \ln \Delta x$ dependence of Δ_{mp} is small and averaged over the considered drift coordinate range. Thus, we impose

$$0.35 < \Delta x < 0.45 \text{ cm} \tag{6.10}$$

which selects about 12000 hits ($\sim 30\%$ of the total sample).

Hits must be further selected from a kinetic energy range where both, the energy loss and the effect of the electron recombination, are expected to be roughly constant. Such a double goal is achieved by selecting hits from muon track segments whose expected mean energy loss per crossed distance (dE/dx) is below a certain threshold, close to the minimum (dE/dx_{mip}). The hits selected in such a way are ensured to be equally affected by the recombination, so that the

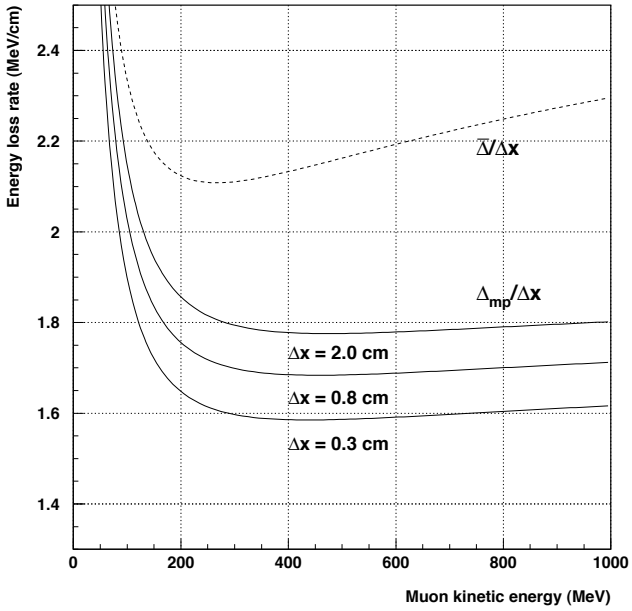

Figure 6.2: Mean (dashed) and most probable (solid) energy loss per crossed distance for various values of the crossed distance (Δx).

observed attenuation of the charge is exclusively due to the electron attachment to impurities. In addition, the selected sample can be coherently used to build the energy loss distributions with a well defined most probable value. In practice, the expected dE/dx for a given hit is computed from equation 5.9, where the needed β is obtained from the range (see equation 5.13 and figure 5.5). The minimal value of the mean energy loss is

$$\left.\frac{dE}{dx}\right|_{mip} = 2.11 \text{ MeV/cm} \tag{6.11}$$

The upper bound of the selection is fixed to $dE/dx = 2.3$ MeV. This is equivalent to select hits with a distance to the end point (range) between 35 and 200 cm. For our muon data sample, and after the selection based on Δx, we keep ~ 10000 hits.

An additional problem is introduced by the fact that different events have different (and unknown) associated t_0 values. In order to cope with this problem, we compute the charge attenuation with respect to the charge at the time t_1 ($\geq t_0$), defined as the time coordinate of the hit with the lowest drift coordinate value within the given muon track. Equation 6.1 can thus be rewritten as:

$$N(t) = N_0\, e^{-(t_1-t_0)/\tau_e}\, e^{-(t-t_1)/\tau_e} \equiv N_1\, e^{-\bar{t}/\tau_e} \tag{6.12}$$

where N_1 is the number of remaining electrons at time $t = t_1$, and $\bar{t} \equiv t - t_1$, hereafter referred to as *normalized* drift time coordinate. In terms of hit area, the previous equation yields:

$$\boxed{A = A_1\, e^{-\bar{t}/\tau_e}} \tag{6.13}$$

where A and A_1 are the signal areas corresponding to N and N_1 collected electrons, respectively. In other words, A is the area of a given hit, and A_1 the area we would have measured if the hit was at drift coordinate $t = t_1$. One could in principle think to fit equation 6.13 to the hit area

as a function of the normalized drift coordinate for every single track, obtaining the values of A_1 and τ_e. Moreover, since N_0 is given by the theory (or from *in time* events with known t_0), the value of t_0 for a given event could in principle be obtained from the fitted values of A_1 and τ_e by:

$$t_0 = t_1 - \tau_e \ln \frac{A_0}{A_1} \tag{6.14}$$

where A_0 is the hit area corresponding to N_0 collected electrons. Nevertheless, as we will show below, such a measurement is in general not possible in practice, due to the relatively low number of hits available in a single track.

By inspection of equations 6.12 and 6.13, we note that the dependence of A on t_0 is fully contained in A_1. For our selected sample of hits, A_1 would have a single common value if all tracks had an equal associated t_0 value. In fact A_1 can be arbitrarily normalized to any value since, for the determination of τ_e, we are not interested in the absolute value of A, but in its attenuation with the drift time. Therefore, for every track, we have to find a normalization factor (f), so that the *normalized area*, defined by $A' \equiv fA$, is given by:

$$\boxed{A' = A'_1 e^{-\bar{t}/\tau_e}} \tag{6.15}$$

where $A'_1 \equiv fA_1$ is a common quantity for the whole selected sample of hits. For a given track, f is computed using all hits, with no selection based on dE/dx or Δx considered, so that the highest possible statistics is available. Since different energy losses are expected in general for different hits, we work with the following *reduced area*:

$$\bar{A} = \frac{A}{\bar{\Delta}} \tag{6.16}$$

with $\bar{\Delta}$ computed as:

$$\bar{\Delta} = -\frac{dE}{dx} \cdot \Delta x \tag{6.17}$$

where dE/dx is obtained from equation 5.9, using the value of β computed from the range, and Δx is the measured crossed distance of the given hit. Finally, equation 6.13 may be rewritten in terms of the reduced area as:

$$\boxed{\bar{A} = \bar{A}_1 \, e^{-\bar{t}/\tau_e}} \tag{6.18}$$

where $\bar{A}_1 \equiv A_1/\bar{\Delta}$. For every track we fit the measured $\bar{A}$ as a function of $\bar{t}$ using the equation 6.18, obtaining the values of $\bar{A}_1$ and τ_e from the fit. The following prescriptions are observed when carrying out the fit:

- The hits of the given track are divided into 10 equally sized bins according to the value of $\bar{t}$.
- For each bin, we compute the *mean* value of $\bar{A}$.
- The error on the measurement of $\bar{A}$ is approximated by the RMS of the distribution divided by $\sqrt{N}$, where N is the number of hits in the given bin.

Figure 6.3 shows the result of such a fit for two muon tracks. As we already mentioned above, one could in principle think to obtain the lifetime directly from the values fitted for the individual tracks. Nevertheless, due to the relatively low number of hits in a single track, this value is highly unstable as shown in figure 6.4 (top). The average relative error on τ_e is of the order of

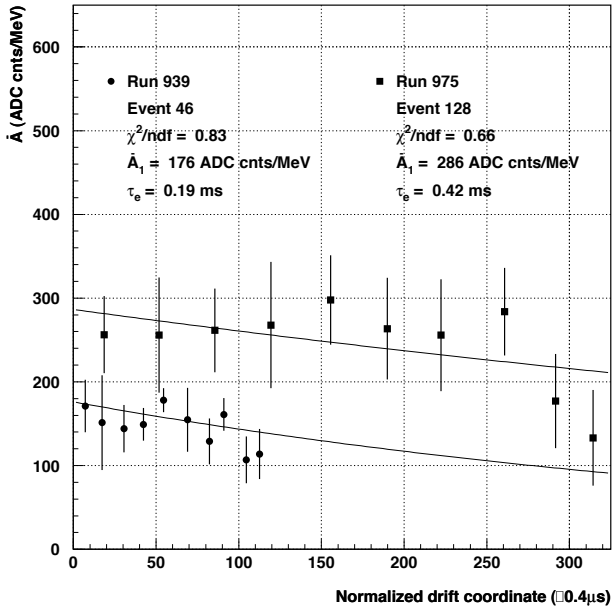

Figure 6.3: Mean normalized hit area as a function of the normalized drift time, measured for two tracks (dots and squares) together with function 6.18 (lines) for the corresponding fitted parameters (quoted in the figure together with the χ^2/ndf value of the fit).

100%. However, the relative average error in $\bar{A}_1$ is about 15%. Therefore, $\bar{A}_1$ may be used to compute the normalization factor:

$$f = \frac{\bar{A}_1^{max}}{\bar{A}_1} \tag{6.19}$$

where for $\bar{A}_1^{max}$ we could, in principle, use any arbitrarily selected value, since we are not interested on the absolute value of the charge but in its attenuation with respect to the (normalized) drift coordinate. However, by selecting the maximum value of $\bar{A}_1$ obtained in our sample ($\bar{A}_1^{max} = 320$ ADC counts/MeV), the normalized hit area (A') is approximately corrected for the shift on t_0. This can be easily understood by noting that the maximum value of $\bar{A}_1$ is obtained for those events for which $t_0 = t_1$, and that the effect of the t_0 shift is to reduce the value of $\bar{A}_1$.

To summarize, in order to compute the drift electron lifetime, the hit charge attenuation as a function of the normalized drift time must be fitted by a negative exponential function. Since both the spatial and calorimetric information of the events are used, the analysis is restricted to the good spatial reconstruction muon sample (see section 5.2.1). Hits are selected according to the associated crossed distance ($\Delta x \in [0.45 - 0.55]$ cm) and the theoretical mean energy loss per crossed distance ($dE/dx < 2.3$ MeV/cm), so that the deposited charge may be quantified in the different normalized drift coordinate bins by the most probable value of the Landau distribution. The hit charge is normalized by the factor $\bar{A}_1^{max}/\bar{A}_1$ computed using all hits from a given track, as described above, which compensates for the different t_0 values of the different events.

For each normalized drift time bin, we build the distribution of the normalized area using the sample of selected hits. A convolution of a Landau and a Gaussian function (see equation 6.6) is fitted to the resulting distribution, The fit has four free parameters, namely: the normalization factor K, the most probable value of the Landau distribution Δ_{mp}, the ξ parameter, and the Gaussian width σ. Although ξ and Δ_{mp} are related by equation 6.3, they are both let free during

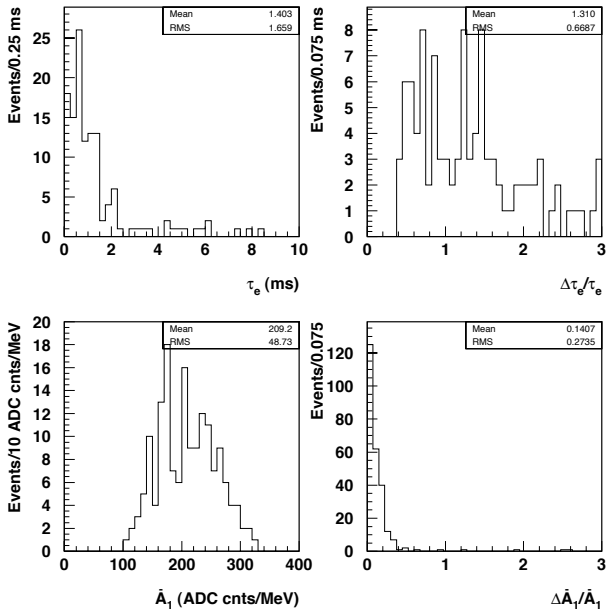

Figure 6.4: Top left: drift electron lifetime obtained from individual tracks. Top right: relative error of the electron lifetime obtained from individual tracks. Bottom left: value of $\bar{A}_1$ obtained from individual tracks. Bottom right: relative error of $\bar{A}_1$ obtained from individual tracks.

the fit, in order to cope with the depopulation of the Landau tail due to the limited number of events, as discussed above.

6.1.2 Results

Average electron drift time

The average electron drift time in the LAr sensitive volume is computed for the different considered data taking periods. Events are classified into four groups according to the date and time of acquisition, as shown in table 6.1. The average drift electron lifetime is computed independently for each of these periods. The last column of the table shows the number of muon tracks available for the electron lifetime computation in each period.

We group the hits from a given period (selected according to Δx and dE/dx as described in the previous section) into bins of the normalized drift coordinate. The bin size is constant, although last bins are merged in the case of low statistics. Figure 6.5 shows, as an example, the distribution of the normalized hit area for the first four bins of the normalized drift coordinate for period III, together with the fitted Landau-Gaussian convolution and the values of the fitted parameters. The fitted Δ_{mp} value and error are used to obtain the electron lifetime by a fit of equation 6.15. The results for periods I, III and IV are shown in figure 6.6 and table 6.2. The quoted errors are of statistical origin only, and include the correlation between A_1' and τ_e. For period II, the lack of statistics prevents a measurement using the stopping muon sample, and the value obtained elsewhere [63], corresponding to the same period, is quoted instead. For period I, the bigger error on the lifetime determination is due to the moderate number of available events. All obtained values agree within the statistical errors with the results from the purity monitors

Group	Runs	Initial date/time	Final date/time	Elapsed time (days)	Total events
I	939	29 July, 19:00	29 July, 21:20	66	33
II	960 961	30 July, 20:50	30 July, 23:30	67	6
III	963 965 966 967 968 969	31 July, 9:15	31 July, 13:30	68	54
IV	973 974 975	31 July, 18:10	31 July, 19:50	68	72

Table 6.1: Summary of the runs used in the present work, grouped in time periods for the drift electron lifetime computation. The last two columns correspond, respectively, to the number of days elapsed since the beginning of the technical run (for comparison with figure 6.1), and the number of available muon tracks.

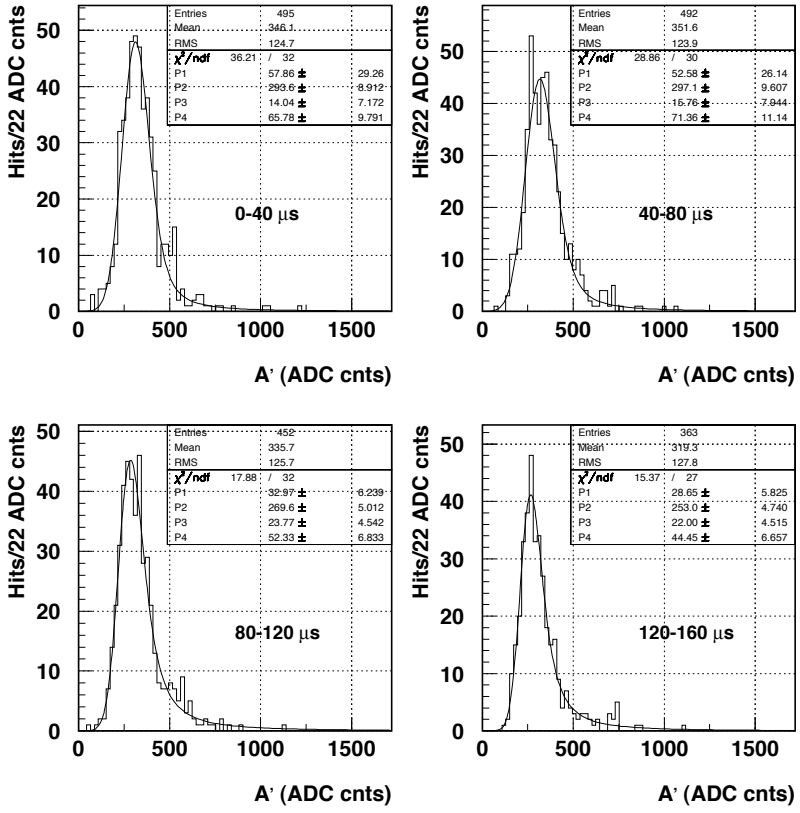

Figure 6.5: Distribution of the normalized hit area for the four first bins of the normalized drift coordinate, for period III. Superimposed are the fitted Landau-Gaussian convoluted functions (see equation 6.6). Quoted are the values of χ^2/ndf and the fitted parameters (P1, P2, P3 and P4 correspond, respectively, to K, Δ_{mp}, and ξ and σ).

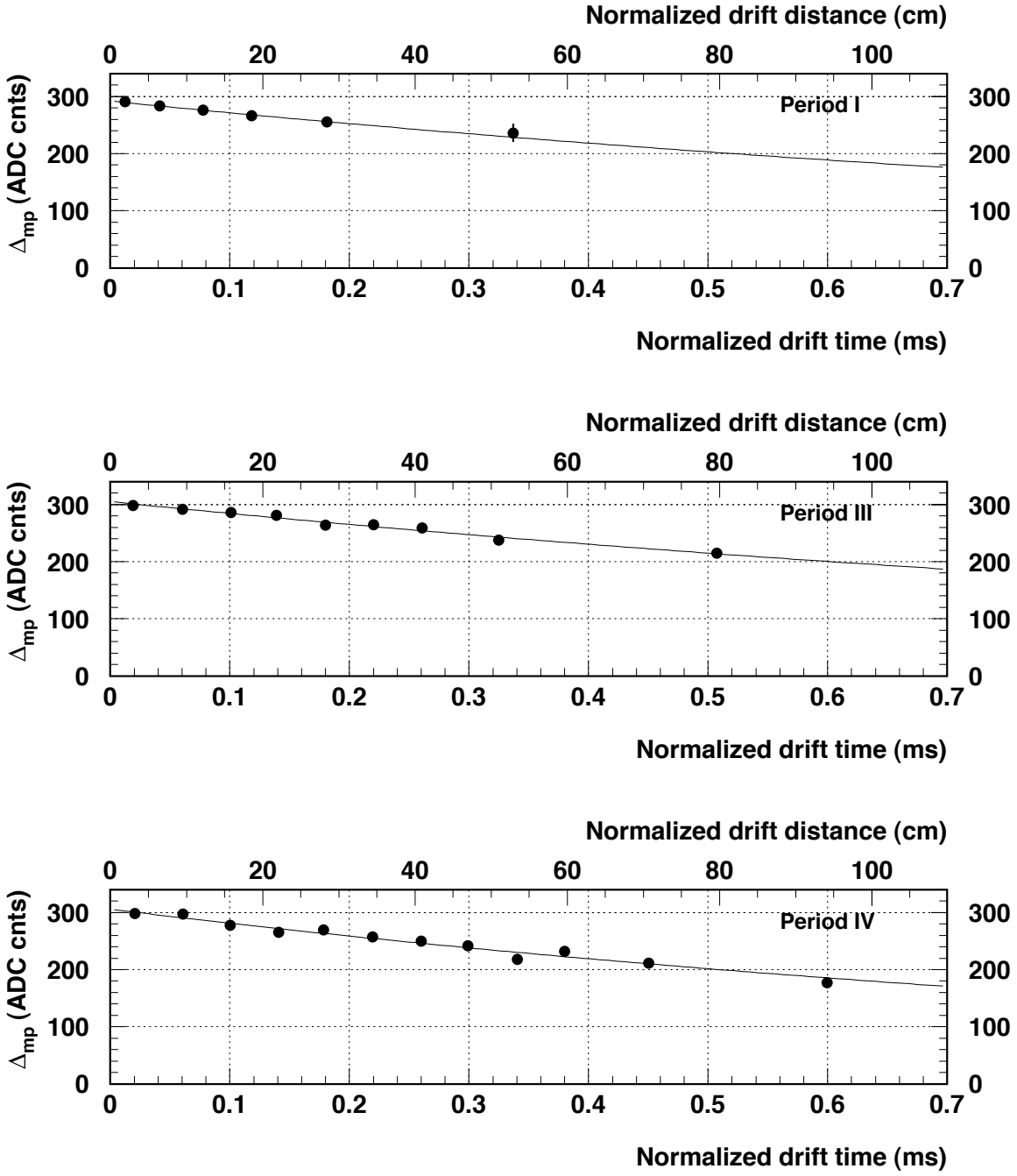

Figure 6.6: Determination of the drift electron lifetime for periods I, III and IV. Dots: measured Δ_{mp} as a function of the normalized drift coordinate (in time (lower axis) and distance (upper axis) units). Line: fitted function. The results of the fit are quoted in table 6.2.

Period	χ^2/ndf	A_1' (ADC cnts)	τ_e (ms)
I	0.50	292± 5	1.38 ± 0.25
II	1.22	—	1.43 ± 0.07
III	0.80	305±3	1.43 ± 0.08
IV	1.49	306±3	1.20 ± 0.06

Table 6.2: Results from the fit to the measured Δ_{mp} vs. normalized drift coordinate for the different data taking periods. The value for period II is taken from ref. [63].

and the off-line analysis of crossing muon tracks (figure 6.1).

The error introduced in the energy measurement by the correction for τ_e can be estimated by:

$$\left.\frac{\Delta E}{E}\right|_{\Delta\tau_e} = \frac{t-t_0}{\tau_e}\frac{\Delta\tau_e}{\tau_e} \tag{6.20}$$

Introducing the average values $\Delta\tau_e/\tau_e = 0.05$, $\tau_e = 1.3$ ms and $t - t_0 = 0.5$ ms (corresponding approximately to half of the maximal drift time), we obtain:

$$\left.\frac{\Delta E}{E}\right|_{\Delta\tau_e} \simeq 2\% \tag{6.21}$$

which constitutes a non-negligible contribution to the total energy resolution. This contribution, together with the one corresponding to the t_0 determination method (described later), must be a posteriori introduced in the MC generation, which does not simulate the presence of impurities in the LAr volume.

Inhomogeneities in the LAr purity

The values of the drift electron lifetime obtained above must be considered as average values over the whole LAr volume; they depend on the average concentration of electronegative impurities in the LAr. However, if the impurities are not homogeneously distributed over the LAr sensitive volume, the electron lifetime might not be constant. We have searched for spatial inhomogeneities of the electron lifetime in the LAr volume. The comparison of the distributions of the hit area for left and right chamber events (see section 4.2.2), discards the existence of (left/right symmetric distributed) inhomogeneities along the drift direction (y coordinate). Inhomogeneities along the x and z directions are searched for by performing the analysis described above for different slices of the LAr sensitive volume along the pertinent coordinate. Considering the limited statistics available, the four data taking periods are merged for this analysis, so that the results must be understood as an average over the whole considered time interval.

The results are shown in figure 6.7 (left) and table 6.3 for the longitudinal direction (z coordinate), and in figure 6.7 (right) and table 6.4 for the height (x coordinate). No evidence of inhomogeneities along the z coordinate is found: all values are compatible with the average. On the other hand, a clear evidence of a decreasing gradient of the electron lifetime toward the top of the LAr volume (high values of x) is found. This effect would be explained by an input of impurities on the top of the LAr volume, an expected fact, since the impurities mainly come from the degassing of the cables in the warm Ar gas. The presence of a leak in any of the electronics flanges (whose existence has been pointed out by the analysis of the Slow Control data in section 3.2.6) would also constitute a source of impurities at the top of the LAr volume. The gradient is probably enhanced since the analyzed data taking period is located in time

z (cm)	χ^2/ndf	A_1' (ADC cnts)	τ_e (ms)
0-1800	0.5	305±4	1.31±0.11
500-1000	0.9	303±3	1.22±0.07
1000-1400	1.9	299±3	1.28±0.08
1400-1800	1.2	297±3	1.25±0.07

Table 6.3: Results from the fit to the measured Δ_{mp} vs. the normalized drift coordinate for different z coordinate (longitudinal direction) bins.

x (cm)	χ^2/ndf	A_1' (ADC cnts)	τ_e (ms)
0-80	0.7	305±4	1.22 ±0.09
80-140	1.6	302±3	1.27 ±0.10
140-190	1.4	302±4	1.39 ±0.10
190-240	1.6	304±4	1.25 ±0.08
240-270	1.9	295±4	1.11 ±0.07
270-316	2.0	301±4	0.92 ±0.06

Table 6.4: Results from the fit to the measured Δ_{mp} vs. the normalized drift coordinate for different x coordinate (height) bins.

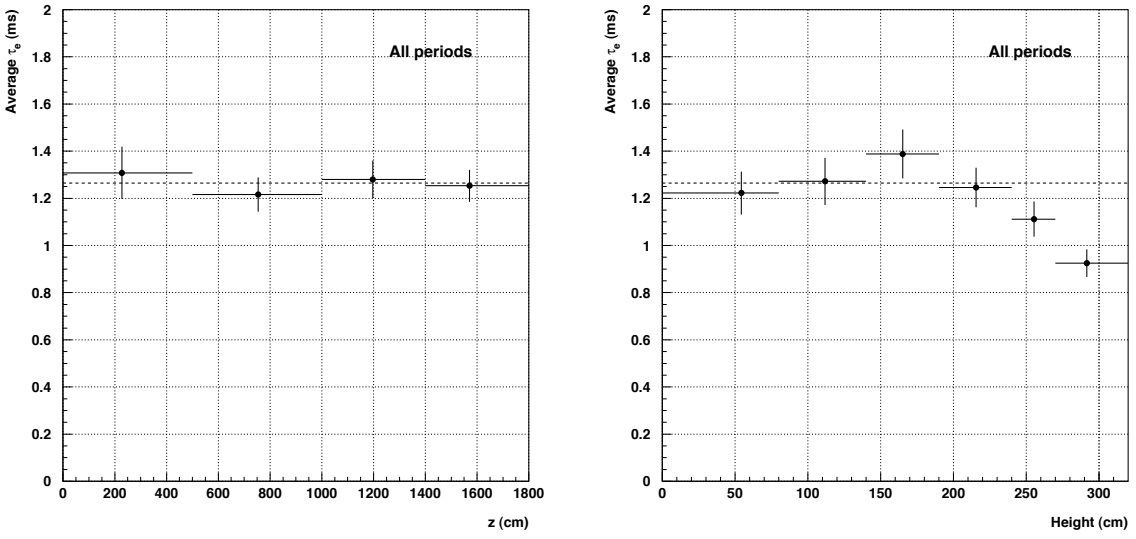

Figure 6.7: Dependence of the electron lifetime on the longitudinal coordinate (left) and height (right). Superimposed (dashed) the average lifetime value.

just after a period when the purification of the gaseous Ar phase had been stopped for several days (see figure 6.1). However, an independent analysis of the LAr purity during the technical run [76] has shown a quick homogenization of the impurity concentration, caused by convective motions of the LAr mass. This seems to be in contradiction with our result. However, it must be pointed out that the present analysis probes a limited period of very particular conditions, and therefore, a similar analysis extended to longer data taking periods should be performed in order to draw a conclusion about the origin of the observed effect.

6.2 Measurement of the electron recombination factor

Ionization electrons produced by the passage of a charged particle through the LAr volume have a non negligible probability to recombine with one of the positively ionized atoms. In such a case, the energy released in the ionization appears in the form of photons and we say that the drift electrons have been quenched. The recombination probability depends on the absorber, on the applied electric field, and on the density of released charge, i.e. on dE/dx. This dependence may be intuitively understood as follows: the higher the field the faster the electrons and ions are separated, and the less time is available for the recombination; on the other hand, the larger the dE/dx, the higher the number of neighbouring positive ions which are available for an electron to recombine. However, the recombination process is not completely understood theoretically, and different models have been proposed to explain the observations. The geminate model [78] considers individual ion-electron pairs moving under the influence of their mutual attraction, the applied field, and the diffusion. The model fails at reproducing data for low values of the electric field (typically below 0.5 kV/cm) [36, 79]. The columnar theory [80, 81] treats the ionization track essentially as an immobile core of positive ions surrounded by a cylindrical distribution of electrons. The columnar model leads to an expression for the recombination factor similar to that of the semi-empirical Birks' law [82], which was proposed to describe the quenching of scintillation light in organic crystals. According to this law, the collected charge per crossed distance is given by:

$$\frac{dQ}{dx} = \frac{A\,\frac{dE}{dx}}{1 + k_B\,\frac{dE}{dx}} \tag{6.22}$$

where both, A and k_B, are constants depending on the applied electric field. A is the linear coefficient relating the measured charge with the deposited energy for low values of the energy loss per crossed distance, and has unit of charge per energy. k_B determines the evolution of the measured charge as a function of the energy loss per crossed distance, and has dimension of length per energy. For $\frac{dE}{dx} \to \infty$ the collected charge is constant, and is given by $\frac{dQ}{dx} \to \frac{A}{k_B}$. For very high electric fields it is expected that $A = 1$ and $k_B = 0$. The recombination factor is the ratio between the measured and the produced (theoretical) charge:

$$R = \frac{\Delta Q^{meas}}{\Delta Q^{th}} \tag{6.23}$$

Therefore, equation 6.22 can be rewritten in terms of the recombination factor by noting that A has units of charge per energy, so that it can be expressed as the inverse of the factor CW (see equation 5.5) times a dimensionless multiplicative constant (a) ranging between 0 and 1. By multiplying both sides of the equation by CW and dividing by dE/dx we obtain[1]:

$$\boxed{R = \frac{a}{1 + k_B\frac{dE}{dx}}} \tag{6.24}$$

[1] An alternative recombination model [83] leads to a slightly different functional dependence ($R = \frac{\ln(1+\alpha\,dE/dx)}{\alpha\,dE/dx}$).

A precise knowledge of the recombination factor is of utmost importance since it determines the absolute energy calibration of the detector. Several sets of experimental measurements of the recombination factor as a function of the electric field are available in the literature [36, 79, 84, 85], although the dependence with the stopping power has been less studied [36, 85]. In the present section we discuss a measurement of the recombination factor as a function of the stopping power, and determine the parameters of Birks' law using the sample of stopping muons events. The measurement procedure consists of the following three steps:

1. The sample of events for which $t_0 = t_1$ is used to compute the value of the recombination factor at the minimal value of dE/dx (i.e. for minimum ionizing particles or *mip*'s). A first estimation of Birks' parameters may be performed based on this subsample.

2. The value of R for mip's is used to obtain the value of t_0 as precise as possible for the rest of the muon sample.

3. The whole sample, t_0 correction included, is used to determine the parameters of Birks' law, hence the dependence of R on the stopping power (dE/dx).

A description of the measurement method and results from the different steps are presented in the next sections. Finally, we apply the results to obtain a lower bound of the δ-ray detection threshold (see section 5.2.2).

6.2.1 Measurement of the recombination factor for minimum ionizing particles

Expression 5.5, which converts charge into energy, may be rewritten in terms of the normalized drift coordinate:

$$E = \frac{CW}{R}\, e^{(t_1 - t_0)/\tau_e}\, e^{\bar{t}/\tau_e} A_i \tag{6.25}$$

So far, both R and t_0 remain unknown, and since both determine the overall energy calibration, they cannot be disentangled from a fit using single events. However, for events with $t_1 = t_0$, the expression becomes:

$$E = \frac{CW}{R}\, e^{\bar{t}/\tau_e} A_i \tag{6.26}$$

where the only parameter remaining undetermined is R. Therefore, by using this kind of events, it is possible to obtain R, hence completing the energy calibration.

Events with $t_0 = t_1$

The search of events with $t_0 = t_1$ (hereafter called *well determined* t_0 *events*) is performed through visual scanning. Two independent kind of hints may indicate a well determined t_0 coordinate, namely:

- A PMT induced signal (see figure 4.3) at drift coordinate $t = t_1$ and close to the stopping muon event (mark A in figure 6.8).

- The signal induced in the Collection wires by the ionization electrons produced *behind* the wire planes, i.e. between the Collection wire plane and the cryostat walls (mark B in figure 6.8).

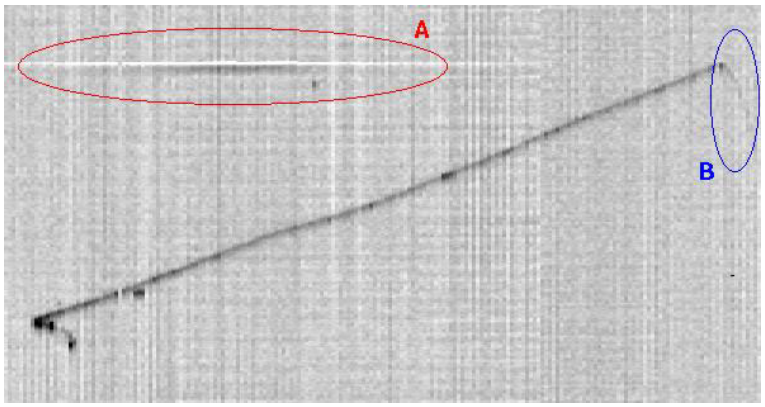

Figure 6.8: Run 975, Event 158, Left chamber. Example of a stopping muon event with $t_0 = t_1$. A) PMT induced signal. B) Signal induced by electrons behind the Collection wire plane.

26 such events have been identified during the scanning phase, out of which 14 belong to the good spatial reconstruction muon sample and are used to determine the value of R for mip's.

Measurement of R_{mip}

As we pointed out in section 6.1.1, the best defined energy loss estimator is given by the most probable value of the energy loss distribution, given, for fixed values of the kinetic energy and crossed distance, by a Landau distribution. We profit from the reliability of this quantity to perform the most precise determination of the minimal value of the recombination factor (R_{mip}), which completely determines the energy calibration of the detector for mip's, in particular, for the sample of electrons produced in the muon decay, studied in section 6.3. The electron from muon decay has an energy in the energy range [0–53] MeV, where the electron behaves as a mip down to distances well below the wire pitch (see figure 5.11). As we will see later, the uncertainty on R_{mip} constitutes the most important source of systematic error in the determination of the Michel ρ parameter.

The construction of the energy deposition distribution (with the correction for the charge attenuation already applied) must be restricted to a sufficiently narrow interval of crossed distance and kinetic energy, so that a convoluted Landau-Gaussian distribution is justified. Identical arguments to those exposed in section 6.1.1 apply in the present case, and hence identical criteria are applied in the selection of the hits, namely:

$$\begin{aligned} \Delta x &\in [0.35 - 0.45] \text{ cm} \\ \text{range} &\in [35 - 200] \text{ cm} \end{aligned} \tag{6.27}$$

which selects 505 hits from the well determined t_0 muon sample. The distribution of the energy deposition associated to this sample of hits is shown in figure 6.9. The most probable value of the fitted Landau distribution is $\Delta_{mp} = 0.437 \pm 0.006$ MeV. On the other hand, from equation 6.3, we can compute the theoretically expected value Δ^{th}_{mp} for the different hits. The average Δ^{th}_{mp} for the selected hit sample is $\Delta^{th}_{mp} = 0.724$ MeV. The value of the recombination factor for mip's is, therefore, given by:

$$\boxed{R_{mip} = R^{t_0=t_1}_{mip} = \frac{\Delta_{mp}}{\Delta^{th}_{mp}} = 0.604 \pm 0.008} \tag{6.28}$$

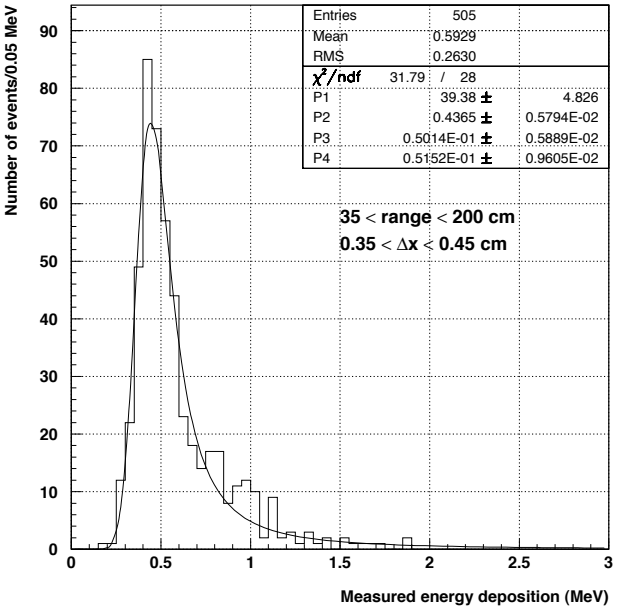

Figure 6.9: Measured energy deposition for the selected hit sample from muons with $t_0 = t_1$ (see the text). The results of a fit with a convoluted Landau-Gaussian function are also shown (see equation 6.6). Quoted are the values of χ^2/ndf and the fitted parameters (P1, P2, P3 and P4 correspond, respectively, to K, Δ_{mp}, ξ and σ).

where the quoted error is of statistical origin. The following possible sources of systematic errors in the measurement of R_{mip} have been investigated:

- To evaluate the effect of the $\Delta x \ln \Delta x$ term in the determination of Δ_{mp} the interval of crossed distance used in the hit selection is alternatively reduced to $[0.35 - 0.40]$ and $[0.4 - 0.45]$ cm. In both cases, the variation on R_{mip} is less than 0.2%.
- The effect of the β dependence in the determination of Δ_{mp} is evaluated by reducing the size of the interval of the range used in the hit selection to [40–100] mm. A variation of $\sim 0.2\%$ is obtained for the central value of R_{mip}.
- Finally, the uncertainty from the correction for the drift electron lifetime is evaluated by letting the lifetime value vary within its confidence intervals (see table 6.2). The central value of $R_{mip}^{t_0=t_1}$ changes by $\sim 0.5\%$.

Therefore, the total systematic error is $\sim$0.6%. The total error, considering also statistical effects is $\sim 1.4\%$ (the uncertainty on the value of R_{mip} is dominated by statistics).

6.2.2 Determination of t_0

The previous result represents the most accurate measurement of R_{mip} that can be obtained using our sample of stopping muon events, since we have used the optimal estimator of the energy deposition (Δ_{mp}), and the selected events are not affected by the ignorance of the t_0 coordinate. This result can be used to determine the t_0 coordinate for the remaining events. In an ideal

case, we would select the hits according to equation 6.27 and, for every track, we would fit a convoluted Landau-Gaussian function to the distribution of the hit energy, adjusting the value of t_0 so that the fitted Δ_{mp} would be equal to the value obtained for the well determined t_0 muon sample. This procedure is not possible in practice since, in general, the number of hits passing the selection cuts in a single track is not large enough to allow a reliable Landau-Gaussian fit (in the extreme case, no hits may be selected). Instead, we determine t_0 by adjusting it so that the value of the *mean* energy loss per crossed distance is equal to that obtained for the well determined t_0 sample. The advantage of working with the mean energy deposition is that, contrary to Δ_{mp}, it depends linearly on the crossed distance, so that no selection based on this variable has to be carried out. The statistics available for a single track is enhanced, although the fit is still not possible in general and hence, the value of the mean energy loss per crossed distance is taken directly from the measured distribution. In order to determine the accuracy of this procedure, we apply it to the sample of events with well determined t_0, and compare the result with the expected value $t_0 = t_1$.

Determination of t_0 using the mean dE/dx

We select mip track *segments* by requiring the range to the end point to be in the interval [35-200] cm. The use of segments rather than hits (see section 5.2.2) in this analysis is motivated by the better determination of Δx (used in the measurement of dE/dx) for the segments; 370 muon segments from the well determined t_0 sample are selected, whose mean value of the measured energy loss is:

$$\langle \frac{dE}{dx} \rangle_{t_0=t_1} = 2.15 \text{ MeV/cm} \tag{6.29}$$

very close to the expected theoretical value given in equation 6.11. This may seem a trivial result since the energy calibration has been tuned with the theoretical most probable value for mip's. However, it must be noted that, for values of the δ-ray detection threshold sufficiently low, equation 5.11 predicts lower values of $\frac{dE}{dx}\big|_{mip}$. A more detailed analysis of this result and its consequences will be carried on in section 6.2.4.

We can use the value $\langle \frac{dE}{dx} \rangle_{t_0=t_1}$ as a reference to determine t_0 for a generic muon event. For this, we compute the mean energy loss per crossed distance for the mip segments of the given muon track ($\langle dE/dx \rangle$), and adjust the value of t_0 by means of the following expression:

$$\boxed{t_0 = t_1 - \tau_e \ln \frac{\langle dE/dx \rangle_{t_0=t_1}}{\langle dE/dx \rangle}} \tag{6.30}$$

We note the similarity of this formula with equation 6.14. The two expressions are equivalent, except for the fact that, in equation 6.14, the value of the electron lifetime was obtained from individual track fits, whereas here the much more accurate common value obtained with all events of a given period is used.

Estimation of the accuracy of the method

As we mentioned above, the accuracy of the t_0 determination by this method can be estimated by applying it to the sample of events with well determined t_0, and compare the result with the expected value $t_0 = t_1$. Figure 6.10 shows the difference between t_1 and the computed t_0 for the well determined t_0 sample. As expected, and despite the low statistics available, we obtain a distribution centered at zero (within some tolerance), and with a certain width. The uncertainty

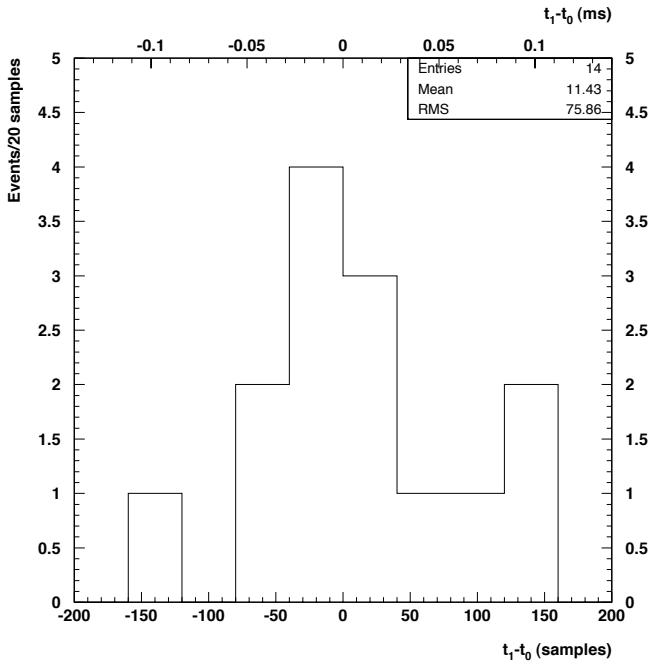

Figure 6.10: Distribution of the difference between t_1 and the measured t_0 for the well determined t_0 muon events. The difference is expressed in drift samples (lower axis) and drift time (upper axis) units.

introduced in the energy measurement by the determination of t_0 using this method may be obtained from equation 5.5, and is given by:

$$\left.\frac{\Delta E}{E}\right|_{\Delta t_0} = \frac{\Delta t_0}{\tau_e} \tag{6.31}$$

Introducing the values $\Delta t_0 = 0.04$ ms (corresponding to 100 samples, a slightly larger value than the width obtained in figure 6.10), and $\tau_e = 1.3$ ms (approximately the average value obtained for the considered data taking periods in section 6.1) we get:

$$\left.\frac{\Delta E}{E}\right|_{\Delta t_0} \simeq 3\% \tag{6.32}$$

This is an important result since, as we will see in more detail in section 6.3.1, it constitutes an important contribution to the energy resolution for the present analysis. Moreover, this contribution must be artificially added to the MC sample, for which no out of time events have been considered.

6.2.3 Measurement of the parameters in Birks' law

By inverting equation 6.24, we obtain:

$$\boxed{\frac{1}{R} = \frac{1}{a} + \frac{k_B}{a}\frac{dE}{dx}} \tag{6.33}$$

an equation linear in dE/dx with $1/a$ and k_B/a the intercept and slope, respectively. This representation of Birk's law offers two main advantages. On the one hand, it provides an easier

visualization of the correlation between R and dE/dx, thanks to the linear dependence. On the other hand, it points out the limitations of the parameterization in terms of a and k_B. Such a parameterization, although useful to compare with previous measurements existing in the literature, does not properly reflect, in our case, the accuracy with which we measure the recombination factor at different dE/dx values. As we pointed out in the previous section, our best estimate of R_{mip} is given by $R_{mip}^{t_0=t_1}$ (see equation 6.28). The value of R at higher dE/dx values is determined with respect to R_{mip}, hence by the slope k_B/a. The problem arises since a is not the inverse of the minimal value R_{mip}, but the extrapolation for $dE/dx \to 0$, which is not experimentally accessible. As we will see below, the relative error on the determination of the slope in equation 6.33 is larger than that of $R_{mip}^{t_0=t_1}$. Therefore, by expressing the dependence of R in terms of a and k_B we shadow the accuracy of R_{mip} by "sharing" the (large) error on the slope between a and k_B. It is, hence, much more convenient to express the evolution of the recombination factor relative to the value for mip's, using the following expression:

$$\boxed{\frac{1}{R} = \frac{1}{R_{mip}} + \frac{k_B}{a}\left(\frac{dE}{dx} - \left.\frac{dE}{dx}\right|_{mip}\right)} \tag{6.34}$$

where $\left.\frac{dE}{dx}\right|_{mip}$ is given in equation 6.11. k_B/a has a dimension of length over energy and is directly obtained from the fit of a straight line (equations 6.33 or 6.34) to $1/R$ vs. dE/dx.

In the present section, we compute the value of k_B/a in three different ways, for the sake of consistency and cross-checking. Using $R_{mip} = R_{mip}^{t_0=t_1}$, we disentangle the values of a and k_B, that can be thus compared with previous measurements. A first estimation of the parameters is carried out using, exclusively, events from the well determined t_0 muon sample. We increase the accuracy of the result by adding the whole good spatial reconstruction muon sample (with the proper correction for t_0 as determined in the previous section). In both cases, R is computed by comparing the measured and theoretically expected *mean* values of the energy loss per crossed distance. As a cross check, we rebuild the analysis by computing R as the ratio between the measured and theoretically expected *most probable* value of the energy loss. Finally, we carry out a comparison of our result with previously reported measurements.

Fit to the well determined t_0 muon sample

In a first determination of the Birks' law parameters, we exclusively use the events from the well determined t_0 muon sample. Muon *segments* are grouped according to the theoretically expected mean energy loss per crossed distance (dE/dx), computed with the Bethe-Bloch formula (equation 5.9), where the value of β is computed from the range. For every dE/dx bin, the value of R is computed as the ratio between the *mean* measured and theoretical dE/dx. The errors are approximated by $RMS/\sqrt{N}$, where the RMS is taken directly from the distribution of measured dE/dx, and N is the number of segments in the given bin. Data are fitted using a straight line (equation 6.33) with both , the slope $(1/a)$ and intercept (k_B/a), as free parameters. The smaller error of R_{mip} is naturally taken into account by the least χ^2 method used for the fit. The measured $1/R$ vs. $\langle dE/dx \rangle$ is shown in figure 6.11 (top), together with the fitted straight line ($\chi^2/ndf = 0.7$). The best fit is found for the following values of the Birks' law parameters:

$$\begin{aligned} a &= 0.74 \pm 0.04 \\ k_B &= 0.104 \pm 0.022 \text{ cm/MeV} \end{aligned} \tag{6.35}$$

Or, alternatively, for $R_{mip} = R_{mip}^{t_0=t_1}$:

$$\frac{k_B}{a} = 0.14 \pm 0.03 \text{ cm/MeV} \tag{6.36}$$

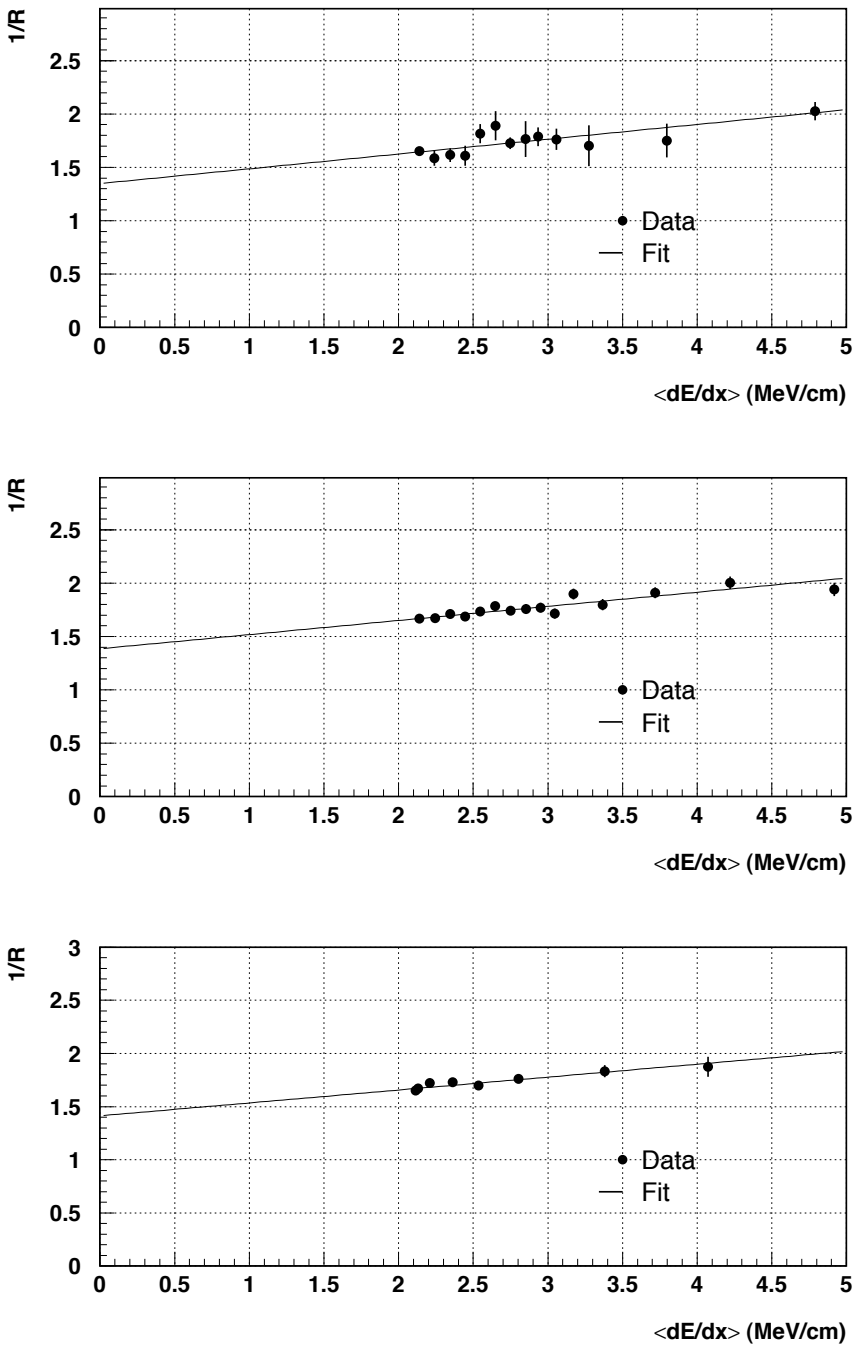

Figure 6.11: Dots: Measured $1/R$ as a function of the mean energy loss per crossed distance, using the segments (top and center) or hits (bottom) from the well determined t_0 (top) or good spatial reconstruction (center and bottom) muon sample. R is computed by comparing the mean (top and center) or most probable (bottom) energy depositions with the theoretically expected value. Lines: best linear fit to the data.

where the quoted errors are of statistical origin.

Fit to the whole muon sample using $\langle dE/dx \rangle$

The previous result is affected by a large statistical uncertainty due to two facts, namely: the limited statistics available (only muons with well determined t_0 are used), and the short lever arm, due to the reduced dE/dx interval experimentally available when using stopping muons. The latter problem is intrinsically related to muons, and particles with higher stopping power in LAr, e.g. protons, should be used to increase the explored dE/dx range. However, the effect of small statistics may be reduced by using the whole muon sample, with the proper energy correction applied using t_0 as computed in the previous section. Care must be taken with the fact that the energy of these events has been tuned so that $R_{mip} = R_{mip}^{t_0=t_1}$ (see equation 6.28). In order not to be biased by this tuning, the value and error of $R_{mip}^{t_0=t_1}$ (rather than the one obtained from the whole muon sample) is assumed during the fit for the first data point (at the lowest measured dE/dx). Subsequent points at higher dE/dx values may be used in the fit since the t_0 tuning does not bias the dependence of R on dE/dx. The values of R and errors are computed in a way identical to the one used for the well determined t_0 sample, described above. The results are shown in figure 6.11 (center) together with the straight line best fitting the data ($\chi^2/ndf = 1.0$). The values of the Birks' law parameters are:

$$\boxed{\begin{array}{rcl} a & = & 0.74 \pm 0.02 \\ k_B & = & 0.096 \pm 0.008 \text{ cm/MeV} \end{array}} \tag{6.37}$$

which, for the $R_{mip} = R_{mip}^{t_0=t_1}$, yields:

$$\boxed{\frac{k_B}{a} = 0.13 \pm 0.01 \text{ cm/MeV}} \tag{6.38}$$

where the quoted errors are of statistical origin. This value, together, with the value of R_{mip} obtained in equation 6.28, represents our best estimate of the parameterization of the evolution of the recombination factor with dE/dx.

Fit to the whole muon sample using Δ_{mp}

In the two previous cases, we have used the ratio between the measured and theoretical *mean* energy losses per crossed distance to compute the recombination factor at the different dE/dx values. The dependence of $1/R$ is very well reproduced by a straight line, as can be seen in figure 6.11, top and center plots. Since the theoretical value of dE/dx, has been computed from the *non-truncated* Bethe-Bloch formula (equation 5.9), this result may be translated into a lower bound of the δ-ray detection threshold entering the truncated Bethe-Bloch formula (equation 5.11), provided that Birks' law is the correct parameterization of R. The idea is that if equation 5.9 provides a good description of the dependence of R on dE/dx, T_{cut} must be high enough so that equation 5.11 does not differ much from equation 5.9 in the considered range of kinetic energies. In order to cross-check the previous argument, we have performed a measurement of the Birks' law parameters by computing R as the ratio of the *most probable* measured and theoretical energy losses, since this quantity is not affected by the δ-ray detection cut-off. We select *hits* (rather than segments) from the good spatial reconstruction muon sample according to the crossed distance (as in section 6.1.1) by $\Delta x \in [0.35 - 0.4]$ cm. For every dE/dx bin, R is computed as the ratio between the measured and theoretical Δ_{mp}. The measured Δ_{mp}

and the error are obtained from a fit of a convoluted Landau-Gaussian function (see equation 6.6) to the distribution of the deposited energy. The theoretical Δ_{mp} is taken as the average for the hits of the given bin. The result is fitted by a straight line ($\chi^2/ndf = 0.7$) as shown in figure 6.11 (bottom). The best fit is provided by the parameters:

$$\begin{aligned} a &= 0.71 \pm 0.04 \\ k_B &= 0.085 \pm 0.022 \text{ cm/MeV} \end{aligned} \tag{6.39}$$

which, for the $R_{mip} = R_{mip}^{t_0=t_1}$, yields:

$$\frac{k_B}{a} = 0.12 \pm 0.03 \text{ cm/MeV} \tag{6.40}$$

where the quoted errors are of statistical origin. This result is compatible within statistical errors with the ones obtained when computing R with the mean dE/dx, reinforcing our previous argument. The lower statistical significance of this result is due to the depletion of the available statistics caused by the selection cut on Δx (compulsory when computing Δ_{mp}). A description of the computation of the lower bound of the δ-ray detection cut-off that can be obtained from this result is performed in the next section.

Comparison with previous measurements

Several authors have measured in the past the recombination factor in LAr as a function of the electric field. We compare our result with the ones obtained by these experiments for the nominal value of the electric field in the T600 during the technical run (500 V/cm). In all the these experiments, as well as in the present analysis, the effect of the finite drift electron lifetime, due to the attachment to impurities in the LAr, has been unfolded by measuring the collected charge for different drift distances. Scalettar et al. [79] have measured the collected charge in a LAr ionization chamber exposed to 364 keV conversion electrons from a ^{113}Sn source. Aprile et al. [84] use a similar method with a 976 keV ^{207}Bi source. Several measurements have been carried out by the ICARUS collaboration using data from different prototypes. Measurements using high energy muons traversing the detector have been performed both with the 50 liter [64] and the T600 [63] detectors. The results obtained by these experiments are summarized and compared with the present analysis in table 6.5. In the two first compared experiments, the ionizing particles are low energy electrons stopping in the LAr volume. In this case dE/dx is not a constant and the measured recombination factor must be considered as a mean value along the electron path ($\langle R \rangle$). We can compute the expected $\langle R \rangle$ using our result by means of:

$$\langle R \rangle = \frac{\int \frac{dE}{dx} R(\frac{dE}{dx})\, dx}{\int \frac{dE}{dx}\, dx} \tag{6.41}$$

where the integrals run over the electron path, from the emission down to the stopping point, dE/dx is given by the Bethe-Bloch formula for electrons (equation 5.27) and $R(dE/dx)$ by equation 6.34 using our best estimates of R_{mip} (equation 6.28) and k_B/a (equation 6.38). The last column in table 6.5 shows the values obtained using such a method. In the second column we quote the average value of dE/dx along the electron path, defined as the value for which the recombination factor obtained with equation 6.34 is equal to $\langle R \rangle$. In the case of the measurements using crossing muons (performed with the 50 liter and T600 detectors), the dE/dx can be considered as a constant and the predicted value of R is computed directly using equation 6.34. All measurements are in very good agreement with the value predicted using our result (and hence among them), except for the slightly higher value obtained by Scalettar et al. However,

these authors do not include the contribution to the error coming from the correction for the electron attachment, which for the considered electric field value should be significant. The disagreement could be also explained by the non-inclusion of the effect of secondary ionization in equation 6.41, or by an incorrect polarization of the Induction wire planes during the T600 technical run (this possibility has been reported in the past [64]), which could lead to a reduced level of transparency and hence to a decrease of the collected charge at the last wire plane.

Experiment	Source	$\langle dE/dx \rangle$ (MeV/cm)	$\langle R \rangle$	$\langle R \rangle$ (this analysis)
Scalettar	364 keV e^-	3.5	0.57 ± 0.01	0.554 ± 0.014
Aprile	976 keV e^-	2.5	0.62 ± 0.03	0.599 ± 0.009
50 liter	crossing μ	2.1–2.7	0.62 ± 0.02	0.58–0.61
T600	crossing μ	2.1–2.7	0.60 ± 0.01	0.58–0.61

Table 6.5: Existing measurements of the recombination factor in LAr at electric field E = 500 V/cm. Last column is the predicted value using equation 6.41 (first two entries) or 6.34 (last two entries) with the best fitted R_{mip} (equation 6.28) and k_B/a (equation 6.38) values. The third column shows the average dE/dx, i.e. the constant value for which we obtain the result in last column (see the text).

We have not found in the literature any measurement of the recombination factor as a function of the energy loss per crossed distance, aside from those performed by the ICARUS collaboration. The fine granularity and large active volumes of the 3 ton, 10 m^3 and T600 detectors allow such a measurement with stopping particles (whose average dE/dx rises rapidly when approaching the end point). In the present analysis, as well as in the one performed with the 10 m^3 detector data [85], we have used stopping muons, hence measuring the recombination factor for dE/dx values ranging from ∼2 to ∼5 MeV/cm. Higher values of dE/dx (up to ∼32 MeV/cm) are investigated with the 3 ton detector [36] including stopping protons. The values of the Birks' law parameters obtained for the different studied electric fields are summarized and compared in table 6.6. We find a disagreement between the results obtained at 500 V/cm with the 3 ton and in this analysis. The difference in a could be attributed to the possible decrease of the transparency of the Induction wire planes mentioned above, or to an effect due to the differences in the signal extraction methods used for both detectors (this possibility is currently under study). However, none of these effects would explain the difference in the value of k_B, which determines the evolution of R with dE/dx. In order to perform a consistency check, we have directly compared the values of R obtained with the 3 ton detector and in this analysis (see figure 6.12). A good fit ($\chi^2/ndf = 1.3$) to the new data is found when fixing k_B to the value obtained with the 3 ton detector and letting a free. It must be noted that the dE/dx range accessible with the 3 ton data is larger (from 2 to 32 MeV/cm) since also stopping protons are studied. The different values of k_B could be thus attributed to the large difference of lever arm available for the different fits.

6.2.4 Lower bound of the δ-ray detection threshold

As a corollary from the determination of the recombination factor as a function of the mean energy loss per crossed distance, we can obtain a lower bound of the δ-ray detection threshold (T_{cut}). This threshold determines the measured energy loss per crossed distance through the Bethe-Bloch truncated formula (equation 5.11), and is associated to the detector and the reconstruction algorithm. The effect is due to the well known fact that the fluctuations of dE/dx are mainly caused by the production of a few high energy δ-rays. In practice, we measure the energy *deposited* (rather than lost) by energy transfers up to some value T_{cut}, for which the produced

Experiment	Electric field (V/cm)	a	k_B (cm/MeV)
3 ton	200	0.85 ± 0.02	0.326 ± 0.019
10 m^3	286	0.78 ± 0.12	0.15 ± 0.06
3 ton	350	0.78 ± 0.02	0.130 ± 0.008
3 ton	500	0.85 ± 0.02	0.072 ± 0.004
This analysis	500	0.74 ± 0.02	0.096 ± 0.008

Table 6.6: Existing measurement of the Birks' law parameters for different values of the electric field.

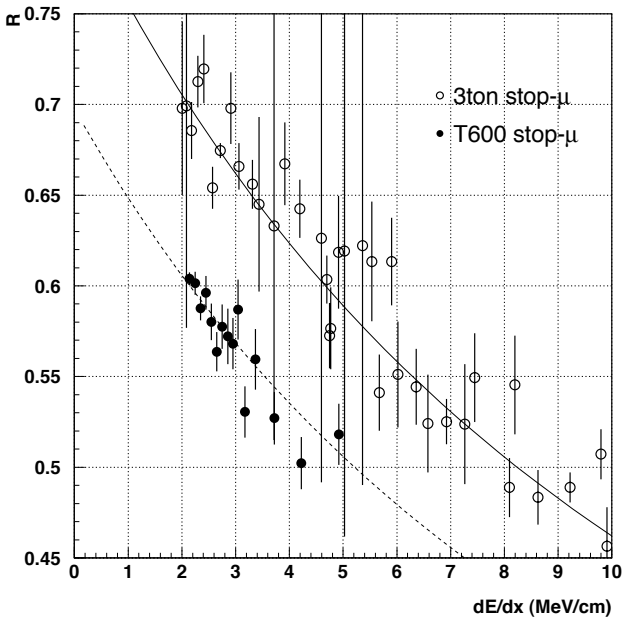

Figure 6.12: Comparison of R as a function of dE/dx as measured by the 3 ton (empty circles) and in this analysis (solid circles). The solid line is the result of the fit of Birks' law to the 3-ton data with a and k_B free parameters. The dashed line is the result of the fit of Birks' law to the values obtained in this analysis, fixing k_B to the value obtained with the 3-ton data and letting a free.

δ-ray is energetic enough to be considered as an independent track by our spatial reconstruction algorithm, hence is not included as part of the muon track. A precise knowledge of T_{cut} can be of utmost importance since, as pointed out by Navas et al. [86], the accurate measurement of the mean energy loss along a muon track may be used to determine the muon momentum in the range [1–3] GeV, with resolutions comparable to that obtained with the multiple scattering method [43], and in a momentum range where the latter method is difficult to apply.

As has been pointed out previously, the good description provided by Birks' law of the recombination data can be translated into a lower limit of T_{cut}. Since we compute the ratio R using the theoretical dE/dx with no cut-off, for values of T_{cut} sufficiently low the measured $1/R$ dependence must be distorted by a factor $\frac{(dE/dx)_{T<T_{cut}}}{dE/dx}$. The effect is shown in figure 6.13, where the measured and fitted $1/R$ for the low dE/dx region are shown together with the behaviour expected for different values of T_{cut}, arbitrarily normalized at high dE/dx values.

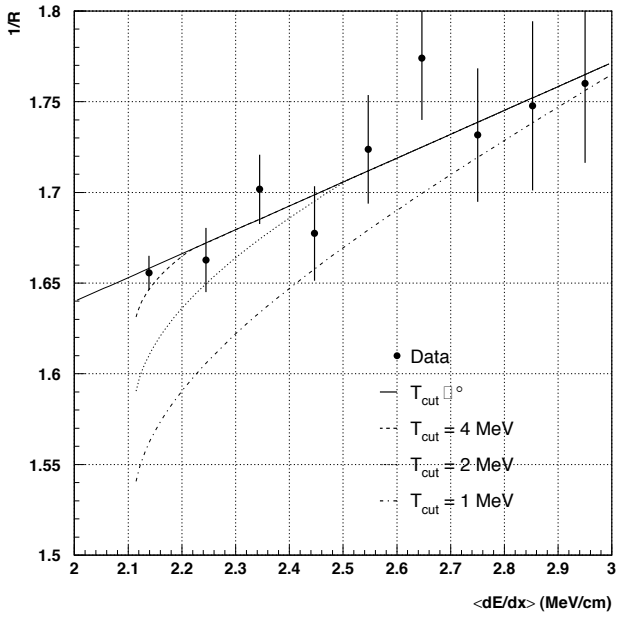

Figure 6.13: Low dE/dx region zoom of figure 6.11 (center). Dots: measured $1/R$. Lines: theoretically expected $1/R$ vs. dE/dx for different values of the δ-ray detection cut-off, when R is measured as the ratio between the measured and theoretical dE/dx with no cut-off. The curves are arbitrarily normalized at high dE/dx values.

T_μ (MeV)	W_{max} (MeV)
10	0.2
100	3
200	7
260	11
300	13
400	21
500	31

Table 6.7: Values of the maximum transferable energy in a single collision for various muon kinetic energies.

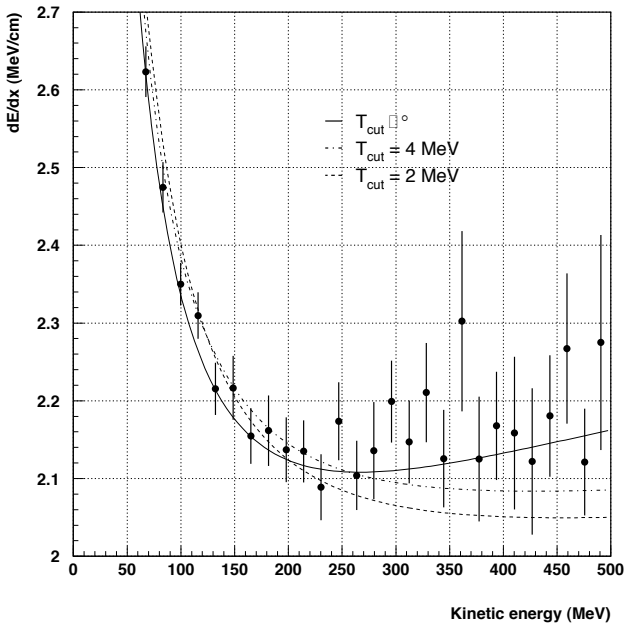

Figure 6.14: Dots: fully calibrated and corrected (by electron lifetime, recombination and t_0) mean energy loss per crossed distance measured with the segments of the good spatial reconstruction muon sample. Line: best fit to the data for various values of T_{cut}.

From inspection of equations 5.9 and 5.11 we observe that $dE/dx = (dE/dx)_{T<T_{cut}}$ for $W_{max} < T_{cut}$, an expected fact since δ-rays are produced in a single muon-electron collision. Table 6.7 shows the value of W_{max} for various values of the muon kinetic energy, the mip corresponds to $T \sim 260$ MeV. If, in first approximation, we consider that the $1/R$ curve is determined by those hits from the mip ($T \simeq 260$ MeV) down to the end point ($T = 0$), a lower bound of T_{cut} is given by the value of W_{max} for mip's, hence 11 MeV. The argument is that any value of T_{cut} below 11 MeV produces a difference in the measured energy for hits below $T = 260$ MeV (which basically determines the shape of $1/R$). Of course, this is a very naïve way of computing the lower bound of T_{cut}, since the distortions in the $1/R$ shape caused by values lower than 11 MeV may be perfectly compatible with the data. In order to better compute the lower bound, we perform a fit of $(dE/dx)_{T<T_{cut}}$ to the data, with T_{cut} as free parameter. The global energy scale must be introduced as a second free parameter during the fit, since it has been arbitrarily adjusted in the data for mip's. The fit procedure and results are illustrated in figure 6.14. We use 30 measuring points (the three at the lowest kinetic energy values are not shown in the figure), hence the fit contains 28 degrees of freedom, and the 95% CL exclusion point is given for $\chi^2/ndf \simeq 1.5$ [14], which is obtained for any value of T_{cut} lower than 4 MeV. Then, at the 95% CL:

$$\boxed{T_{cut} > 4 \text{ MeV}} \tag{6.42}$$

The best fit to the data obtained for T_{cut} values 2 and 4 MeV are shown in the figure, together with the measured data and the theoretical curve for no cut-off (in the latter case $\chi^2/ndf = 1.1$, which is at the limit of exclusion at 68% CL). The best fit is obtained for $T_{cut} = 26$ MeV ($\chi^2/ndf = 0.8$). An independent measurement of T_{cut} in ICARUS has been performed by other authors [87] comparing the number of δ-rays selected and measured by visual scanning with the number of the theoretically expected, as a function of the kinetic energy. The value $T_{cut} \simeq 2$ MeV is found using such a procedure. The difference between this value and the one

obtained in the present analysis are not inconsistent since, as we have pointed out above, T_{cut} depends on the detector *and* on the reconstruction algorithm. It is expected that the dedicated visual inspection of the event is more sensitive to low energy δ-rays, which in the case of the automatic reconstruction are typically associated to the muon track.

6.2.5 Conclusions on the determination of the recombination factor

The electron recombination in LAr has been determined for a field strength of 500 V/cm with a precision of $\sim 1.4\%$ for mip's. The dependence of the recombination factor on the mean energy loss per crossed distance has been parameterized using Birks' law. The obtained values of the parameters agree well with previous measurements. In the procedure to compute the Birk's parameters in the most precise way, a method to determine the t_0 coordinate of out-of-time events has been developed and applied to the data, hence completing the calorimetric reconstruction of the events, expressed by equation 5.5. The joint calorimetric and spatial reconstruction of the events will be used in the next section to analyze the sample of electrons/positrons resulting from the decay of the muons. Finally, we have computed a lower limit of the δ-ray detection cut-off by performing a fit of equation 5.11 to the fully calibrated and corrected measurements of the mean energy loss per crossed distance as a function of the kinetic energy.

6.3 Electron sample

With the computed corrections for the drift electron lifetime, recombination and t_0 determination (described in the previous sections), we can finally fully reconstruct (spatially and calorimetrically) the whole stopping muon event. In this chapter, we focus on the study of the fully reconstructed sample of electrons coming from the muon decay. We determine the Michel parameter ρ by means of the combined analysis of the MC and data samples. The contribution to the energy resolution coming from the electronic noise and signal digitization is estimated from the MC sample. We finally study the angular distribution of the electron events, and the resolution that can be achieved by estimating the electron energy using the range.

Two parallel analyses are performed, namely: excluding and including the radiation energy losses, respectively. Data samples used in both analyses are selected from the good reconstruction muon sample (see section 5.2.1), since otherwise the range along the muon track is not properly determined and both, the t_0 determination and correction for the recombination factor (directly relying on the range), cannot be properly carried out. The selection based on the muon reconstruction quality must be combined with that of the electron reconstruction quality. In the first considered analysis, we do not rely on the spatial reconstruction and, hence, events are chosen from the good calorimetry electron sample. With the combined selection 160 events are kept. In the second one, the search for bremsstrahlung tracks requires the electrons to be selected from the good spatial reconstruction electron sample, which selects 123 events.

We compare our data with a MC sample composed of 5000 electron events from muon decay. The generation of the MC sample includes two basic modifications with respect to what has already been described in section 5.4.3, in order to get a more realistic simulation of the experimental conditions:

- As pointed out in section 5.4.3, the efficiency of the bremsstrahlung reconstruction is overestimated in the MC since the noise and signal shapes of both, the main and the secondary generated views, are simulated using the pattern corresponding to the Collection view. As shown in section 4.1.2, the hit detection efficiency is about 20% lower for Induction than for Collection wires. Hence, an additional hit detection inefficiency of 20% is imposed to the MC secondary wire plane during the hit reconstruction. This has a negligible effect on the electron track reconstruction, since during the cluster expansion (cluster reconstruction pass II, see section 4.3.1), most of the undetected hits are recovered. The largest effect is produced on the detection of low energy bremsstrahlung tracks since, in many cases, all the hits from the track remain undetected and thus no cluster expansion can be carried out to recover them. The total kinetic energy spectrum of the reconstructed bremsstrahlung tracks from the MC sample (including the extra 20% hit detection inefficiency) is compared in figure 6.15 to the spectrum of the total generated sample. An increasing detection inefficiency is observed toward low energy, whereas for energies larger than about 10 MeV, the effect is almost negligible.

- Two of the effects contributing to the energy resolution have not been simulated in the MC generation, namely: the presence of impurities in the LAr volume and the fact that most of the stopping muon events are out of time, so that the associated t_0 coordinate must be computed as described in the previous section. However, the effects of the electron recombination are included. As we showed in sections 6.1.2 and 6.2.2, the contribution to the energy resolution from the drift electron lifetime corrections and the t_0 determination are about 2% and 3%, respectively. Therefore, in order to render the comparison between real data and MC samples more reliable, the energy reconstructed for the MC events are smeared using a Gaussian function of width $\sigma = 0.04E$, where E is the measured energy.

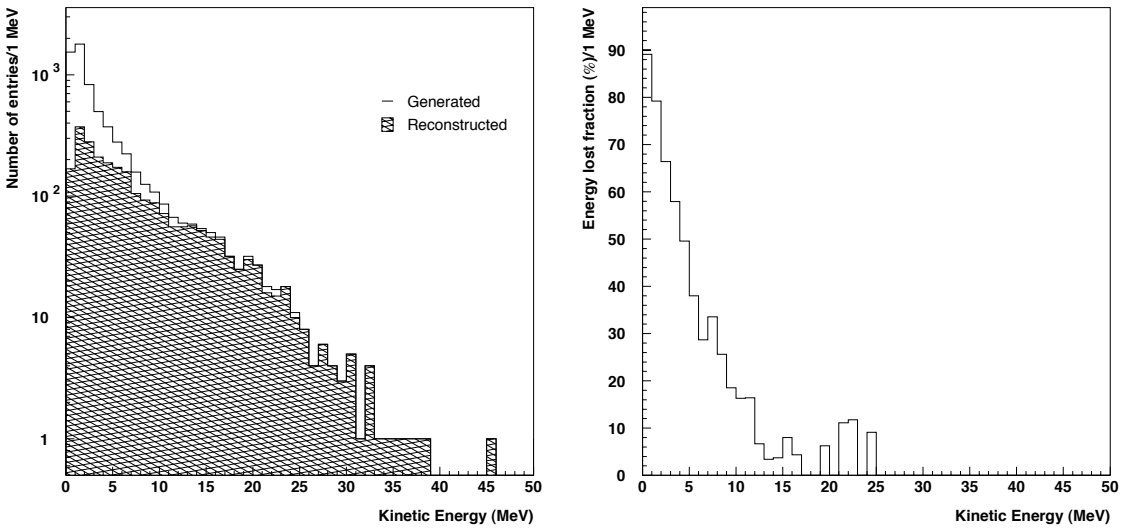

Figure 6.15: Left: Comparison between the MC total generated (empty) and measured (hashed) bremsstrahlung reconstructed energy spectra. Right: fraction of undetected bremsstrahlung tracks as a function of the generated kinetic energy.

6.3.1 Electron energy spectrum and determination of the Michel parameters

The muon decay process was first described in a model-independent way by Michel [88], using the most general local, derivative-free, lepton-number conserving, four fermion interaction. For unpolarized muons, the decay probability is given by:

$$\frac{dP}{dx}(x;\rho,\eta) = \frac{1}{N}x^2\left(3(1-x)+\frac{2}{3}\rho(4x-3)+3\eta\frac{m_e}{E_{max}}\frac{1-x}{x}+\frac{1}{2}f(x)+\mathcal{O}(\frac{m_e^2}{E_{max}^2})\right) \quad (6.43)$$

where $x = \frac{E_e}{E_{max}}$ is called *reduced* energy (ranging from m_e/E_{max} to 1); E_e is the total energy of the electron produced in the decay; $E_{max} = 52.8$ MeV is the end-point of the electron spectrum; $f(x)$ is the term accounting for the first order radiative corrections, given by [89, 90]:

$$f(x) = \frac{\alpha}{2\pi}x^2\left\{2(3-2x)R(x) - 3\ln x + \frac{1-x}{3x^2}\left[(5+17x-34x^2)(\ln x+\lambda) - 22x + 34x^2\right]\right\} \quad (6.44)$$

with $\lambda \equiv \ln\frac{m_\mu}{m_e}$ and $R(x)$ given by

$$R(x) = (2\lambda-1)\ln(1-x) - \frac{1}{x}\ln(1-x) + 2L_2(x) + (-\frac{\pi^2}{3}+\frac{3}{2}\lambda - 2) \quad (6.45)$$

where $L_2(x)$ is the Euler's dilogarithm:

$$L_2(x) = -\int_0^x \frac{\ln(1-t)}{t}dt = \sum_{\nu=1}^{\infty}\frac{x^\nu}{\nu^2} \quad (6.46)$$

N is the normalization factor that, for a total probability normalized to one, takes the value

$$N = \frac{1}{4}+\frac{1}{2}\eta\frac{m_e}{E_{max}} + \frac{\alpha}{36\pi}[-9L_2(1)+\frac{1}{8}(225-24\pi^2)] \quad (6.47)$$

finally, ρ and η are the so-called Michel parameters, defined in terms of bilinear combinations of the coupling constants of the general four fermion interaction, and hence depending on the type of interaction governing the decay process. For the Standard Model (SM) V-A interaction, the parameters take the values:

$$\begin{aligned} \rho_{SM} &= 0.75 \\ \eta_{SM} &= 0 \end{aligned} \tag{6.48}$$

The V-A assumption has been already confirmed in muon decay with high precision [14, 91] by the determination of the whole set of Michel parameters and complementary measurements. Figure 6.16 (left) shows the shape of the Michel electron energy spectrum for various values of the parameters ρ and η. As shown in the figure, and expected from inspection of equation 6.43, the shape of the energy spectrum is more sensitive to ρ, since η is weighted by m_e/E_{max}, and hence determines the shape of the spectrum at low energy. The radiative corrections, shown in figure 6.16 (right), determine the shape of the spectrum near the end-point and therefore the value of ρ is very sensitive to them. It has been shown that the overall effect of the radiative corrections on the ρ value is of the order of 6% [90].

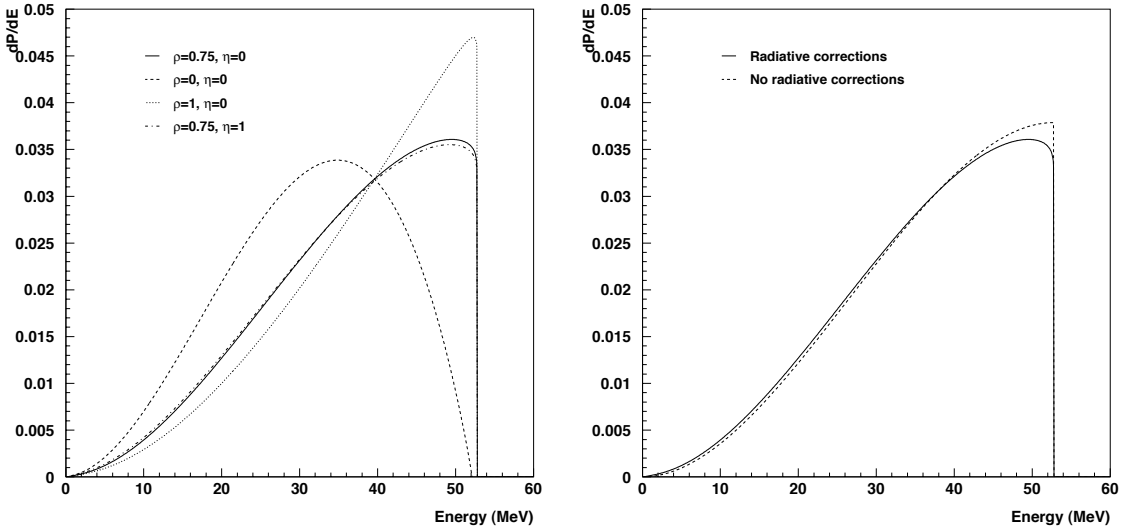

Figure 6.16: Left: energy spectra of muon decay electrons for various values of the Michel parameters ρ and η including (solid line) the V-A values. Right: Effect of the first order radiative corrections on the muon decay spectrum. The integrated probability is normalized in all cases to one.

Electron track energy spectrum

The electron kinetic energy loss by ionization (hereafter called *electron track energy*) is a better determined quantity than the total energy loss or *electron total kinetic energy* (including radiation losses), since it does not depend on the bremsstrahlung detection efficiency. Therefore, it provides a bias-free way to measure the energy resolution and Michel parameters.

We can extract the values of the Michel parameters as those for which the best fit between the simulated and measured energy spectra is obtained. The fit is performed by a χ^2 minimization, which compares the MC and data histograms built using 15 equally sized energy bins in the range

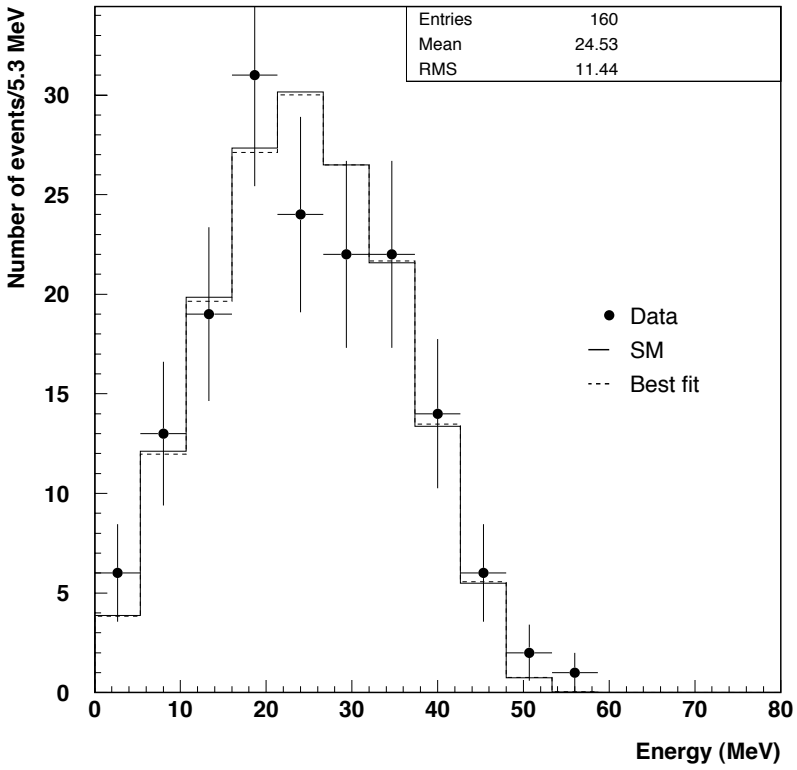

Figure 6.17: Measured, MC generated and fitted electron track energy spectra.

[0–80] MeV. Since the MC sample is generated using the SM values of the Michel parameters (ρ_{SM} and η_{SM}), the histogram for an arbitrary pair of values, ρ and η, is built by applying, to every simulated event, a weight (w) depending on the generated reduced energy:

$$w = \frac{\frac{dP}{dx}(x_{MC};\rho,\eta)}{\frac{dP}{dx}(x_{MC};\rho_{SM},\eta_{SM})} \tag{6.49}$$

where $x_{MC} = E_{MC}/E_{max}$, and E_{MC} is the MC generated total electron energy.

First of all, we quantify the agreement between the measured and SM expected energy distributions by computing the χ^2 function using the data and the MC generated with the V-A Michel parameters. The distributions are found to be in good agreement ($\chi^2/ndf = 5.94/11$) as shown in figure 6.17. It is important to remark the agreement at the low energy part of the spectrum, demonstrating the good performance of the reconstruction tools even for low energy tracks. We can compute the values of ρ and η by fitting the data distribution with a MC where both parameters are let free. The best fit, ($\chi^2/ndf = 5.2/9$) is obtained for:

$$\begin{aligned} \rho &= 0.9 \pm 0.5 \\ \eta &= 12 \pm 22 \end{aligned} \tag{6.50}$$

where the quoted errors are of statistical origin. The accuracy in the determination of η is much lower, since this parameter is weighted by m_e/E_{max} in the decay probability (see equation 6.43 and figure 6.16). Furthermore, the correlation between the two parameters is high, as can be seen in equation 6.43 and from the correlation factor obtained from the fit (0.88). It is

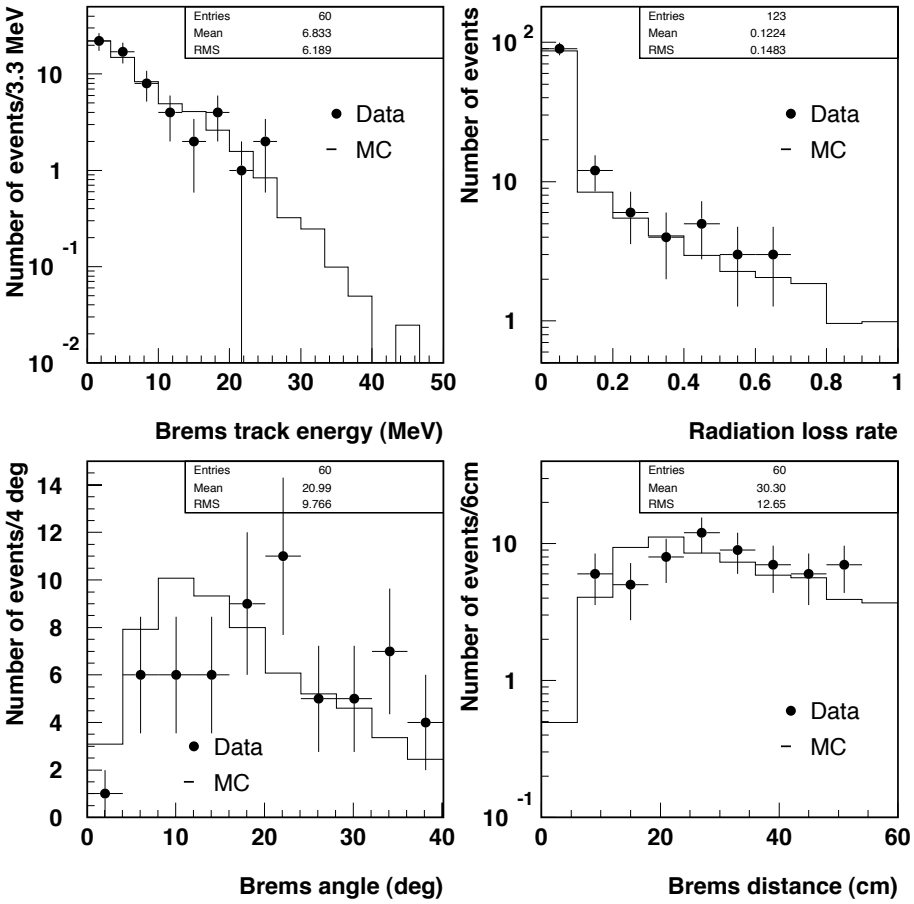

Figure 6.18: Comparison of data and MC generated bremsstrahlung tracks. Top-left: energy spectrum; Top-right: fraction of the total measured electron energy carried by the bremsstrahlung tracks; Bottom-left: angle between bremsstrahlung and electron tracks (defined in section 5.4); Bottom-right: distance to the electron track (defined in section 5.4).

customary [92, 93, 94] to fit the value of one of the parameters while fixing the other to the SM value. In our case, in view of the sensitivity of the fit to each of the parameters, we restrict the value of η to its physically allowed region ($|\eta| \leq 1$) and fit the value of ρ, which yields:

$$\boxed{\rho = 0.77 \pm 0.22} \tag{6.51}$$

where the error is of statistical origin and includes the correlation with η (an evaluation of different systematic error sources is carried out at the end of the section). When performing the fit without including the effect of the radiative corrections in the MC sample we obtain $\rho = 0.72 \pm 0.22$, about 6% less as expected. The energy spectrum corresponding to the fitted value of ρ is shown in figure 6.17. All the obtained results are compatible within the error bounds with the V-A values.

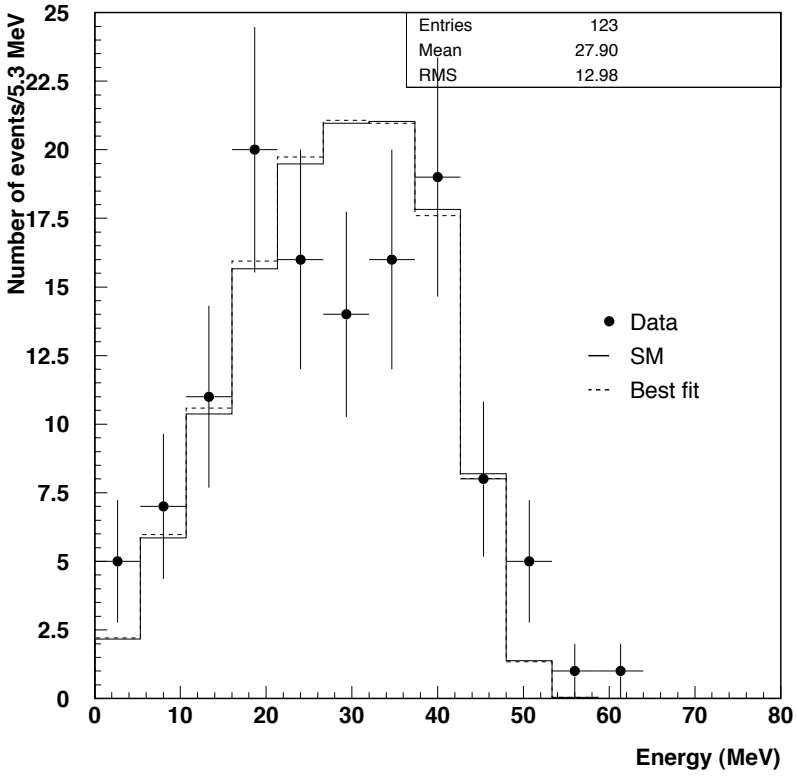

Figure 6.19: Measured, MC generated and fitted spectra of the reconstructed energy of Michel electrons.

Measured total electron energy

A similar study can be performed with the electron's *total measured energy* spectrum, which includes the energy from the reconstructed bremsstrahlung tracks. 60 bremsstrahlung tracks have been identified out of the 123 considered electron events. The features of the reconstructed bremsstrahlung tracks for data and MC generated events (kinetic energy, fraction of energy with respect to the total electron energy, angle and distance with respect to the electron track) are compared in figure 6.18. A very good agreement is observed between data and MC samples, showing that the contamination of other kind of tracks different from bremsstrahlung tracks is low in the data sample. The distribution of the angle between electron and bremsstrahlung tracks present some disagreements, most likely due to the large sensitivity of the electron direction determination to the imperfections on the spatial reconstruction.

The determination of the Michel parameters from the spectrum of the total reconstructed electron energy is carried out following the same procedure described in the previous section. Figure 6.19 shows the comparison of the total reconstructed electron energy spectra for measured and MC generated events using SM Michel parameters; they show good agreement ($\chi^2/ndf = 12.6/12$). Also shown is the energy distribution for the value of ρ providing the best fit ($\chi^2/ndf = 13/11$) to the experimental distribution:

$$\boxed{\rho = 0.72 \pm 0.19} \tag{6.52}$$

where the quoted error is of statistical origin. The result is compatible within the error bounds

with the SM value.

Estimation of the systematic errors

There are two main possible sources of systematic errors affecting our measurement of ρ, namely: an underestimation of the energy resolution in the MC sample and a shift in the global energy scale. In the measurement of ρ using the electron *total* energy we have two extra contributions. The first contribution comes from a possible bad estimation of the bremsstrahlung photon detection efficiency in the MC simulation. The second one comes from the fact that the radiative corrections calculated by equation 6.44 includes the contribution of both, the virtual photon and inner bremsstrahlung terms. Inner bremsstrahlung processes above a given energy threshold, say 1 MeV, are detectable in ICARUS (with a certain efficiency) and are not distinguishable from the bremsstrahlung emissions produced by the electron. This effect has been estimated to account for about half of the radiative correction of the ρ value ($\sim$3%) [90].

The contributions to the uncertainty of the measurement of ρ from each of the previous sources are estimated using the MC sample. We have alternatively applied to the MC energy spectrum a Gaussian smearing (which simulates the effect of an extra contribution to the energy resolution), an overall shift of the energy scale and a bad estimation of the bremsstrahlung detection efficiency. Table 6.8 summarizes the effects of each of these error sources on the determination of ρ, for both, the measurements using the electron track and electron total kinetic energy.

	Electron track	Total
$\rho \pm \Delta\rho^{st}$	0.77 $\pm$ 0.22	0.72 $\pm$ 0.19
$\Delta\rho^{\sigma}$ $\sigma = 5\%$	$\pm$0.01	$\pm$0.01
$\sigma = 10\%$	$\pm$0.03	$\pm$0.02
$\Delta\rho^{\Delta}$ $\Delta = \pm 1\%$	$\pm$0.05	$\pm$0.05
$\Delta = \pm 2\%$	$\pm$0.10	$\pm$0.10
$\Delta\rho^{\epsilon}$ $\epsilon = \pm 5\%$	—	$\pm$0.02
$\epsilon = \pm 10\%$	—	$\pm$0.03
$\Delta\rho^{rad}$	—	$\pm$0.02

Table 6.8: Summary of the different systematic error sources and their impact on the determination of ρ. The second (third) column refers to the effect on the result obtained with the analysis of the electron track (total) energy. $\Delta\rho^{st}$ is the statistical error. $\Delta\rho^{\sigma}$, $\Delta\rho^{\Delta}$ and $\Delta\rho^{\epsilon}$ are the systematic errors inferred on ρ by assuming an uncertainty σ, Δ and ϵ of the energy resolution, absolute energy scale and bremsstrahlung detection efficiency, respectively. $\Delta\rho^{rad}$ is the systematic uncertainty coming from the inclusion of the inner bremsstrahlung contribution to the radiative corrections.

Some remarks concerning table 6.8 can be done:

- The error is clearly dominated at this level by the statistical uncertainty ($\sim$30%). The expected improvement, when adding the whole available stopping muon event sample from the technical run, is about a factor 3, since approximately 9–10 times the statistics used in the present analysis will be available.
- The underestimation of the energy resolution is not expected to be much larger than 5%, since it is esentially determined by the signal/noise ratio and the additional contribution

from the electron lifetime, recombination and t_0 corrections, all included in the MC sample. As mentioned in section 5.4.3, both the signal and noise shapes have been obtained from a fit to the patterns observed during the T600 technical run. We have considered a Gaussian smearing of width σ with conservative width values $\sigma = 5\%$ and 10%, and found contributions of about 2% and 4%, respectively, to the measurement error. However, it must be noted that the main difference introduced by the extra energy resolution contribution is at the high energy tail, around the end-point. Therefore, the related systematic error can be reduced by performing the fit exclusively using the low and center parts of the spectrum. We have checked this hypothesis by removing alternatively the last and the last two bins of the measured Michel spectrum during the fit. In the latter case, no significant contribution to the systematic error is found for $\sigma = 5\%$ and about 1% for $\sigma = 10\%$.

- The most important source of a systematic error comes from a possible bad estimation of the overall energy scale. The energy scale for a mip has been determined in section 6.2.1, and the value is quoted in equation 6.28. The accuracy of the measurement is between 1% and 2% including systematic effects. The corresponding change of the measured value of ρ is between 7% and 15%, below the statistical error for the given data sample. Moreover, the accuracy of the absolute energy scale also depends on $\sqrt{N}$ (with N the number of events), and therefore is expected to be reduced by the same factor as the statistical error when more events will be added. For a 10 times bigger data sample we expect this error to be reduced to $\sim 4\%$.

- For the measurement using the total electron energy we must also take into account possible systematic effects introduced by the bremsstrahlung track detection efficiency, which is tuned in the MC sample. The efficiency has alternatively been shifted (up and down) by 5% and 10%. The change on ρ is about 3% at most, which is below both, the statistical and systematic errors from the energy scale shift. However, this error does not depend on the statistics and therefore is expected to be (relatively) more significant when increasing the size of the data sample.

- Since inner bremsstrahlung emissions above a given threshold are detected in ICARUS (with a given efficiency), the radiative corrections are overestimated in the case of the electron *total* energy spectrum, and an extra 3% contribution to the systematic uncertainty must be added. In order to properly correct for this effect, one should compute the contribution of the inner bremsstrahlung emissions to the muon decay spectrum properly folded with the bremsstrahlung detection efficiency. However, at this level, this contribution is negligible with respect to the statistical error or the systematic error from the absolute energy scale.

To summarize, the error of our determination of ρ is about 30% from statistical sources and about 15% from systematic sources. By multiplying the statistics of the data sample by a factor 10 (which is expected when including the whole stopping muon event sample from the technical run) and selecting the optimal physical region of the Michel spectrum where to perform the fit, we can reduce these errors down to 10% statistical and 4% (6%) systematic for the measurement using the electron track (total) energy.

Comparison with existing measurements

The Michel parameter ρ has been measured in the past by several authors (see table 6.9). Peoples [92], Sherwood [93] and Fryberger [94] have measured ρ in the late 60's using the high

Author	Value	Assumption
Peoples	0.750 ± 0.003	$\eta \equiv 0$
Sherwood	0.760 ± 0.009	$\eta \equiv 0$
Fryberger	0.762 ± 0.008	$\eta \equiv 0$
Derenzo	0.752 ± 0.003	$-0.13 < \eta < 0.07$
SLD	$0.72 \pm 0.09 \pm 0.03$	lepton univers.
CLEO	$0.747 \pm 0.010 \pm 0.006$	lepton univers.
ARGUS	0.731 ± 0.031	lepton univers.
OPAL	$0.78 \pm 0.03 \pm 0.02$	lepton univers.
DELPHI	$0.78 \pm 0.02 \pm 0.02$	lepton univers.
ALEPH	0.742 ± 0.016	lepton univers.
This analysis	$0.77 \pm 0.22 \pm 0.10$	$\lvert\eta\rvert \leq 1$
Statistics $\times 10$	$\pm 0.07 \pm 0.03$	$\lvert\eta\rvert \leq 1$

Table 6.9: Results from previous measurements of the Michel ρ parameters. First (second) quoted error is of statistical (systematical) origin. Single error bounds correspond to statistical and systematic errors added in quadrature.

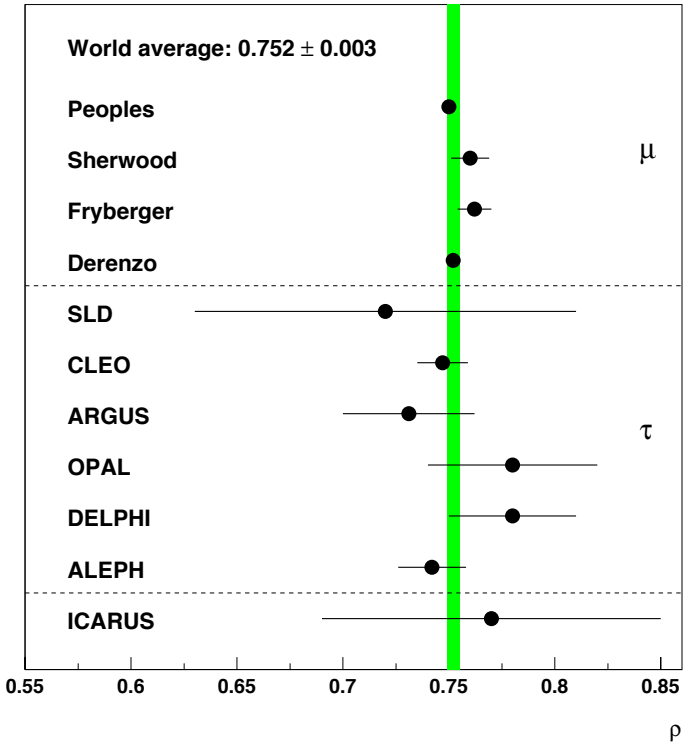

Figure 6.20: Comparison of the existing measurements of ρ in μ and τ decays with the obtained value with ICARUS (foreseen error for increased statistics).

energy part of the decay electron spectrum with data obtained from magnetized spark-chambers. Given the high correlation of ρ and η for this part of the spectrum, it is not possible to measure both parameters at the same time (as we have seen above in our case), and all these authors assume the V-A value $\eta = 0$. Derenzo [95] used a liquid hydrogen bubble chamber to measure the lower part of the energy spectrum, and combined his data with the previous ones (essentially those from Peoples) into a common two-parameter fit, obtaining ρ with a precision of about 0.4%, the most accurate existing measurement with no assumptions on the value of η.

The previous results have been obtained using dedicated experiments, where data samples amount typically to several hundred thousand events. More recently, the data from electron-positron colliders have been used to measure the Michel parameters from the purely leptonic τ decay [96, 97, 98, 99, 100, 101] near the Z_0 resonance. These measurements are based on the analysis of samples typically amounting up to several ten thousand events. The results are compared with those from the dedicated experiments in table 6.9 and figure 6.20. A result of the order of the ones obtained from τ decay experiments is expected from the analysis of the total stopping muon sample from the ICARUS T600 technical run (about 5000 events).

6.3.2 Electron energy resolution

The Michel electron energy spectrum can be used to determine the detector energy calibration and resolution without relying on the MC sample. This is usually possible due to the simple and well known analytical dependence of the decay probability, as well as to the presence of the sharp end-point in the energy spectrum. In our case this standard procedure is not possible, given the non-negligible fraction of non-accounted for kinetic energy when measuring Michel electrons. The effect is illustrated in figure 6.21 where, for the MC sample, we show the electron generated and reconstructed kinetic energy distributions (left) and the difference between them (right). The mean difference between the generated and reconstructed energies is about 20%, and is due to the fraction of energy escaping the LAr sensitive volume and inefficiencies in the reconstruction procedure, mostly from the bremsstrahlung track reconstruction. Such inefficiencies, as we showed in section 5.4.3, are partially due to the tight criteria required on the spatial selection of the bremsstrahlung candidates imposed by the presence of different (out of time) events in the same region of the detector and are, therefore, expected to be reduced in data taken at underground conditions.

In the present analysis we follow an approach based on the study of the MC sample to extract the energy resolution of the detector. It must be noted that the contributions from the electron lifetime correction and t_0 determination are not included and they have been computed separately in sections 6.1.2 and 6.2.2 respectively.

Resolution in the electron track energy measurement

We have computed the energy resolution as a function of the *electron track energy*, since this quantity is not biased by the effects resulting from the bremsstrahlung detection inefficiency. We divide the MC sample in bins according to the value of the generated electron track energy (E^e_{MC}). For every bin, a Gaussian fit is performed to the distribution of $(E^e_{reco} - E^e_{MC})/E^e_{MC}$, where E^e_{reco} is the reconstructed electron track energy. Only the central part of the distributions are fitted, in order to avoid the non-Gaussian tails. The fitted range ([-0.15–0.1]) is selected arbitrarily so that the fit yields $\chi^2/ndf \simeq 1$ for all considered bins, and the effect of choosing wider ranges is included as a systematic error in the final result. Figure 6.22 (top) shows, for four bins of the generated electron track energy, the distribution of $(E^e_{reco} - E^e_{MC})/E^e_{MC}$ together

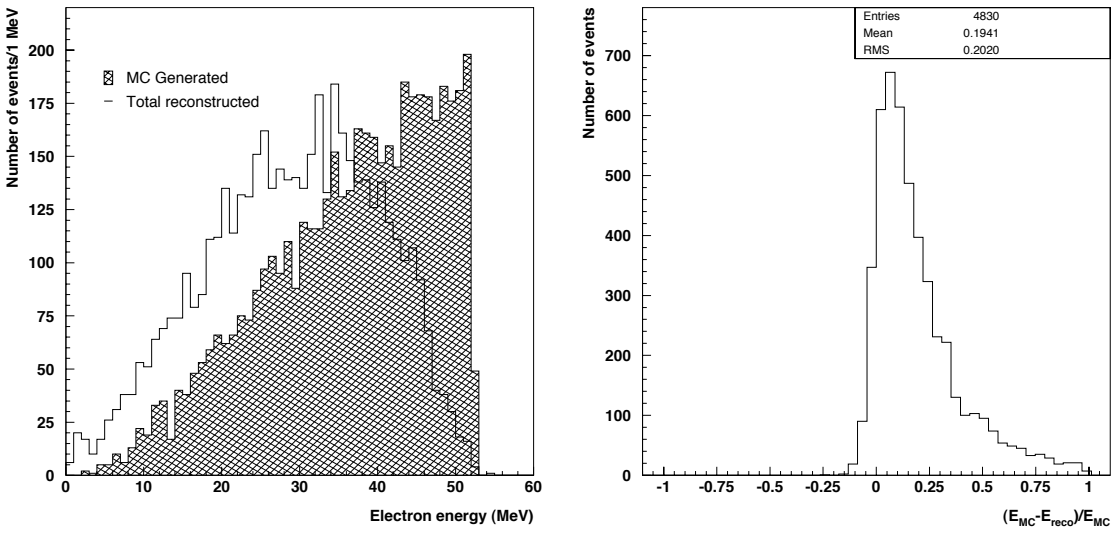

Figure 6.21: Left: Comparison of the MC generated and reconstructed kinetic energy distribution for the electron sample. Right: Difference between generated and reconstructed kinetic energies (normalized to the generated energy) for the electron MC sample.

with the fitted Gaussian function. Events in the tails at both, negative and positive values, have been visually inspected. In both cases they are due to inefficiencies of the reconstruction procedure. The tail at negative values is produced by events where the actual electron track is not properly identified and a bremsstrahlung or a fake track (generally of lower energy than the real electron track) is taken instead. The tail at positive values is mostly produced by events where one or more bremsstrahlung tracks are close to the electron track in the main view, so that the reconstruction algorithm merge them together into a single (more energetic) track. Both tails are depleted for high electron track energies, since in this case almost all the electron energy is lost by ionization and hence fewer (and less energetic) bremsstrahlung tracks are expected.

Figure 6.22 (bottom) shows the values of the energy resolution (σ/E^e_{MC}) as a function of the generated electron track energy, measured in the MC sample. The central and error values are taken from the Gaussian fit performed at every E^e_{MC} bin. A fit of the measured points is performed by the function:

$$\frac{\sigma}{E^e_{MC}} = \frac{a}{\sqrt{E\ [\mathrm{MeV}]}} \oplus b \tag{6.53}$$

where a and b are free parameters. The minimal χ^2 value ($\chi^2/ndf = 0.7$) is yielded by the following values of the parameters:

$$\boxed{\begin{array}{rcl} a & = & (9 \pm 1 \pm 1)\% \\ b & = & (3.9 \pm 0.2 \pm 0.1)\% \end{array}} \tag{6.54}$$

where the first quoted errors are of statistical origin and the second ones are the systematics obtained by varying the bounds of the interval used in the Gaussian fits.

Resolution in the measurement of the total electron energy

A similar procedure can be carried out to extract the energy resolution in the measurement of the total electron energy. The MC sample is divided into bins according to the value of the generated

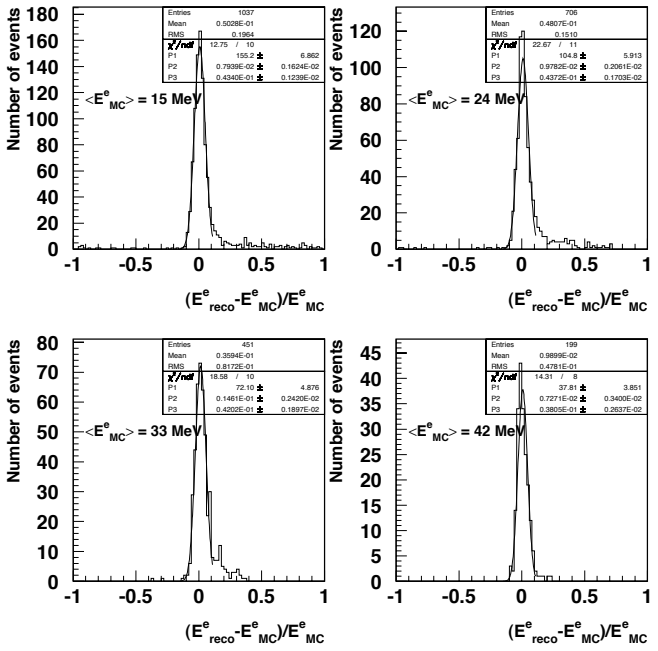

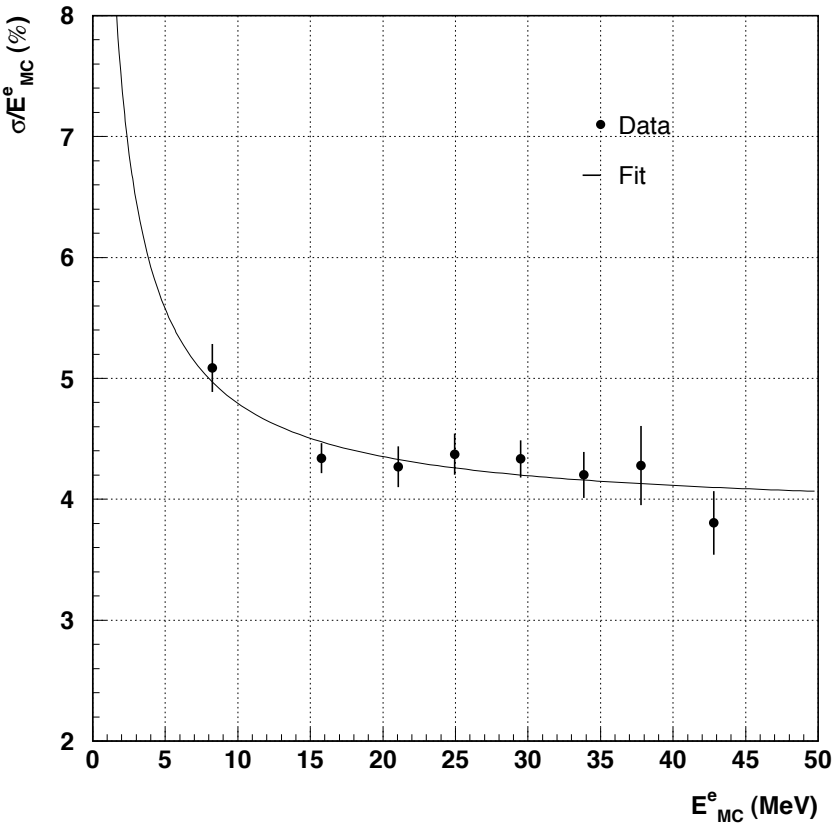

Figure 6.22: Top: distribution of $(E^e_{reco} - E^e_{MC})/E^e_{MC}$ for four E^e_{MC} bins of the MC sample; superimposed is the fitted Gaussian; quoted are the values of the fitted parameters (P1 is the overall normalization, P2 and P3 the Gaussian mean value and σ, respectively). Bottom: measured energy resolution (in %) as a function of the MC generated electron track energy; superimposed is the fitted resolution curve.

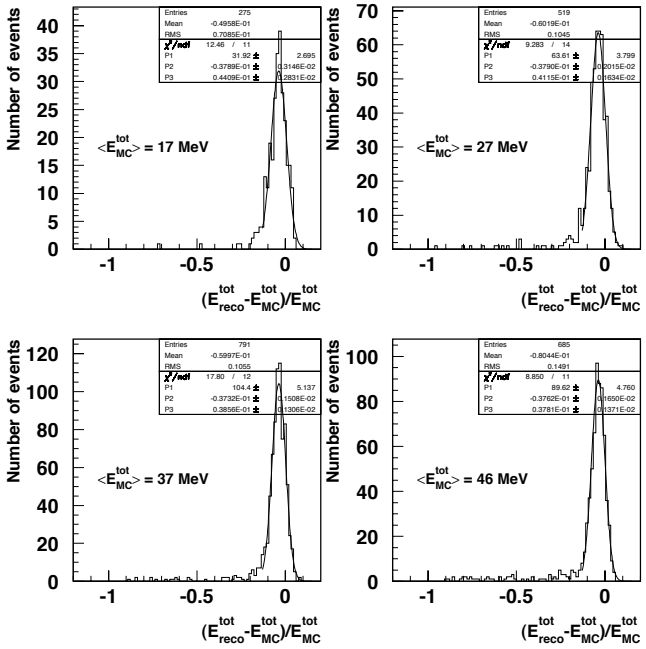

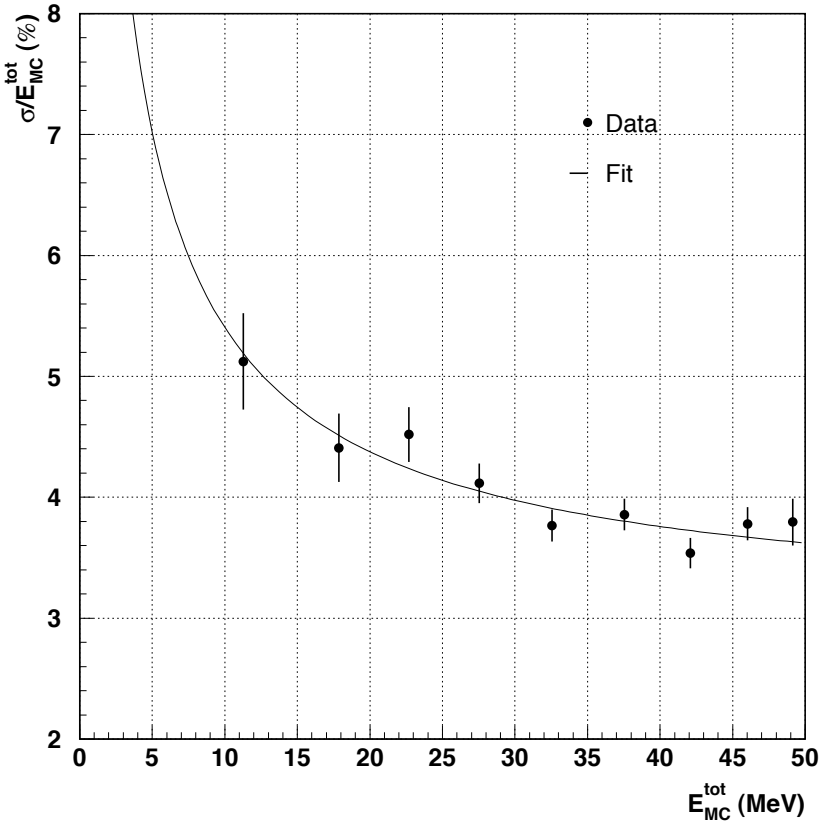

Figure 6.23: Top: distribution of $(E^{tot}_{reco} - E^{tot}_{MC})/E^{tot}_{MC}$ for four E^{tot}_{MC} bins of the MC sample; superimposed is the fitted Gaussian; quoted are the values of the fitted parameters (P1 is the overall normalization, P2 and P3 the Gaussian mean value and σ, respectively). Bottom: measured energy resolution (in %) as a function of the MC generated electron total energy; superimposed is the fitted resolution curve.

total electron energy (E^{tot}_{MC}). The generated energy is compared with the reconstructed energy (E^{tot}_{reco}), including the contribution of all reconstructed bremsstrahlung tracks, regardless of the spatial selection criteria or detection inefficiencies. A Gaussian fit is carried out to the central part of the distribution, in order to get the resolution (σ/E^{tot}_{MC}). The interval used in the fit is fixed to [-1.2–0.2] so that $\chi^2/ndf \simeq 1$, and the effects of varying this interval is included in the final result as a systematic error. Figure 6.23 (top) shows, for four bins of the generated total energy, the distribution of $(E^{tot}_{reco} - E^{tot}_{MC})/E^{tot}_{MC}$ together with the fitted Gaussian distribution. The systematic shift (about 4%) and tail at negative values are due to the energy losses produced by various effects, namely: photons escaping the LAr sensitive volume, bremsstrahlung tracks not reconstructed (because of failures of the reconstruction procedure or because the energy is below the energy detection threshold) and the energy of the mass of the electron/positron pair when the bremsstrahlung photon undergoes a pair creation process (this energy is not accounted since no distinction between Compton and pair production processes is carried out at the reconstruction level).

The values and errors of the resolution as a function of the MC total energy, obtained from the Gaussian fits, are shown in figure 6.23 (bottom). They can be fitted using the function in equation 6.53. The parameters yielding the minimal χ^2 value ($\chi^2/ndf = 1.0$) are:

$$\begin{aligned} a &= (14 \pm 2 \pm 2)\% \\ b &= (3.0 \pm 0.2 \pm 0.1)\% \end{aligned} \tag{6.55}$$

where the first errors are of statistical origin and the second ones are the systematic errors obtained from varying the size of the interval in the Gaussian fits. A worse resolution is obtained in this case in comparison to the one obtained for the electron track energy. This is an expected result since the bremsstrahlung tracks are, on average, of lower energy and thus their contribution to the total resolution is higher.

6.3.3 Angular distribution

The angular distribution of the Michel electron sample provides a test of the isotropy and homogeneity of the detector and the performance of the reconstruction tools. The direction of the electron is defined as the one of the vector joining the initial and final hits of the first electron segment, and is described by the zenith and azimuth angles, θ and ϕ (defined in section 4.4.1). Also useful is the angle between the electron and muon tracks (α), where the muon direction is defined by the vector joining the initial and final hits of the first muon segment. The data sample used to build the different angular distributions is the intersection of the good spatial reconstruction muon sample with the good calorimetry electron samples (160 events).

The distribution of the angle ϕ is shown in figure 6.24. A good homogeneity (within statistical fluctuations) is observed for both, MC and data samples. In particular, it is important to note the absence of any depletion of events near 0 and 180 degrees, i.e. for electrons traveling along the drift direction. This is an important result, since the reconstruction procedure (see chapter 4), and in particular the hit fine reconstruction, could be less efficient for events extending along the drift direction.

The situation is somewhat different for the distribution of $\cos\theta$, shown in figure 6.25 (left). Although the MC sample distribution is compatible with a flat distribution, there is a clear slope in the distribution of the data sample. The effect is explained by the presence of the muon track. Figure 6.25 shows, for the data sample (no muon track is present in the MC), the distribution of the cosine of the angle between the electron and muon tracks (α). There is

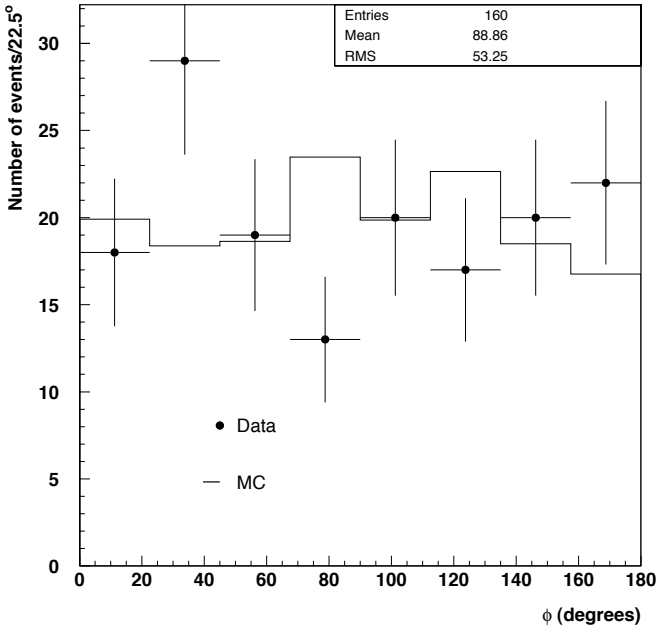

Figure 6.24: Distribution of the angle ϕ for MC and data electron samples

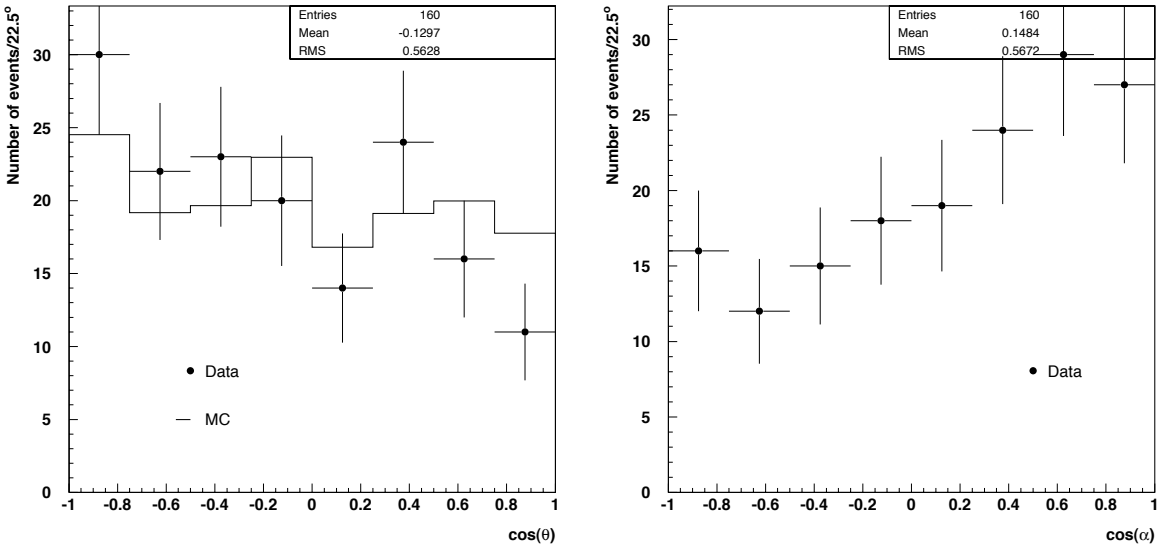

Figure 6.25: Left: $\cos\theta$ distribution of the MC and data electron sample. Right: $\cos\alpha$ distribution for the data sample.

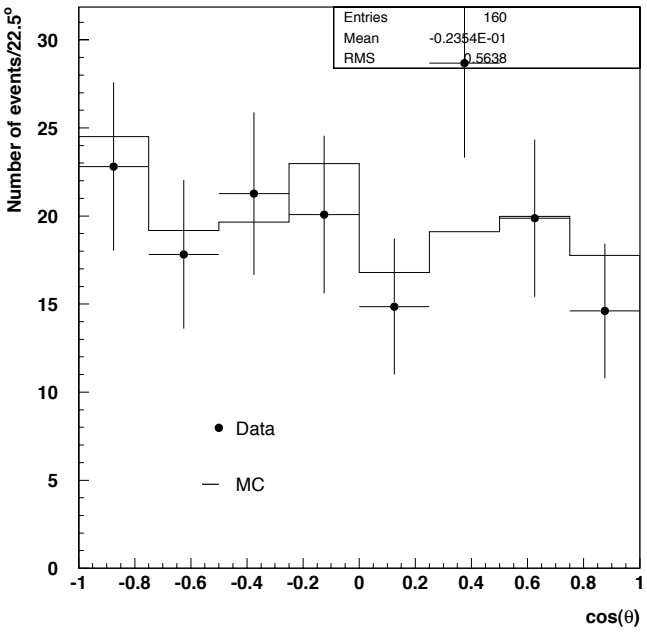

Figure 6.26: $\cos\theta$ distribution of the MC and the corrected data electron samples (see text for details).

an excess of events in the direction of the muon (positive $\cos\alpha$) due to the inefficiencies in the reconstruction of events in the direction opposite to the muon (negative $\cos\alpha$). This excess is expected since the probability of the electron and muon tracks to overlap in the main view is higher for negative values of $\cos\alpha$ and, as we showed in section 5.1.2, these events are rejected from the data sample during the event quality selection. Since the muon tracks are produced by cosmic ray interactions, they are all downward going, i.e. they have negative $\cos\theta$ values, hence the downward direction is also favored for the electron tracks. We can try to correct for this effect using the distribution of $\cos\alpha$ which, aside from reconstruction inefficiencies, is expected to be flat. Every event is weighted by the following factor:

$$w = \frac{N_{tot}}{n_{bins} \cdot N_i} \tag{6.56}$$

with N_{tot} the total number of events, n_{bins} the number of bins in the $\cos\alpha$ histogram (8 in our case), and N_i the number of entries in the bin of the $\cos\alpha$ histogram containing the event to be weighted. The resulting $\cos\theta$ distribution of the data sample is shown in figure 6.26 compared to the (unweighted) distribution for the MC sample. The agreement between data and MC samples is clearly improved, yielding a good homogeneity within the statistical fluctuations.

6.3.4 Range

The range constitutes an indirect measure of a particle's kinetic energy, provided the stopping power of the medium for the given particle (dE/dx) is known. The electron *track* energy can be estimated from the range by integrating the Bethe-Bloch equation for electrons/positrons (equation 5.27), which accounts for the energy transfer through ionization only. On the other hand, by integrating the whole expression of the dE/dx, including radiation losses (equation 5.26)

we can obtain the mean *total* kinetic energy of the electron as a function of the range. We have measured both, the electron track and total kinetic energies, using the range, and we have compared the results with the direct measurement based on the calorimetric reconstruction, to evaluate the resolution that can be achieved using this method. In order to better evaluate the power of the method, data and MC events are further selected by imposing that at least 50% of the hits from the electron track in the main view match with a hit from the secondary view, during the spatial reconstruction (section 5.3.1). This ensures an optimal quality of the reconstructed range, and selects 51 electron data events.

Three different methods of computing the electron range are tested:

- Method 1. The sum over the crossed distances associated to the hits.
- Method 2. The sum over the crossed distances associated to the segments.
- Method 3. The distance between the initial and final hits.

The reconstructed range spectra using the three methods for both, data and MC samples, are compared in figure 6.27. Very good agreement is found between data and MC distributions for the three methods, despite the low statistics available in the data sample.

In order to evaluate which of the three methods provides the best estimate of the electron range, a comparison between the measured range and the corresponding theoretical value, as a function of the generated kinetic energy, is performed in the MC sample. Figure 6.28 shows the values of the mean range measured as a function of the generated electron track energy (top plot) and of the total generated electron energy (bottom plot), together with the theoretically expected curves. Data points and errors are the mean value and error obtained from a Gaussian fit to the distribution of the range for the different bins of the generated energy. In both cases the best agreement between the measurement and the theoretical expectation is achieved by the segment based measurement method (method 2).

Method 2 is therefore used to estimate the electron track and total kinetic energies. The energy resolution can be obtained from the range resolution for both, the electron track and total energies. Since the electron track energy depends linearly on the mean range (see top figure 6.28), the electron track energy resolution is equal to the resolution in the range measurement. On the other hand, since the electron total kinetic energy grows with the range faster than linearly, the resolution obtained from the range provides a lower bound of the resolution in the total energy measurement. Figure 6.29 shows the resolution in the range obtained from the MC sample as a function of the generated electron track energy (top) and of the generated electron total kinetic energy (bottom). The central values and error bars are obtained from a Gaussian fit to the measured range in the different bins of generated electron track or total kinetic energy.

The electron *track* energy can thus be determined from the range with the resolution shown in figure 6.29 (top): about 15% for energies above 30 MeV and increasing at lower energies to about 35% at 10 MeV. The resolution at low energy is dominated by the error on the range determination and fluctuations in the energy loss. Both effects are averaged for longer (more energetic) tracks, resulting in a better energy resolution. As expected, a better result is obtained for the whole energy range using the calorimetric reconstruction of the event. On the other hand, the resolution in the determination of the electron *total* energy is independent of the energy (about 45%) due to the radiation losses. The measured *mean* range value as a function of the electron energy is well reproduced by the theoretical curve as shown in figure 6.28 (bottom). However, this curve is computed assuming the continuous slowing down approximation (CSDA) [73]. In this approximation, the rate of energy loss at every point along the track is assumed to be equal

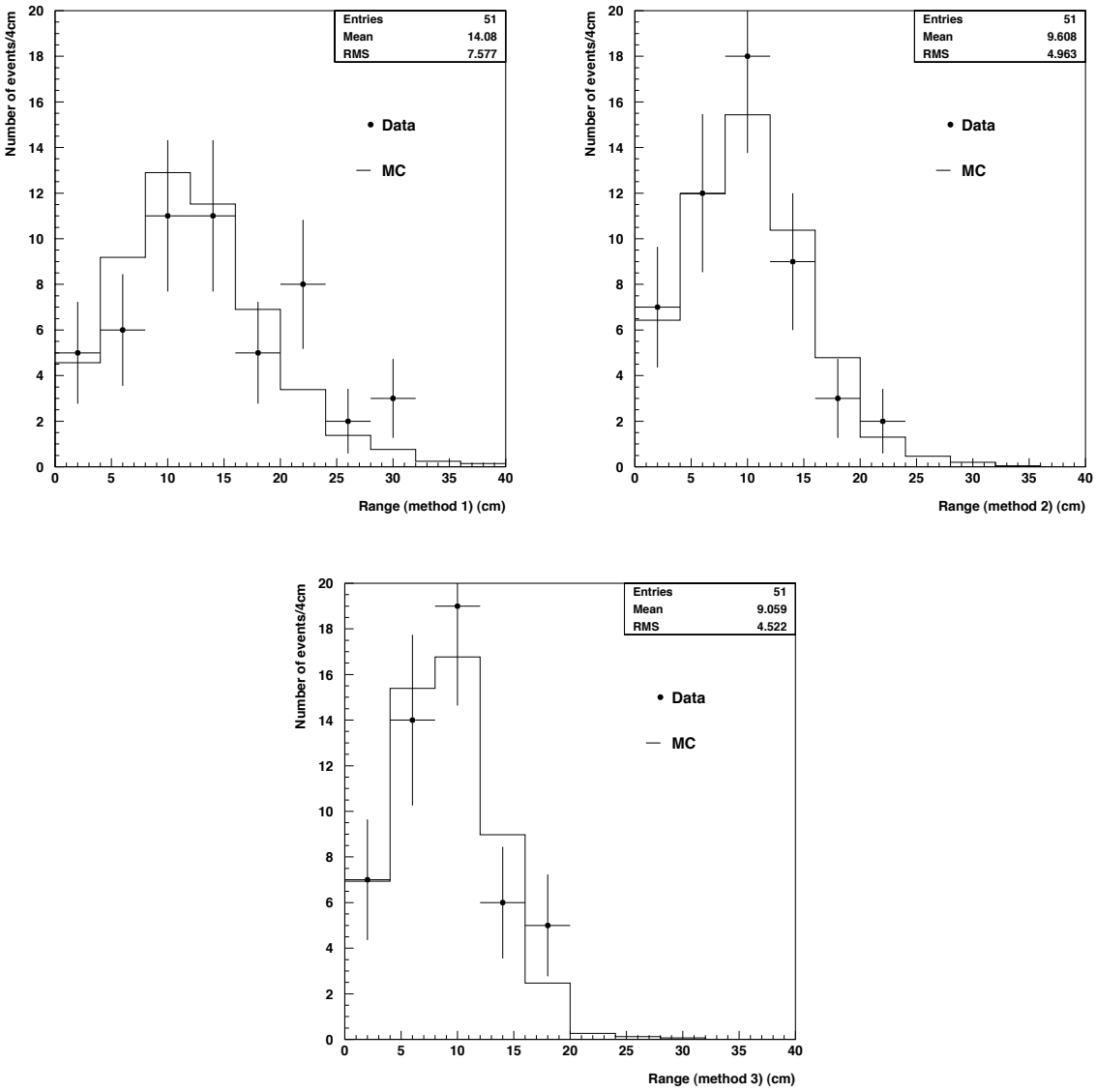

Figure 6.27: Electron track range measured with 3 different methods for MC and real (data) events.

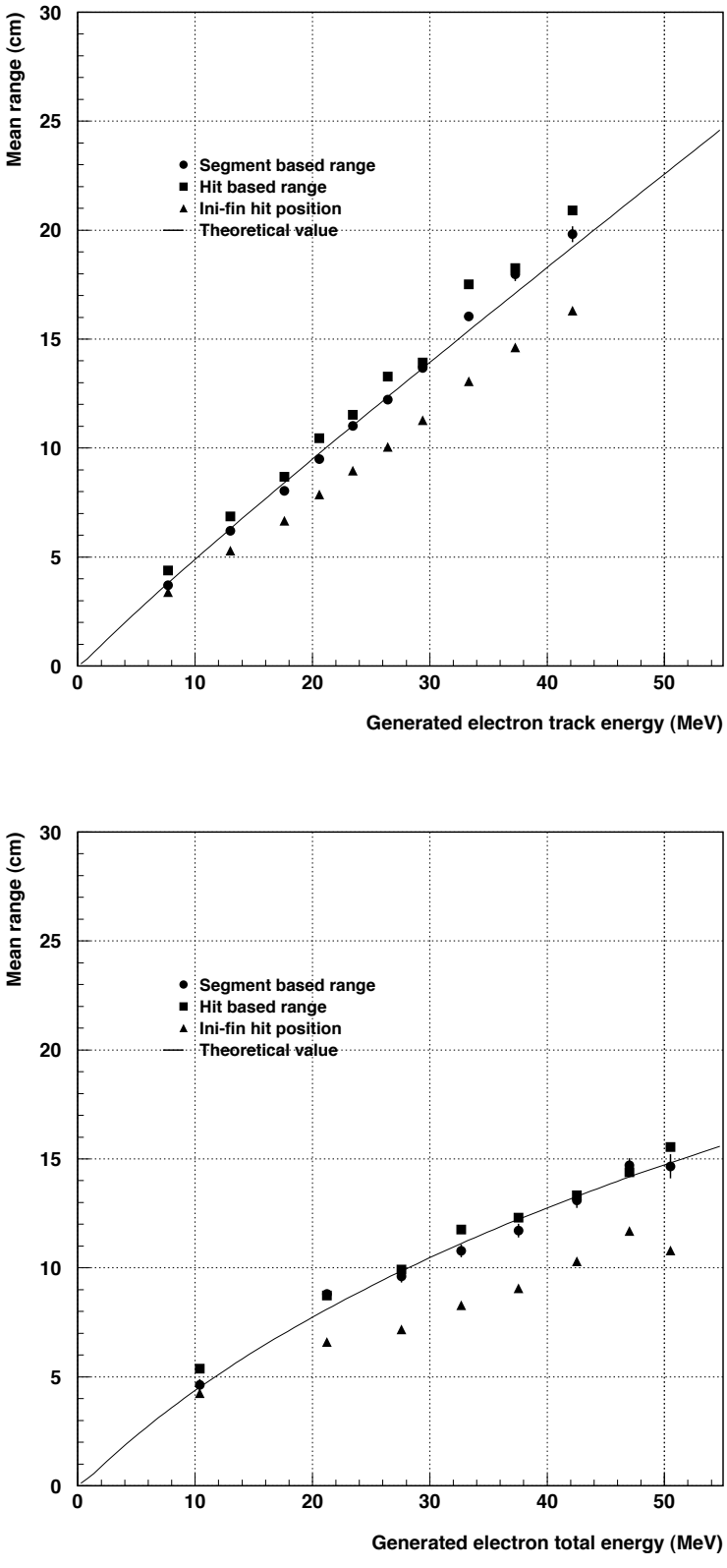

Figure 6.28: Comparison of the three range measuring methods (obtained from the MC sample) and the theoretical range vs. kinetic energy curve for both, the electron track with no radiation included (top) and electron total event including the radiation losses (bottom).

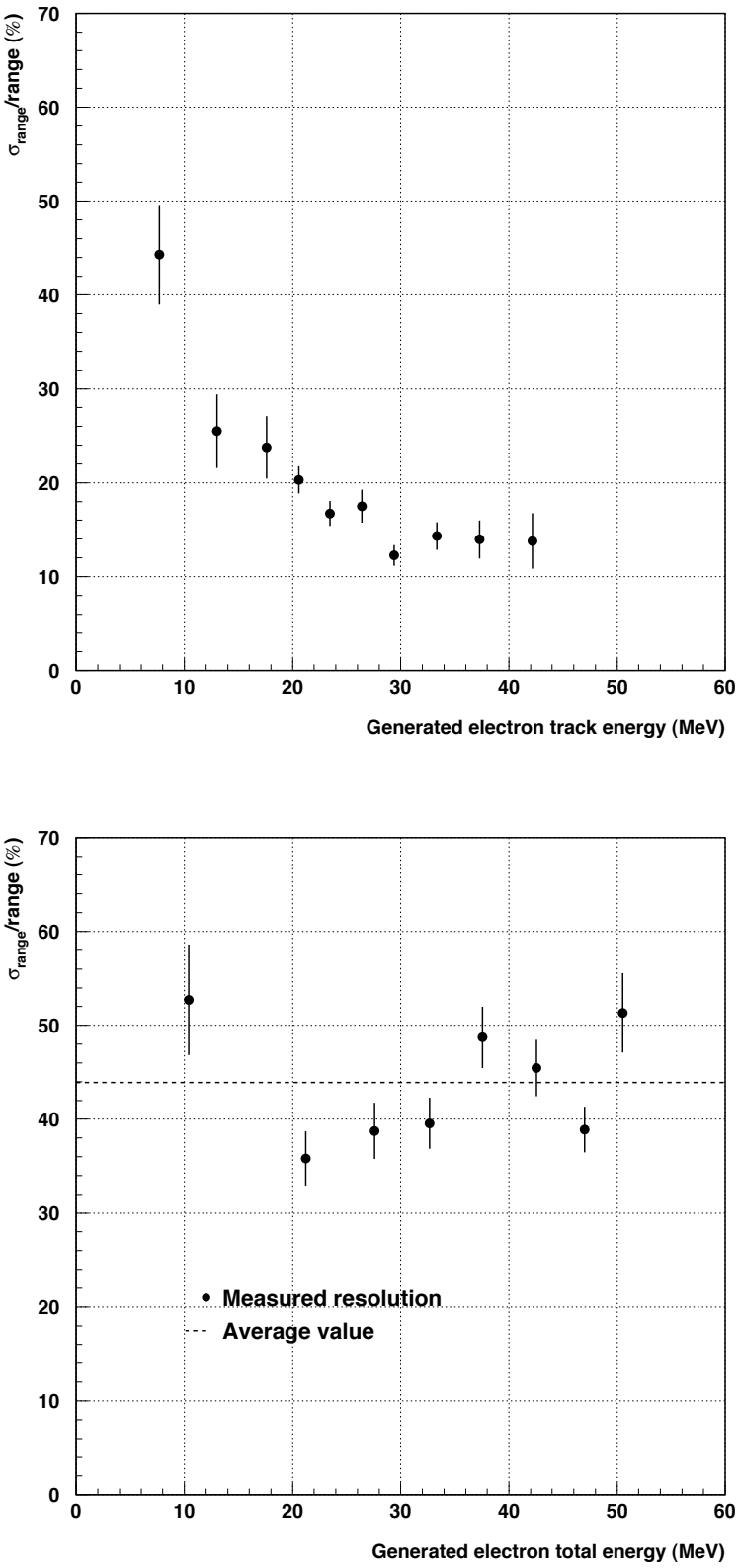

Figure 6.29: Range resolution as a function of the generated electron track energy (top) and generated total electron energy (bottom).

to the total stopping power, neglecting energy loss fluctuations. Since bremsstrahlung photon emission is a discrete process, the CSDA approximation describes it correctly only on the average, but not on an event by event basis. This effect results in a large dispersion on the actual range for a given value of the electron total energy, as further illustrated in figure 6.30, where the scatter plots show the dispersion on the measured range with respect to the expected mean value as a function of both, the electron track and electron total energies. The measured electron track and total kinetic energy spectra in both, MC and data samples, is shown in figure 6.31. The agreement between data and MC is very good despite the low statistics available in the data sample. As expected the electron track energy is better determined than the total energy, for which a long tail, up to 150 MeV is found, due to the effect of radiation energy losses.

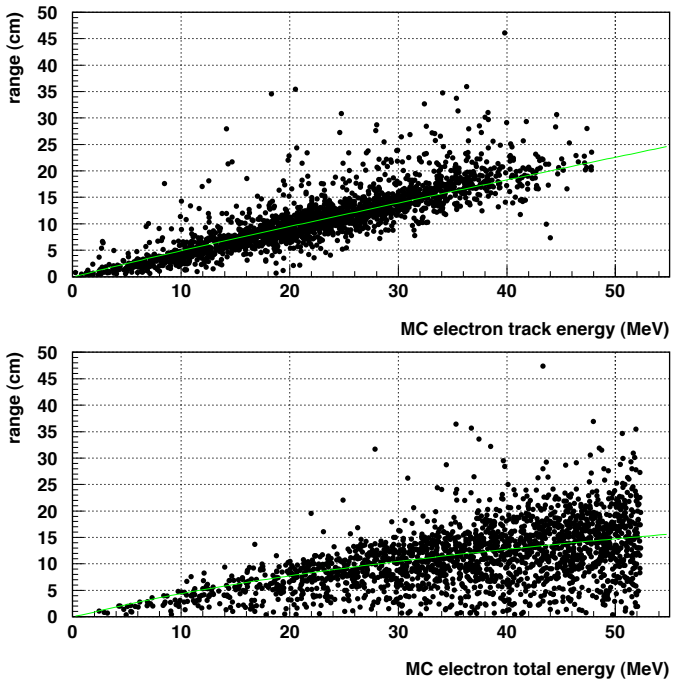

Figure 6.30: Measured (dots) and theoretical (line) range as a function of the generated electron track energy (top) and generated total electron energy (bottom) for the MC sample.

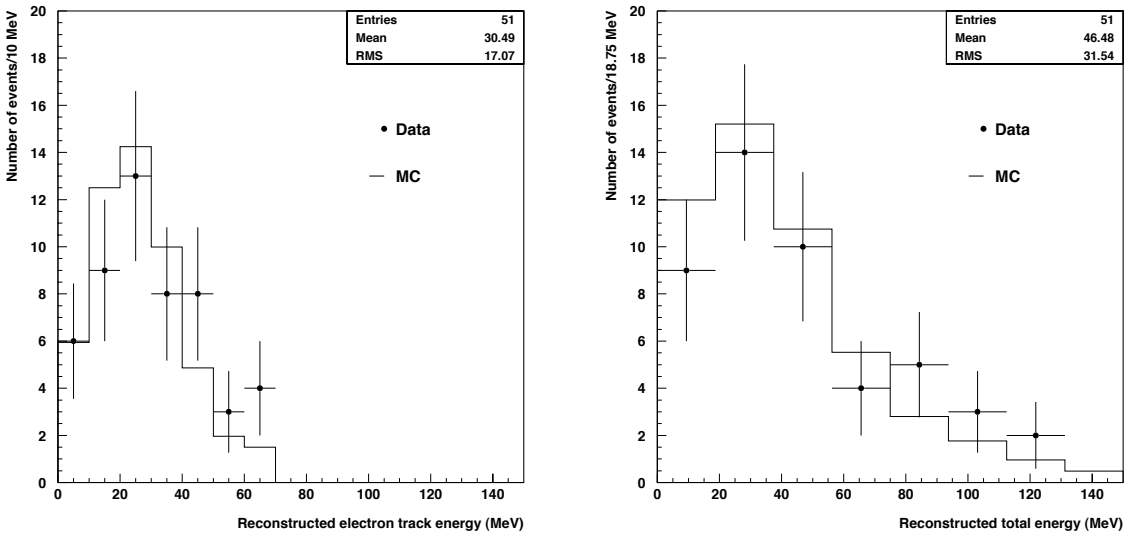

Figure 6.31: Data and MC electron track (left) and total kinetic energy (right) measured from the electron track range.

Conclusions

The results of this dissertation are separated in two different parts. The first one regards the study of the Slow Control data acquired during the technical run of the detector, in summer 2001, treated in chapter 3. The second part regards the reconstruction and analysis of the T600 cosmic ray data (chapters 4, 5 and 6).

A **Slow Control system** composed of several sensors built and/or tested at ETH was installed in the ICARUS T600 detector. This system was intended to monitor on-line the responses of the detector to the extreme pressure and temperature conditions happening during the vacuum and cooling phases, and to control the LAr level and temperature during the filling, data taking and draining phases. The sensors measured the distance between the dewar wall and wire chamber frame, the elongation of the springs attached to the wires of the wire chamber, as well as the LAr level and temperature in the dewar. The **off-line analysis of the Slow Control data** has led us to a better understanding of the thermodynamical and mechanical behaviour of the detector as a large, ultra-pure LAr, cryogenic device. In particular, this analysis has demonstrated the following features:

- the elastic deformation of the dewar walls with pressure, with displacement coefficients ranging between 20 and 28 μm/mbar.
- the stability and uniformity of the temperature in the LAr volume all along the technical run: the average temperature is constant within less than 0.5 K, and the measured maximum temperature difference between any two points in the LAr sensitive volume is less than 0.7 K.
- the absence of a significant contraction of the wires above 300 μm during the cooling and warming up phases.

On the other hand, this analysis has pointed out some unexpected features that should be avoided or corrected for future runs, namely:

- we have found evidences of a contact between the one of the dewar walls and the wire chamber frame at the end of the vacuum phase; although no major consequences on the detector have been observed, a contact must be avoided in order to reduce the risk of permanent deformations both in the dewar and frame;
- the measured temperature gradients during the cooling and warming up phases have been found to be above the prescription (up to 76 K where found for a prescription of 40 K); this fact could have led to a (small) deformation of the dewar wall and/or frame, as also pointed out by the observed remnant wall/frame relative displacement (1.2 mm) at the end of the run, with respect to the positions measured before the run started;

- we have found evidences of the existence of a leak in the dewar causing a loss of LAr at a rate of about 40 l/day.

The second part of this work has been devoted to the **reconstruction and analysis of the cosmic ray data** acquired during the ICARUS T600 technical run. To this purpose, a set of tools for the automatic three-dimensional reconstruction of the events have been developed, and their performance has been evaluated using cosmic ray data. The reconstruction tools have been optimized for the case of stopping/decaying muons, and a sample of 259 events of this type has been reconstructed and analyzed. The muon track sample has been used to compute the drift electron lifetime and the electron-ion recombination factor in LAr at 500 V/cm.

The **drift electron lifetime** is computed by fitting an exponential function to the measured charge attenuation as a function of the drift distance. A method for the calculation of the charge attenuation when the absolute drift distance is unknown (out of time events) has been developed, and the event sample has been used to compute the electron drift lifetime along the period of the considered data sample. The measured values are in the range

$$\boxed{\tau_e = 1.2 - 1.4 \text{ ms}}$$

corresponding to a mean drift distance between 1.9 and 2.2 m (the maximum possible drift distance in the T600 detector being 1.5 m). These results are in agreement with the ones obtained by a dedicated set of LAr purity monitors and by the off-line analysis of crossing muon tracks.

We have used the measured electron lifetime to unfold the effect of the charge attenuation from the subsample of events with known absolute drift distance. This subsample has been used to compute the **recombination factor** (R) for the minimal value of the energy loss per crossed distance (dE/dx). This value is used as a reference to tune the absolute drift coordinate of the remaining events, that can be then also corrected for the charge attenuation. Finally, we have used the whole data sample to parameterize the evolution of R with dE/dx, using an expression similar to the Birks' law. The measured recombination factor is given by

$$\boxed{\frac{1}{R} = \frac{1}{0.604 \pm 0.008} + (0.13 \pm 0.01[\text{cm/MeV}]) \cdot \left(\frac{dE}{dx} - \left.\frac{dE}{dx}\right|_{mip} \right)}$$

We have compared our results with previous measurements existing in the literature. A disagreement with the data acquired with the 3 ton detector has been found, which is presently under investigation.

The measured values of the drift electron lifetime and the recombination factor have been used to perform the full calorimetric reconstruction of the stopping muon data sample. The electrons from the muon decay have been then studied. We have measured the Michel ρ parameter using a sample of 160 electron tracks, and obtained the value

$$\boxed{\rho = 0.77 \pm 0.22 \text{ (stat.)} \pm 0.10 \text{ (sys.)}}$$

The overall expected error when including the whole stopping muon sample from the T600 technical run has been estimated in about 10%. We have also determined the **energy resolution**

due to the electronic noise and reconstruction effects from a MC sample of muon decay electron, and obtained:

$$\boxed{\frac{\sigma}{E} = \frac{(9 \pm 1)\%}{\sqrt{E[MeV]}} \oplus (3.9 \pm 0.2)\%}$$

The total resolution must also account for the contributions (also determined in this work) of the correction for the charge attenuation (2%) and the estimation of the absolute drift distance for out of time events (3%). We have also studied the **angular distribution** of the electron events finding, although limited by the low statistics, a good homogeneous and isotropic response of the detector. Finally, we have studied the **energy resolution** that can be obtained in the electron energy when computed **using the track length**. The electron energy loss by ionization can be estimated with a resolution of about 20% for energies around 20 MeV, whereas the resolution in measuring the total energy, due to the effect of the bremsstrahlung emissions, is found to be constant and between 40% and 50%.

To summarize, the main achievement of this thesis consists of both, the development of the general reconstruction and analysis set of tools suitable for the study of a wide class of events, and their use in a first study of the stopping muon sample collected with the ICARUS T600 during its technical run. This work demonstrates the capabilities of the ICARUS detector to perform physics analysis and shows that the collaboration is ready for the study of neutrino events and matter stability, once the detector will be installed in the LNGS laboratory in 2003.

Acknowledgements

All my gratitude goes in first place to Professor A. Rubbia to whom I am deeply indebted for having offered me the unique opportunity to work in this exciting project. His guidance and illuminating advice were truly fundamental throughout the elaboration of the present thesis.

The Slow Control sensors were designed, constructed, installed and tested by A. Badertscher, L. Knecht, M. Laffranchi, B. Lisowski, G. Natterer and A. Rubbia. To them my warmest thanks. The continuous help of R. Brunetti, C. Montanari, A. Rappoldi and C. Vignoli was crucial for the steady operation and excellent performance of the system during the T600 technical run. The off-line analysis was carried out in collaboration with A. Badertscher and A. Rubbia. Some technical aspects were understood and clarified thanks to the very helpful discussions with R. Chamizo, C. Montanari and B. Perea.

The development of the display program and the tools for the three-dimensional event reconstruction were carried out in close collaboration with A. Bueno and A. Rubbia. I appreciate the help of I. Gil-Botella and S. Navas-Concha in the optimization of some technical aspects of the hit reconstruction.

The visual scanning of the cosmic ray data was carried out by N. Makrouchina. Thanks to her efficient work, a quick selection of the stopping muon sample was possible. The Monte Carlo files were provided by P. Sala and the signal and noise digitization optimized with the help of I. Gil-Botella and A. Ferrari.

The study of the drift electron lifetime and recombination factor in argon benefited from help, bibliographic orientation and discussions with S. Navas-Concha, F. Pietropaolo, A Rubbia and P. Sala. The healthy competition with R. Dolfini made the study of the electron sample more stimulating. I benefited from many of his suggestions and ideas. Professor W. Fetscher kindly pointed out the importance of the radiative corrections when computing the Michel parameters.

I am indebted to A. Badertscher, A. Bueno and S. Navas-Concha for the careful reading of the manuscript.

In general, I thank all the members of the ICARUS Collaboration since all of them have, to some extent, helped in the realization of the present work.

Very special thanks to R. Bächli, for having taken care of every single detail regarding my studentship at ETH and the correct submission of this dissertation.

During these years I shared wonderful moments with many people, friends and relatives, mainly from Spain and Switzerland, that were drastically reduced during the long final phase of the work. My final and sincere gratitude goes to all of them for their patience, understanding and moral support.

Bibliography

[1] W. Pauli, Letter to the Physical Society of Tubingen (1930) (unpublished); reproduced in Neutrino Physics, ed. K. Winter, Cambridge (1991) 4.

[2] C. L. Cowan Jr. *et al.*, Science **124** (1956) 103.

[3] B. Pontecorvo, Zh. Eksp. theor. Fiz. **33** (1957) 549.
B. Pontecorvo, Sov. Phys. JETP **6** (1958) 429.

[4] SuperKamiokande Collaboration (Y. Fukuda *et al.*), Phys. Rev. Lett. **81** (1998) 1562.

[5] MACRO Collaboration (G. Giacomelli *et al.*), "Atmospheric neutrino oscillations in MACRO". Talk given at NO-VE, Int. Workshop on Neutrino Oscillations in VEnice, Venice, Italy, 24-26 July 2001. hep-ex/0110021.

[6] Soudan-2 Collaboration (W. Anthony Mann *et al.*). Nucl. Phys. Proc. Suppl. **91** (2000) 134.

[7] SNO Collaboration (Q. R. Ahmad *et al.*), Phys. Rev. Lett. **87** (2001) 071301.

[8] SNO Collaboration (Q. R. Ahmad *et al.*), Phys. Rev. Lett. **89** (2002) 011301.

[9] SNO Collaboration (Q. R. Ahmad *et al.*), Phys. Rev. Lett. **89** (2002) 011302.

[10] C. W. Kim and A. Pevsner, "Neutrinos in Physics and Astrophysics", Harwood Academic Publishers, Chur (Switzerland) 1993.

[11] G. Gelmini and R. Roulet, CERN-TH 7541/1994.

[12] E. Majorana, Nuovo Cim. **14** (1937) 171.

[13] M. Gell-Mann, P. Ramond and R. Slansky, "Supergravity", North Holland, Amsterdam (1979).
T. Yanagida, Prog. Theor. Phys. **B135** (1978) 66.

[14] Particle Data Group (K. Hagiwara *et al.*), Phys. Rev. **D66** (2002) 010001.

[15] G. Danby *et al.*, Phys. Rev. Lett. **9** (1962) 193.

[16] Z. Maki *et al.*, Prog. Theor. Phys. **28** (1962) 870.

[17] N. Cabibbo, Phys. Lett. **72B** (1978) 333.

[18] LSND Collaboration (A. Aguilar *et al.*), Phys. Rev. **D64** (2001) 112007.

[19] KARMEN Collaboration (B. Armbruster *et al.*), Phys. Rev. **D65** (2002) 112001.
E. D. Church *et al.*, Phys. Rev. **D66** (2002) 103001.

[20] S. Geer, Phys. Rev. **D57** (1998) 6989.

[21] D. A. Glaser, Phys. Rev. **87** (1952) 665.
D. A. Glaser, Phys. Rev. **91** (1953) 762.
D. A. Glaser, Nuovo Cim. Suppl. **2** (1954) 361.

[22] C. Rubbia, "The Liquid Argon Time Projection Chamber: a New Concept for Neutrino Detector", CERN-EP/77-08, 1977.

[23] ICARUS Collaboration, "ICARUS-I: a proposal for the Gran Sasso Laboratory", INFN/AE-85/7, Frascati (Italy), 1985.

[24] ICARUS Collaboration, "ICARUS-II: A Second-Generation Proton Decay Experiment and Neutrino Observatory at the Gran Sasso Laboratory", Proposal Vol. I & II, LNGS-94/99, 1994.

[25] C. Grupen, "Particle Detectors", Cambridge University Press, Cambridge (1996).

[26] L. S. Miller, S. Howe and W. E. Spear, Phys. Rev. **166** (1968) 871.

[27] B. E. Springett, J. Jortner and M. H. Cohen, J. Chem. Phys. **69** (1978) 2401.

[28] O. Bunemann *et al.*, Can. J. Res. **27** (1949) 191.

[29] E. Buckley *et al.* Nucl. Instr. and Meth. **A275** (1989) 364.

[30] E. Gatti *et al.*, IEEE Trans. Nucl. Sci. **NS-26** (1970) 2910.

[31] P. Cennini *et al.* Nucl. Instr. and Meth. **A342** (1999) 240.

[32] P. Benetti *et al.* Nucl. Instr. and Meth. **A327** (1993) 173.

[33] P. Benetti *et al.* Nucl. Instr. and Meth. **A332** (1993) 395.

[34] P. Benetti *et al.* Nucl. Instr. and Meth. **A333** (1993) 567.

[35] P. Benetti *et al.* Nucl. Instr. and Meth. **A346** (1994) 550.

[36] P. Cennini *et al.* Nucl. Instr. and Meth. **A345** (1994) 230.

[37] ICARUS Collaboration, Nucl. Instr. and Meth. **A333** (1993) 567.

[38] ICARUS Collaboration (F. Arneodo *et al.*), "The ICARUS 50 l LAr TPC in the CERN ν Beam", Proceedings of 36th Workshop On New Detectors, Erice, Italy, 1997, World Scientific (1999) 3.

[39] ICARUS Collaboration (F. Arneodo *et al.*) "Operation of a 10 M^3 ICARUS detector module". 8th Pisa Meeting on Advanced Detector: Frontier Detectors for Frontier Physics, La Biodola, Isola d'Elba, Italy, 21-25 May 2000. Nucl. Instr. and Meth. **A461** (2001) 286.

[40] ICARUS Collaboration, "A first 600 ton ICARUS Detector Installed at the Gran Sasso Laboratory", Addendum to proposal, LNGS-95/10, 1995.

[41] ICARUS Collaboration. "The ICARUS experiment: A second-generation proton decay and neutrino observatory at the Gran Sasso Laboratory. Addendum: Cloning of T600 modules to reach the design sensitive mass", LNGS-EXP 13/89 add. 2/01. ICARUS-TM/2001-09, 2001.

[42] ICARUS Collaboration, "The ICARUS Experiment: A Second-Generation Proton Decay Experiment and Neutrino Observatory at the Gran Sasso Laboratory", LNGS P28/01, LNGS-EXP 13/89 add.1/01 and arXiv:hep-ex/0103008.

[43] A. Ferrari and C. Rubbia, "Muon Momentum Determination by Multiple Scattering in Liquid Argon", ICARUS-TM/99-10, 1999.

[44] G. Acquistapace *et al.*, "The CERN Neutrino beam to Gran Sasso (NGS)", Conceptual Technical Design, CERN 98-02, INFN/AE-98/05, 1998.

[45] C. K. Jung, "Feasibility of a next generation underground water Cherenkov detector: UNO", NNN99 at Stony Brook, hep-ex/0005046, 2000.

[46] ICARUS Collaboration, "Short report on performance evaluation of the ICARUS $10m^3$ Prototype", ICARUS-TM/99-09, 1999.

[47] A. Badertscher *et al.*, "Sensors for the Slow Control of the first T600 half-module", ICARUS-TM/2001-02, 2001.

[48] A. Badertscher, J. Rico and A. Rubbia, "Slow Control results from technical Run in Pavia with the first T600 half-module", ICARUS-TM/2001-06, 2001.

[49] A. Badertscher *et al.*, "Calibration of Pt1000 resistors for their usage as temperature sensors at low temperatures", ICARUS-TM/2000-03, 2000.

[50] P. Cennini, Nucl. Phys. Proc. Suppl. **54** (1997) 133.

[51] Intelligent Instrumentation™, web page: http://www.instrument.com/.

[52] R. J. Yarger, G. Reese and T. King, "MySQL and mSQL", O'Reilly, Sebastopol 1999.

[53] Trolltech, "Qt: a C++ multi-platform toolkit for application development", version 2.3, available: http://www.trolltech.com.

[54] P. Benetti *et al.*, "Pumping system for the ICARUS 600 ton detector", ICARUS-TM/98-17, 1998.

[55] J.E.Jensen *et al.*, "Selected Cryogenic Data Notebook", Volume I. Brookhaven National Laboratory. August 1980.

[56] D. Cline *et al.*, "The High Voltage System for ICARUS-T600", ICARUS-TM/2001-01, 2001.

[57] W. H. Press *et al.*, "Numerical Recipes in C: the art of scientific computing", 2nd edition. Cambridge University Press. Melbourne 1997.

[58] F. James, "MINUIT - Function Minimization and Error Analysis", CERN Program Library, CERN, Geneva (Switzerland) 1998.

[59] S. Navas and A. Rubbia, "A measurement of the drift velocity in the T600 data", ICARUS-TM/2002-01, 2002.

[60] H. Primakoff, Rev. Mod. Phys. **31** (1959) 802.

[61] J. C. Sens, Phys. Rev. **113** (1959) 679.

[62] A. Bertin *et al.*, Phys. Rev. **A7**, Comments and Addenda (1973) 2214.

[63] S. Navas *et al.*, "A measurement of the electron Lifetime and the electron Recombination factor with the T600 data", ICARUS-TM/2002-04, 2002.

[64] S. Amerio, "Status of analysis of muon tracks and calibration in 50 liter". Presentation at the ICARUS Software Meeting, Padova (Italy) September 11-12 2002. (Unpublished).

[65] M. Miyajima *et al.*, Phys. Rev. **A9** (1974) 1438.

[66] W. R. Leo, "Techniques for Nuclear and Particle Physics Experiments", Springer-Verlag, Berlin Heidelberg (1987).

[67] W. Lohmann, R. Kopp and R. Voss, "Energy loss of muons in the range 1-10000 GeV", CERN-85-03 (1985).

[68] H. A. Bethe, Phys. Rev. **89** (1953) 1256.

[69] G. Musiol *et al.*, "Kern- und Elementarteilchenphysik", VCH Verlagsgesellschft, Weinheim, 1988.

[70] W. Heitler, "The Quantum Theory of Radiation", Oxford, 1954.

[71] J. Kremer *et al.* Phys. Rev. Lett. **83** (1999) 4241.

[72] M. Motoki *et al.* Proc. 27th Int. Cosmic Ray Conf. Hamburg, Vol. 3 (2001) 927.

[73] M. J. Berger, J. S. Coursey and M. A. Zucker, "ESTAR, PSTAR, and ASTAR: Computer Programs for Calculating Stopping-Power and Range Tables for Electrons", Protons, and Helium Ions (version 1.21) Available: http://physics.nist.gov/Star. National Institute of Standards and Technology, Gaithersburg (MD) 1999.

[74] A. Fassò, A. Ferrari, J. Ranft and P. R. Sala, "Electron-photon transport in FLUKA: status", Proc. of the Monte Carlo 2000 Conference, Lisbon, 23-26 October 2000, A. Kling *et al.* eds., (Springer, Berlin, 2001).

[75] I. Gil-Botella and J. Rico, "Simulation of signal digitization and noise in Monte-Carlo". Presentation at the ICARUS Software Meeting, CERN, Geneva (Switzerland) March 25-26 2002. (Unpublished).

[76] ICARUS Collaboration, "Analysis of the liquid Argon purity in the very large ICARUS 300 ton time projection chamber". Paper in preparation.

[77] L. D. Landau; J. Exp. Phys. (USSR) **8** (1944) 201;
D. H. Wilkinson; Nucl. Instr. and Meth. **A383** (1996) 513.

[78] L. Onsager, Phys. Rev. **54** (1938) 554.

[79] R. T. Scalettar *et al.*, Phys. Rev. **A25** (1982) 2419.

[80] G. Jaffe, Ann. Phys. (Leipzig) **42** (1913) 303.

[81] H. A. Kramers, Physica (Utrecht) **18** (1952) 665.

[82] J. B. Birks, Proc. Phys. Soc. **A64** (1951) 874.

[83] J. Thomas and D. A. Imel, Phys. Rev. **A36** (1987) 614.

[84] E. Aprile *et al.*, Nucl. Instr. and Meth. **A261** (1987) 519.

[85] E. Bernardini, "Performance of the 10 m^3 Liquid Argon ICARUS module", Ph. D. thesis, Università di L'Aquila (2002).

[86] S. Navas, A. Rubbia and F. Pietropaolo, "On the use of a precise measurement of the most probable energy loss (Δ_{mp}) to estimate a (muon) track momentum", ICARUS-TM/2002-11.

[87] R. Dolfini, presentation at the ICARUS Software Meeting, Padova, Sep. 11-12 2002. (Paper in preparation).

[88] L. Michel, Proc. Phys. Rep. **A63** (1950) 514.

[89] R. E. Behrends, R. J. Finkelstein and A. Sirlin, Phys. Rev. **101** (1956) 866.

[90] T. Kinoshita and A. Sirlin, Phys. Rev. **113** (1959) 1652.

[91] W. Fetscher, H. J. Gerber and K. F. Johnson, Phys. Lett. **B173** (1986) 102.

[92] J. Peoples, Columbia Univerity Report No. NEVIS-147, 1966 (Unpublished).
M. Bardon *et al.*, Phys. Rev. Lett. **14** (1965) 449.

[93] B. A. Sherwood, Phys. Rev. **156** (1967) 1475.

[94] D. Fryberger, Phys. Rev. **166** (1968) 1379.

[95] S. E. Derenzo, Phys. Rev. **181** (1969) 1854.

[96] SLD Collaboration (K. Abe *et al.*), Phys. Rev. Lett. **78** (1997) 4691.

[97] CLEO Collaboration (J. P. Alexander *et al.*) Phys. Rev. **D56** (1997) 5320.

[98] ARGUS Collaboration (H. Albrecht *et al.*), Phys. Lett. **B431** (1998) 179.

[99] OPAL Collaboration (K. Ackerstaff *et al.*), Eur. Phys. J. **C8** (1999) 3.

[100] DELPHI Collaboration (P. Abreu *et al.*), Eur. Phys. J. **C16** (2000) 229.

[101] ALEPH Collaboration (A. Heister *et al.*), Eur. Phys. J. **C22** (2001) 217.

Curriculum Vitae

Personal Data

First Names	Francisco Javier
Last Names	Rico Castro
Date of birth	December 2nd, 1973
Place of birth	Granada (Spain)
Nationality	Spanish

Education

1979-1987	Primary School. Granada (Spain).
1987-1990	High School. Granada (Spain).
1990-1996	Undergraduate studies in Theoretical High Energy Physics. University of Granada (Spain).
1996-1998	Diploma in Theoretical High Energy Physics, University of Granada (Spain). Title of the thesis: "Study of the Contact Terms in Charged Current Processes at HERA".
1998-2002	Graduate education in Experimental Particle Physics at ETH-Zürich.